

# Structure and Properties of Porous Ceramic ZrO<sub>2</sub>-MgO Composites for Biomedical Application

# Ph.D. Dissertation

by

**Rusul Ahmed Shakir Alshalal** 

(MSc in Materials Engineering)

# **Antal Kerpely Doctoral School of Materials Science and Technology**

Hungary, Miskolc

2025





# Structure and Properties of Porous Ceramic ZrO<sub>2</sub>-MgO Composites for Biomedical Application

A PhD dissertation submitted to Antal Kerpely Doctoral School of Materials Science and Technology for the degree of Doctor of Philosophy in the material and chemical engineering as a part of Stipendium Hungaricum Scholarship

By **Rusul Ahmed Shakir Alshalal**(MSc in Materials Engineering)

Supervisor:

Dr. Róbert Géber, associate professor

Head of the Doctoral School:

Prof. Dr. Valéria Mertinger, DSc.

Institute of Energy, Ceramics and Polymer Technology
Faculty of Materials and Chemical Engineering
University of Miskolc
Hungary, 2025

#### Acknowledgements

God is the first and foremost should get all the praise and glory since He has been my source of strength and direction during this whole journey. Nothing would have been possible on this voyage had He not given His blessing.

My sincere appreciation is extended to my supervisor, Dr. Róbert Géber, for his important advice, inspiration, and unwavering support throughout my PhD studies. His knowledge, and enlightening feedback have been crucial to accomplishing this Ph.D. dissertation.

The members of my thesis reviewers also have my deepest gratitude for the insightful feedback, helpful recommendations, and words of encouragement they provided, all of which improved my research and helped shape my dissertation.

To my amazing husband (Marwan) and son (Julian), I am eternally grateful for your unfaltering love, patience, and support throughout this whole process. My husband, I am eternally grateful to you for your unending love, understanding, and encouragement, even during the worst of times. Your faith in me has served as my main source of inspiration. My heartfelt thanks go to my parents for their endless love and support.

My sincere gratitude is extended to my colleagues Dr. Garami Attila, Dr. Emese Kurovics, Dr. Jamal Eldin Fadoul Mohammed, Alexandra Hamza, Peter Almasi, and Mr. Árpád Kovács for their help, support, and motivation, their participation, conversations, and fellowship have made the journey both fruitful and delightful. I deeply appreciate the support and assistance of Ágnes Solczi, I am grateful for her guidance and for facilitating all the administrative tasks with great care.

I am also grateful for the funding provided by the Stipendium Hungaricum Scholarship, which is offered by the University of Miskolc, Institute of Energy, Ceramics and Polymer Technology and the Hungarian government. Additionally, from the application process until graduation, the Tempus Public Foundation (TPF) in Hungary provided me with ongoing administrative help, for which I am grateful.

I express my gratitude to the Ministry of Higher Education and Scientific Research (Iraq) and the Embassy of the Republic of Iraq for their constant encouragement throughout my Ph.D. studies.

Rusul
Miskolc, 2025

#### **Supervisor's recommendation**

Rusul Ahmed Shakir Alshalal started her PhD studies in September 2021, then with a different supervisor. Due to the unexpected and sudden passing of her supervisor in February 2022, a change of supervisor was required.

Rusul carried out her research on "Structure and Properties of Porous Ceramic ZrO<sub>2</sub>-MgO Composites for Biomedical Application". Her experiments involved the preparation, and characterization of zirconia-alumina-magnesia porous ceramics using an eco-friendly method, called starch consolidation casting (SCC). To achieve her goals, she used potato and tapioca starches as body and pore-forming additives. By changing the quantity and type of materials used together with the optimalization of sintering parameters, the candidate aimed to influence the pore structure and mechanical strength of porous bone replacement ceramics to make the developed ceramic suitable for medical applications. The Candidate identified a potential application for the porous ceramic composites developed during the investigation in the area of bone replacement ceramics.

During her research, she conducted several studies. She then used the results of these studies to optimise the microstructure and properties of porous ceramics. She used advanced testing methods to characterize her samples and evaluated her data using statistical methods and novel machine learning techniques.

The Candidate carried out her research work with great enthusiasm and commitment. She always performed her laboratory work with due diligence and attempted to find solutions to any problems that arose independently. She planned her experiments independently, taking into account her previous results, and then consulted with her supervisor. She was always open to acquiring new knowledge.

She presented her results at numerous national and international conferences and published them in high ranked journals, thereby fulfilling the publication requirements of the Antal Kerpely Doctoral School of Materials Science and Technology.

As her supervisor, I recommend the dissertation and the theses formulated therein for acceptance, and I support the awarding of the PhD degree.

Miskolc, 14th October 2025

Róbert Géber

# List of abbreviations and notations

A	Cross-sectional area
AD	Apparent density
Al	Aluminum
Al <sub>2</sub> O <sub>3</sub>	Aluminum oxide
Al <sub>2</sub> CiO <sub>5</sub>	Aluminum titanate
AP	Apparent porosity
ASTM	American Society for Testing and Materials
ATZ	All <sub>2</sub> O <sub>3</sub> toughened ZrO <sub>2</sub>
	Barium zirconate
BaZrO <sub>3</sub>	
BCP	Biphasic calcium phosphate
CaCO <sub>3</sub>	Calcium carbonate
CaO	Calcium oxide
CO <sub>2</sub>	Carbon dioxide
c-ZrO <sub>2</sub>	Cubic zirconia phase
DLP	Digital light processing
Dolapix CE64	Deflocculant
E	Young's modulus
EA	Energy absorption
EDS	Energy dispersive spectroscopy
F	Applied load
Fap	Fluorapatite
FDM	Fused deposition modelling
Н	Hardness
h	Hours
HA	Hydroxyapatite
HV	Vickers hardness
K	Fracture toughness
k	Thermal conductivity
LS	Linear shrinkage
Mg	Magnesium
MgO	Magnesium oxide
MIP	Mercury intrusion porosimetry
mol.%	Mole percentage
m-ZrO <sub>2</sub>	Monoclinic-zirconia
0	Oxygen
P	Pressure
PCL	Polycaprolactone
PFA	Pore forming agents
PICN	Polymer-infiltrated ceramic network
PMMA	Polymethyl methacrylate
PP	Polypropylene
PVP	Polyvinylpyrrolidone
r	Correlation coefficient
	Pore radius
$\frac{r}{r^2}$	Radius squared
SCC	Starch consolidation casting
	Scanning Electron Microscope
SEM	<u> </u>
SiC	Silicon Carbide
SiO <sub>2</sub>	Silicon dioxide
ST	Sintering time
TiO <sub>2</sub>	Titanium Dioxide
TMA	Dilatometric, thermomechanical analysis

t-ZrO <sub>2</sub>	Tetragonal zirconia phase		
UTS	Maximum ultimate tensile strength		
$V_0$	Volume of the samples before sintering		
$V_1$	Volume of the samples after sintering		
Vol %	Volume percentage		
VS	Volume shrinkage		
WA	Water absorption		
W <sub>imm</sub> .	Weight after immersing in water for 24 hours		
W <sub>sat.</sub>	Weight after saturating with water		
W <sub>sint.</sub>	Weight after sintering		
wt.%	Weight percentage		
XRD	X-Ray diffraction		
$Y_2O_3$	Yttrium (III) oxide		
YSZ	Yttria stabilized zirconia		
Zr	Zirconium		
$ZrO_2$	zirconia		
ZrSiO <sub>4</sub>	Zirconium (IV) silicate		
ZTA	ZrO <sub>2</sub> toughened Al <sub>2</sub> O <sub>3</sub>		
θ	Contact angle		
2Θ	Diffraction angles		
50:50 P+T	Potato and tapioca starch at 50:50 percent ratio		
σ	Compressive strength		
$\sigma_t$	Tensile strength		
$\sigma_f$	Flexural strength		
ρ	Electrical resistivity		
π Mathematical constant, approximate			
α-Al <sub>2</sub> O <sub>3</sub> Corundum alumina phase			
γ Mercury surface tension			
β-Ca <sub>2</sub> SiO <sub>4</sub> Dicalcium silicate			
β-ТСР	Beta-tricalcium phosphate		

# List of units

°C	Degree Celsius			
°C/min	Degree Celsius per minute			
μm	Micrometer			
g	Gram			
g/cm <sup>3</sup>	Gram per cubic centimeter			
GPa	Giga pascal			
GΩ·m	Gigaohm-meter			
J/g	Joule per gram			
$mm^2$	Millimeter squared			
MPa	Newton per square millimeter			
MPa√m	Newton per square millimeter- square root of meter			
nm	Nanometer			
nN/m	Nanonewtons per meter			
rpm	Revolutions per minute			
sec	Second			
W/m·K	Watts per meter Kelvin			

### **Table of contents**

Acknowledgements	I
Supervisor's recommendation	II
List of abbreviations and notations	II
List of units	V
List of figures	VIII
List of tables	XI
Abstract	1
1. Chapter One – Literature review, knowledge gaps and the aims	3
1.1 Theoretical background and literature overview	3
1.1.1 ZrO <sub>2</sub> ceramics in general	3
1.1.2 ZrO <sub>2</sub> -Al <sub>2</sub> O <sub>3</sub> -MgO ceramic composites	4
1.1.3 Porous ceramics	5
1.1.4 Techniques for producing porous-structured ceramic composites	7
1.1.5 Starch consolidation casting	10
1.1.6 ZrO <sub>2</sub> -based porous structures ceramic composites for biomedical applications	12
1.2 Knowledge gaps and the aims of the thesis	13
2. Chapter Two – Experimental part	17
2.1 Materials	17
2.2 Preparation of moulds	17
2.3 Preparation of porous structured ceramics	18
2.3.1 Preparation of slip slurries	18
2.3.2 Ceramic composites consolidation	20
2.3.3 Pre-sintering and sintering	21
2.4 Testing methods	22
2.4.1 Characterization of raw materials	22
2.4.2 Characterization techniques of porous ceramic composites	24
3. Chapter Three - Results and discussion	29
3.1 Raw materials characterization results	29
3.1.1 XRD test results of raw materials	29
3.1.2 SEM test results for raw materials	30
3.1.3 Particle size distribution test results of raw materials	33
3.1.4. Moisture content and swelling factor of the starches test results	34
3.2 Porous ceramics characterization results	35

	distilled water content	35
	3.2.2 Test results of studying the effect on different content of Al <sub>2</sub> O <sub>3</sub> with different types of starch	
	3.2.3 Test results of studying the effect of using progressive pre-sintering and sintering at different temperatures	ıt
	3.2.4 Test results of studying the effect of using different sintering holding time	73
4. C	Chapter Four - Conclusions	84
	.1 Conclusion of studying the effect of different content and type of starches with different distilled vater content	
4.	.2 Conclusion of studying the effect of different content of Al <sub>2</sub> O <sub>3</sub> with different types of starches	85
	.3 Conclusion of studying the effect of progressive pre-sintering and sintering at different emperatures	87
4.	.4 Conclusion of studying the effect of different sintering holding time	88
5. C	Chapter Five - Claims/New scientific results	90
List	of Publications	105
Refe	erences	107
App	pendix A	122
App	pendix B	127

# List of figures

Fig. 1.1 Crystallographic phases of ZrO <sub>2</sub> ceramic	3
Fig. 1.2 The main characteristics of porous ceramics	6
Fig. 1.3 Figure illustrating several processing methods for the manufacturing of porous ceramics	7
Fig. 1.4 The principal mechanism of the starch consolidation casting technique	10
Fig. 2.1 (a) The 3D printing process, (b) Stereolithography 3D image of designed moulds	17
Fig. 2.2 The 3D printed moulds	18
Fig. 2.3 Laboratory milling machine	18
Fig. 2.4 Preparation of slurry by magnetic stirrer	18
Fig. 2.5 The prepared ceramic green bodies after de-moulding	20
Fig. 2.6 The pre-sintering and sintering profiles	21
Fig. 2.7 The preparation procedure for porous-structured ceramic	22
Fig. 2.8 CILAS 715 equipment.	23
Fig. 2.9 Moisture determination balance.	23
Fig. 2.10 Dilatometry (TMA) test	25
Fig. 2.11 Saturated sample	26
Fig. 3.1 XRD pattern for m-ZrO <sub>2</sub> powder.  Fig. 3.2 XRD pattern for Al <sub>2</sub> O <sub>3</sub> powder.	
Fig. 3.3 XRD pattern for MgO powder	29
Fig. 3.4 SEM images for m-ZrO <sub>2</sub> powder	30
Fig. 3.5 SEM images for Al <sub>2</sub> O <sub>3</sub> powder	31
Fig. 3.6 SEM images for MgO powder	31
Fig. 3.7 SEM image for tapioca starch particles	32
Fig. 3.8 SEM image for potato starch particles	33
Fig. 3.9 The particle size distribution of the ceramic raw materials	33
Fig. 3.10 Swelling factor via mixing time for potato and tapioca starches	34
Fig. 3.11 Apparent density via potato starch content (a) and tapioca starch content (b)	35
Fig. 3.12 Apparent porosity via potato starch content (a) and tapioca starch content (b)	36
Fig. 3.13 Volume shrinkage via potato starch content (a) and tapioca starch content (b)	36
Fig. 3.14 SEM micrographs of samples with:	37
- Potato starch at 10 wt.% (a), 30 wt.% (b), - Tapioca starch at 10 wt.% (c), 30 wt.% (d)	37
Fig. 3.15 SEM micrographs of samples with:	38
(a) 30 wt.% tapioca starch and 60 wt.% suspension concentration	38
(b) 10 wt.% potato starch and 70 wt.% suspension concentration	38
Fig. 3.16 Compressive strength via potato starch content (a) and tapioca starch content (b)	38

Fig. 3.17 Pair plot of four study features of samples prepared with different potato starch wt.%	40
Fig. 3.18 Pair plot of four study features of samples prepared with different tapioca starch wt.%	41
Fig. 3.19 Pair plot of four study features of samples prepared with different suspension wt.%	42
Fig. 3.20 Bar plot of the coefficient of variation (CV%) for the samples with different starches and w wt.%	
Fig. 3.21 Apparent density via Al <sub>2</sub> O <sub>3</sub> content: (a) after pre-sintering, (b) after sintering	44
Fig. 3.22 Apparent porosity via Al <sub>2</sub> O <sub>3</sub> content: (a) after pre-sintering, (b) after sintering	45
Fig. 3.23 Volume shrinkage via Al <sub>2</sub> O <sub>3</sub> content: (a) after pre-sintering, (b) after sintering	46
Fig. 3.24 SEM micrographs of porous ceramics after pre-sintering,	46
using potato starch, (b) using tapioca starch, and (c) using 50:50 wt.% tapioca + potato	46
Fig. 3.25 SEM micrographs of porous ceramics after sintering,	47
(a) using potato starch, (b) using tapioca starch, and (c) using 50:50 wt.% tapioca + potato	47
Fig. 3.26 XRD pattern for pre-sintered ceramic with 15 wt.% Al <sub>2</sub> O <sub>3</sub>	48
Fig. 3.27 XRD pattern for pre-sintered ceramic with 30 wt.% Al <sub>2</sub> O <sub>3</sub>	48
Fig. 3.28 XRD pattern for sintered ceramic with 15 wt.% Al <sub>2</sub> O <sub>3</sub>	49
Fig. 3.29 XRD pattern for sintered ceramic with 30 wt.% Al <sub>2</sub> O <sub>3</sub>	49
Fig. 3.30 Pore size distribution of 67.5 wt.% ZrO <sub>2</sub> , 30 wt.% Al <sub>2</sub> O <sub>3</sub> , and 2.5 wt.% MgO samples	50
<b>Fig. 3.31</b> The pore size distribution via Relative pore volume of 67.5 wt.% ZrO <sub>2</sub> , 30 wt.% Al <sub>2</sub> O <sub>3</sub> , and wt.% MgO samples	
Fig. 3.32 Compressive strength vs. Al <sub>2</sub> O <sub>3</sub> content	52
$\textbf{Fig. 3.33} \ \text{Fracture mode on both sides of the fractured surface of sample containing 15 wt.} \% \ Al_2O_3$	53
Fig. 3.34 Pair plot of four study features of samples prepared with different Al <sub>2</sub> O <sub>3</sub> wt.%	54
Fig. 3.35 Bar plot of the coefficient of variation (CV%)	55
<b>Fig. 3.36</b> SEM micrographs of sintered porous ceramics (67.5 wt.% m-ZrO <sub>2</sub> , 2.5 wt.% MgO, and 30 v Al <sub>2</sub> O <sub>3</sub> ): (a) and (b) without pre-sintering, (c) and (d) with pre-sintering	
Fig. 3.37 Compressive strength of the samples	57
Fig. 3.38 Apparent density at different sintering temperatures	58
Fig. 3.39 Apparent porosity at different sintering temperatures	58
Fig. 3.40 volume shrinkage at different sintering temperatures	59
Fig. 3.41 Compressive strength at different sintering temperatures	59
Fig. 3.42 Thermal shrinkage behavior of the sample during sintering process	60
Fig. 3.43 XRD pattern after sintering at 1400°C or 1500°C (with pre-sintering)	61
Fig. 3.44 XRD pattern after sintering at 1600°C (with pre-sintering)	61
Fig. 3.45 SEM micrographs for porous ceramics sintered at:1400°C (a, b), 1500°C (c, d), and 1600°C (f)	
<b>Fig. 3.46</b> EDS point analysis of two different points in the sample sintered at 1600°C	64

Fig. 3.47 EDS point analysis of two different points in the sample sintered at 1400°C65
<b>Fig. 3.48</b> SEM micrographs for sintered porous ceramics at: 1400°C (a), 1500°C (b), 1600°C (c) (67.5 wt.% m-ZrO <sub>2</sub> , 2.5 wt.% MgO, and 30 wt.% Al <sub>2</sub> O <sub>3</sub> )
<b>Fig. 3.49</b> Pore size distribution of porous structured sample sintered at 1400°C (67.5 wt.% m-ZrO <sub>2</sub> , 2.5 wt.% MgO, and 30 wt.% Al <sub>2</sub> O <sub>3</sub> )
<b>Fig. 3.50</b> Pore size distribution of porous structured sample sintered at 1500°C (67.5 wt.% m-ZrO <sub>2</sub> , 2.5 wt.% MgO, and 30 wt.% Al <sub>2</sub> O <sub>3</sub> )
<b>Fig. 3.51</b> Pore size distribution of porous structured sample sintered at 1600°C (67.5 wt.% m-ZrO <sub>2</sub> , 2.5 wt.% MgO, and 30 wt.% Al <sub>2</sub> O <sub>3</sub> )
Fig. 3.52 Pair plot of four study features for the samples after sintering at 1400°C or 1500°C71
Fig. 3.53 Pair plot of four study features for the samples after sintering at 1600°C71
Fig. 3.54 Bar plot of the coefficient of variation (CV%)
Fig. 3.55 Apparent density at different sintering holding time
Fig. 3.56 Apparent porosity at different sintering holding time
Fig. 3.57 Volume shrinkage at different sintering holding time
Fig. 3.58 Compressive strength at different sintering holding time
Fig. 3.59 Sample (67.5 wt.% m-ZrO <sub>2</sub> , 2.5 wt.% MgO, and 30 wt.% Al <sub>2</sub> O <sub>3</sub> ) after 4 hours sintering holding time
<b>Fig. 3.60</b> SEM micrographs for porous ceramics (67.5 wt.% m-ZrO <sub>2</sub> , 2.5 wt.% MgO, and 30 wt.% Al <sub>2</sub> O <sub>3</sub> ) sintered at 1600°C for: 2 hours (a, b), 3 hours (c, d), and 4 hours (e, f)
<b>Fig. 3.61</b> XRD pattern for sintered porous ceramic (67.5 wt.% m-ZrO <sub>2</sub> , 2.5 wt.% MgO, and 30 wt.% Al <sub>2</sub> O <sub>3</sub> ) at 1600°C for 3 hours
<b>Fig. 3.62</b> The pore size distribution of the sample (67.5 wt.% m-ZrO <sub>2</sub> , 2.5 wt.% MgO, and 30 wt.% Al <sub>2</sub> O <sub>3</sub> ) sintered at 1600°C for 2 hours
<b>Fig. 3.63</b> The pore size distribution of the sample (67.5 wt.% m-ZrO <sub>2</sub> , 2.5 wt.% MgO, and 30 wt.% Al <sub>2</sub> O <sub>3</sub> ) sintered at 1600°C for 3 or 4 hours
Fig. 3.64 Pair plot of four study features for the samples after 2 hours sintering holding time
Fig. 3.65 Pair plot of four study features for the samples after 3 hours or 4 hours sintering holding time 81
Fig. 3.66 Bar plot of the coefficient of variation (CV%)

# List of tables

<b>Table 1.1</b> Various outcomes of using distinct manufacturing processes in the fabrication of ceramic porous structures (The full version of this table can be seen in Appendix A.)
<b>Table 1.2</b> Some results from using various pore-forming agents in the fabrication of ceramic porous structures. (The full version of this table can be seen in Appendix A.)
<b>Table 1.3</b> Some results of the use of ZrO <sub>2</sub> -based ceramics in biomedical applications (The full version of this table can be seen in Appendix A.)
Table 2.1 Properties and origin of raw materials   17
Table 2.2 Mix compositions for the first study (in wt.%).   19
Table 2.3 Mix compositions for the second study (in wt.%)   19
Table 2.4 Mix compositions for the third and fourth studies (in wt.%)
Table 3.1 The D10, D50, and D90 of the ceramic raw materials
Table 3.2 The correlation matrix with using of potato starch
Table 3.3 The correlation matrix with using of tapioca starch   39
Table 3.4 Correlation relationships between the variables for samples prepared with potato and tapioca starches
Table 3.5 Correlation relationships between the variables for samples prepared with different suspension wt.%         43
<b>Table 3.6</b> MIP results of 67.5 wt.% ZrO <sub>2</sub> , 30 wt.% Al <sub>2</sub> O <sub>3</sub> , and 2.5 wt.% MgO samples
Table 3.7 Pearson correlation matrix for the experimental data with using tapioca starch         53
Table 3.8 Pearson correlation matrix for the experimental data with using potato starch         53
Table 3.9 Pearson correlation matrix for the experimental data with using tapioca + tapioca starch 53
$\textbf{Table 3.10} \ \text{Correlation relationships between the variables for the samples with different } Al_2O_3 \ wt.\% \ 55$
Table 3.11 MIP results
Table 3.12 The Pearson correlation matrix of the experimental data.    70
Table 3.13 Correlation relationships between the variables after sintering at different temperature70
$\textbf{Table 3.14} \ MIP results of the samples (67.5 wt.\% m-ZrO_2, 2.5 wt.\% MgO, and 30 wt.\% Al_2O_3)79$
Table 3.15 The Pearson correlation matrix of the experimental data.    80
<b>Table 3.16</b> Correlation relationships between the variables after sintering for different holding time 80

#### Abstract

Porous ceramics are composite materials that consist of a ceramic substrate and pores that are dispersed throughout the ceramic matrix. The special characteristics of porous ceramics – their low density, large surface area, and chemical inertness – have made them an increasingly popular product in the ceramics industry recently. Zirconia-based porous ceramics have emerged as potential materials for biomedical applications, especially in bone replacement, owing to their biocompatibility, mechanical durability, and adjustable porosity. Their mechanical characteristics and performance are controlled by the porosity, pore morphology and pore size distribution, which is the key to their effectiveness. Diverse techniques, including gel casting, freeze casting, and direct foaming, have been used to fabricate porous structures that replicate the natural architecture of the bone. Nonetheless, these approaches often encounter difficulties in attaining a balance among porosity, mechanical strength, and structural homogeneity, all of which are essential for effective bone implantation. The intricacy and expense of these processes necessitated the exploration of more accessible and cost-effective techniques for the production of porous materials. Therefore, other techniques were developed, for example the starch consolidation casting technique, that provide a direct control of porosity during production.

This PhD research work focuses on the manufacturing, characterisation, and optimisation of novel zirconia-alumina-magnesia porous ceramics via the starch consolidation casting method, an economical and eco-friendly methodology for producing porous structures. Potato and tapioca starches were used as body and pore-forming agents, while the distilled water content was altered to improve the rheological properties of the ceramic slurries. The morphology of the pores in the surface of the samples is essential for medical applications, particularly in bone replacement, since these pores enhance surface area and hence improve the bonding strength between the artificial bone and the living tissue. This PhD study assessed the influence of varying starch percentages and types on achieving the desired pore morphology. Mechanical properties are also essential in bone replacement applications; hence, this PhD research evaluated the impact of varying ratios of ceramics oxides and starches to achieve optimal mechanical strength.

To produce the porous structure, ceramic slurries were prepared with different starch type and content, zirconia-to-alumina ratios, and powder-to-water ratios; subsequently, these slurries were poured into impermeable plastic moulds and heated at 80°C for 2 hours to allow the starch to swell and gelatinize. The samples are then de-moulded and gradually pre-sintered at 1100°C. The

sintering temperature is critical and influences the mechanical characteristics and pore morphology on the surface. Consequently, it is essential to investigate the impact of varying sintering temperatures and holding time. Therefore, the samples were sintered at 1400°C, 1500°C, and 1600°C for varying holding time to investigate their effects on microstructural development, densification, and mechanical characteristics. A thorough assessment was performed to evaluate the impact of these factors (starch type and content, zirconia-to-alumina ratios, powder-to-water ratios, sintering temperatures, and sintering holding time) on the final characteristics of the ceramics, including apparent density, apparent porosity, volume shrinkage, and compressive strength. Microstructural characterization was conducted utilizing scanning electron microscopy (SEM) to investigate pore morphology and interconnectivity, X-ray diffraction (XRD) to identify phase compositions and transformations, and mercury intrusion porosimetry (MIP) to measure pore opening size distribution.

SEM analysis illustrates that in all the pre-sintered and sintered samples, large areas with a uniform distribution of alumina and zirconia grains were present. It confirms the effectiveness of the mixing procedure that was followed. The findings indicated that increasing the starch content markedly improved overall porosity, decreased density, and affected the mechanical strength of the resultant porous ceramics. A higher alumina content was associated with an increase in apparent porosity and a reduction in volume shrinkage and apparent densities. The main advantage of alumina is its ability to improve compressive strength serving as a barrier against fracture development. Pre-sintering effectively reduced the rate of shrinkage during the final sintering stage; this resulted in more controlled and predictable shrinkage, leading to better dimensional stability and reduced risk of defects in the final product. Porous ceramics with adequate mechanical strength, interconnected porosity, and bio-functionality were generated by optimizing sintering conditions and material combinations, making them ideal for biomedical applications, notably bone replacement. The results of the study highlight the efficacy of starch consolidation casting as a technique for producing bio-ceramics with customized characteristics. To comprehend the intricate interactions among the different variables in the experimental data, it is crucial to analyse their pairwise correlations. Pair plots serve as an effective exploratory method for visualizing distributions and correlations among numerous variables, therefore clarifying the impact of processing conditions and compositions on the prepared bone replacement ceramics performance.

#### 1. Chapter One - Literature review, knowledge gaps and the aims

#### 1.1 Theoretical background and literature overview

#### 1.1.1 ZrO<sub>2</sub> ceramics in general

ZrO<sub>2</sub> is a crystalline structure of zirconium dioxide. It comes in several phases and it is a type of polycrystalline ceramic that does not have a glassy phase [1]. The spatial configuration of atoms in ZrO<sub>2</sub> is defined by certain crystallographic structures, which exemplify a feature referred to as polymorphism. ZrO<sub>2</sub> crystals are organized into crystalline cells that can be classified into three crystallographic phases (Fig. 1.1):

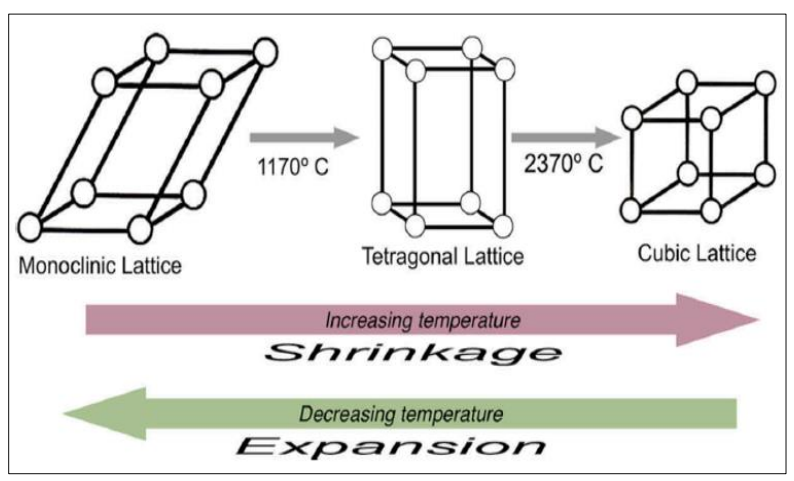


Fig. 1.1 Crystallographic phases of ZrO<sub>2</sub> ceramic [2]

The cubic (c-ZrO<sub>2</sub>) phase, characterized by a straight prism with square faces. The tetragonal (t-ZrO<sub>2</sub>) is characterized by a straight prism with rectangular sides, whereas the monoclinic (m-ZrO<sub>2</sub>), known as mineral baddeleyite, is represented by a distorted prism with parallel sides. The c-ZrO<sub>2</sub> phase is stable above 2370°C and exhibits moderate mechanical properties. The t-ZrO<sub>2</sub> phase is stable between 1170°C and 2370°C, facilitating the production of ceramics with enhanced mechanical properties. In contrast, the m-ZrO<sub>2</sub> phase stable at room temperature up to 1170°C, demonstrates diminished mechanical performance and may lead to decreased cohesion among ceramic particles, thereby reducing density [2]. The properties of m-ZrO<sub>2</sub> can be enhanced with the addition of other ceramic oxides [3]. During heating, at 1170°C, the m-ZrO<sub>2</sub> changes to a t-ZrO<sub>2</sub> and shrinks by 4-5 vol%. At 2370°C, the t-ZrO<sub>2</sub> structure deforms even further into a c-ZrO<sub>2</sub>. During cooling, at a temperature of roughly 950°C, pure ZrO<sub>2</sub> transforms from t-ZrO<sub>2</sub> to m-ZrO<sub>2</sub>, with a 4% volume expansion. As a result of this volume expansion, shear stresses are generated, and these stresses forbid the opening of a proceeding crack, this leads to increase the toughness of ZrO<sub>2</sub> at room temperature [3]. The coordination number of c-ZrO<sub>2</sub> and t-ZrO<sub>2</sub> is eight, while that

of m-ZrO<sub>2</sub> is seven. Because of the strong Zr-O covalent bond in a coordination number of seven, m-ZrO<sub>2</sub> is shown to be thermodynamically stable at lower temperatures [4].

ZrO<sub>2</sub> is prepared by the calcination process of zirconium compounds and taking advantage of their great thermostability. ZrO<sub>2</sub> is a cost-effective, non-toxic, and sustainable metal oxide with many potential applications [5]. ZrO<sub>2</sub> ceramic is an advanced biomaterial extensively used in medical engineering due to its exceptional biocompatibility and mechanical strength compared to other ceramic materials. The surface strength rises as the particle area is minimized, aligning the theoretical and actual density values [6]. ZrO<sub>2</sub> has good mechanical properties similar to those of metals with a white colour similar to tooth colour [7]. Therefore, it is widely used in dental applications. In contrast to most ceramics, ZrO<sub>2</sub> has high fracture toughness, making it very resistant to mechanical stress and fracturing. It has superior wear resistance, making it suitable for applications requiring extended service life. ZrO<sub>2</sub> has a melting point of around 2715°C, enabling it to endure harsh temperatures. It serves as an exceptional thermal insulator, making It appropriate for applications necessitating heat resistance [8]. It can withstand harsh conditions since it is resistant to acid, alkali, and oxidation chemical attacks [9]. Both in vitro and in vivo investigations have validated the superior biocompatibility of ZrO<sub>2</sub> powders [10]. They are chemically harmless, which allows for strong cell adhesion, thus, there have been no reports of any side effects, either local or systemic. Neither fibroblasts nor blood cells showed any signs of mutagenicity or oncogenicity. The dust generated by milling ZrO<sub>2</sub>, as opposed to that from asbestos, may not induce health issues [11].

#### 1.1.2 ZrO<sub>2</sub>-Al<sub>2</sub>O<sub>3</sub>-MgO ceramic composites

ZrO<sub>2</sub> showed the most promise as a biomaterial when combined with Al<sub>2</sub>O<sub>3</sub> ceramics [12]. When Al<sub>2</sub>O<sub>3</sub> is the primary component, the materials are named ZrO<sub>2</sub> toughened Al<sub>2</sub>O<sub>3</sub> (ZTA), and when ZrO<sub>2</sub> is the predominant component, they are called Al<sub>2</sub>O<sub>3</sub> toughened ZrO<sub>2</sub> (ATZ). The advantages of ZrO<sub>2</sub>-Al<sub>2</sub>O<sub>3</sub> composites are the merging of the features of Al<sub>2</sub>O<sub>3</sub> (high stiffness, high hardness) with the properties of ZrO<sub>2</sub> (high toughness, high strength), with the added benefit of improved slow crack growth resistance. The advantages of this combination make the ZrO<sub>2</sub>-Al<sub>2</sub>O<sub>3</sub> composites system a good choice for functional and structural applications [13]. The presence of Al<sub>2</sub>O<sub>3</sub> increases the overall stiffness of the matrix due to its elastic modulus, which is twice that of ZrO<sub>2</sub>. The inclusion of secondary hard particles resulted in fracture deflection, which is known as micro-crack toughening. This phenomenon ultimately increased the overall toughness of the

composites [14]. Many investigations on the tribological and mechanical characteristics of various ATZ compositions were published in recent years [15]. The density of ATZ composites is influenced by the Al<sub>2</sub>O<sub>3</sub> amount present. Typically, increased Al<sub>2</sub>O<sub>3</sub> content results in reduced compound density. The size of the Al<sub>2</sub>O<sub>3</sub> grains is crucial, since smaller grains are more efficient at pinning grain borders. This is due to smaller grains possessing a greater surface area to volume ratio, enabling them to engage with a higher number of grain boundaries. In ATZ composites, Al<sub>2</sub>O<sub>3</sub> particles serve as reinforcement, enhancing the hardness. ATZ composites provide superior resistance to fracture propagation relative to pure ZrO<sub>2</sub> [16].

The addition of MgO with a concentration about 3 wt.%, for example, has been shown to improve the mechanical characteristics and wear performance of ZrO<sub>2</sub> ceramic composites [17]. MgO is often employed as a sintering aid because it forms a liquid at high temperatures in the grain boundary [18], leading to the reduction in the sintering temperature of the materials. Furthermore, MgO can restrain the growth of the grains [19].

Very limited research has been conducted on ZrO<sub>2</sub>-Al<sub>2</sub>O<sub>3</sub>-MgO ternary composite materials. Tokas et al. [20] developed ZrO<sub>2</sub>-Al<sub>2</sub>O<sub>3</sub>-MgO ternary composite multilayer thin film devices for laser and photophysical applications. These thin films exhibit remarkable spectrum stability and optical characteristics. Raveendra et al. [21] evaluate the thermo-mechanical characteristics of the ZrSiO<sub>4</sub>-Al<sub>2</sub>O<sub>3</sub>-MgO composite in the field of the refractory applications. Hard, dense, and volumetrically stable ZrSiO<sub>4</sub>-Al<sub>2</sub>O<sub>3</sub>-MgO refractory bodies were fabricated from a suitable blend of graded ZrSiO<sub>4</sub>, Al<sub>2</sub>O<sub>3</sub> and MgO powders, and then burned at 1540°C.

#### 1.1.3 Porous ceramics

Porous ceramics are a specific category of materials that have high porosity, imparting unique characteristics such as enhanced permeability, reduced density, and extensive surface area. These materials consist of a network of interconnected pores distributed across a ceramic matrix. Porous ceramics combine the benefits of traditional ceramics, like resistance to severe temperatures, corrosion, and oxidation, while also being lightweight, featuring a substantial surface area, and exhibiting a low thermal conductivity coefficient [22]. Selection of pore-forming agents and ceramic constituents significantly affects the ultimate properties of the porous ceramics [23, 24]. These ceramics possess low density attributable to their elevated porosity, rendering them lightweight materials. This property is advantageous in sectors like aircraft, automotive, transportation, and bone replacement application, where minimizing weight is essential without

compromising structural integrity. Porous ceramics have a large surface area due to their linked pore architecture. This characteristic is particularly advantageous for activities such as adsorption, catalysis, bone replacement application that need extensive surface interactions [25, 26]. Differential characteristics of porous ceramics make them useful in numerous applications. Fig. 1.2 illustrates the main characteristics of porous ceramics.

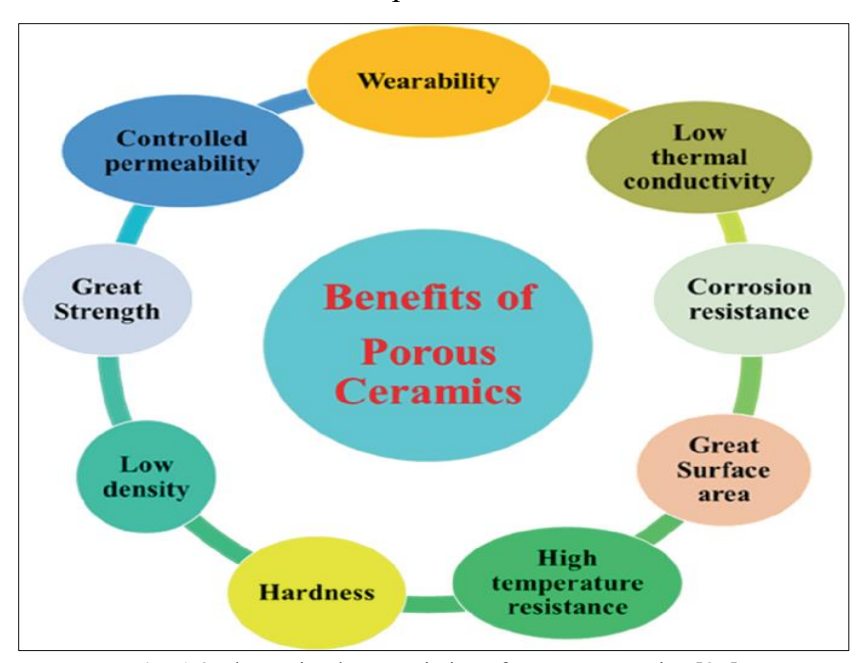


Fig. 1.2 The main characteristics of porous ceramics [27]

A major aspect of porous ceramics is their high porosity, which allows gases and liquids to flow via their many interconnected pores. This increased porosity enables processes like filtration, absorption, and adsorption to work effectively [28]. Porous ceramic materials are extensively used in many technologies, such as thermal insulation systems, filtration membranes, bone tissue engineering, and ceramic preform manufacturing. Notwithstanding its porosity, porous ceramics have a comparatively low density, yielding a lightweight substance. The mechanical strength of porous ceramics is dictated by the critical crack size, with pores acting as the principal origin of cracks [29]. Moreover, porous ceramics exhibit resistance to many chemicals, such as acids, bases, and organic solvents. Their chemical stability makes them suitable for use in demanding environments, including chemical processing, water treatment, and the pharmaceutical industry.

Porous ceramics are conventionally categorized based on pore size into three primary classifications: macro-porosity (pores exceeding 50 nm), meso-porosity (pores ranging from 2 to 50 nm), and micro-porosity (pores measuring less than 2 nm) [30]. Porous ceramics can also be classified based on certain characteristics, including the chemical composition of the base

ceramic material, porosity percent, physical state of the product, and refractoriness concerning service temperature, intended use, and application domain [31].

#### 1.1.4 Techniques for producing porous-structured ceramic composites

Porous ceramic materials can potentially be produced by many methods. Porous ceramics may be shaped into many forms, such as cylindrical fibres, tubes, flat surfaces, and different complex shapes. Ceramic materials undergo four treatment stages: 1) material preparation, 2) manufacturing, 3) sintering, and 4) finishing. Diverse processes can be used to fabricate porous ceramics exhibiting varying morphologies and pore size distributions. 1.3 illustrates numerous processing methods for the manufacturing of porous ceramics and the corresponding pore morphology achieved by various techniques. Examples include the firing of polymer sponges infused with a ceramic slurry [32], solid-state sintering [33], sol-gel techniques [34], replication of polymer foams by impregnation [35], gel casting methodologies [36], and freeze casting method [37].

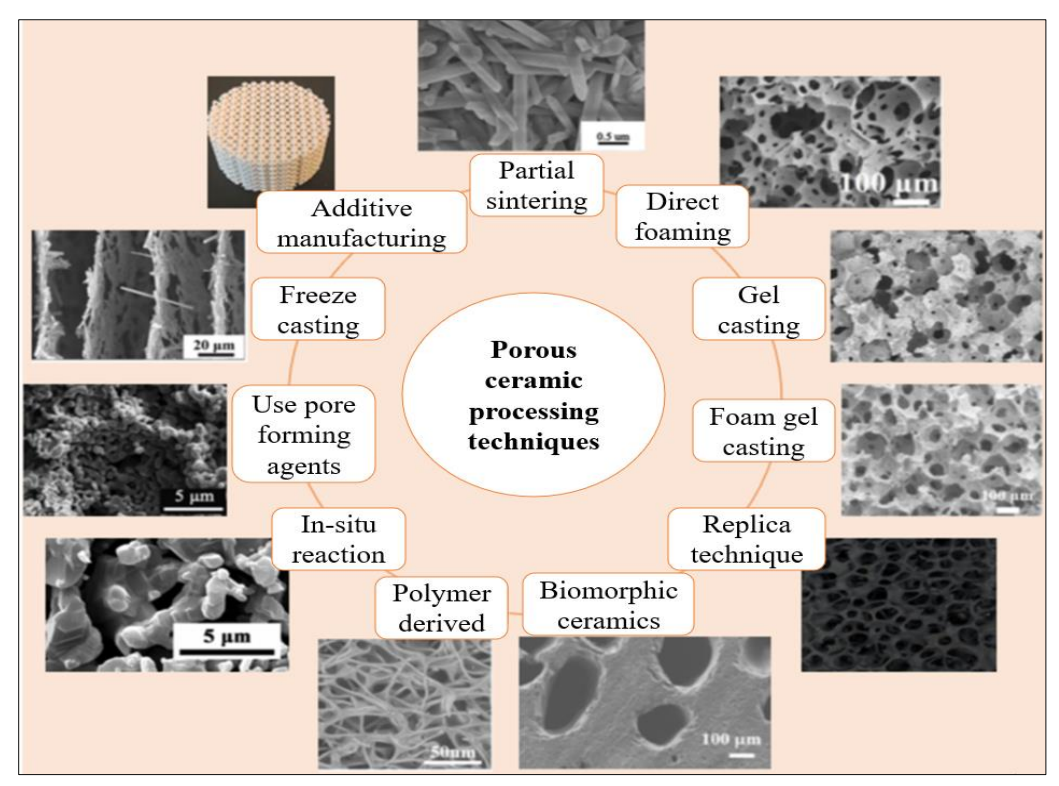


Fig. 1.3 Figure illustrating several processing methods for the manufacturing of porous ceramics [38]

One creative approach for making porous ceramics is the gel casting technique. A threedimensional crosslinked polymer is formed when initiators catalyse the free radical polymerization of organic monomers and cross-linking agents. This polymer then helps the ceramic powder to retain its structure. The disintegration and volatilization of the polymer during sintering result in the formation of pores. Gel casting must be conducted under secure and ideal circumstances. However, in industrial manufacturing, using a protective environment complicates control and increases production costs. Gel casting, a reliable process using in situ polymerization with natural monomers, is used to produce porous ceramics with intricate shapes and durable foams. Nonetheless, industrial gel casting presents difficulties because of the toxicity linked to organic monomers [39]. Direct foaming generates porous ceramics by incorporating air into the solution via a froth stabilizer, followed by drying and fire processes. Nonetheless, porous ceramics created by direct foaming are prone to fracture due to their inferior mechanical characteristics [40]. Most porous ceramics with complex forms and elevated porosity are produced using high-temperature foaming techniques. A foaming agent is included into the green body prior to sintering at elevated temperatures [41]. The gas produced by the foaming agent ascends and is either held or released from the ceramic, leading to porosity. High-temperature foaming has gained prominence due to its ability to produce porous ceramics with significantly closed porosity. A porous ceramic with 69% porosity and a compressive strength of around 7 MPa was sintered at 980°C [42]. At 1140°C, a porous ceramic is produced with a low bulk density of 0.39 g/cm<sup>3</sup> and an appropriate flexural modulus of 2.4 MPa [43]. Pore-forming agents have an ability to attain substantial porosity, since they inherently combust throughout the heating process to the firing temperature, resulting in pores within the ceramic material [44]. The shape and size of these pores will be dictated by the poreforming agent used and may thus be modulated by altering the absorption content and the distribution of particle sizes. Pore-forming agents, including starch [45-48], graphite [49], lycopodium [50], sucrose [51], polymethyl methacrylate (PMMA) [52], polypropylene (PP) [53], and carbon black [54], have been thoroughly investigated. Starch is the predominant pore-forming agent; at present, it is seldom used for creating large apertures, possibly owing to its biological origin and availability, challenges in preserving the configuration of pores generated by starch combustion, and the diminutive size of the particles. Numerous types of starch are extensively produced, with sizes ranging from 5 µm to 50 µm [55]. PP and PMMA serve as the principal porogen chemicals used. PP was selected because of its extensive production capabilities and costeffectiveness, making it economically advantageous for industrial applications. PMMA was often used in ceramics as a porogen due to its excellent thermal properties suitable for the intended

application. PMMA decomposes almost entirely into monomers and combusts at a rapid and consistent pace.

The structure, porosity, and mechanical properties of porous ceramics are significantly affected by the choice of pore-forming agent and the method of pore creation. The configuration of pore size and distribution within the ceramic matrix is mostly influenced by the kind and sizes of the pore-forming agent. Larger polymer particles often provide larger pores, whereas smaller, more uniform pores are usually generated by finer particles or gas-release agents [56]. The interrelation of these pores is substantially affected by their formation process. The depletion of organic molecules often results in the formation of interconnected voids, hence increasing fluid permeability and mechanical rigidity. The quantity of pore-forming agent used into the ceramic mixture significantly influences the overall porosity of the final product [57]. The kind of poreforming agent used also influences the morphology and configuration of the pores [58]. While fibrous materials such as cellulose provide elongated holes that may influence mechanical properties differently, spherical polymer particles typically yield round pores, resulting in a uniform pore morphology. The mechanical properties of ceramics are directly influenced by porosity. Ceramic materials often experience a decline in mechanical strength with increasing porosity. Nonetheless, enhancing the distribution and morphology of pores may alleviate this adverse impact. A balance between porosity and mechanical strength may be attained by integrating suitable pore-forming agents with non-oxide ceramics [59]. Additionally, pores may operate as stress concentrators, hence elevating the likelihood of fracture initiation and propagation under load. A well-designed pore structure may resist fracture and enhance the overall durability of ceramics [60].

The sintering temperature significantly influences the final properties of the porous ceramics. Increased sintering temperatures often provide a denser structure with less porosity. Nonetheless, they may also promote grain development and reduce mechanical strength. Lowered sintering temperatures, which promote increased porosity, may undermine mechanical properties while providing benefits in energy efficiency and reduced processing time [61]. The selection of poreforming agents and the optimization of sintering conditions are essential processes in tailoring the properties of porous ceramics for specific purposes. Table 1.1 summarizes various outcomes of using distinct manufacturing processes in the fabrication of ceramic porous structures.

**Table 1.1** Various outcomes of using distinct manufacturing processes in the fabrication of ceramic porous

structures (The full version of this table can be seen in Appendix A.)

Fabrication technique	Ceramic material	Sintering conditions	Pore size	Porosity	Other properties	Application	Ref.
Ice templating	8 mol.% YSZ	1390°C, 6 h	2.5-38.1 μm	54-75%	CO <sub>2</sub> permeance = $1.5 \times 10^{-7}$ $mol Pa^{-1} \cdot s^{-1} \cdot m^{-2}$ Membrane support		[62] 2025
3D printing	3 mol% YSZ	1450°C, 180 min	-	60, 70, and 80%	$\sigma = 109-1029 \text{ MPa}$	-	[64] 2025
Gel-forming	ZrO <sub>2</sub> / Al <sub>2</sub> O <sub>3</sub>	1350°C, 1450°C, and 1550°C, 1 h	450-640 μm	34-74%	σ = 5.8-129 MPa	-	[69] 2023
Use of pore formers	Al <sub>2</sub> O <sub>3</sub> - ZrO <sub>2</sub>	1650°C	10-40 μm	21.9- 69%	$\sigma = 4.5-658 \text{ MPa}$	Insulation	[70] 2023
Direct foaming	8 mol. % YSZ	1500°C, 2 h	-	45-84%	$\sigma = 1.5-267 \text{ MPa}$	Insulation	[71] 2022

#### 1.1.5 Starch consolidation casting

Starch consolidation casting (SCC) is based on the consolidation of a concentrated water and starch slurry. The consolidation of the slurry not only ensures the desired porosity but also offers flexibility in shaping the final structure. Fig. 1.4 shows the principal mechanism of the starch consolidation casting technique.

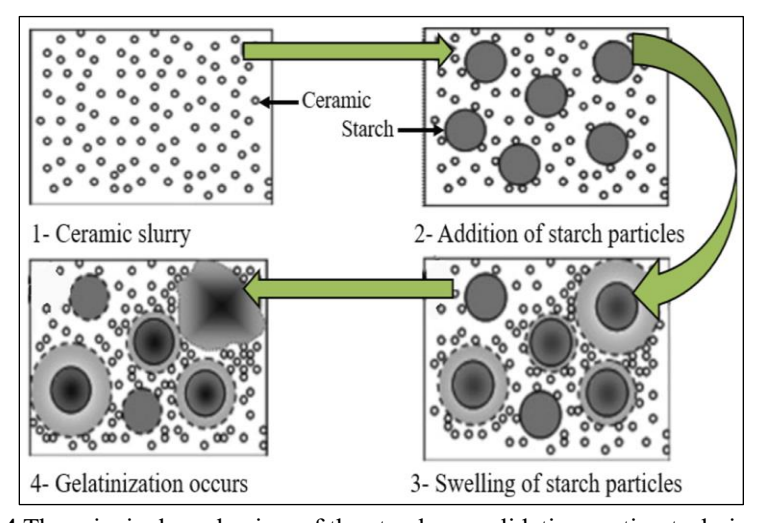


Fig. 1.4 The principal mechanism of the starch consolidation casting technique [92]

SCC primarily entails the following stages: slurry preparation, casting, gelation, drying, and sintering. Each stage is crucial for achieving a controlled porosity structure in the final ceramic

product. The initial stage is to produce a ceramic slurry by mixing ceramic granules with starch and water. While starch acts as a binder and pore-former, ceramic powder serves as the primary structural component of the product. Slurries can be stabilised, and ceramic particles can be prevented from aggregating by adding dispersants or surfactants during production. Following this, the slurry is poured into a mould, which establishes the final form of the product. The viscosity of the slurry, which is impacted by the starch content and the size of the ceramic particles, determines the ease of casting and the quality of the finished product. After casting, the temperature of the slurry should rise to a range of 60°C to 80°C, contingent upon the type of starch used. This heating process initiates the gelatinisation of starch granules, causing them to absorb water, swell, and create a gel-like matrix. This network immobilises the ceramic particles, resulting in the consolidation of the slurry into a semi-solid state [93]. Starch, the predominant reserve polysaccharide, is extensively used in many food and industrial sectors due to its natural, economical, biodegradable, and non-toxic characteristics [94]. Starch granules are microparticles including crystalline and amorphous areas, primarily consisting of amylose linked by α-1,4glycosidic bonds and amylopectin linked by α-1,6-glycosidic bonds [95]. The swelling and gelatinisation of starch are separate phenomena that occur under varying circumstances and are of considerable significance in the industry fields. Starch gelatinisation entails a complete decomposition of starch molecules and the physical disintegration of granules [96]. Starch swelling is the phenomenon whereby starch granules expand in water via the absorption of water. It may render starch granules soft and brittle, thus impacting the texture. Upon heating in excess water, starch granules absorb water and swell, resulting in a fast rise in volume. The first step of the swelling mechanism is the hydration stage, which generally happens below the gelatinization temperatures and entails a little rise in granule diameter. Throughout this process, water molecules infiltrate the amorphous regions of the starch granules and establish new hydrogen bonds with the starch molecules. As the granules enlarge, amylose molecules are released from the enlarged granules, resulting in an increase in the viscosity of the system. The second step is the irreversible phase, distinguished by a significant increase in the diameter of the starch granules and the viscosity of the solution, occurring at elevated temperatures (exceeding the gelatinization temperatures). Continued heating of starch leading to the rupture of granules. At the maximum viscosity point, the hydrogen bonds among the starch molecules are entirely disrupted and substituted by hydrogen bonds between water and starch molecules, resulting in the formation of starch pastes [97]. Table 1.2 summarizes the literature reviews of the use of different types of starches as a pore forming agent (PFA) in the preparation of ceramic porous structure via the starch consolidation casting technique.

Table 1.2 Some results from using various pore-forming agents in the fabrication of ceramic porous

structures. (The full version of this table can be seen in Appendix A.)

Ceramic Materials	PFA	PFA content	Sintering conditions	Pore size	Porosity	Other properties	Ref.
m-ZrO <sub>2</sub>	Corn starch	5 wt.%	1750°C, 3 h	4.4-10.7 μm	5.1-16.5 %	$k = 1.37 \text{ W m}^{-1} \text{ K}^{-1}$ .	[101] 2024
Al <sub>2</sub> O <sub>3</sub>	Corn starch	4-10 wt.%	1250°C, 2 h	-	54.05- 70.70 %.	LS = 1.07-3.39 %, $\sigma_f = 0.5$ -1.9 MPa	[103] 2021
α-Al <sub>2</sub> O <sub>3</sub> - m-ZrO <sub>2</sub> - MgO	Corn starch	10, 20 and 30 wt.%	1300°C, 1400°C, 1460°C and 1550°C, 2 h	1	43-60 %	WA = 16-34 %, $\sigma_f = 0$ -17 MPa	[110] 2013
Al <sub>2</sub> O <sub>3</sub> – ZrO <sub>2</sub>	Rice and corn starches	10, 20, 25, 30, and 50 vol.%	1530°C, 2 h	1	50 %.	LS = 10-40%	[111] 2012
Al <sub>2</sub> O <sub>3</sub> - ZrO <sub>2</sub>	Corn starch	10-50. vol.%	1100°C - 1530°C, 2 h	0.1-17 μm	50-71%	E = 331-383 GPa	[112] 2011

### 1.1.6 ZrO2-based porous structures ceramic composites for biomedical applications

The investigation of ZrO<sub>2</sub>-based porous materials in biomedical applications has attracted substantial interest in recent years, notably owing to its promising mechanical characteristics and biocompatibility. Because of its unique combination of features, ZrO<sub>2</sub> has been the subject of much biomedical study since the 1970s, with applications ranging from dentistry to stress-bearing roles where its strength is comparable to that of several alloys [115]. Hadjicharalambous et al. [116] emphasized the significant impact of porosity on cellular responses to ZrO<sub>2</sub> and Al<sub>2</sub>O<sub>3</sub> ceramics, often used in orthopaedic implants. Their research demonstrated that an ideal hole size of roughly 150 µm and a porosity of about 50 % markedly improved the adhesion and proliferation of preosteoblastic cells, indicating that customized porosity may increase the integration of these materials with bone tissue. Altmann et al. [117] revealed that alterations in surface properties may result in substantial differences in cellular activities, highlighting the significance of both chemical composition and structural design in the efficacy of implant materials. Chopra et al. [118] examined the extensive consequences of ZrO<sub>2</sub> in dental implants, comparing its efficacy with that

of titanium. ZrO<sub>2</sub> has advantageous properties, including decreased bacterial adherence and enhanced soft-tissue integration, making it a potential substitute when constraints of titanium are evident. Recently, Yang et al. [119] investigated the compressive fracture behaviour of ZrO<sub>2</sub>/resin composites, emphasizing the efficacy of fused deposition modelling in conjunction with vacuum infiltration to produce porous structures with improved mechanical characteristics. Their results showed that pore shape design substantially affects the mechanical performance of composites, which is essential for guaranteeing the longevity and dependability of biomedical implants. ZrO<sub>2</sub> biomaterials have been proposed as an artificial bone filler for the healing of bone defects [120]. ZrO<sub>2</sub> have orthopaedical uses, including hip and knee prosthesis, temporary supports for hip joint heads, tibial plates, and dental crowns [121]. Al<sub>2</sub>O<sub>3</sub> and ZrO<sub>2</sub> oxide are recognized bio-inert ceramics used in traditional bone regeneration applications [122]. Table 1.3 summarizes the literature reviews of the use of ZrO<sub>2</sub>-based ceramics in biomedical application.

**Table 1.3** Some results of the use of ZrO<sub>2</sub>-based ceramics in biomedical applications (The full version of

this table can be seen in Appendix A.)

Materials	Fabrication techniques	Sintering		Porosity (%)	Other properties	Application	Ref.
8YSZ	DLP 3D printing	1 1450°C 3 h		20-41	$\sigma_f = 25-71$ MPa	Biomedical implants	[124] 2025
3YSZ	Direct ink printing	1325°C, 1350°C, and 1375°C, 1 h, 1.5 h, and 2 h	0.1-400	80	σ = 24 MPa	Osteogenic differentiation and bone regeneration	[125] 2024
YSZ	Direct ink writing	1450°C, 2 h	-	61.1- 75.3	$\sigma = 20.8-62.9$ MPa	Scaffolds for bone tissue	[127] 2021
Al <sub>2</sub> O <sub>3</sub> /ZrO <sub>2</sub>	Replica method	1500°C, 1 h	5-2560	78.8	$\sigma = 6.5 \text{ MPa}$	Replacement or bone filling	[134] 2018
YSZ-Al <sub>2</sub> O <sub>3</sub>	Robocasting	1350°C, 2 h	245	50	-	Substrate for bone cells ingrowth	[135] 2018

#### 1.2 Knowledge gaps and the aims of the thesis

According to the literature review, the majority of research focuses on manufacturing and investigating different porous ceramic structures, while another group of research discusses techniques to modify the characteristics of ZrO<sub>2</sub>-based porous structures. Nevertheless, there is a deficiency in research being conducted on porous ZrO<sub>2</sub>-Al<sub>2</sub>O<sub>3</sub>-MgO ternary composite materials.

This PhD research work addresses the knowledge gap through the preparation and characterisation of porous ZrO<sub>2</sub>-Al<sub>2</sub>O<sub>3</sub>-MgO ternary composite materials. The composites prepared by using a very simple, cost-effective, and environmentally friendly method, incorporating varying proportions of ceramic oxides, starches, and distilled water, and sintering at diverse temperatures and holding time. Concerns about how the composition of ceramic composites, the content of pore forming agents, and distilled water content affects the apparent density, apparent porosity, volume shrinkage and the response of material to compressive stresses, especially in ZrO<sub>2</sub>-Al<sub>2</sub>O<sub>3</sub>-MgO composite, have not been well investigated. To cover a knowledge gap regarding the combined function of these components in biomedical porous structures, this work investigates the effect of these parameters. Moreover, the study delves into the impact of changing the weight ratios of these components on the final microstructure and mechanical characteristics, offering a thorough comprehension of the correlation between composition, microstructure, and performance. This study also has comprehensively examined how the structure, porosity, and mechanical properties of porous ceramics are affected by the choice of pore-forming agent type (potato, tapioca, or potato and tapioca starches together). The definitive characteristics of this material are dictated by the interaction between the pore-forming agent and the ceramic component. Another significant knowledge gap pertains to the relationship between porosity and mechanical properties of the ZrO<sub>2</sub>-Al<sub>2</sub>O<sub>3</sub>-MgO composite when subjected to compressive loads. While high porosity is desirable for bone ingrowth, it often leads to a reduction in mechanical strength. Moreover, the biocompatibility and bioactivity of ceramic composites are influenced by their surface characteristics, including apparent porosity, and surface morphology. SEM is utilized to analyse the surface morphology and microstructural features. This comprehensive analysis helps in correlating surface characteristics with the potential of the material to support the osteoblast adhesion, proliferation, and differentiation.

Previous research has largely focused on single-starch systems, without properly exploring the comparative performance of combining two distinct starches on the mechanical and morphological aspects of the ceramic matrix. This PhD research work addresses the knowledge gap through investigating the pore morphology of the porous structure when two types of starch are combined together to work as pore and body-forming agents. The research included the combination of two starch types to create bigger pores appropriate for bone replacement applications, since these

enlarged pores enhance the surface area and thus improve the adhesion strength between the synthetic bone and the living tissue.

The sintering temperature is a crucial factor that influences the microstructure, phase composition, and general technical characteristics of the ceramic composites. Optimizing the sintering parameters to improve both the mechanical strength and bio-functionality of porous ceramics presents an additional difficulty in the fabrication of porous structured ceramics. Numerous studies have investigated the influence of sintering temperatures on material density, porosity, granular growth, and intergranular connectivity; however, insufficient research has concentrated on the impact of sintering temperatures on the morphology of the resultant pores within the porous matrix, as well as the formation or absence of openings connecting these pores. Furthermore, existing studies do not adequately address the sizes of these openings, despite the critical importance of pore and openings size in bone replacement applications. It is important to investigate the sintering process, sintering temperature, and sintering holding time to get a defectfree ceramic. This PhD research work addresses these knowledge gaps by investigating the impact of sintering conditions on pore morphology, the presence or absence of the openings between the pores, and the size of these openings. While numerous investigations have concentrated on optimizing sintering conditions to improve the microstructural and mechanical characteristics of ZrO<sub>2</sub>-based ceramics, there has been less consideration on the influence of pre-sintering methods on crack development. The function of progressive pre-sintering in reducing surface fractures after sintering is inadequately investigated. This PhD thesis demonstrates that gradual pre-sintering of ZrO<sub>2</sub>-Al<sub>2</sub>O<sub>3</sub>-MgO porous ceramic composite samples significantly decreases the surface crack formation during the final sintering process.

In addition, the literature does not provide an adequate explanation of how processing conditions (sintering holding time and temperature), compositional variations (different ZrO<sub>2</sub> and Al<sub>2</sub>O<sub>3</sub> wt.%), and pore-forming agents (potato and tapioca starches) concurrently affect various performance measures (apparent density, apparent porosity, volume shrinkage, and compressive strength). Addressing this knowledge gap is essential to obtaining an improved comprehension of the processing-structure-property interactions in porous bio ceramics. Pair plots serve as an effective exploratory method for concurrently visualizing distributions and correlations among numerous variables, therefore clarifying the impact of processing conditions and compositions on

the prepared bone replacement ceramics performance. Based on the previous explanation, many questions need answers:

- Could the low-cost SCC method be used to produce the porous ZrO<sub>2</sub>-Al<sub>2</sub>O<sub>3</sub>-MgO ternary composite materials?
- What kind of phases could develop after sintering at different conditions? Furthermore, are the produced phases suitable for biomedical applications?
- Would it be possible to enhance the properties of the ZrO<sub>2</sub> porous structure by using Al<sub>2</sub>O<sub>3</sub> and MgO additive materials?
- To make the porous structure more suitable for bone growth applications, would it be possible to improve the pore morphology utilising different types and contents of starches?
- Could progressive pre-sintering and sintering procedures reduce the surface cracks development in the prepared ZrO<sub>2</sub>-Al<sub>2</sub>O<sub>3</sub>-MgO ceramic composites?
- How are the processing conditions, compositional variations, and pore-forming agents and the properties of the porous bio ceramics correlated with each other?

The questions mentioned previously delineate the objectives of this PhD thesis:

- The PhD thesis focused on the preparation and characterization of ZrO<sub>2</sub>-Al<sub>2</sub>O<sub>3</sub>-MgO ternary ceramic composites, designed with the necessary porous structures to meet the mechanical property requirements for biomedical applications at a reduced cost.
- Studying the effect of using different amount and type of starches on the properties (apparent density, apparent porosity, volume shrinkage, and compressive strength), porous structure, and pore surface morphology.
- Studying the effect of adding different amount of distilled water on the properties of the prepared porous structure.
- Studying the effect of using different amount of Al<sub>2</sub>O<sub>3</sub> on the properties and phase composition of the prepared porous structure.
- Studying the effect of progressive pre-sintering and sintering conditions on the microstructure, properties, porous structure, pore surface morphology, and the formed phases of the prepared porous structure.
- To explore an adequate explanation of how processing conditions, compositional variations, and pore-forming agents concurrently affect various properties.

#### 2. Chapter Two – Experimental part

#### 2.1 Materials

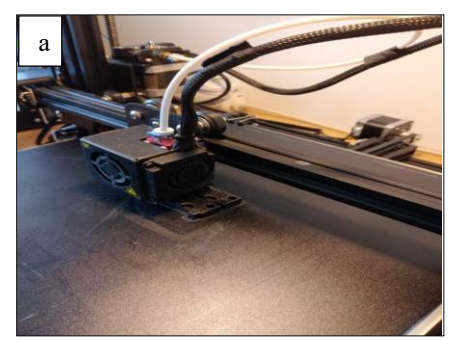
The following materials were employed in this PhD research work: monoclinic zirconia (m-ZrO<sub>2</sub>), magnesia (MgO), alumina (Al<sub>2</sub>O<sub>3</sub>), distilled water, deflocculant (Dolapix CE64), and potato and tapioca starches. m-ZrO<sub>2</sub> was selected due to its biocompatibility, osteo-conductivity, good mechanical properties and its chemical inertness. To enhance the properties of m-ZrO<sub>2</sub>, Al<sub>2</sub>O<sub>3</sub> and MgO as additive oxides were used. During the process of preparing ceramic slurries, the Dolapix CE64 and distilled water were both used as necessary components. A commercial ammonium salt of a polycarboxylic acid (Dolapix CE 64) is an ionic dispersant, and it is considered as a stronger surface charge modifier. Potato and tapioca starches, due to their high swelling factor as compared with other types of starch, have been utilised as pore-forming and body-forming agents. Experiments were carried out using the as-received starches, without any subsequent processing. Purity, density and source of raw materials were listed in Table 2.1 below.

**Table 2.1** Properties and origin of raw materials

Material	Purity (%)	Density (g/cm <sup>3</sup> )	Source	
m-ZrO <sub>2</sub>	99.99	5.71	Interkeram Kft., distributor	
$Al_2O_3$	99.99	3.04	Interkeram Kft., distributor	
MgO	99.5	3.58	Sigmaaldrich.com, Germany	
Potato starch	98.2	0.65	Balance food Kft., distributor	
Tapioca starch	97.7	0.6	Balance food Kft., distributor	
Dolapix CE 64	-	-	Zschimmers and Schwartz, Germany	

#### 2.2 Preparation of moulds

For the aim of the casting procedure, impermeable plastic moulds were prepared and made with the assistance of the 3D printing method (Crealty 3D printer, manufactured by Shenzen Creality 3D technology Corporation). The impermeable plastic moulds were printed by using High Impact Polystyrene filament.



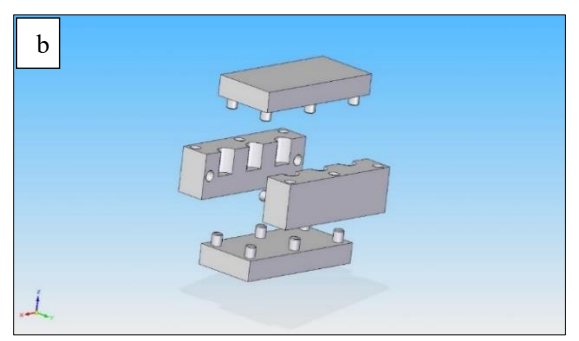


Fig. 2.1 (a) The 3D printing process, (b) Stereolithography 3D image of designed moulds

Fig. 2.1 (a) illustrates the 3D printing process of the mould, whereas (b) depicts the stereolithography 3D image for the designed mould. The plastic mould was designed as a cylindrical rod with a diameter and height of 7.5 mm to measure the density, porosity, volume shrinkage, and pore and pore opening size of the prepared porous structure, as shown in Fig. 2.2 (a), and with dimensions of 6 mm in diameter and 10 mm in height to evaluate the compressive strength as shown in Fig. 2.2 (b).

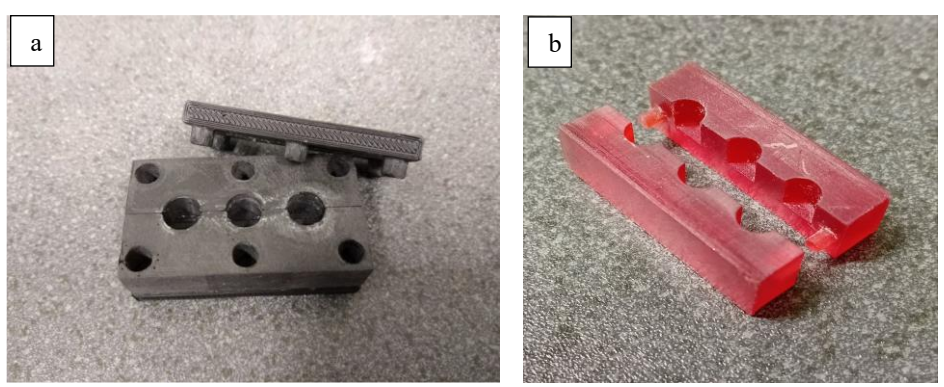


Fig. 2.2 The 3D printed moulds

#### 2.3 Preparation of porous structured ceramics

#### 2.3.1 Preparation of slip slurries

In order to begin the process of preparing slurries, the ceramic raw ingredients first mixed in a laboratory milling machine shown in Fig. 2.3.



Fig. 2.3 Laboratory milling machine



Fig. 2.4 Preparation of slurry by magnetic stirrer

The mixing procedure began after various amounts of ceramic powder were weighed and placed in plastic bottles. The bottles were then fixed within the machine container. The maximum rotating speed of the milling machine was 60 rpm. Due to the low rotating speed of the machine, the mixing period was prolonged to 5 hours. After five hours of mixing, the ceramic powders began to adhere to the walls of the plastic bottles. The objective of this mixing process is to preliminarily mix the ceramic powders without diminishing the particle size of the materials; hence, the mixing was

conducted without the use of ball milling media. For the preparation of the casting slurries, the ceramic and starch powders were rapidly stirred (600 rpm) in distilled water containing 1.5 wt.% of the deflocculant. The procedure of stirring was maintained for a total of 2 hours at room temperature while the beaker was kept covered in order to prevent any water from evaporating. Fig. 2.4 shows the prepared slurry using magnetic stirrer equipment. The various mixed compositions that were produced for this PhD research work are detailed in tables 2.2, 2.3, and 2.4. Suspension concentration expresses the solid-to-liquid ratio. The expression of "starch content P/T/50:50P+T" denoted to uses different type of starch, P for using potato starch, T for using tapioca starch, while 50:50P+T when using potato and tapioca starch at 50:50 percent ratio. Table 2.2 detailed the mixed compositions that prepared for the first study of this PhD thesis. The first study explored the effects of utilizing different types and content of starches with varying amounts of distilled water. In this study, the concentrations of ceramic powder remained constant, although the concentrations of starches and distilled water changed. Table 2.3 delineates the mixed compositions that prepared for the second study of this PhD thesis.

**Table 2.2** Mix compositions for the first study (in wt.%)

m-ZrO <sub>2</sub>	MgO	Al <sub>2</sub> O <sub>3</sub>	Dolapix CE 64	Potato or tapioca starch			Suspension Conc.
77.5	2.5	20	1.5	10	20	30	70
77.5	2.5	20	1.5	10	20	30	68
77.5	2.5	20	1.5	10	20	30	65
77.5	2.5	20	1.5	10	20	30	60

**Table 2.3** Mix compositions for the second study (in wt.%)

m-ZrO <sub>2</sub>	MgO	Al <sub>2</sub> O <sub>3</sub>	Dolapix CE 64	Starch content P/T/50:50P+T	Suspension Conc.
82.5	2.5	15	1.5	20	60
80	2.5	17.5	1.5	20	60
77.5	2.5	20	1.5	20	60
75	2.5	22.5	1.5	20	60
72.5	2.5	25	1.5	20	60
70	2.5	27.5	1.5	20	60
67.5	2.5	30	1.5	20	60

The second study evaluated the impact of varying content of ceramic oxides. Consequently, the starch and water content are established based on the optimal findings from the first study, but the ceramic powder concentration was changed. This study used a 20 wt.% potato, tapioca, or 50:50 potato and tapioca starch together with 60 wt.% suspension concentration. Table 2.4 presents the mix compositions of the third and fourth studies, focusing on the impact of varying sintering temperatures and holding times. Based on the optimal outcomes of the second study, this study

used a 50:50 mixture of potato and tapioca starch, while varying the concentration of the ceramic powder.

**Table 2.4** Mix compositions for the third and fourth studies (in wt.%)

m-ZrO <sub>2</sub>	MgO	Al <sub>2</sub> O <sub>3</sub>	Dolapix CE 64	50:50 P+T	Suspension Conc.
82.5	2.5	15	1.5	20	60
80	2.5	17.5	1.5	20	60
77.5	2.5	20	1.5	20	60
75	2.5	22.5	1.5	20	60
72.5	2.5	25	1.5	20	60
70	2.5	27.5	1.5	20	60
67.5	2.5	30	1.5	20	60

#### 2.3.2 Ceramic composites consolidation

The prepared slurries with different compositions were poured into the prepared impermeable plastic moulds. Covering of moulds is very important to avoid evaporation of water and enables the starch granules to absorb that water from the suspension and then to swell. The moulds containing the slurries was then placed in an oven in the laboratory (Drying oven manufactured by POL-EKO APARATURA) and heated up to 80°C for 2 hours in order to enable the starch to swell. A consolidation temperature of 80°C and a holding time of 2 hours were chosen in this PhD thesis based on several trials that were conducted with the goal of creating ceramics with better consolidation and easier de-moulded properties. Nevertheless, the predicted minimum consolidation times of less than two hours in most cases are generally too short for complete consolidation of the ceramic suspension. When the moulds are opened at this stage, the suspension still has the consistency of a highly viscous paste, which is unacceptable for the de-moulding of ceramic green bodies. After cooling to room temperature and setting overnight the moulds were opened and the ceramic bodies were de-moulded, as shown in Fig. 2.5.

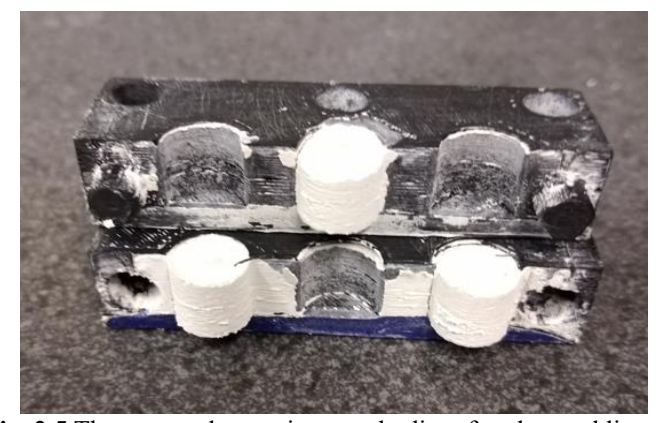


Fig. 2.5 The prepared ceramic green bodies after de-moulding

At this stage, the ceramic green body consists of a compressed powder compact connected by a starch gel matrix, and its strength and rigidity allow safe de-moulding.

#### 2.3.3 Pre-sintering and sintering

The prepared ceramic samples were subjected to gradual pre-sintering in the laboratory furnace at temperatures of 500°C and 1100°C. The samples were held at 500°C for 1 hour and then at 1100°C for 2 hours. The pre-sintering process included heating the samples at a rate of 2 °C/min until they reached temperatures of 1100°C. After the pre-sintering stage, the specimens were gradually cooled to the ambient temperature inside the furnace. Following pre-sintering, the pre-sintered ceramic samples underwent a gradual sintering process in the laboratory furnace (Nabertherm GmbH, Bahnhofstr. 20, 28865 Lilienthal/Bremen, Germany). Fig. 2.6 shows the pre-sintering and sintering profiles when the holding time was 2 hours.

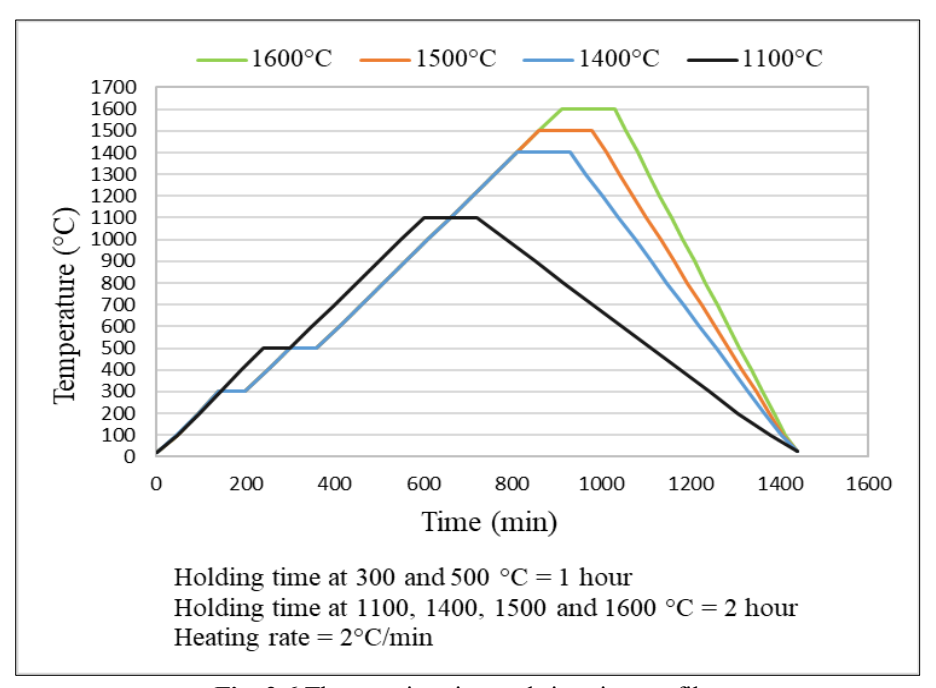


Fig. 2.6 The pre-sintering and sintering profiles

The gradual sintering was first conducted at temperatures of 300°C and 500°C for 1 hour, followed by 1400°C, 1500°C, or 1600°C, with a heating rate of 2 °C/min. At sintering temperatures of 1400°C and 1500°C, the sintering holding time was 2 hours; while at 1600°C, the holding time varied between 2, 3, or 4 hours. After the sintering process, the specimens were left inside the furnace to cool down to room temperature. The gradual implementation of the pre-sintering and sintering process serves the objective of minimizing the production of internal defects and the

occurrence of surface cracks on the samples. Fig. 2.7 shows the preparation procedure of porous-structured ceramic.

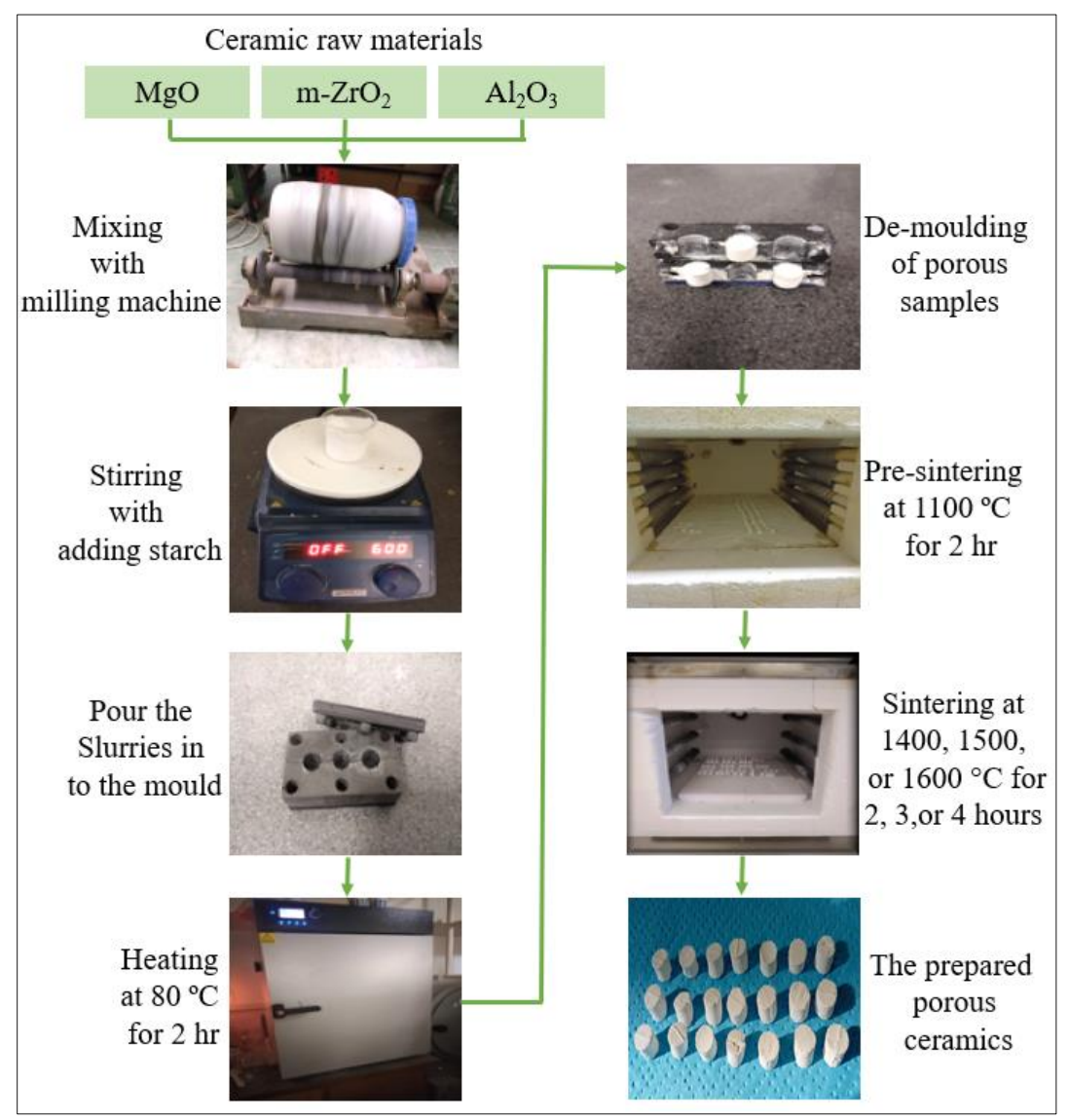


Fig. 2.7 The preparation procedure for porous-structured ceramic

#### 2.4 Testing methods

#### 2.4.1 Characterization of raw materials

Microstructural characterization for monoclinic-ZrO<sub>2</sub>, Al<sub>2</sub>O<sub>3</sub> and MgO ceramic powders was carried out with using of X-ray diffractometer (XRD) with Cu Kα radiation in the 2Θ range of 3-90°, with a step width of 0.01 and 1 second of exposure time per position. The morphology of ceramic particles, and potato and tapioca starch granules were observed via utilizing scanning electron microscopy (SEM). Density determination of ceramic powders was carried out utilizing a pycnometer. For increasing the accuracy of measurement, the experiment was repeated for three

times and the average value was taken. The particle size distribution of ceramic powders was characterized by using CILAS 715 equipment as shown in Fig. 2.8.





Fig. 2.8 CILAS 715 equipment

Fig. 2.9 Moisture determination balance

The measurements were carried out at room temperature with the addition of two drops of sodium-tripolyphosphate diluted solution as a dispersion agent. The dispersion process was enhanced by the aid of ultrasonic for 60 sec. A moisture determination balance (RADWAG MA110R) was used to measure the moisture content of the potato and tapioca starches. The moisture determination balance, as shown in Fig. 2.9, consists of an electric heater to vaporise moisture and a highly accurate balance to measure the weight loss. The test started with placing 6 grams of starch in the empty balance pan, followed by evenly spreading the starch powder to make a thin, uniform layer. The weight of the starch powder decreased throughout the drying process as moisture evaporated. Upon completion of the test, the moisture content displayed on the screen of the device was recorded.

The hydrothermal technique used to determine the rate of starch granule swelling in distilled water. This method involves heating starch in water at regulated temperatures to observe swelling characteristics. The first step of this method is the preparation of samples by measuring a certain quantity of both potato and tapioca starches (1 gram) and incorporating it into a designated volume of distilled water, often maintaining a starch-to-water ratio of 1:100 (w/v). Then, the solution was comprehensively mixed to guarantee uniform distribution of starch granules. The mixing was conducted using magnetic stirrer equipment at a rotational speed of 200 rpm. The second step is the hydrothermal treatment of starch granules. The starch-water suspension is heated using a temperature-regulated magnetic stirrer, often maintained at 65°C, for different durations (10, 20, 30, 40, 50, and 60 min). The heat induces the swelling of starch granules as they absorbed water. After heating, the sample was allowed to cool to ambient temperature. Then, filter paper utilized

to separate the hydrated starch granules from the water. Then, the weight of the sediment (swollen starch granules) is measured. The swelling factor measures how much starch granules expand relative to their original volume. There are no units, hence it is dimensionless. The following equation was used to measure the swelling factor (SF) of potato and tapioca starch:

SF = Weight of swollen starch/ Weight of dry starch

# 2.4.2 Characterization techniques of porous ceramic composites

An XRD equipped with Cu Kα radiation in the 2θ range of 3 - 90° was used to carry out the crystalline structure and phase identification of the prepared porous structured ceramics. The step width was 0.01 and the exposure period per location was 2 seconds. Preparation for the XRD test involves either finely grinding the samples to a powder to guarantee crystals are oriented randomly or polishing them to a flat surface. After that, the sample is carefully placed in the sample holder inside the equipment. SEM was used to examine the porosity, pore size, pore surface morphology, and the surfaces of the pre-sintered and sintered porous-structured samples. It is important to thoroughly clean the surface of the samples before imaging them to remove any contamination. Image quality might be diminished due to dust obstructing the electron path. Since ceramic is not a conductive material, a conductive gold coating should be applied to the surfaces to eliminate the charging effects. Then the sample secured in the SEM chamber using a suitable stub and conductive adhesive (carbon paste or tape). Mercury intrusion porosimetry (MIP) was used to analyse the size distribution of the channels (openings) that connect the pores together. MIP depends on the entrance of mercury into the pore space; hence, it can only detect open pores. The pore openings size distribution was determined with a maximum intrusion pressure of 400 MPa, enabling the detection of opening sizes as fine as 4 nm. Before analysis, the sample was evacuated to remove any adsorbed material that may cover its porosity. The experiment used a mercury surface tension of 480 nN/m and a contact angle of 141.3° (at 25°C). The principle behind MIP is that under pressure, only nonwetting liquids (those with a contact angle larger than 90°) may penetrate capillaries. The equivalent diameters calculated by MIP are size measurements based on the Washburn equation (1).

$$P \cdot r = -2.\gamma \cdot \cos\Theta$$
 (1)

Where P is the absolute applied pressure, r is the pore radius,  $\gamma$  is the mercury surface tension, and  $\Theta$  is the contact angle. This indicates that the mercury porosity results in a pore throat diameter distribution in the case of large pore cavities (cells) linked by tiny pore channels or throats (window

cells). Dilatometric (TMA, thermomechanical analysis) test was conducted on a SETARAM SETSYS 2400 system to assess the shrinkage of the sample under heat treatment in an air environment. As shown in Fig. 2.10, the green specimen (6.5 mm in length) was positioned in the dilatometer and contacted by an Al<sub>2</sub>O<sub>3</sub> hemispherical probe, ensuring uniform force distribution and precise displacement measurement.



Fig. 2.10 Dilatometry (TMA) test

The test was performed in ambient air to replicate normal sintering conditions that followed in the preparation of the samples. The heating process included a regulated temperature increase from ambient temperature to around 1500°C. The heating rate was designed to facilitate progressive thermal contraction, followed by a high-temperature plateau during which the sample was maintained in equilibrium to enhance densification. After the holding period, the furnace was gradually cooled to ambient temperature. The system consistently recorded the linear dimensional changes of the sample during the whole operation. The raw displacement measurements were subsequently corrected for the thermal change of the measuring instrument, using the Al<sub>2</sub>O<sub>3</sub> probe as a reference.

The apparent densities of the ceramic samples were determined by measuring both their weight and size after sintering. The water absorption method was used to calculate the apparent porosity of the samples. In order to determine the apparent porosity (AP), the samples were weighed after sintering ( $w_{sint.}$ ), then again after being immersed in water for 24 hours at room temperature ( $w_{imm.}$ ), and after being saturated with water ( $w_{sat.}$ ). Fig. 2.11 shows the sample being weighted when it was completely saturated with water.



Fig. 2.11 Saturated sample

The apparent porosity (AP) was determined by solving the equation (2):

$$AP = \frac{w_{imm.} - w_{sint.}}{w_{imm.} - w_{sat.}} \cdot 100\%; (\%)$$
 (2)

The volume shrinkage (VS) was determined by measuring the volume of the samples before sintering  $(V_0)$  and the volume of the samples after sintering  $(V_1)$  using equation (3). The volume of the samples is calculated by using the average of three measurements taken with a digital Vernier calliper.

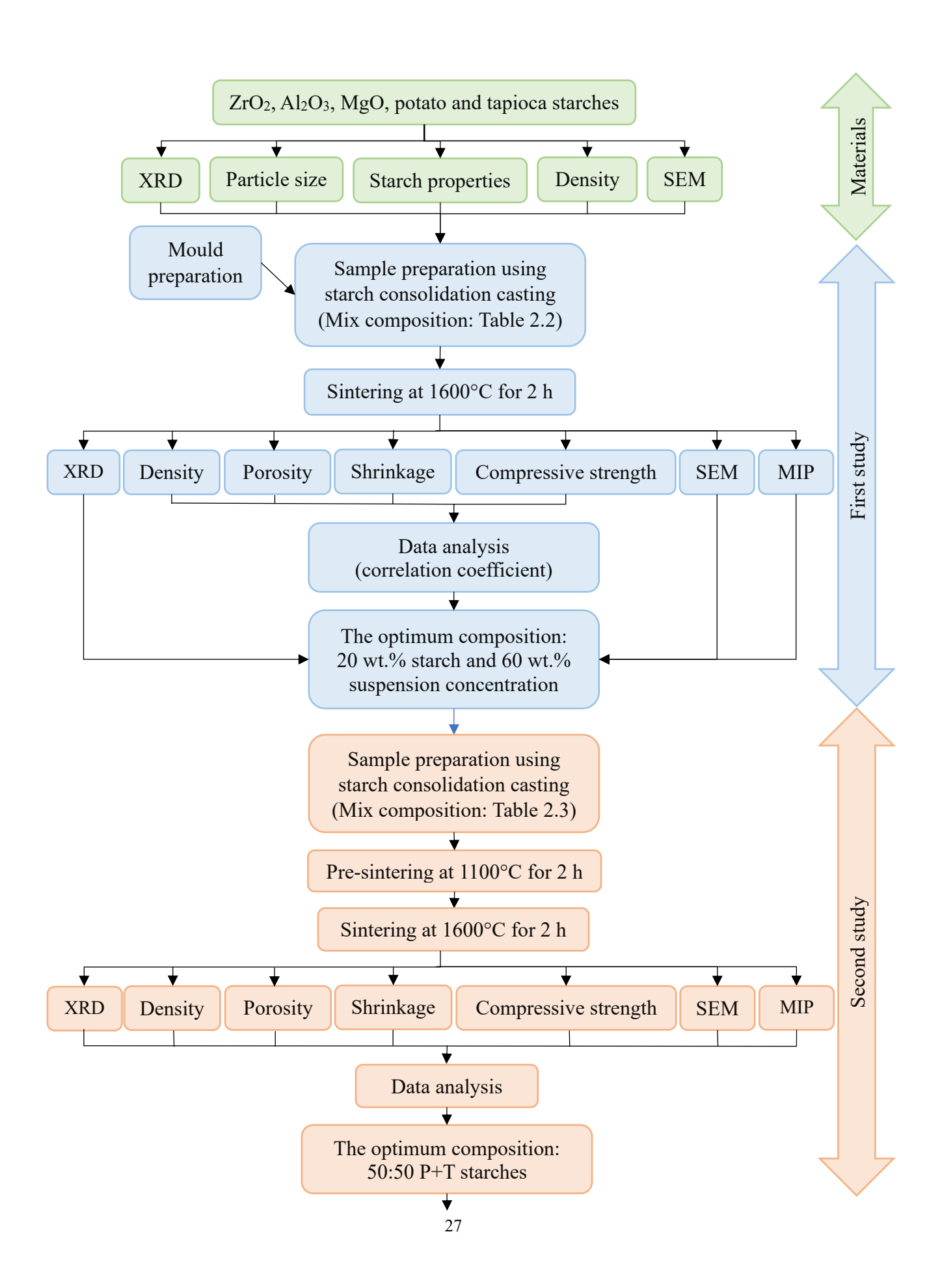
$$vs = \frac{v_0 - v_1}{v_0} \cdot 100\%; (\%)$$
 (3)

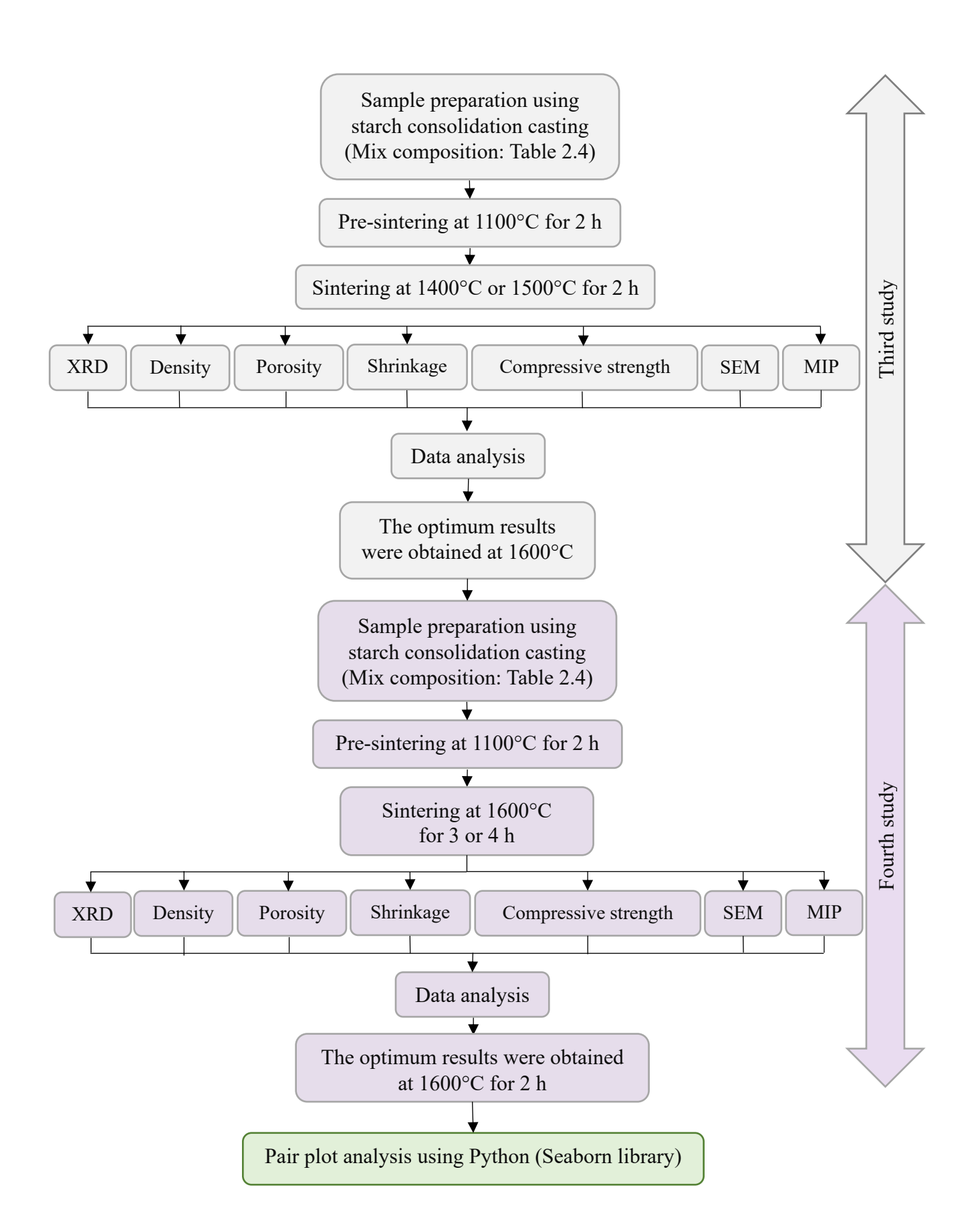
Universal testing machine (Zwick) was used to measure compressive stress of the sintered cylindrical samples with approximately 5 mm diameter and 8 mm height at 2 mm·min<sup>-1</sup> loading rate. Compressive strength was measured by using the equation (4), taking the average of six samples for each composition to ensure that they were as accurate as possible.

$$\sigma = F/A \tag{4}$$

Where  $\sigma$  is the compressive strength, F is the applied load, and A is the cross-sectional area of the samples (A =  $\pi \cdot r^2$  mm<sup>2</sup>). The following flow chart summarizes the progress on the PhD thesis, detailing the research work carried out in each study.

The pair plot analysis was performed using Seaborn library in Python to explore the correlations among processing conditions, compositional variations, pore-forming agents, and different characteristics (apparent density, apparent porosity, volume shrinkage, and compressive strength) of the sintered ZrO<sub>2</sub>-Al<sub>2</sub>O<sub>3</sub>-MgO porous bio ceramics. This visualisation presents the univariate distributions of each parameter and the bivariate relationships among all variable pairs.





# 3. Chapter Three - Results and discussion

### 3.1 Raw materials characterization results

### 3.1.1 XRD test results of raw materials

The XRD technique was used to characterize the phase composition of the raw ceramic powders. The as-received commercial monoclinic-ZrO<sub>2</sub> powder diffraction pattern is shown in Fig. 3.1 (The full size of XRD pattern can be seen in Appendix B.). As expected, the ZrO<sub>2</sub> powder sample only presents the monoclinic phase peaks. The results clearly show that the highest two peaks, which are the (111) and (-111) at 2 $\Theta$  are about 28° and 31°, they are both for monoclinic crystal structure (baddeleyite).

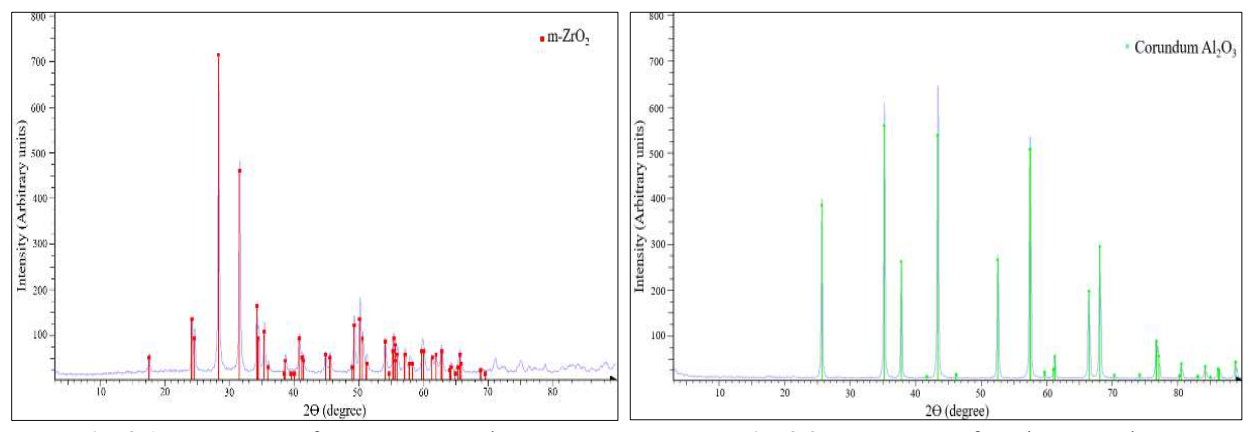


Fig. 3.1 XRD pattern for m-ZrO<sub>2</sub> powder

Fig. 3.2 XRD pattern for Al<sub>2</sub>O<sub>3</sub> powder

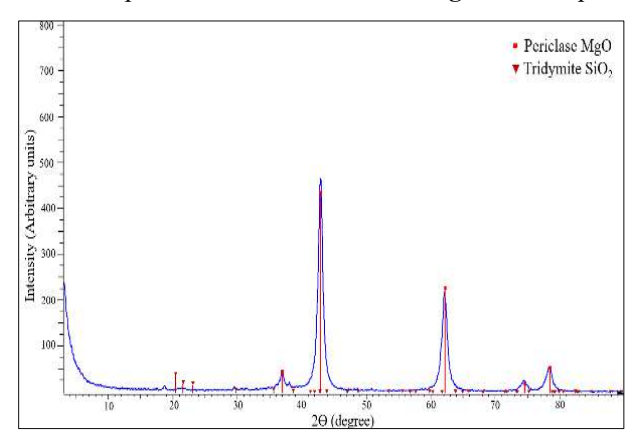


Fig. 3.3 XRD pattern for MgO powder

XRD pattern of the  $Al_2O_3$  powder, as shown in Fig. 3.2 (The full size of XRD pattern can be seen in Appendix B.), shows that only pure corundum  $Al_2O_3$  phase detected with several high intensity peaks at  $2\Theta = 26^{\circ}$ ,  $35^{\circ}$ ,  $38^{\circ}$ ,  $43^{\circ}$ ,  $52^{\circ}$ ,  $57^{\circ}$ ,  $66^{\circ}$ , and  $68^{\circ}$  for planes (012), (104), (110), (113), (024), (116), (216) and (300), respectively. The XRD pattern for MgO powder, that is shown in Fig 3.3 (The full size of XRD pattern can be seen in Appendix B.), shows that the sharper and more intense

peaks at diffraction angles of  $2\Theta = 37^{\circ}$ ,  $43^{\circ}$ ,  $62^{\circ}$  are mainly ascribed to diffraction by basal planes (1 1 1), (2 0 0), (2 2 0) of periclase MgO phase, respectively. The result also shows the presence of low intensity peaks for tridymite SiO<sub>2</sub> phase as impurity. The XRD finding indicates that there is no presence of hazardous or poisonous compounds that may threaten human health, making the material particularly appropriate for bio-medical devices, implants, or tissue engineering.

### 3.1.2 SEM test results for raw materials

The microstructure and properties of ceramics are greatly impacted by variations in the morphology of the raw ceramic oxide particles. Smaller particles possess a larger surface area, enhancing their capacity for denser packing. Spherical or equiaxed particles have enhanced packing efficiency, resulting in a more homogeneous microstructure in the finished ceramic [141-143]. The SEM micrographs of m-ZrO<sub>2</sub> powder are shown in Fig. 3.4 (a) and (b).

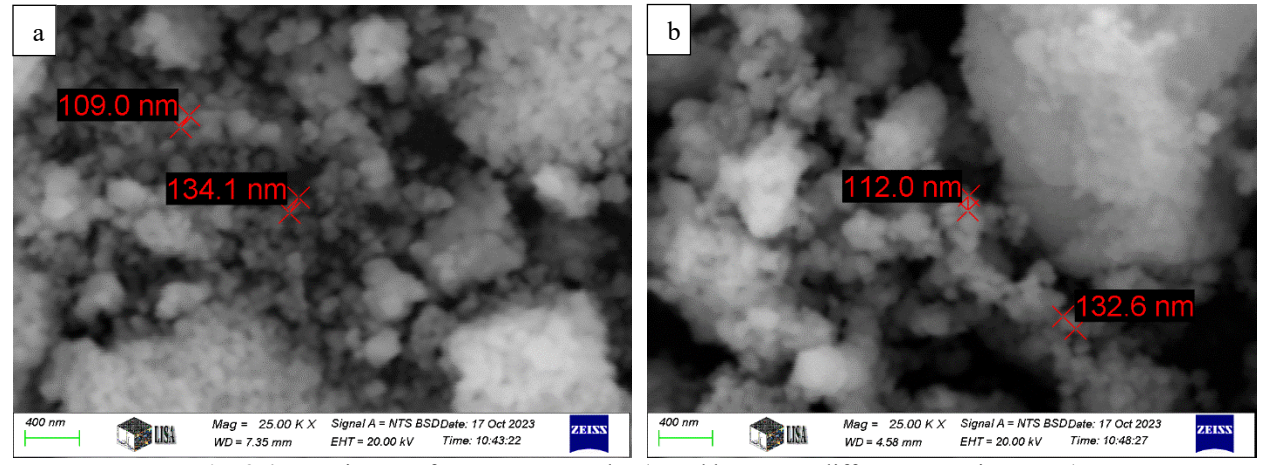


Fig. 3.4 SEM images for m-ZrO<sub>2</sub> powder (a and b are two different scanning areas)

The SEM micrographs reveal that the m-ZrO<sub>2</sub> powder has a hierarchical structure in which nanoscale particles aggregate to create bigger micron-sized grains. As shown in Fig. 3.4, the main particle size was slightly more than 100 nm. Materials in nanoparticles scale possess a substantial surface area in relation to their volume, resulting in an increased number of exposed surface atoms. These atoms enhance surface energy, rendering nanoparticles intrinsically less stable and more prone to interactions with adjacent particles. Materials often want to decrease their energy to attain a more stable state; hence, for nanoparticles, aggregation is a spontaneous process that facilitates the particles in achieving a lower-energy, more stable form. In m-ZrO<sub>2</sub> fine powder, van der Waals forces attract the nanoparticles, resulting in their aggregation into clusters [144, 145]. Fig. 3.5 (a), and (b) illustrate the SEM micrographs of Al<sub>2</sub>O<sub>3</sub> powder. Al<sub>2</sub>O<sub>3</sub> powder comprises fine particles

with very little agglomerations. The majority of the Al<sub>2</sub>O<sub>3</sub> particles exhibit elliptical, or longitudinal forms. The SEM micrographs indicate that the Al<sub>2</sub>O<sub>3</sub> particle size exceeded 100 nm.

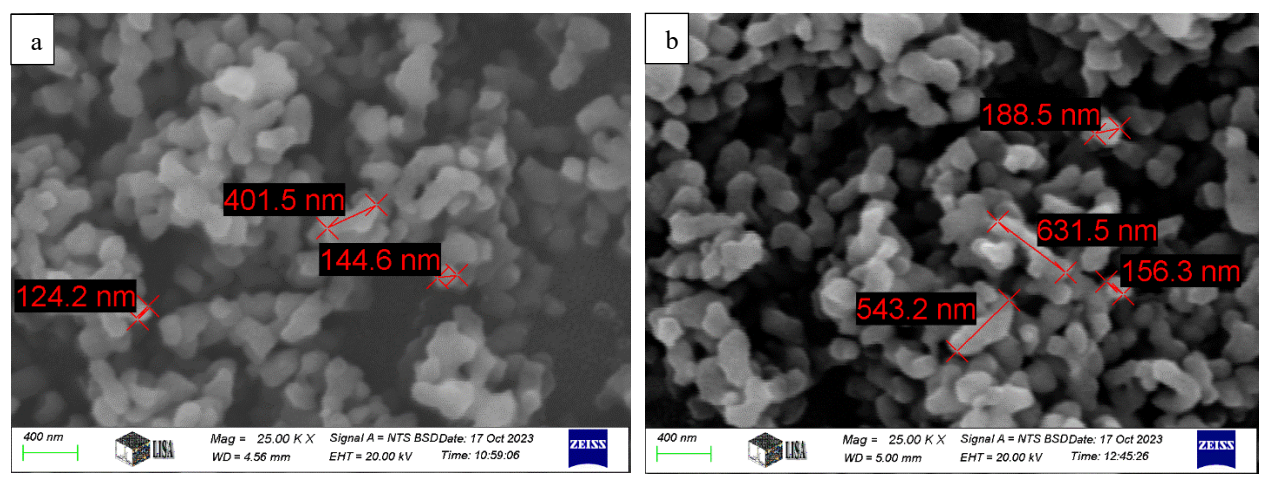


Fig. 3.5 SEM images for Al<sub>2</sub>O<sub>3</sub> powder (a and b are two different scanning areas)

MgO powder SEM micrographs are shown in fig. 3.6 (a) and (b). Micrographs show that the MgO powder is mostly fine particles that have not clumped together. The particle shape of MgO particles is irregular, but most of them can be considered to have a faceted shape. The size of the MgO particles was larger than 100 nm.

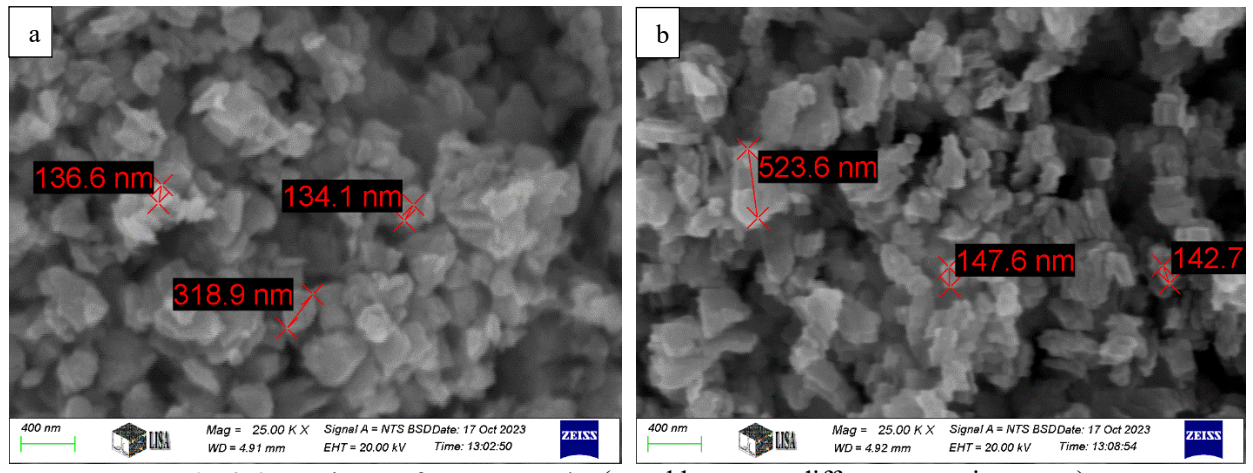


Fig. 3.6 SEM images for MgO powder (a and b are two different scanning areas)

The morphology of the pore-forming agent used in the fabrication of porous structures significantly affect their characteristics, especially if the porous structure is used in biomedical applications like in bone replacement applications. In biomedical application, the shape and size of generated pores must be suitable to facilitate the cell migration, bone ingrowth, proliferation and vascularization. Larger pore forming agent particles generate larger pores, hence increasing the surface area of the porous material. The increasing surface area of porous materials leads to improved bonding with the living tissues. The increased surface area of the pore offers a greater

number of interconnected pores by increasing the number or the size of the channels or openings between the pores. Interconnection pores facilitate cell migration, nutrient transport, and vascularization and also enhance the connection between the living tissue and the artificial part. The quantity of pore-forming agent significantly influences the properties of porous structures. Employing a small content results in a denser structure with reduced porosity. Although this may enhance compressive strength, it diminishes porosity, so restricts cell infiltration and vascularization. In contrast, increasing the quantity of pore-forming agent leads to a structure characterized by enhanced porosity but decreased compressive strength. Therefore, when designing the porous structure for bone replacement applications, it is crucial to consider the balance between porosity and compressive strength [146-149]. The SEM was used to evaluate the potato and tapioca starch particle morphology. Fig. 3.7 (a) and (b) illustrates the SEM images of tapioca starch at different magnifications.

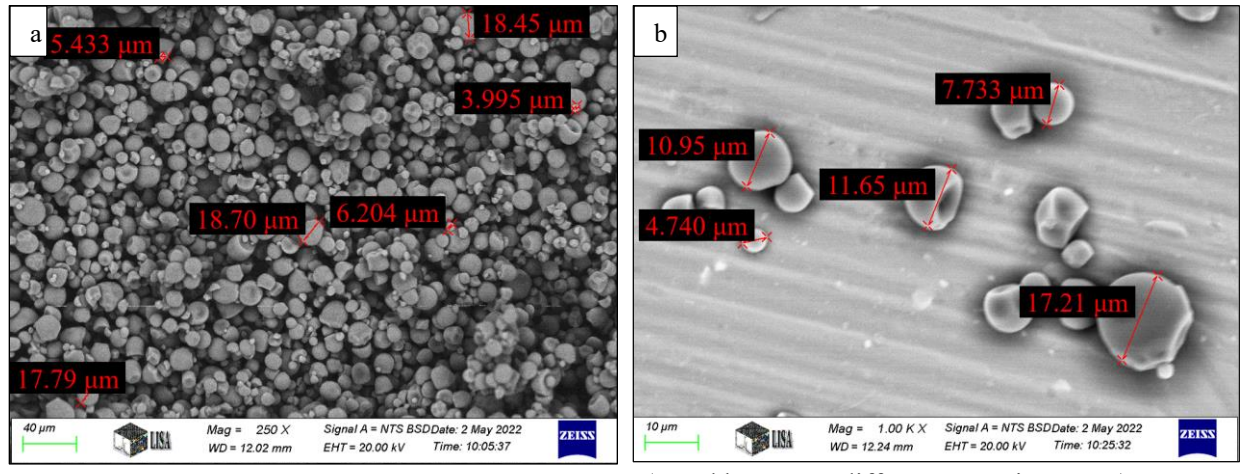


Fig. 3.7 SEM image for tapioca starch particles (a and b are two different scanning areas)

Tapioca starch particles present approximately round (spherical) shapes with different particle size distribution. As shown in Fig. 3.7, tapioca starches have an average particle diameter greater than 10µm. The SEM micrographs in Fig. 3.8 (a) and (b) for potato starch powder. The granules seem generally oval to spherical in form, with smooth, well-defined surfaces. The size of the granules varies, which is common for potato starch, and this heterogeneity impact the gelatinization behaviour and functional qualities of the starch. No essential surface damage, fractures, or abnormalities are noticed on the granules, suggesting that the granules remain essentially intact and unchanged. The smoothness of the surface and the absence of apparent pores suggest a natural, non-gelatinized starch structure. The micrographs show that the granules do not

display any evidence of aggregation or collapse. As compared with tapioca starch, potato starch particles have a bigger size (the mean particle size approximately more than 25 µm).

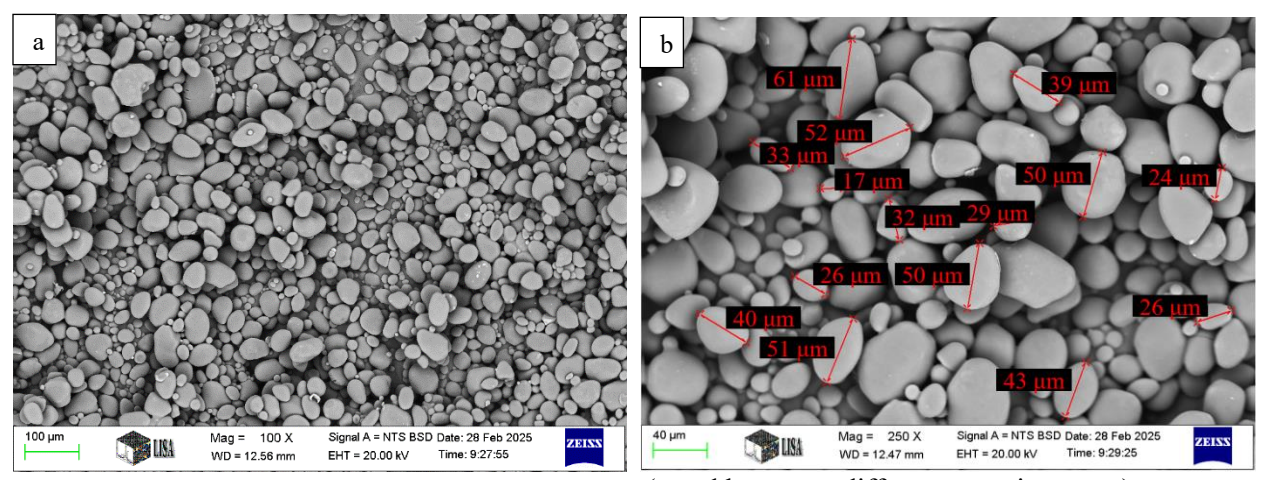


Fig. 3.8 SEM image for potato starch particles (a and b are two different scanning areas)

### 3.1.3 Particle size distribution test results of raw materials

CILAS Granulometry 715 equipment was used to determine the particle size distribution of ceramic raw materials. Fig. 3.9 illustrates the cumulative particle size distributions of the three ceramic raw materials: m-ZrO<sub>2</sub>, Al<sub>2</sub>O<sub>3</sub>, and MgO.

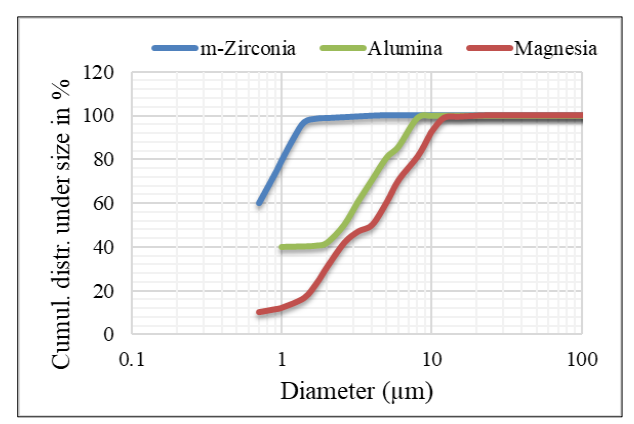


Fig. 3.9 The particle size distribution of the ceramic raw materials

The x-axis represents the particle diameters on the logarithmic scale (ranging from 0.1 to 100 μm), whereas y-axis represents the cumulative percentage of the particles that have a size smaller than a given size. The particle size distribution curve of m-ZrO<sub>2</sub> rises steeply between approximately 0.8 and 2 μm, reaching nearly 100% passing with a size of 2 μm, indicating a fine and narrow particle size distribution. The particle size distribution curve of Al<sub>2</sub>O<sub>3</sub> shows a wider distribution, starting at about 40% passing with about 1 μm and reaching 100% passing at around 8 μm. The particle size distribution curve of MgO displays the coarsest and broadest distribution, with a particle size gradually increased from about 1 μm to 100% passing more than 10 μm. The

differences in the particle size distributions affect the processing and properties of the materials. The smallest particle size powder such as ZrO<sub>2</sub> offers larger surface area and enhanced sintering behaviour, while coarser particle size powder such as magnesia can offer lower shrinkage and improved thermal shock resistance. Table 3.1 summarizes the D10, D50, and D90 that extracted from the curves in Fig. 3.9.

Table 3.1 The D10, D50, and D90 of the ceramic raw materials

Ceramic powder	D10 (μm)	D50 (µm)	D90 (μm)
m-ZrO <sub>2</sub>	no data	no data	1.8
Al <sub>2</sub> O <sub>3</sub>	$Al_2O_3$ 1.5		8.0
MgO	2.0	6.0	15.0

Where D10 represent the particle size where 10% are finer, D50 represents the median particle size (50% of particles are finer and 50% are coarser), and D90 represents the particle size where 90% of the particles are finer.

## 3.1.4. Moisture content and swelling factor of the starches test results

The moisture content of potato and tapioca starches has been determined using a moisture determination balance. Upon completion of the test, the moisture content, expressed as a percentage, is displayed on the screen of the device. The measured moisture content of potato starch powder was 15.17 %, whereas that of tapioca starch powder was 11.63 %. Fig. 3.10 analyses the swelling characteristics of potato and tapioca starch.

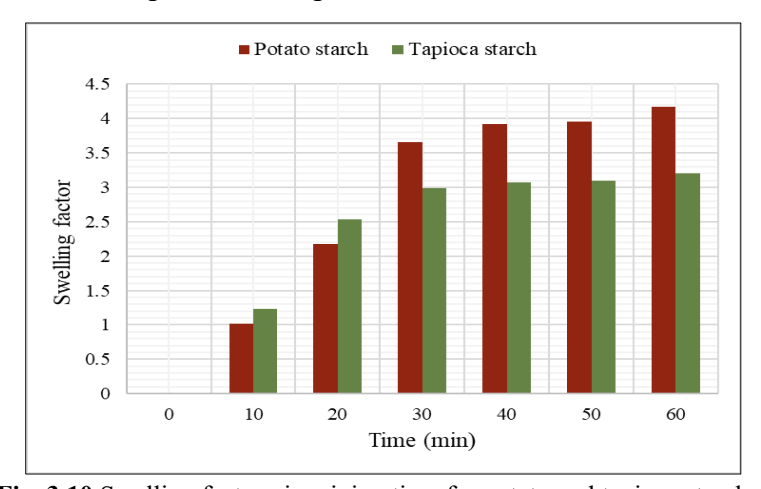


Fig. 3.10 Swelling factor via mixing time for potato and tapioca starches

Tapioca starch has a more rapid swelling rate and attains its peak swelling capacity quicker than potato starch. The accelerated swelling results from the higher amylopectin content in tapioca starch, facilitating water penetration and the disruption of the granule structure more effectively [150, 151]. Potato starch, has bigger granules, expands considerably, exhibiting enlargement with rising temperatures. The swelling characteristics of starch directly affect the pore morphology of

the resultant ceramic product. Potato starch, characterised by its bigger granules and enhanced swelling ability, often yields ceramics with larger pores. The swelling factor (ratio of final to initial size after swelling) of potato starch (about 4.1) is greater than that of tapioca starch (about 3.2).

### 3.2 Porous ceramics characterization results

# 3.2.1 Test results of studying the effect on different content and type of starches with different distilled water content

Density and porosity are the most important characteristics that influence the properties of the prepared porous structure. Fig. 3.11 (a) and (b) illustrate the relation between the apparent densities of porous ceramic samples and the amount of starch present in the suspension at varying concentrations.

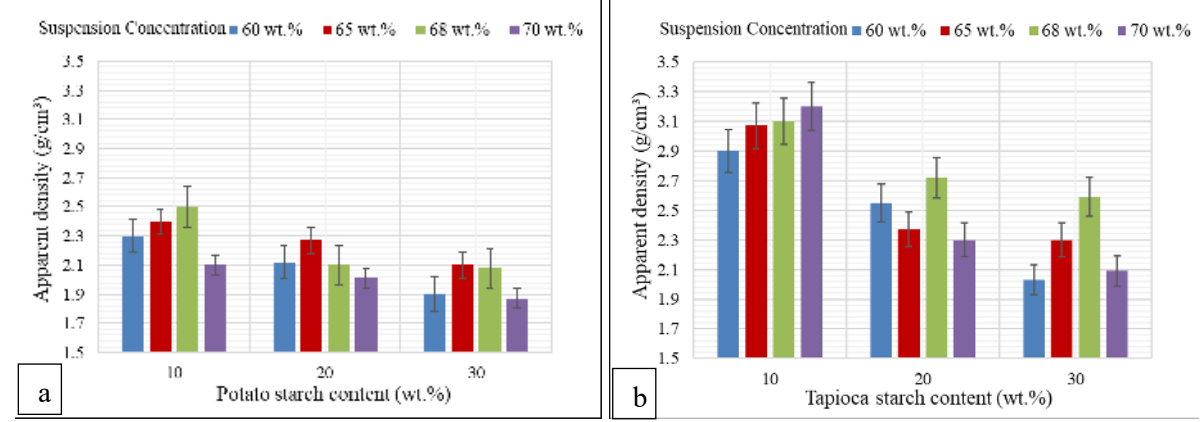


Fig. 3.11 Apparent density via potato starch content (a) and tapioca starch content (b)

Fig. 3.11 (a) depicts samples made with potato starch, while (b) depicts other samples made with tapioca starch. According to the findings, the apparent densities of the samples decrease as the amounts of potato and tapioca starch increase. As the amounts of starch increased, less ceramic particles were packed between the starch granules; thus, the decrease in the ceramic powders content was accompanied by a decrease in the density. There is no consistent influence that the concentration of the suspension has on the apparent densities of the samples. Fig 3.12 (a) and (b) shows the relation between the apparent porosity and starch content at different suspension concentration. The results illustrate that the apparent porosity is largely controlled by the starch content in the suspension. As potato starch has a larger swelling factor than tapioca starch, it undergoes more significant shape changes during swelling and gelatinization, resulting in higher apparent porosity for most samples. The high starch content in the slurry will be able to draw in a significant quantity of moisture from the surrounding environment, then swell and gelatinize. This

starch then burns off during the sintering process, creating pores in the structure that reduce the density of the structure and increase its porosity.

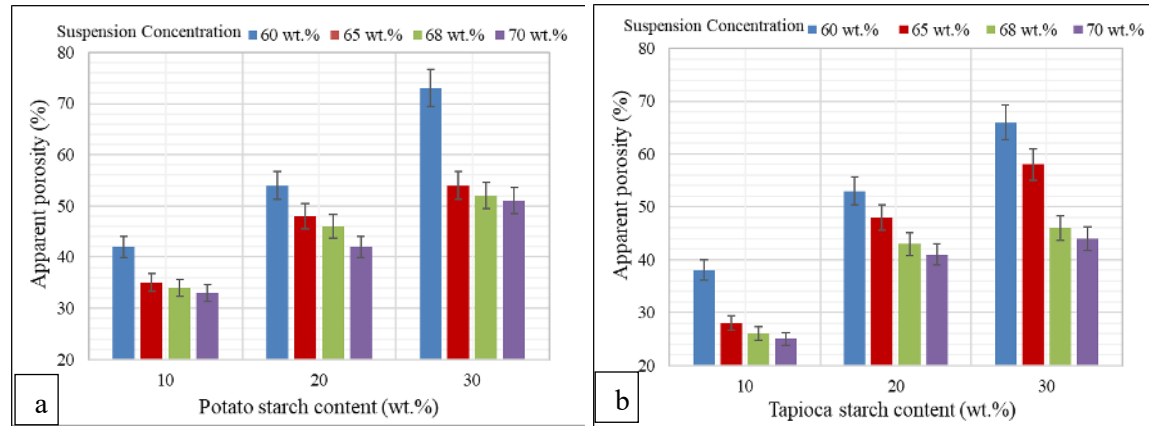


Fig. 3.12 Apparent porosity via potato starch content (a) and tapioca starch content (b)

Fig. 3.13 (a) and (b) provide a comparison of the values of volume shrinkage as a function of the starch content and the suspension concentration.

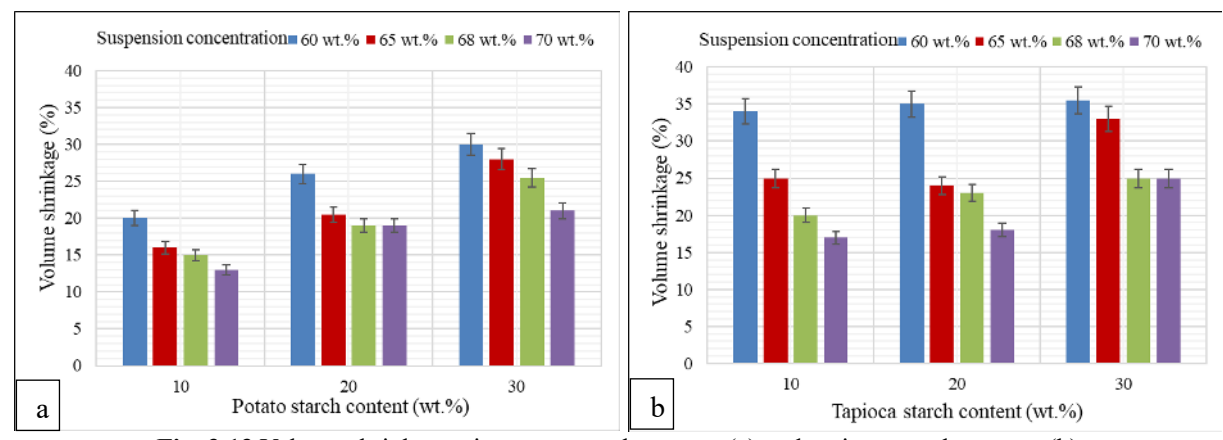


Fig. 3.13 Volume shrinkage via potato starch content (a) and tapioca starch content (b)

As the proportion of ceramic powder in the suspension increases, the volume shrinkage reduces. In addition, the volume shrinkage is increased by an increase in the amount of starch present. The samples with 30 wt.% potato starch shrank the most; by about 35.5%. The size of pores is increased in samples that include potato starch; therefore, these samples have higher volume shrinkage. SEM was used in order to explore the pore and surface morphology of the prepared samples. Fig. 3.14 (a) shows the SEM image of a sample with 10 wt.% potato starch and 70 wt.% suspension concentration. This sample has apparent porosity of about 33%. The sample shown in (b) has 30 wt.% potato starch and 60 wt.% suspension concentration. This sample has an apparent porosity that is roughly 73% higher than any other. In this sample the pores do not have a regular form, despite the fact that there are many pores as indicated in the image. From the results, it is possible

to conclude that the pore size decreased and the shape irregularity increased along with the potato starch content. This agrees with the results of the research by Garrido et al [152].

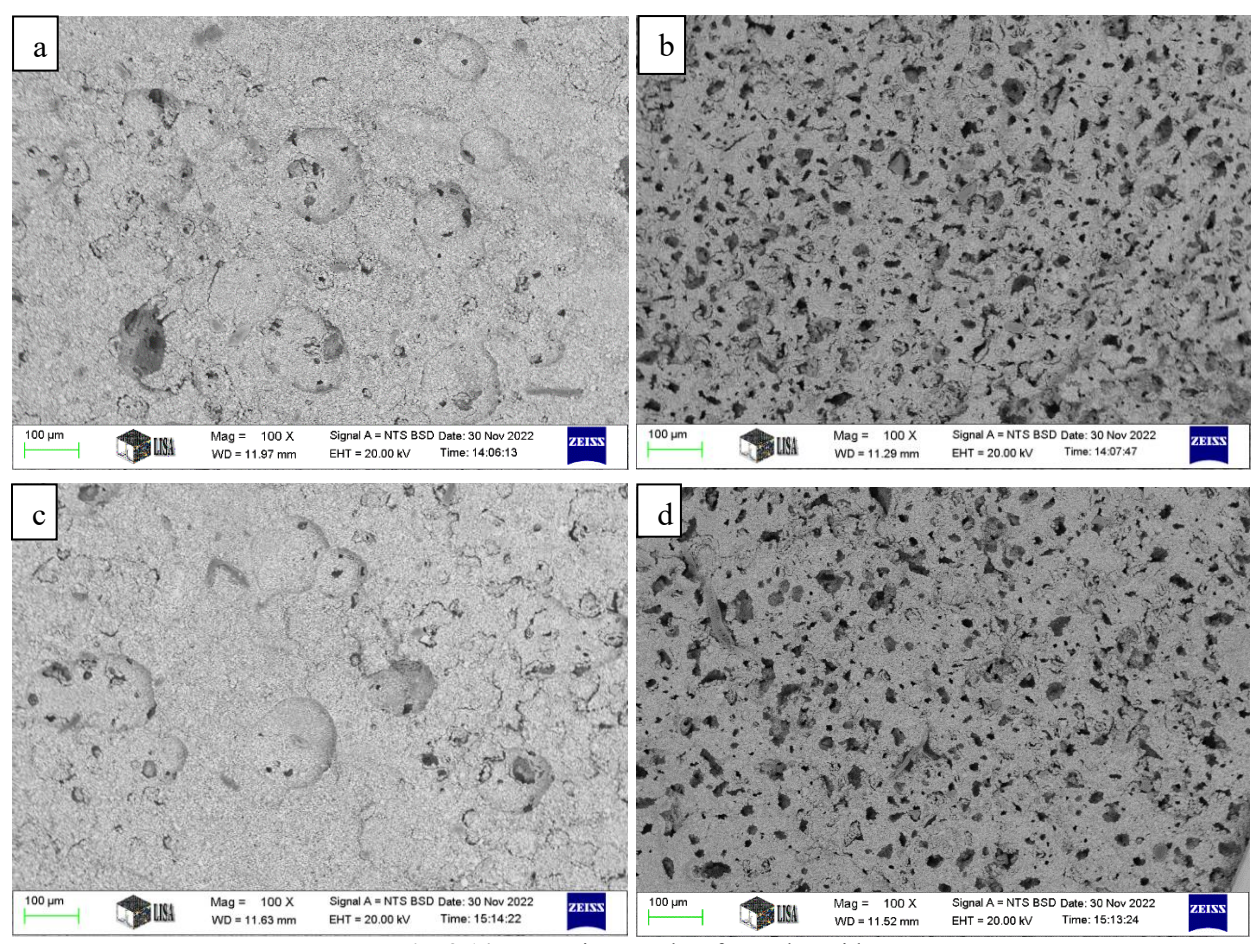


Fig. 3.14 SEM micrographs of samples with:
- Potato starch at 10 wt.% (a), 30 wt.% (b),
- Tapioca starch at 10 wt.% (c), 30 wt.% (d)

The same behaviour is seen when tapioca starch is used, as shown in (c) and (d), where (c) is for samples containing 10 wt.% tapioca starch and 70 wt.% suspension concentration and (d) is for samples containing 30 wt.% starch and 60 wt.% suspension concentrations. In general, it is clear that the ceramic composites produced from suspensions containing a low starch content (10 wt.%) have substantially bigger pores than those produced from suspensions containing a higher starch content (30 wt.%). This finding is in full accordance with the principle of starch consolidation casting, and it verifies a large number of findings in previous study [153,154]. As can be observed in Fig. 3.15 (a) and (b), the ceramic shells are visible inside the pores. It is clearly evident that the interaction between the ceramic particles and the starch granules had a significant role in the formation of these shells. During the process of heating, a layer of ceramic particles that

adhered to the surface of the starch granule is separated from the rest of the ceramic matrix and moves in the same direction as the starch granule as they shrink.

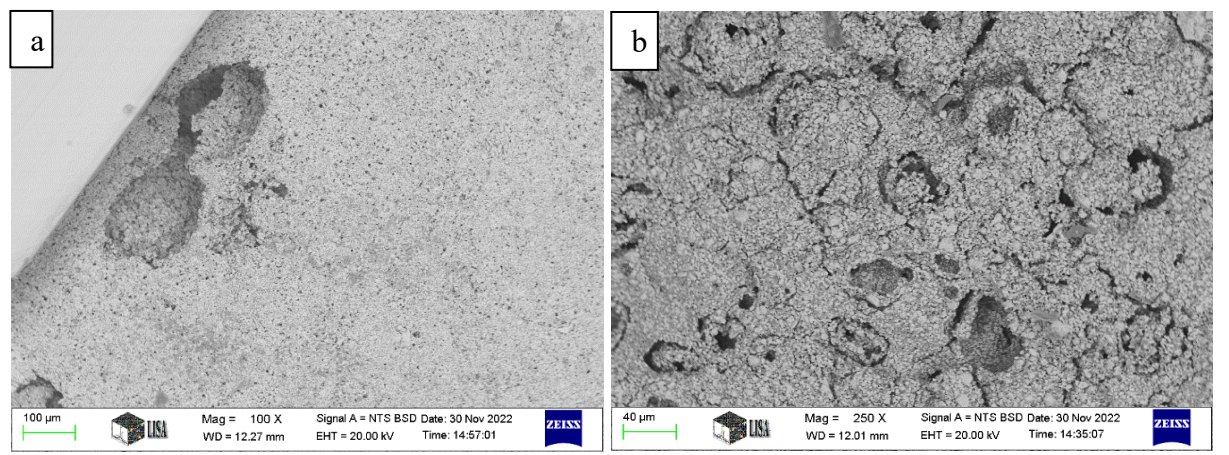


Fig. 3.15 SEM micrographs of samples with:

- (a) 30 wt.% tapioca starch and 60 wt.% suspension concentration
- (b) 10 wt.% potato starch and 70 wt.% suspension concentration

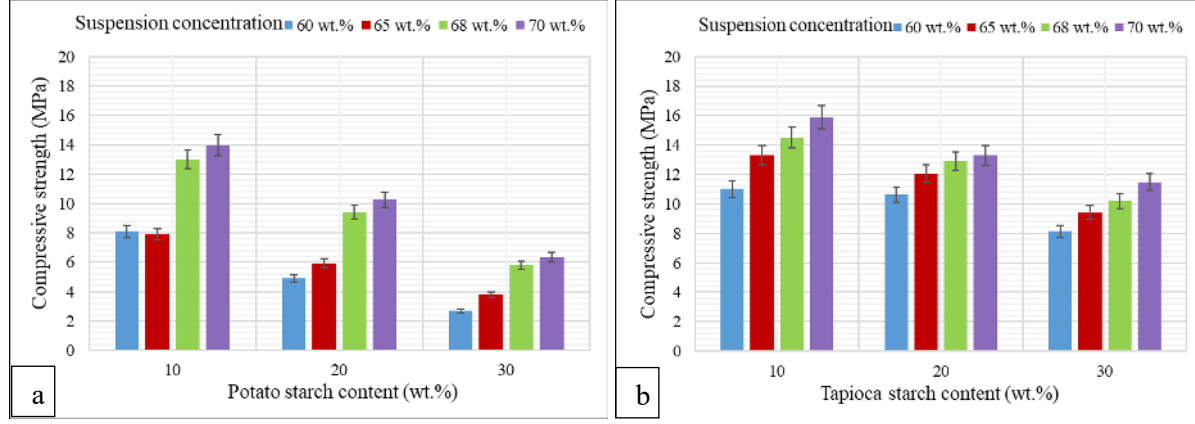


Fig. 3.16 Compressive strength via potato starch content (a) and tapioca starch content (b)

Fig. 3.16 (a) and (b) illustrate the variation in compressive strength with potato and tapioca starch contents at varied suspension concentrations. The compressive strength decreased (from 13.97 to 2.7 MPa with using potato starch and from 15.87 to 8.14 MPa with using tapioca starch) with the increase in starch content from 10 wt.% to 30 wt.% and with the decrease in suspension concentration from 70 wt.% to 60 wt.% (increase in water content). The strength was significantly lower than the identical value [155] of dense ZrO<sub>2</sub> ceramics, owing to the considerable porosity that caused an exponential reduction in strength. Compressive strength testing shows that the produced samples have values between 2.7 MPa and 15.87 MPa, which is comparable to trabecular bone (0.1 MPa - 30 MPa) [156]. The Pearson correlation coefficient values for the experimental data were calculated by using a data analysis tool pack in Microsoft Excel to represent the strength of correlation between the experimental data. The experimental data are denoted by Sus. (wt.%)

for suspension concentration, AD for apparent density, AP for apparent porosity, VS volume shrinkage, and  $\sigma$  for the compressive strength. Tables 3.2 and 3.3 show the correlation matrix of the experimental data.

**Table 3.2** The correlation matrix with using of potato starch

	Starch (wt.%)	Sus. (wt.%)	AD	AP	VS	σ
Starch (wt.%)	1					
Sus. (wt.%)	0	1				
AD	-0.738	-0.268	1			
AP	0.819	-0.499	-0.549	1		
VS	0.545	-0.737	-0.031	0.769	1	
σ	-0.761	0.517	0.292	-0.848	-0.842	1

**Table 3.3** The correlation matrix with using of tapioca starch

	Starch (wt.%)	Sus. (wt.%)	AD	AP	VS	σ
Starch (wt.%)	1					
Sus. (wt.%)	0	1				
AD	-0.873	-0.095	1			
AP	0.726	-0.472	-0.774	1		
VS	0.187	-0.909	-0.084	0.574	1	
σ	-0.798	0.516	0.639	-0.265	-0.371	1

The correlation coefficient values range from +1 (which means that there is a perfectly positive linear correlation) to -1 (which means that there is a perfectly negative linear correlation), while the zero value means that there is no linear correlation between the two variables. The results indicate that there is a strong negative correlation between the starch content and the apparent density and compressive strength. The results also show that there is a strong positive correlation between the starch content and the apparent porosity. The suspension concentration has a strong negative correlation with the volume shrinkage, which means that with decreasing water content the volume shrinkage decreases. To provide a comprehensive analysis of the inter-variable correlations and understand the fundamental data structure, the pair plot was generated with the Seaborn library in Python. Figs. 3.17 (with different potato starch wt.%), 3.18 (with different tapioca starch wt.%), and 3.19 (with different suspension wt.%) illustrate a pair plot of four study features: apparent density, apparent porosity, volume shrinkage, and compressive strength. The diagonal subplot illustrates the distribution of an individual variable, while the off-diagonal plots provide scatter plots that demonstrate the interactions between pairs of variables.

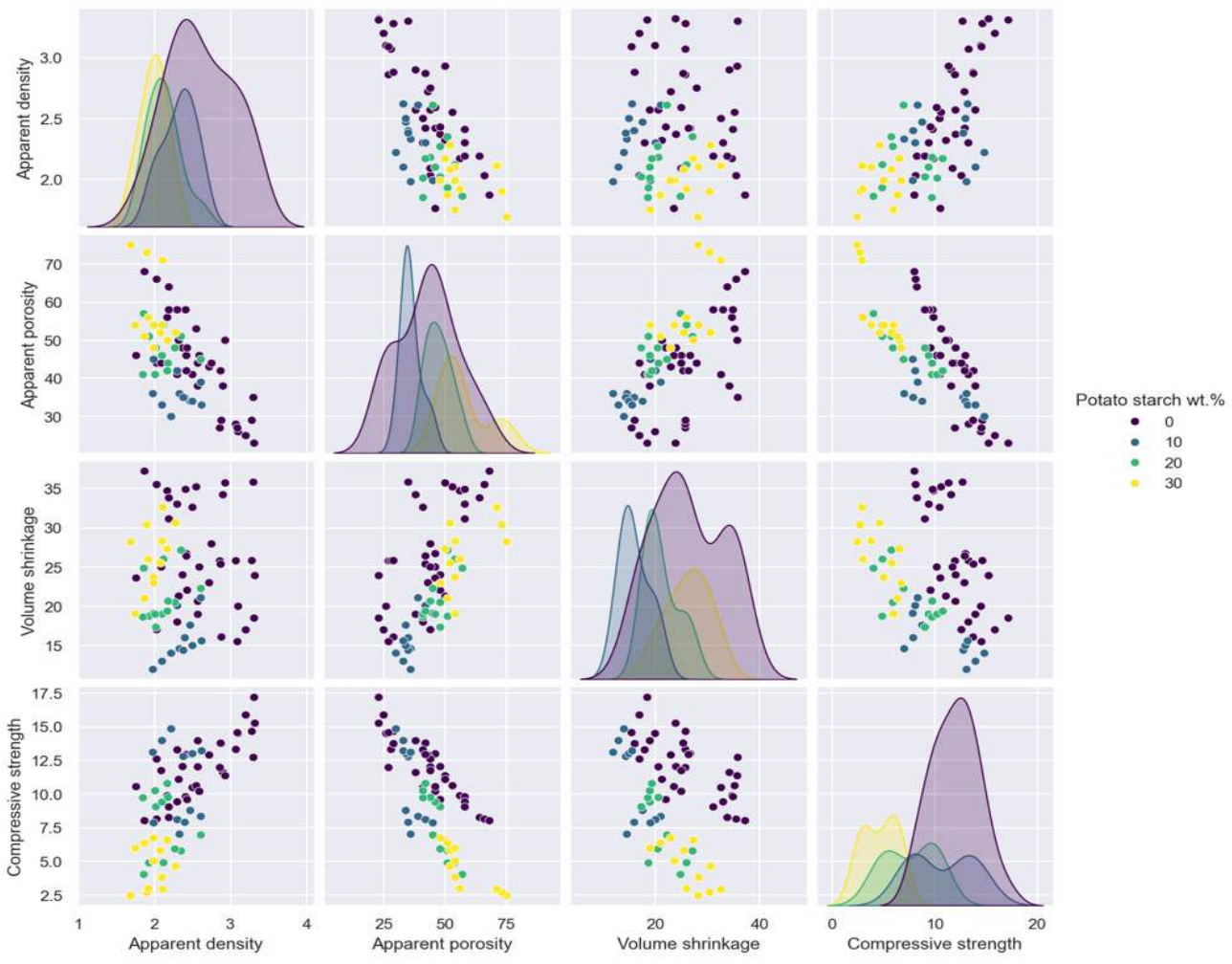


Fig. 3.17 Pair plot of four study features of samples prepared with different potato starch wt.%

Figs. 3.17 and 3.18 demonstrate that the apparent density and compressive strength are highest in the absence of starch and decrease with the incorporation of starches. The apparent porosity and volume shrinkage increased as the potato and tapioca starches wt.% increased. In summary, the starches weaken the strength of the prepared porous ceramics while increasing its porosity. Table 3.4 summarize the type of correlation between the variables in Figs. 3.17 and 3.18.

**Table 3.4** Correlation relationships between the variables for samples prepared with potato and tapioca starches

Variables	AD	AP	VS	σ
AD	_	Negative	Weak	Positive
AP	Negative	_	Positive	Negative
VS	Weak	Positive	-	Negative
σ	Positive	Negative	Negative	_

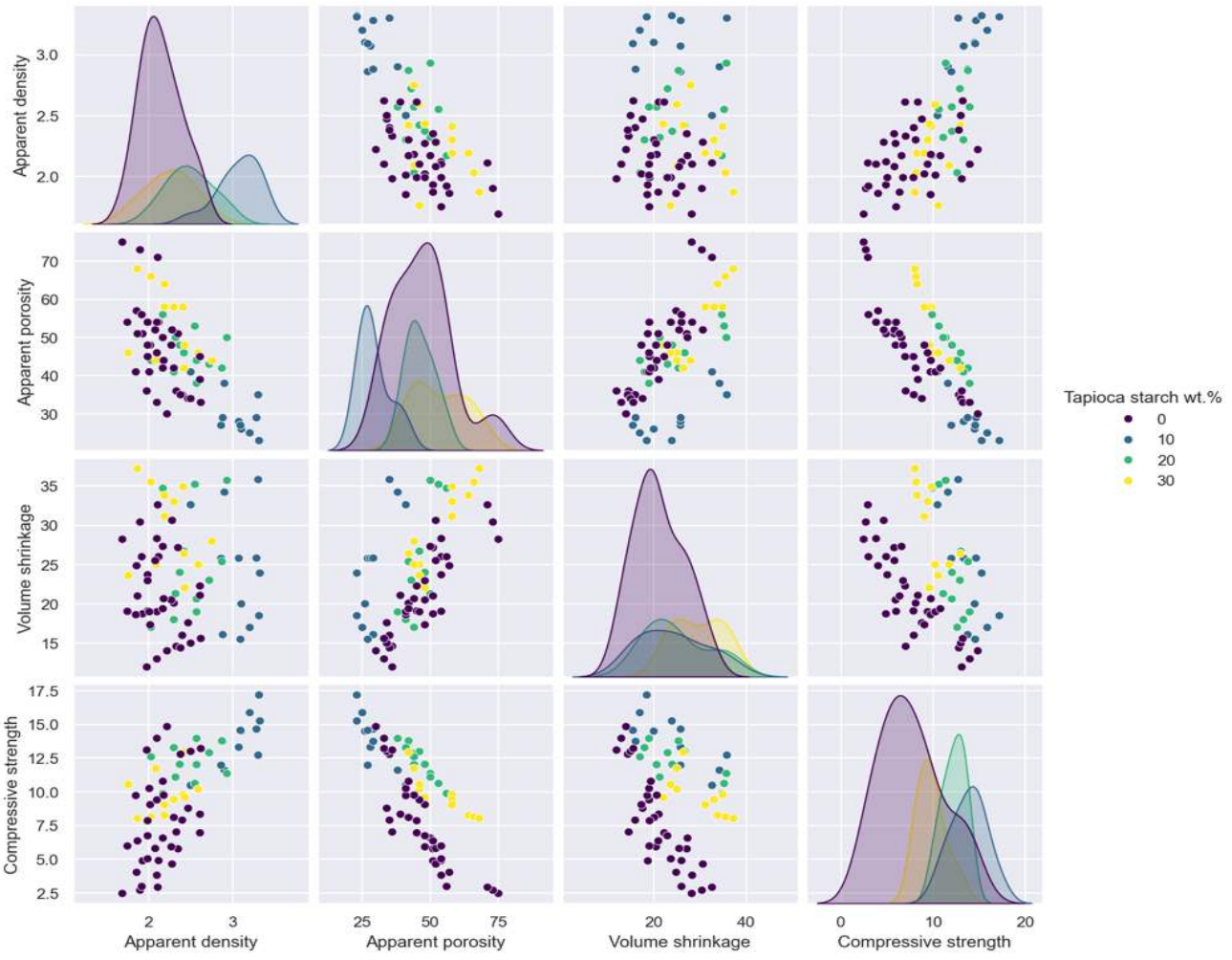


Fig. 3.18 Pair plot of four study features of samples prepared with different tapioca starch wt.%

The findings demonstrate a negative correlation between apparent density and apparent porosity, as anticipated, as a reduction in porosity after sintering leads to an increase in material density. The weak correlation between apparent density and volume shrinkage indicates that densification may be non-uniform, since pore coalescence and enlargement (the pore coalescence and enlargement occurrence will be demonstrated using SEM in the third study of the thesis) occurring at elevated temperatures might result in incomplete shrinking. The positive correlation between apparent density and compressive strength suggests that increased density often enhances mechanical strength, a characteristic commonly observed in ceramics. The apparent porosity has a positive correlation with volume shrinkage and a negative correlation with compressive strength, indicating that increased porosity not only facilitates dimensional change during sintering but also diminishes the strength of the materials. The negative correlation between volume shrinkage and compressive strength further indicates that excessive shrinkage or atypical microstructural

evolution, such as pore coarsening, can offset the strengthening impact of densification. The correlations illustrate the complex relationship between densification, pore evolution, and mechanical performance during the sintering of the multiphase ceramic system. The diagonal in Fig. 3.19 illustrates the distribution of a single variable over varying suspension concentrations.

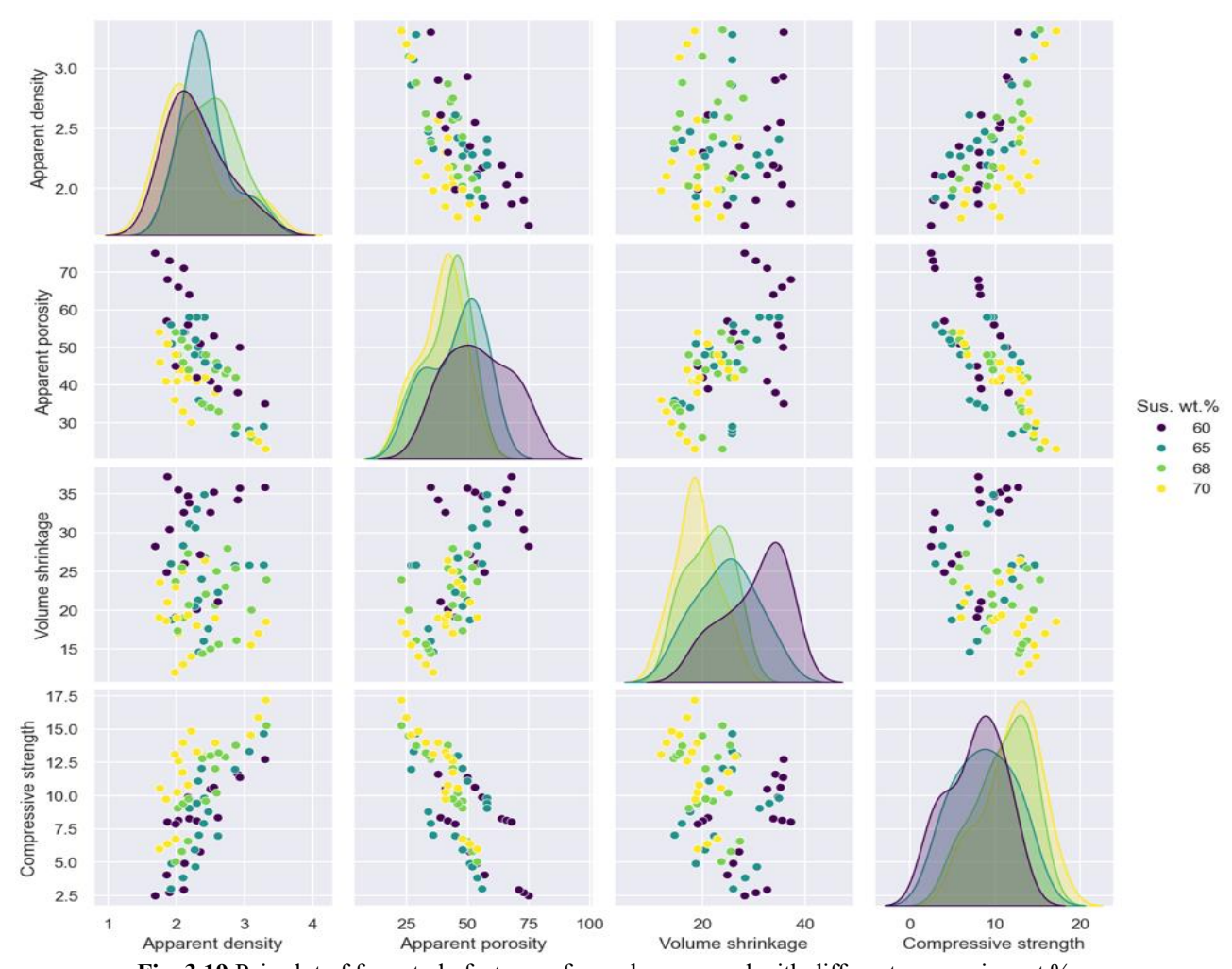


Fig. 3.19 Pair plot of four study features of samples prepared with different suspension wt.%

The suspension concentration has no discernible impact on the apparent density. With a rise in suspension wt.%, both apparent porosity and volume shrinkage often decrease, attributable to changes in packing behaviour and microstructural evolution of the material during drying and sintering. At higher suspension wt.%, the slurry has a larger fraction of solid particles compared to the liquid phase, resulting in denser particle packing and reduced interparticle spacing leading to reduced volume shrinkage. At higher suspension wt.%, the water amount is not sufficient for the starch absorption and swelling, resulting to lower porosity. Fig. 3.19 also illustrate that there is

a positive correlation between the suspension wt.% and compressive strength. Table 3.5 summarize the type of correlation between the variables.

**Table 3.5** Correlation relationships between the variables for samples prepared with different suspension wt.%

Variables	AD	AP	VS	σ
AD	_	Negative	Weak	Positive
AP	Negative	_	Positive	Negative
VS	Weak	Positive	-	Negative
σ	Positive	Negative	Negative	_

Fig. 3.20 illustrates four bar charts, each indicating the coefficient of variation (CV%) for a particular feature measured over 24 group (each group is the average of 3 samples).

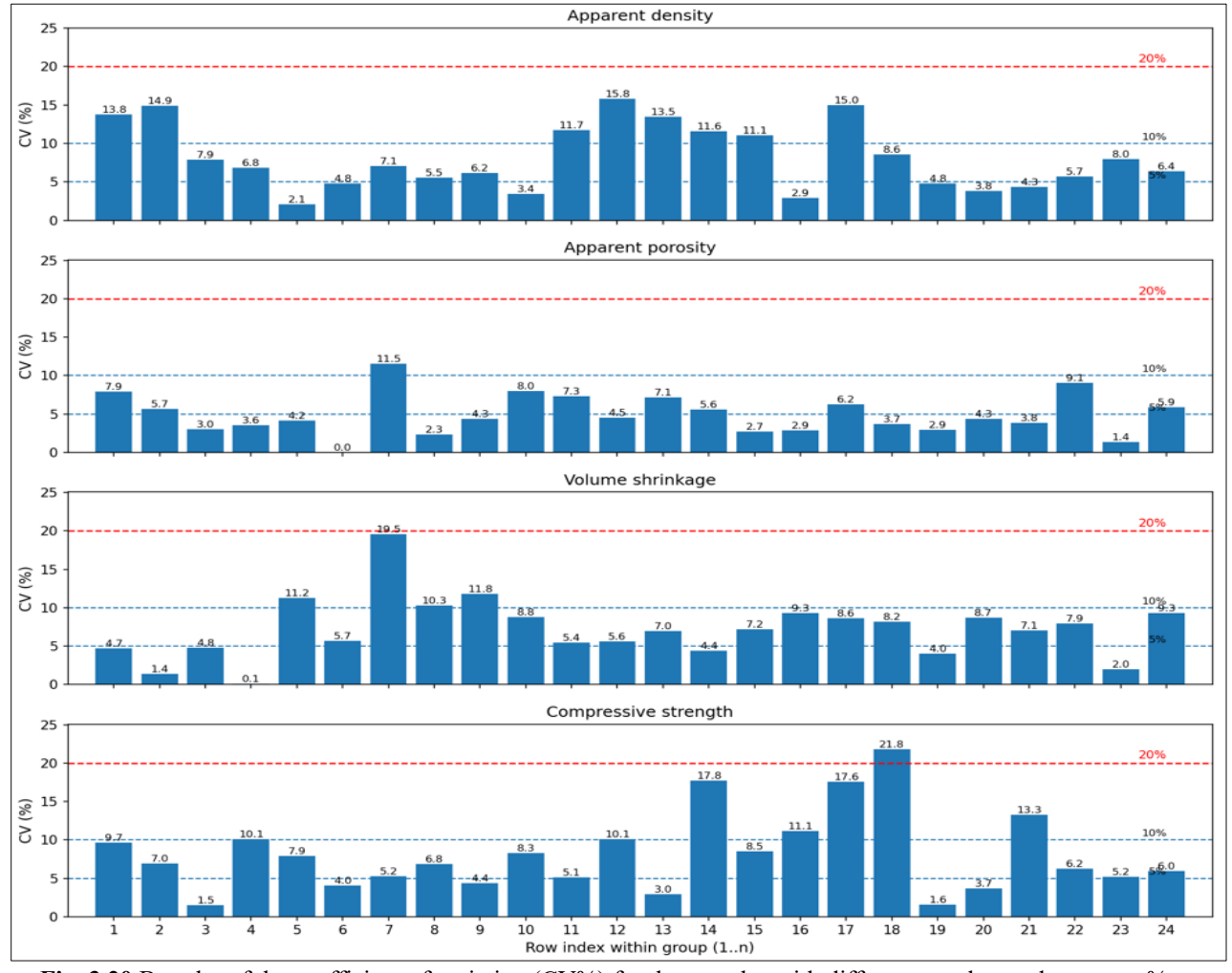


Fig. 3.20 Bar plot of the coefficient of variation (CV%) for the samples with different starches and water wt.%

The plots indicate that the majority of samples display CV (%) values under 10%, implying strong measurement consistency and minimal data dispersion. A limited number of samples

exceeding the 10% threshold, suggesting marginally increased variability potentially resulting from experimental or material heterogeneity. The findings indicate that the experimental measures are mostly reliable, with the majority of data sets remaining within acceptable variability thresholds (under 20%).

In order to meet the requirements of using prepared porous ceramics in biomedical applications such as bone replacement, it is essential to achieve a balance among apparent porosity, density, and mechanical properties. Upon concluding the first study of the thesis, it was determined that using a 20 wt.% starch content combined with a 60 wt.% suspension concentration yields good apparent porosity (54% with potato and 53% with tapioca), apparent density (2.12 g/cm³ with potato and 2.55 g/cm³ with tapioca), and compressive strength (4.9 MPa with potato and 10.6MPa with tapioca) that are appropriate for bone replacement applications.

# 3.2.2 Test results of studying the effect on different content of Al<sub>2</sub>O<sub>3</sub> with different types of starches

Depending on the optimum results of the first study, the used starch content in this study is 20 wt.% (based on solid ceramics) and the suspension concentration is 60 wt.% (based on solids). To reduce the occurrence of cracks and defects on the surface of the samples, gradual pre-sintering and sintering procedure was followed during this study. The effect of adding different content of Al<sub>2</sub>O<sub>3</sub> and different types of starches on the apparent density after pre-sintering and sintering are presented in Fig. 3.21 (a) and (b), respectively.

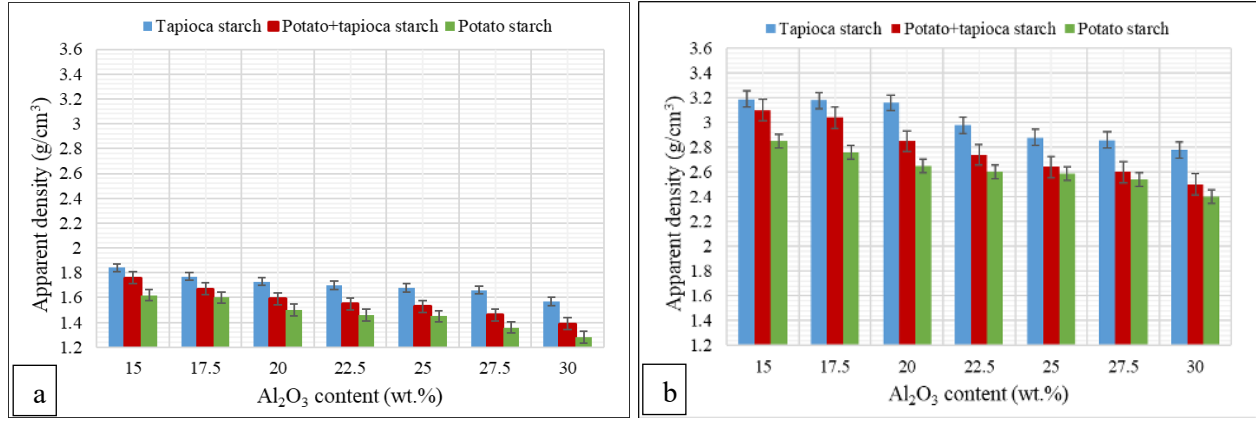


Fig. 3.21 Apparent density via Al<sub>2</sub>O<sub>3</sub> content: (a) after pre-sintering, (b) after sintering

Three distinct categories of starch were employed: potato, tapioca, and a combination of potato and tapioca starches in equal proportions (50:50 wt.%). According to the findings, Al<sub>2</sub>O<sub>3</sub> content negatively correlates with the apparent densities. The reduction in density was seen with an increase in Al<sub>2</sub>O<sub>3</sub> content since the density of Al<sub>2</sub>O<sub>3</sub>, about 3.04 g/cm<sup>3</sup>, is lower than that of ZrO<sub>2</sub>,

which is approximately 5.71 g/cm<sup>3</sup>. The heating with slow rate of 2 °C/min during pre-sintering and sintering, which enabled the good diffusion and binding of ceramic particles leads to pore minimization. The density of the ceramic composite samples is directly proportional to its porosity. The apparent porosities of the porous structured ceramics after pre-sintering and after sintering are compared in Fig. 3.22 (a) and (b).

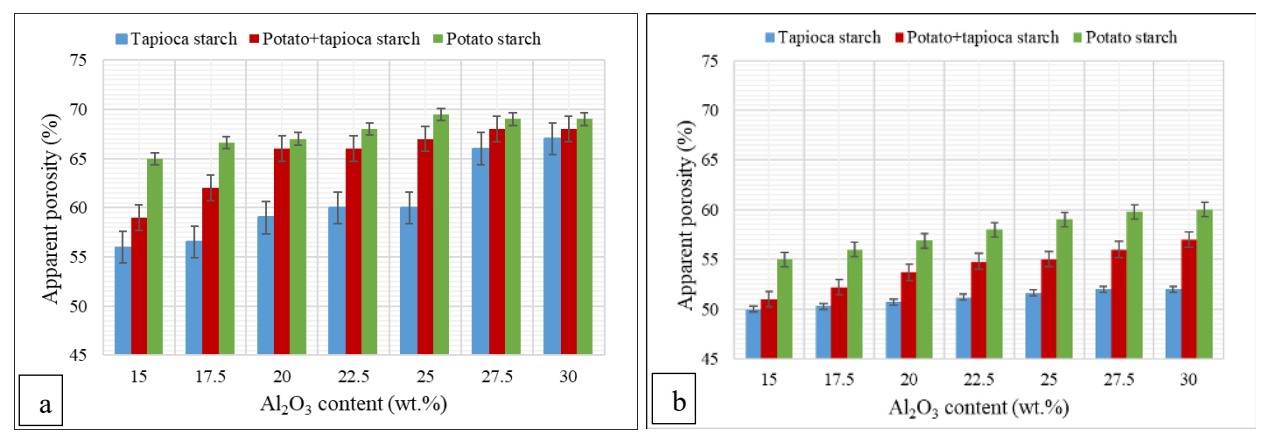


Fig. 3.22 Apparent porosity via Al<sub>2</sub>O<sub>3</sub> content: (a) after pre-sintering, (b) after sintering

Fig. 3.22 indicates that the porosity of ceramics is mostly influenced by the Al<sub>2</sub>O<sub>3</sub> content, since Al<sub>2</sub>O<sub>3</sub> has a significant impact on the density of the samples. The apparent porosity for all samples was increased with the addition of Al<sub>2</sub>O<sub>3</sub>. The calculated apparent porosity after pre-sintering varies from roughly 56 % for a sample consisting of 15 wt.% Al<sub>2</sub>O<sub>3</sub> and made with tapioca starch to around 69% for a sample consisting of 30 wt.% Al<sub>2</sub>O<sub>3</sub> and made with potato starch. While the apparent porosity of sintered samples ranges from approximately 50 % for a sample prepared with tapioca starch and 15 wt.% Al<sub>2</sub>O<sub>3</sub> to about 60 % for a sample prepared with potato starch and 30 wt.% Al<sub>2</sub>O<sub>3</sub>. Fig. 3.23 (a) and (b) provide a comparison of the values of volume shrinkage after pre-sintering and sintering as a function of the Al<sub>2</sub>O<sub>3</sub> content with different type of starch. Al<sub>2</sub>O<sub>3</sub> functions as a grain-boundary stabilizer; its presence hinders grain-boundary movement during sintering, essentially pinning grains and reducing the densification that induces shrinkage [157]. Furthermore, Al<sub>2</sub>O<sub>3</sub> often has a lower melting point than ZrO<sub>2</sub>, which also influences sintering kinetics and densification processes. The combined effects explain why increased alumina content results in reduced shrinkage: increased porosity restricts densification, while the microstructural functions of alumina mitigate mass transfer that induces shrinkage. Higher shrinkage occurs when using potato starch because the swelling factor of potato starch is higher producing higher volume of porosity. A matrix with a high volume of porosity has more tendency to shrink during sintering due to the empty space existing between the matrix particles. However, large pores in the matrix

were not removed during sintering; their size decreases only in proportional relation to the overall shrinkage of the ceramic matrix. The reason is that due to the large diameter (low curvature) of these pores. The driving force of sintering (the so-called sintering pressure) is too low for large pore shrinkage to occur.

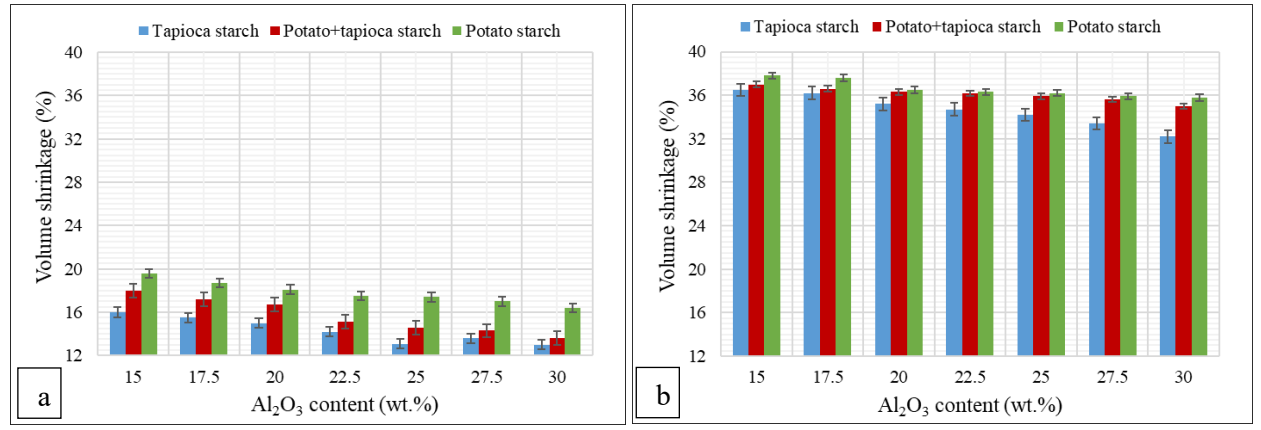


Fig. 3.23 Volume shrinkage via Al<sub>2</sub>O<sub>3</sub> content: (a) after pre-sintering, (b) after sintering

The pore and surface morphology of the porous-structured ceramics after pre-sintering and sintering are shown in Fig. 3.24 and 3.25, respectively.

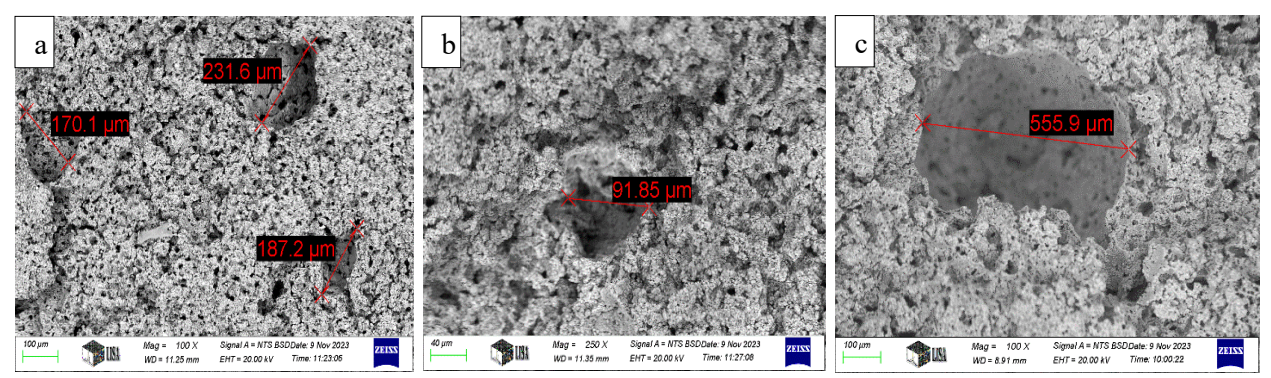
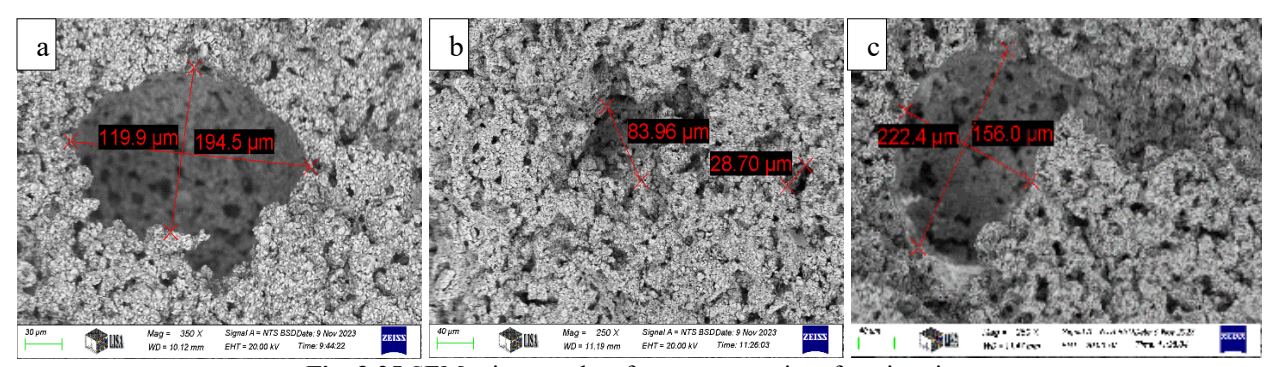


Fig. 3.24 SEM micrographs of porous ceramics after pre-sintering, using potato starch, (b) using tapioca starch, and (c) using 50:50 wt.% tapioca + potato

All of the samples that were utilized in the SEM test have a composition that is composed of 67.5 wt.% ZrO<sub>2</sub>, 2.5 wt.% MgO, and 30 wt.% Al<sub>2</sub>O<sub>3</sub>, and they have the highest apparent porosity. The results illustrate that there were two kinds of pores dispersed throughout the ceramic matrix: larger, starch granule created pores, and smaller, channel-like pores between the ceramic particles. Additionally, Fig. 3.24 present a comparison of the pore size and shape produced by three distinct types of starch after pre-sintering. Compared to the microstructures produced using tapioca starch, porous ceramics manufactured with potato starch have larger pores and a longitudinal pore morphology. Following pre-sintering, the pores derived from the potato starch exhibited sizes greater than 150 µm. While the pores created by the tapioca starch have a diameter of less than

100  $\mu$ m. Fig. (c) depicts the existence of largest pore diameter (555.9  $\mu$ m) as a result of the presence of two distinct starch types. The interaction between the two types of starch leads to the formation of extremely large pores. A comparison of the pore size and shape after sintering is shown in Fig. 3.25 (a), (b) and (c).



**Fig. 3.25** SEM micrographs of porous ceramics after sintering, (a) using potato starch, (b) using tapioca starch, and (c) using 50:50 wt.% tapioca + potato

As a consequence of the process of sintering, the ceramic particles that are situated in the vicinity of the pore surface experience volumetric shrinkage, which ultimately leads to a decrease in the size of the pores. When potato starch was used, the pores in the produced ceramics were larger than 100 µm, while the pores produced by tapioca starch were around 84 µm in diameter. Fig. (c) shows the pore shape and size obtained by sintering the ceramics with using a mixture of potato and tapioca starch in a 50:50 wt.% ratio. The presence of two different types of starch causes the pores to have different shape and diameter. The pore is quite large and irregularly shaped, measuring more than 200 µm in dimensions. In all cases, the pore morphology of the produced porous structure depends on the type and amount of pore-forming agent. SEM micrographs verified that the ceramic matrix did not achieve complete densification after the graded presintering or sintering procedure. The higher porosity attributed to an insufficient compaction of the ceramic matrix during the sintering process. The ceramic composites were examined using XRD to determine the crystallographic phases after the pre-sintering and sintering procedures. Figs. 3.26 and 3.27 show the diffraction patterns of the composite materials after the pre-sintering procedure. Figs. 3.28 and 3.29 show the diffraction patterns of the composite materials after the sintering process. The composition of the samples shown in Fig. 3.26 and 3.28 is 82.5 wt.% ZrO<sub>2</sub>, 15 wt.% Al<sub>2</sub>O<sub>3</sub>, and 2.5 wt.% MgO. While the samples shown in Fig. 3.27 and 3.29 consist of 67.5 wt.% ZrO<sub>2</sub>, 30 wt.% Al<sub>2</sub>O<sub>3</sub>, and 2.5 wt.% MgO. The results clearly show that the highest two peaks, which are the (111) and (-111) at 20 are about 28° and 31°, they are both for monoclinic crystal structure (baddeleyite). Several peaks of corundum ( $\alpha$ -Al<sub>2</sub>O<sub>3</sub>) were detected at  $2\Theta = 26^{\circ}$ ,

 $35^{\circ}$ ,  $38^{\circ}$ ,  $43^{\circ}$ ,  $52^{\circ}$ ,  $57^{\circ}$ ,  $66^{\circ}$ , and  $68^{\circ}$  for planes (012), (104), (110), (113), (024), (116), (216) and (300), respectively. The findings indicate that the peak seen at a diffraction angle of  $2\Theta = 37^{\circ}$  is mostly caused by diffraction from the basal plane (111) of the periclase MgO phase.

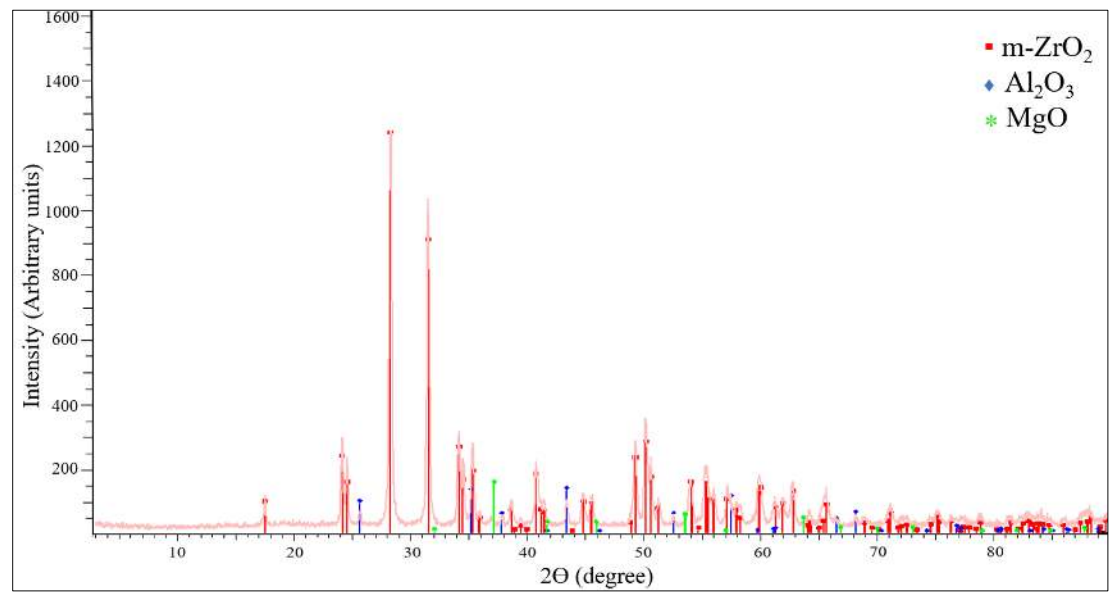


Fig. 3.26 XRD pattern for pre-sintered ceramic with 15 wt.% Al<sub>2</sub>O<sub>3</sub>

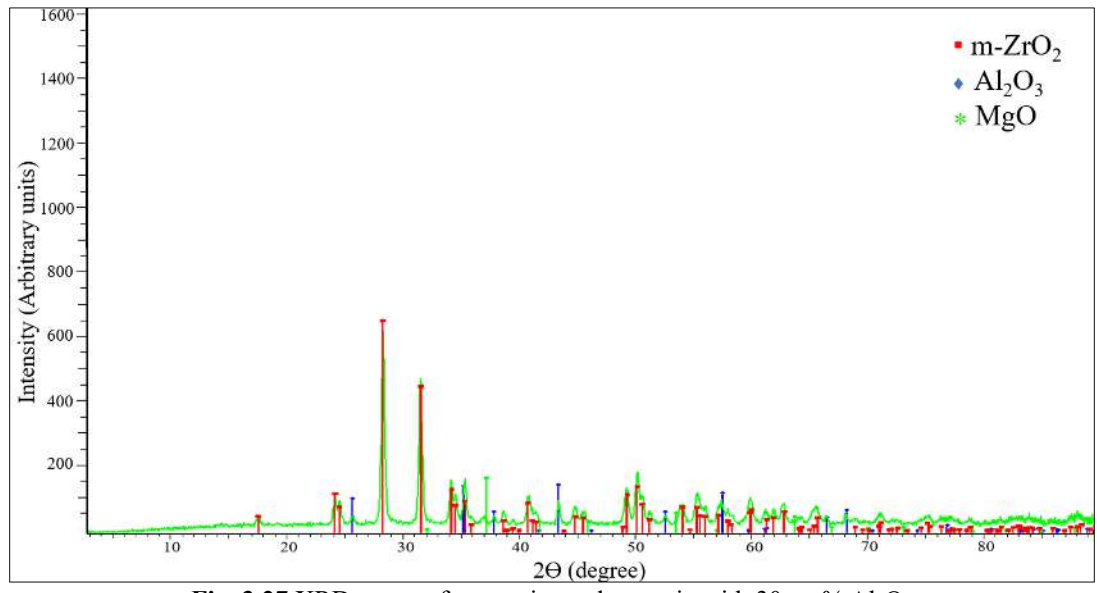


Fig. 3.27 XRD pattern for pre-sintered ceramic with 30 wt.% Al<sub>2</sub>O<sub>3</sub>

The XRD patterns indicate that the intensity of the peaks related to ZrO<sub>2</sub> increased after the sintering process. Sintering improves the crystallinity of materials by facilitating the reorganization and bonding of atoms inside the crystal lattice. In addition, sintering generally results in the compaction of materials, hence decreasing the level of porosity. Reducing the number of defects and voids in the material allows for a greater concentration of atoms that can participate

in X-ray scattering, leading to higher peak intensities. Additionally, the findings show a reduction in the peak intensity of the ZrO<sub>2</sub> phase as the Al<sub>2</sub>O<sub>3</sub> content increases from 15 wt.% to 30 wt.%. As the Al<sub>2</sub>O<sub>3</sub> content rises, the fraction of ZrO<sub>2</sub> in the composite drops. Reducing ZrO<sub>2</sub> content results in a decrease in the strength of the XRD peaks associated with the ZrO<sub>2</sub> phase.

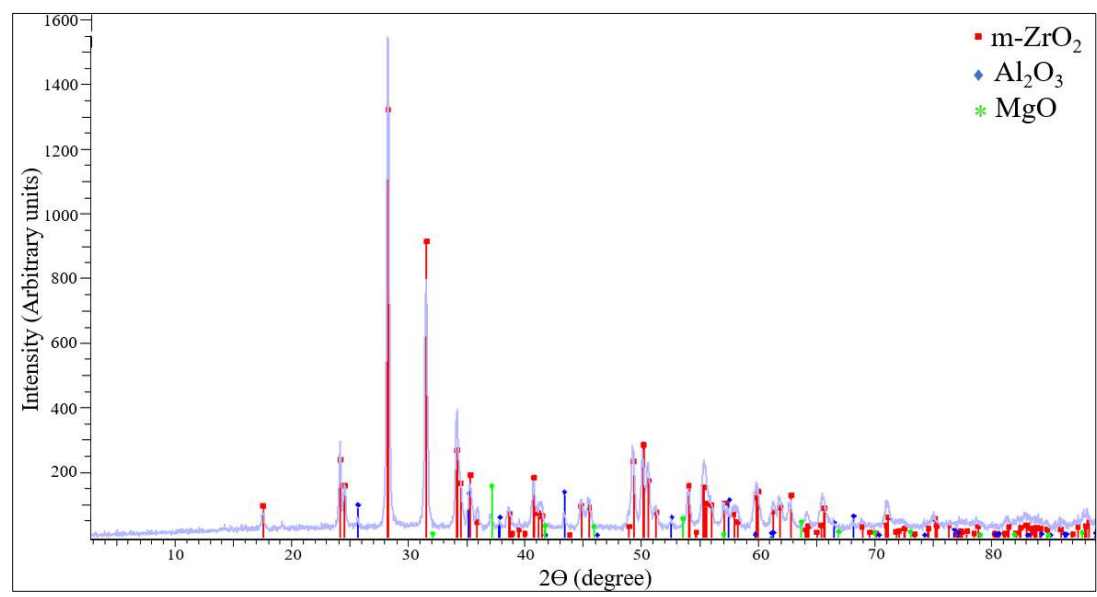


Fig. 3.28 XRD pattern for sintered ceramic with 15 wt.% Al<sub>2</sub>O<sub>3</sub>

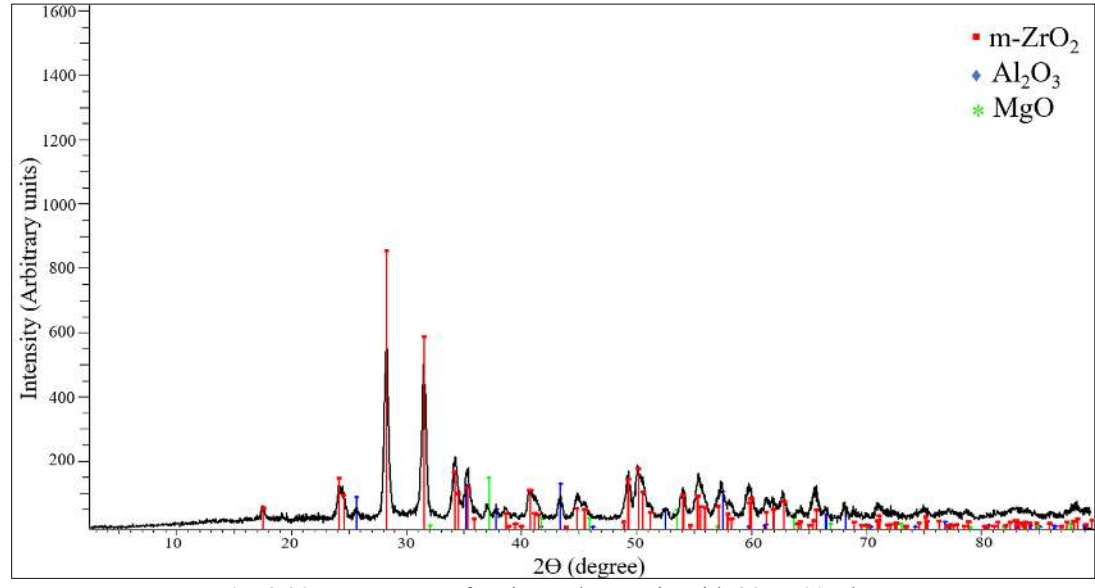


Fig. 3.29 XRD pattern for sintered ceramic with 30 wt.% Al<sub>2</sub>O<sub>3</sub>

Fig. 3.30 shows the results of pore opening size distribution measurement performed on different ceramic samples. The composition of the samples shown in Fig. 3.30 is 67.5 wt.% ZrO<sub>2</sub>, 30 wt.% Al<sub>2</sub>O<sub>3</sub>, and 2.5 wt.% MgO. MIP result clearly demonstrates that the four samples have different total pore volumes. However, the four samples vary in the distribution of this

pore volume among pores of specific sizes. The predominant portion of the overall pore volume in all samples exists in pores with a diameter exceeding 1  $\mu$ m.

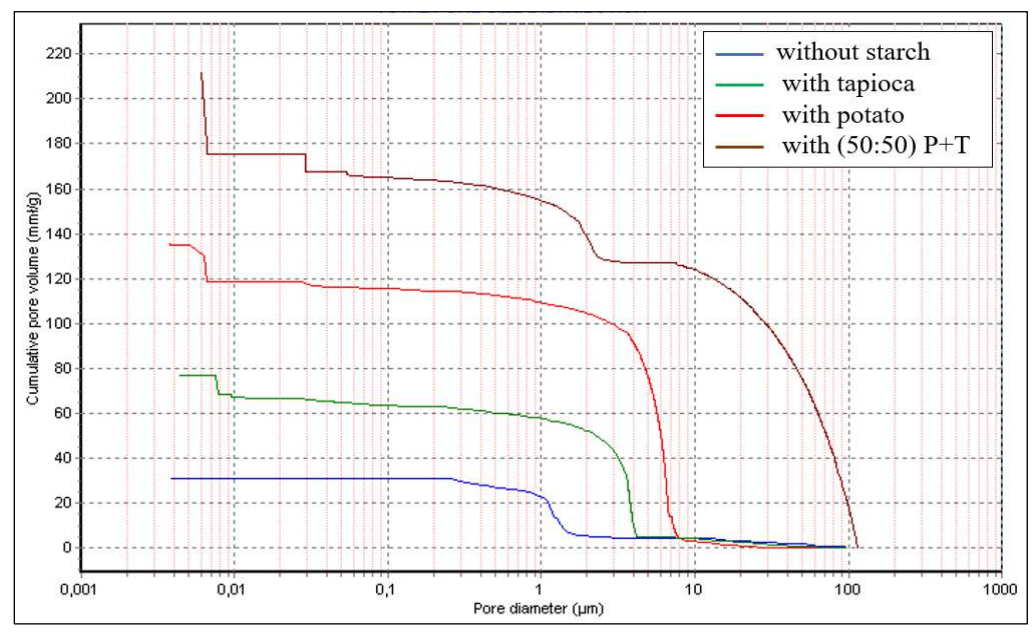


Fig. 3.30 Pore size distribution of 67.5 wt.% ZrO<sub>2</sub>, 30 wt.% Al<sub>2</sub>O<sub>3</sub>, and 2.5 wt.% MgO samples

The quantification can be determined by the median pore size obtained from MIP measurements. The median pore diameter, also referred to as the most probable pore opening size, represents the point at which the concentration of pores corresponding to a specific size is highest. Table 3.6 presents the most significant findings from the MIP testing.

Table 3.6 MIP results of 67.5 wt.% ZrO<sub>2</sub>, 30 wt.% Al<sub>2</sub>O<sub>3</sub>, and 2.5 wt.% MgO samples

Sample	Total intruded volume (cm <sup>3</sup> /g)	Total pore surface area (m²/g)	Median pore size (μm)
Without starch	30.97	0.151	1.1947
With tapioca	77.21	5.685	3.2937
With potato	136.48	12.702	5.321
(50:50) P+T	212.21	24.454	24.0811

The surface area is calculated by adding up the equivalent surface areas of all the pores in the test sample per unit mass. Total intruded volume shows how much mercury has penetrated into the sample at each pressure point. It begins at zero and grows in relation to the applied pressure. The total pore volume, also known as the total mercury volume, refers to the overall volume of pores determined by MIP per unit mass, expressed in cm<sup>3</sup>/g. To be precise, MIP does not reveal the actual diameters of the macropores; rather, it reveals information on the characteristics that regulate the entry of mercury, namely, the openings connecting the neighbouring macropores. MIP plot demonstrates that as the pore diameter diminishes, cumulative pore volume rises. This phenomenon occurs when smaller pores need more high pressure to be filled with mercury. The

sample that contains (50:50) P+T starch (brown curve in Fig. 26) exhibits three distinct incursion steps throughout the range of pore sizes from 0.01 to 100 µm. Clearly, this sample shows a pore opening with a size polydispersity that is rather large. In contrast to other samples, the pores in sample without starch vanish in two specific ranges: the lower range ranges from 0.01 to 0.3 μm, while the higher range spans from 1.5 to 100 µm. This might be attributed to the combination of the diminished presence of smaller connecting openings and the shrinkage in the size of the larger ones. The pore size distribution curve clearly demonstrates a change towards smaller pore sizes when no starch is used, suggesting a denser microstructure of the samples. Fig. 3.31 displays the distribution of pore sizes as a function of relative pore volume. The sample that is prepared without starch exhibits around 42% of the pore opening volume within a 1-2 µm range. About 39% of the pore opening volume in the sample with tapioca starch is between the 3-7 µm range and about 10% less than 0.01 µm. On the other hand, the potato starch sample has a larger opening, which makes up around 45% of the volume of the pores in the 6-9 μm range and about 12% less than 0.01 μm. The sample produced with a (50:50) mixture of potato and tapioca starches has a distinct pattern: the curve representing the distribution of pore opening size shows four distinct peaks, each corresponding to a different diameter of pore opening. In this sample, almost 17% of the volume of pore openings has a diameter less than 0.01 μm, 4% has a diameter between 0.03 and 0.05 μm, 6% has a diameter between 2 and 6 μm, and approximately 17% has larger openings with diameters ranging from 10 to 100 µm.

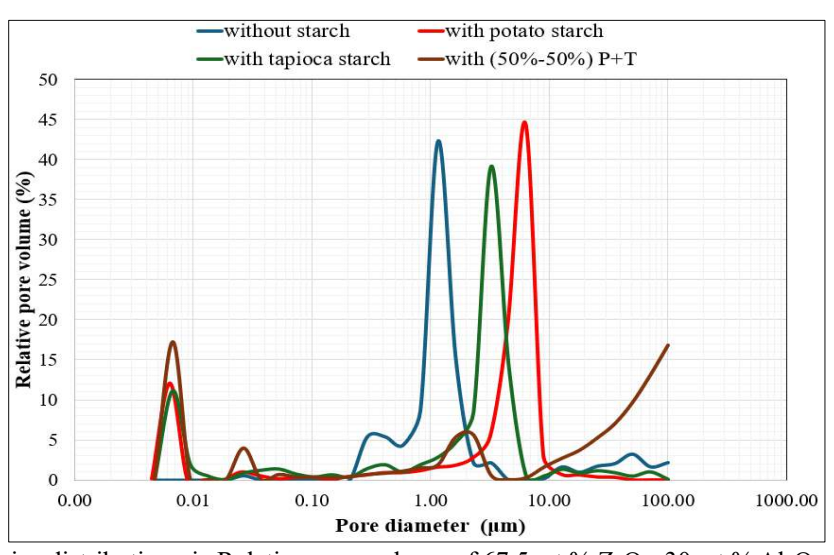


Fig. 3.31 The pore size distribution via Relative pore volume of 67.5 wt.% ZrO<sub>2</sub>, 30 wt.% Al<sub>2</sub>O<sub>3</sub>, and 2.5 wt.% MgO samples

Fig. 3.32 illustrates the variation in compressive strength of sintered porous-structured ceramics with the Al<sub>2</sub>O<sub>3</sub> content at varied starch types.

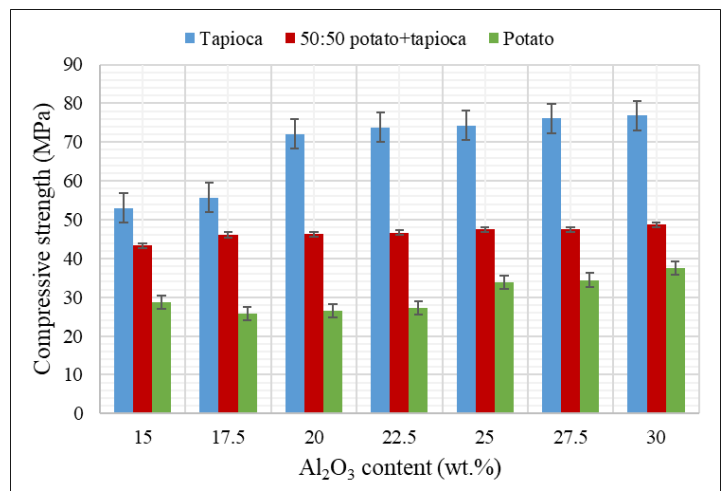


Fig. 3.32 Compressive strength vs. Al<sub>2</sub>O<sub>3</sub> content

The highest calculated compressive strength was 76.89 MPa for a sample with a porous structure, which was manufactured using 20 wt.% tapioca starch and 30 wt.% Al<sub>2</sub>O<sub>3</sub> content. The measured apparent density of this sample is 2.78 g/cm<sup>3</sup>, whereas the observed apparent porosity is about 52%. While the lowest calculated compressive strength was 25.82 MPa for a sample with a porous structure, which was prepared using 20 wt.% potato starch and 17.5 wt.% Al<sub>2</sub>O<sub>3</sub> content. The measured apparent density of this sample is 2.76 g/cm<sup>3</sup>, whereas the observed apparent porosity is 56%. Fig. 3.32 also demonstrates a positive correlation between the compressive strength and the amount of Al<sub>2</sub>O<sub>3</sub> present. The main advantage of Al<sub>2</sub>O<sub>3</sub> is its ability to improve compressive strength by serving as a barrier against fracture development. Al<sub>2</sub>O<sub>3</sub> is essential in the crack-deflection mechanism. When a crack comes into contact with a rigid Al<sub>2</sub>O<sub>3</sub> particle, it is either redirected or compelled to alter its direction. The presence of a zigzag fracture route increases the energy demand for crack propagation, hence significantly enhancing the strength of the material. Fracture deflection is a mechanism that absorbs energy that would otherwise promote fracture propagation. The fracture resistance under compressive stresses is enhanced by the absorption of energy [158]. The mechanism of fracture occurred when the load application was parallel to the origin, as seen in Fig. 3.33. Compression failure occurs in brittle ceramics by progressive microfracture, when microcracks grow to create failure planes [159]. Under compression, microscopic cracks propagate steadily, widening in response to rising stress levels, and eventually coalesce to produce ultimate collapse [160,161]. Fig. 3.33 shows the "kneading" phenomena, which is an intriguing finding since it shows the sample hardening at the start of the

load application. The microstructural components in porous materials might fail due to the existence of many pores, which causes microcracking.



Fig. 3.33 Fracture mode on both sides of the fractured surface of sample containing 15 wt.% Al<sub>2</sub>O<sub>3</sub>

Tables 3.7, 3.8, and 3.9 show the Pearson correlation matrix for the experimental data after sintering with different type of starches

Table 3.7 Pearson correlation matrix for the experimental data with using tapioca starch

	Al <sub>2</sub> O <sub>3</sub> (wt.%)	AD	AP	VS	σ
Al <sub>2</sub> O <sub>3</sub> (wt.%)	1				
AD	-0.9664	1			
AP	0.9871	-0.9691	1		
VS	-0.9886	0.1482	-0.1582	1	
σ	0.8794	0.7101	-0.8979	-0.3591	1

Table 3.8 Pearson correlation matrix for the experimental data with using potato starch

	Al <sub>2</sub> O <sub>3</sub> wt.%	AD	AP	VS	σ
Al <sub>2</sub> O <sub>3</sub> (wt.%)	1				
AD	-0.9728	1			
AP	0.9905	-0.9493	1		
VS	-0.9368	0.1439	-0.1509	1	
σ	0.8579	0.7661	-0.8253	-0.3905	1

Table 3.9 Pearson correlation matrix for the experimental data with using tapioca + tapioca starch

	$Al_2O_3$ (wt.%)	AD	AP	VS	σ
Al <sub>2</sub> O <sub>3</sub> (wt.%)	1				
AD	-0.9858	1			
AP	0.9863	-0.9891	1		
VS	-0.9828	0.1546	-0.1679	1	
σ	0.9208	0.7071	-0.9346	-0.3266	1

The results indicate that there is a very strong negative correlation between the Al<sub>2</sub>O<sub>3</sub> content and the apparent density and volume shrinkage. The results also show that there is a strong positive correlation between the Al<sub>2</sub>O<sub>3</sub> content and the apparent porosity and compressive strength. A pair plot was created using the Seaborn library in Python to conduct a comprehensive analysis of intervariable correlations and to better understand the fundamental data structure. Figures 3.34 depict a pair plot of four study parameters: apparent density, apparent porosity, volume shrinkage, and compressive strength, determined for samples prepared with varying Al<sub>2</sub>O<sub>3</sub> wt.%.

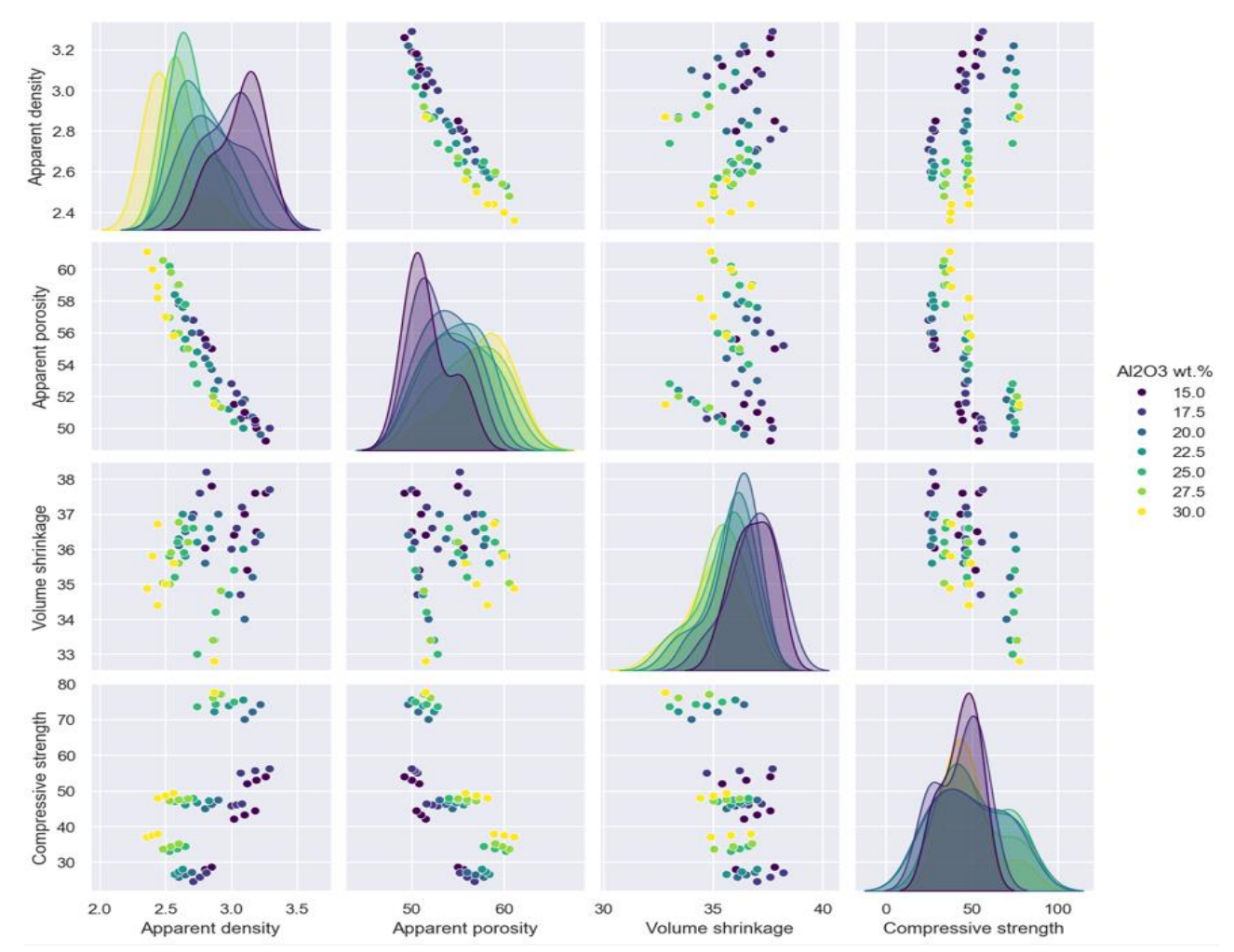


Fig. 3.34 Pair plot of four study features of samples prepared with different Al<sub>2</sub>O<sub>3</sub> wt.%

The diagonal subplot illustrates the distribution of an individual variable, while the off-diagonal plots provide scatter plots that demonstrate the interactions between pairs of variables. Figure 3.34 demonstrates that when Al<sub>2</sub>O<sub>3</sub> wt.% rises, apparent density and volume shrinkage decrease, while apparent porosity and compressive strength increase. Table 3.10 summarises the correlation types among the four variables shown in Fig. 3.34.

Table 3.10 Correlation relationships between the variables for the samples with different Al<sub>2</sub>O<sub>3</sub> wt.%

Variables	AD	AP	VS	σ
AD	_	Negative	Weak	Positive
AP	Negative	-	Weak	Negative
VS	Weak	Weak	_	Negative
σ	Positive	Negative	Negative	_

The correlation between apparent density and apparent porosity is strongly negative. As apparent density rises, volume shrinkage slightly increases, as denser compacts undergo increased particle rearrangement and pore elimination during sintering, resulting in more dimensional shrinkage. Conversely, apparent porosity diminishes as volume shrinkage increases, since shrinking leads to pore closure and structural densification, thus establishing a weak negative correlation. The compressive strength diminishes slightly with increased volume shrinkage, indicating that excessive shrinkage can induce internal stresses or microcracks, hence diminishing the strength of the material.

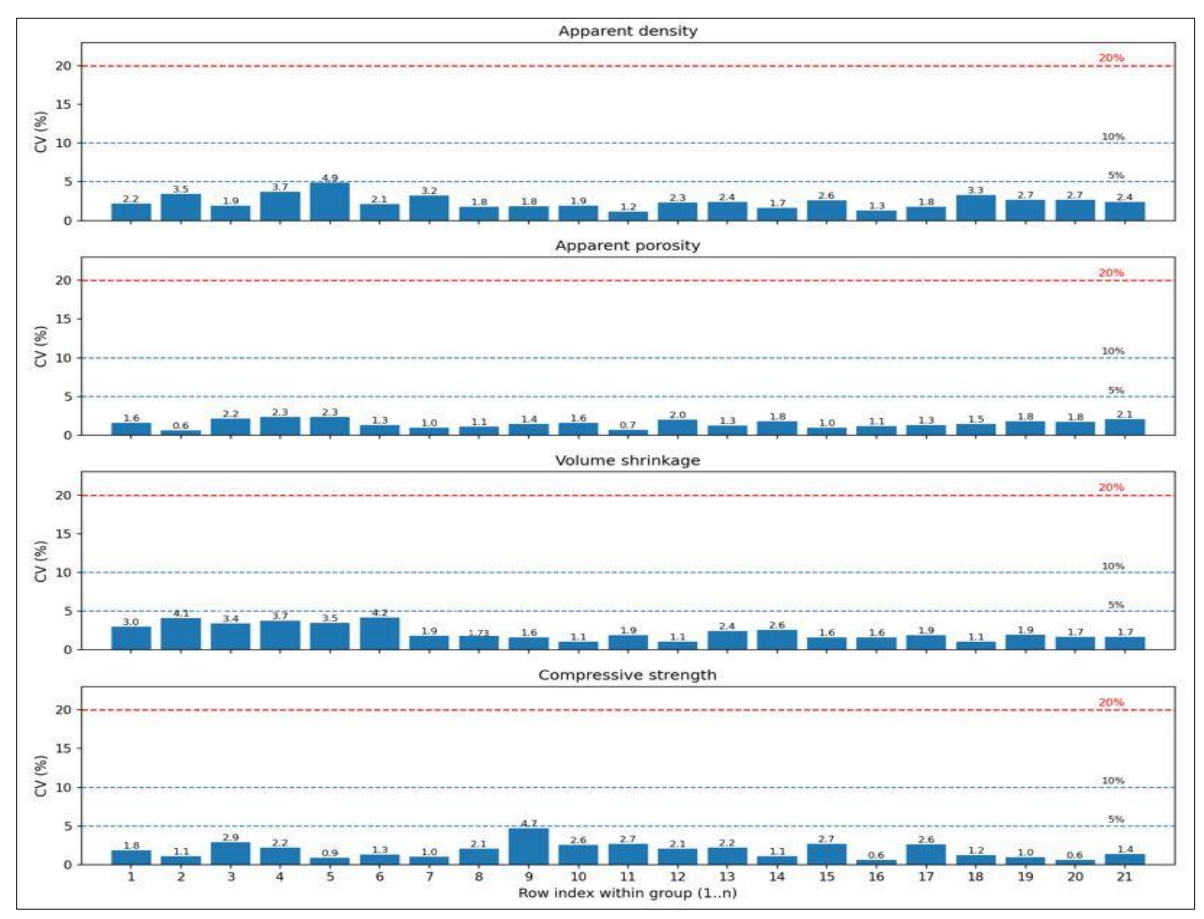


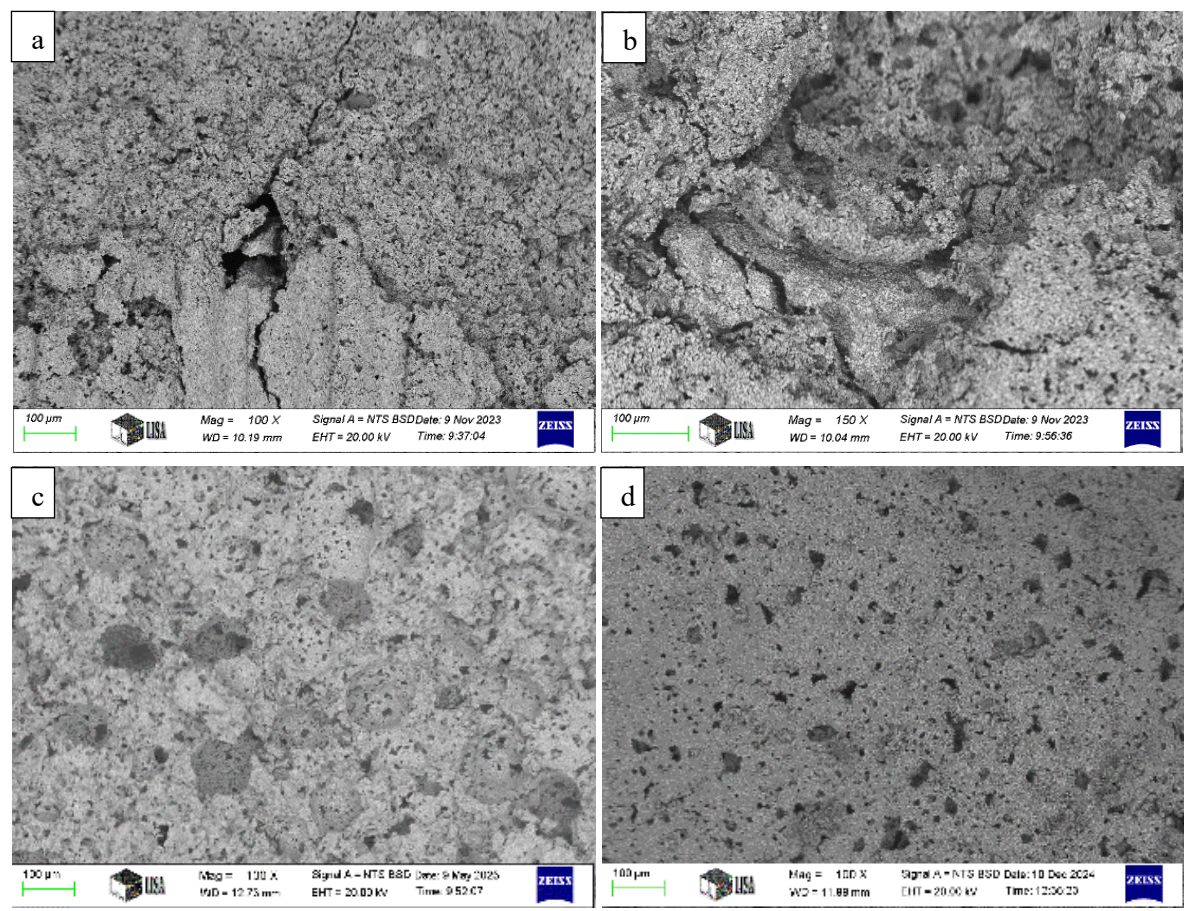
Fig. 3.35 Bar plot of the coefficient of variation (CV%)

Fig. 3.35 illustrates four bar charts, each indicating the coefficient of variation (CV%) for a particular feature measured over 21 group (each group is the average of 3 samples). The plots indicate that the majority of samples display CV (%) values under 5%, implying strong measurement consistency and minimal data dispersion. The findings indicate that the experimental measures are mostly reliable, with the majority of data sets remaining within acceptable variability thresholds (under 20%). Upon completing the second study of the thesis, it was concluded that a 50:50 wt.% combination of tapioca and potato starches results in a larger pore size (larger than 100 μm) with desirable pore openings (median pore openings size about 25 μm), apparent porosity (51-57%), apparent density (2.5-3.1 g/cm3), and mechanical compressive strength (~43-48 MPa) suitable for bone replacement applications. The progressive pre-sintering and sintering process may diminish the occurrence of fractures on the sample surfaces. Consequently, the subsequent investigation of the thesis utilises a starch combination of 50:50 wt.% tapioca and potato starch. In addition, all the samples were progressively pre-sintered and then sintered.

# 3.2.3 Test results of studying the effect of using progressive pre-sintering and sintering at different temperatures

Pre-sintering offers several benefits in ceramic technology. The current study employs presintering to decrease the rate of shrinkage during the final sintering process and mitigate thermal stresses. Pre-sintering decreases the rate of volume shrinkage by allowing a substantial fraction of densification and particle rearrangement to take place during the pre-sintering stage. This minimises the amount of further shrinkage required during the final higher sintering temperature. By enabling partial densification of the ceramic material in the pre-sintering stage, thermal stress is minimised during the final sintering process. Thermal stress and cracking occur due to the rapid and uneven heating that takes place during the final sintering process. Pre-sintering mitigates these concerns by dividing the densification process into two parts. The SEM micrographs in Fig. 3.36 (a), (b), (c), and (d) show a comparison between the samples that were sintered with pre-sintering and samples that sintered without pre-sintering. Based on the findings, it seems that the presintering method is effective in reducing the development of cracks on the surface of the samples. Furthermore, a comparison of the compressive strength between the progressively pre-sintered and sintered samples (illustrated previously in Fig. 3.32) and the samples sintered without pre-sintering and progressive sintering (depicted previously in Fig. 3.16) indicates that the compressive strength is significantly higher in the progressively pre-sintered and sintered samples. Fig. 3.37, extracted

from Figs. 3.32 and 3.16, shows the correlation between the compressive strength of the samples that sintered with pre-sintered and other samples sintered without pre-sintering.



**Fig. 3.36** SEM micrographs of sintered porous ceramics (67.5 wt.% m-ZrO<sub>2</sub>, 2.5 wt.% MgO, and 30 wt.% Al<sub>2</sub>O<sub>3</sub>): (a) and (b) without pre-sintering, (c) and (d) with pre-sintering

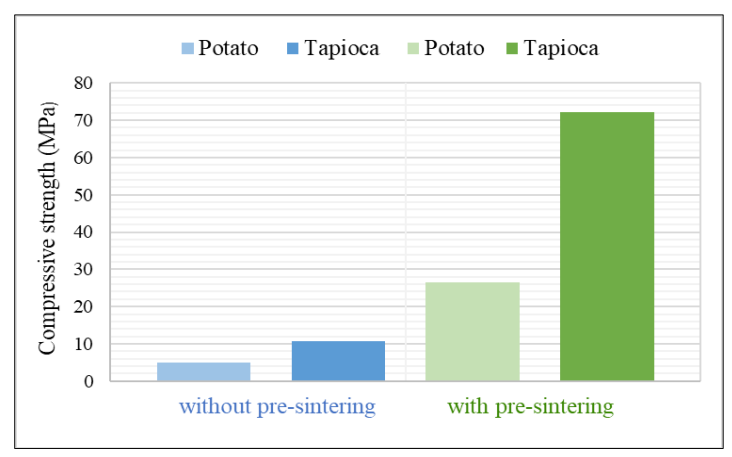
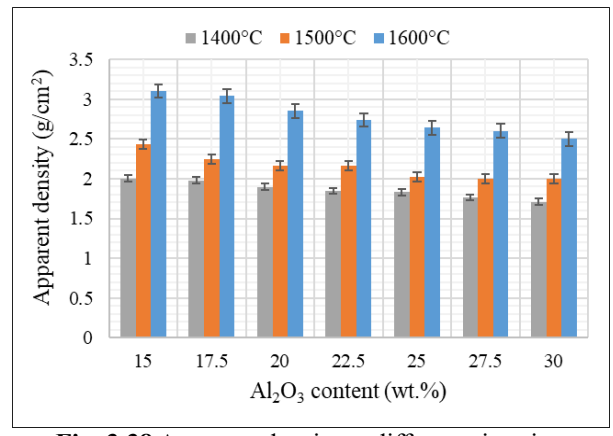


Fig. 3.37 Compressive strength of the samples

The maximum compressive strength of the sample prepared with 20 wt.% potato starch, without pre-sintering, was 10.25 MPa, whereas the sample made with 20 wt.% tapioca starch, also without pre-sintering, exhibited a maximum compressive strength of 13.28 MPa. The pre-sintered and

subsequently sintered samples shown in Fig. 3.32 exhibit a higher compressive strength, with a maximum value of 76.89 MPa when produced with 20 wt.% tapioca starch and 30 wt.% Al<sub>2</sub>O<sub>3</sub> content, and with a maximum value of 37.53 MPa when produced with 20 wt.% potato starch and 30 wt.% Al<sub>2</sub>O<sub>3</sub> content. Fig. 3.38 illustrates the correlation between apparent density and Al<sub>2</sub>O<sub>3</sub> content for the prepared porous ceramics after progressively pre-sintered and then sintered to three distinct temperatures, 1400°C, 1500°C, and 1600°C.



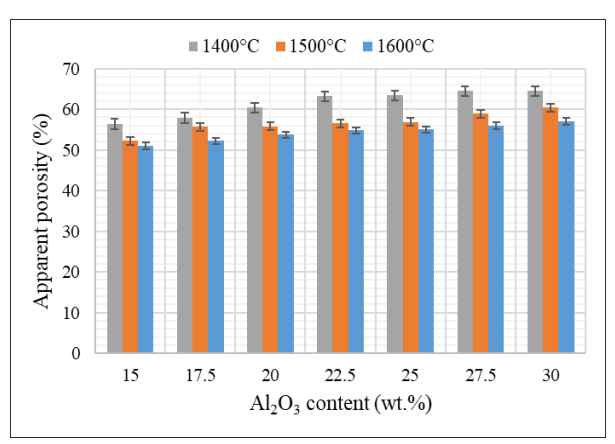
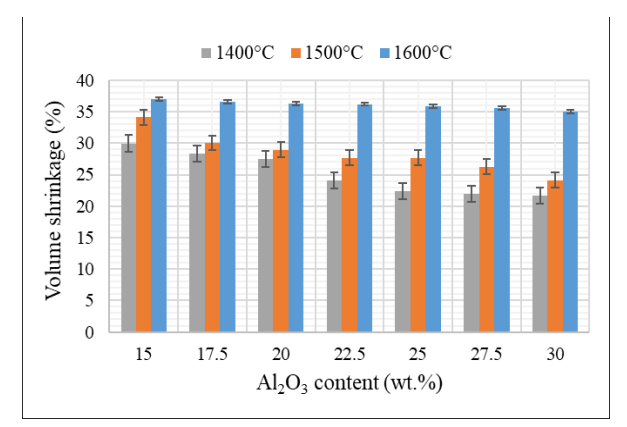


Fig. 3.38 Apparent density at different sintering temperatures

**Fig. 3.39** Apparent porosity at different sintering temperatures

As the Al<sub>2</sub>O<sub>3</sub> content increases, the apparent density decreases over all three-sintering temperatures. The apparent density values are maximal for samples heated at 1600°C, moderate for 1500°C, and minimal for 1400°C. This suggests that higher sintering temperatures lead to increase the density of the materials. The impact of temperature on densification is apparent, since higher temperatures tend to enhance particle bonding and decrease porosity. The highest measured apparent density was 3.1 g/cm<sup>3</sup> for samples prepared with 15 wt.% Al<sub>2</sub>O<sub>3</sub> and sintered at 1600°C. While the lowest measured apparent density was 1.8 g/cm<sup>3</sup> for samples prepared with 30 wt.% Al<sub>2</sub>O<sub>3</sub> and sintered at 1400°C. Fig. 3.39 illustrate the correlation between the apparent porosity and Al<sub>2</sub>O<sub>3</sub> content for the samples after sintering at three distinct temperatures. The apparent porosity increases in relation to the Al<sub>2</sub>O<sub>3</sub> content throughout all three-sintering temperatures. With a constant Al<sub>2</sub>O<sub>3</sub> concentration, the apparent porosity diminishes as the sintering temperature rises. Samples sintered at 1400°C with a 30 wt.% Al<sub>2</sub>O<sub>3</sub> had the highest apparent porosity, at 64%. While samples sintered at 1600°C and produced with 15 wt.% Al<sub>2</sub>O<sub>3</sub> had the lowest value approximately 51%. Fig. 3.40 illustrates the relation between the volume shrinkage of the prepared porous ceramics and the Al<sub>2</sub>O<sub>3</sub> contents at different sintering temperatures. The volume shrinkage increases as the sintering temperature increase. The process of densification is controlled by the

sintering temperature. As the temperature rises during sintering, the diffusion of particles intensifies, resulting in enhanced particle rearrangement and pore elimination. This induces shrinking as pores diminish, leading to tighter particle packing and increased densification. Al<sub>2</sub>O<sub>3</sub> and ZrO<sub>2</sub> exhibit divergent sintering behaviours attributable to their unique thermal and mechanical characteristics. Generally, increasing the Al<sub>2</sub>O<sub>3</sub> in the samples increases porosity by inhibiting fast densification, hence keeping a greater number of open pores. At high temperatures (1600°C), both Al<sub>2</sub>O<sub>3</sub> and ZrO<sub>2</sub> undergo faster densification, resulting in a less relative difference in shrinkage attributable to variations in Al<sub>2</sub>O<sub>3</sub> content. At reduced sintering temperatures, grain growth generally occurs at a slower rate, resulting in prolonged retention of a porous structure, which significantly affects shrinkage due to porosity.



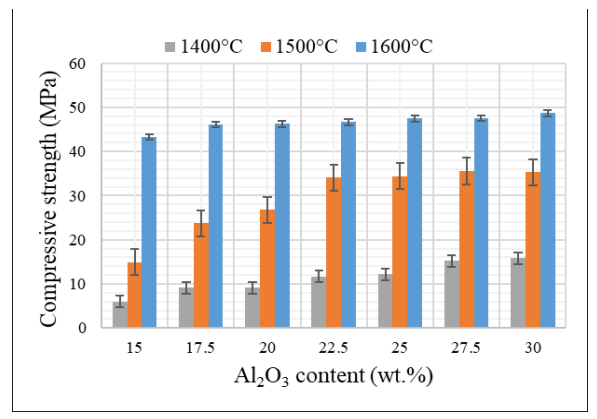


**Fig. 3.40** volume shrinkage at different sintering temperatures

**Fig. 3.41** Compressive strength at different sintering temperatures

Fig. 3.41 shows the relation between the compressive strength of the prepared porous ceramics and the Al<sub>2</sub>O<sub>3</sub> content at different sintering temperatures. The result indicates that the compressive strength is markedly enhanced with increasing sintering temperature. Increased sintering temperatures result in improved densification of the porous structure. Densification increases the mechanical strength and decreases void space. The material can withstand greater compressive loads due to its improved interparticle bonding and reduced pore number. Porosity directly weakens the material, as it acts as a stress concentrator and a site for fracture initiation under compressive stress. The highest calculated compressive strength was 48.66 MPa for a sample with a porous structure, which was manufactured using 30 wt.% Al<sub>2</sub>O<sub>3</sub> content and sintered at 1600°C. While the lowest calculated compressive strength was 5.99 MPa for a sample with a porous structure, which was prepared using 15 wt.% Al<sub>2</sub>O<sub>3</sub> content and sintered at 1400°C. Fig. 3.42

illustrates the results of the dilatometric analysis test, which examines the thermal shrinkage behaviour of the sample during the sintering process in an air atmosphere.

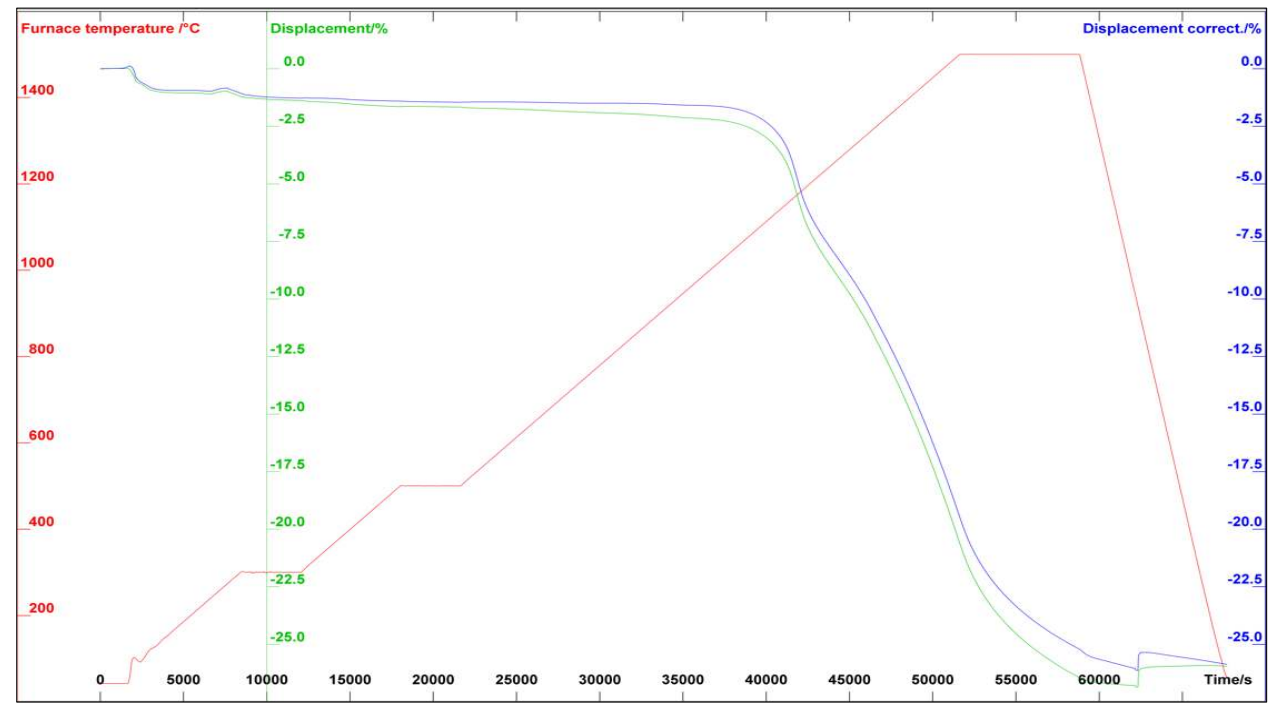


Fig. 3.42 Thermal shrinkage behaviour of the sample during sintering process

The composition of the sample shown in Fig. 3.42 is 67.5 wt.% ZrO<sub>2</sub>, 30 wt.% Al<sub>2</sub>O<sub>3</sub>, and 2.5 wt.% MgO. The test included elevating the temperature from room temperature to 1500°C, maintaining it at that elevated temperature, and then returning it to ambient conditions. The displacement curves, uncorrected (green) and adjusted for baseline effects (blue), demonstrate that the sample experienced a little dimensional alteration during the first heating period. As the temperature reached the sintering range, considerable shrinkage occurred. This shrinkage is ascribed to the densification process often found in ceramics during sintering. While subjected to solid-state sintering, oxide ceramic materials often experience a maximum shrinkage of around 25% of their original length. By comparing the green and blue curves, it can observe that the thermal expansion of Al<sub>2</sub>O<sub>3</sub> probe was properly accounted in the measurement, which ensures accurate results. The uniform contraction behaviour without sudden alterations indicates the lack of phase transitions or flaws during thermal cycling. The dilatometric data indicate satisfactory densification of the material, with the thermal profile accurately reflecting the sintering kinetics and shrinkage characteristics of the sample. The prepared ceramic composites were analysed by XRD to identify the crystallographic phases after sintering at various temperatures. Fig. 3.43 illustrates the diffraction patterns of the samples that progressively pre-sintered and then sintered at 1400°C or 1500°C, while Fig. 3.44 depicts the sample progressively pre-sintered and then sintered at 1600°C.

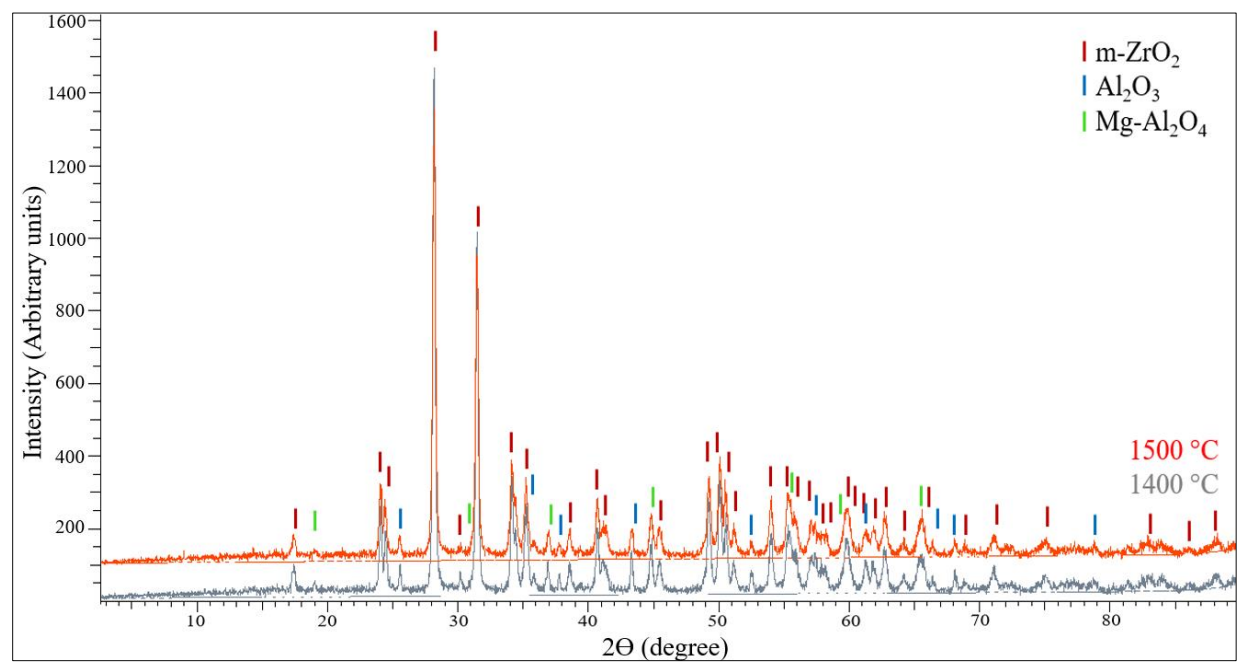


Fig. 3.43 XRD pattern after sintering at 1400°C or 1500°C (with pre-sintering)

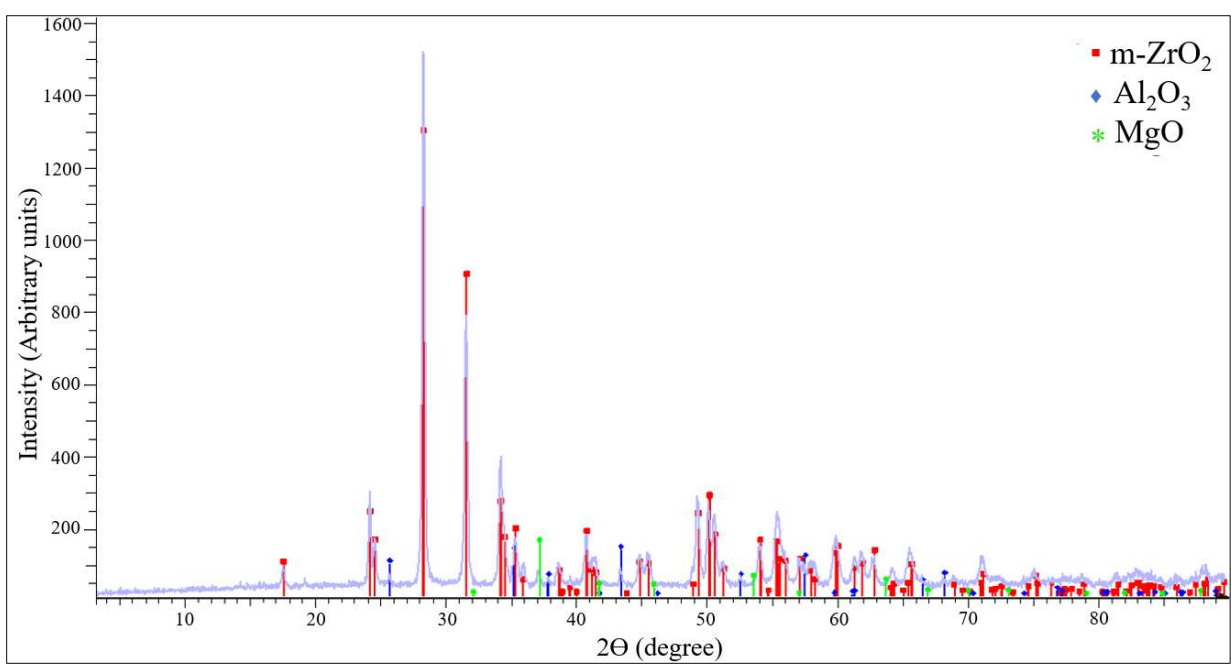


Fig. 3.44 XRD pattern after sintering at 1600°C (with pre-sintering)

The composition of the samples shown in the XRD patterns is 82.5 wt.% ZrO<sub>2</sub>, 15 wt.% Al<sub>2</sub>O<sub>3</sub>, and 2.5 wt.% MgO. The results clearly show that the highest two peaks, which are the (111) and (-111) at  $2\Theta$  are about  $28^{\circ}$  and  $31^{\circ}$ , they are both for m-ZrO<sub>2</sub> (baddeleyite). Several peaks of corundum ( $\alpha$ -Al<sub>2</sub>O<sub>3</sub>) were detected at  $2\Theta = 26^{\circ}$ ,  $35^{\circ}$ ,  $38^{\circ}$ ,  $43^{\circ}$ ,  $52^{\circ}$ ,  $57^{\circ}$ ,  $66^{\circ}$ , and  $68^{\circ}$  for planes

(012), (104), (110), (113), (024), (116), (216) and (300), respectively. The XRD pattern in Fig. 3.43 also demonstrate the existence of low intensity peaks for spinel (Mg-Al<sub>2</sub>O<sub>4</sub>) at  $2\Theta = 19^{\circ}$ ,  $31^{\circ}$ , 37°, 45°, 59°, and 65° for planes (111), (220), (311), (400), (511) and (440), respectively. The findings in Fig. 3.44 indicate that the peak seen at a diffraction angle of  $2\Theta = 37^{\circ}$  is mostly caused by diffraction from the basal plane (111) of the periclase MgO phase. The XRD results demonstrate that at reduced sintering temperatures of 1400°C or 1500°C, MgO interacts with Al<sub>2</sub>O<sub>3</sub> to form the cubic structure typical of the spinel phase (Mg-Al<sub>2</sub>O<sub>4</sub>). The reaction did not occur at 1600°C, and the MgO remains in the MgO phase inside the structure. At 1600°C, accelerated growth of grains and densification may diminish diffusion pathways and reactive surface area, thereby hindering more spinel production. The sintering process may result in pore closure, therefore restricting mass transfer and reaction kinetics at 1600°C. At elevated temperatures, ZrO<sub>2</sub> may influence the MgO-Al<sub>2</sub>O<sub>3</sub> reaction by stabilizing distinct phases or altering diffusion paths, thus inhibiting the continual creation of the spinel phase [162, 163]. The biomedical and mechanical characteristics of the Mg-Al<sub>2</sub>O<sub>4</sub> spinel structure are very desired, as it combines high strength with excellent corrosion resistance and the ability to enhance the porous-structured features. The surface and pore morphology of the sintered porous-structured ceramic were investigated using SEM. The samples utilized for the SEM analysis contain 67.5 wt.% m-ZrO<sub>2</sub>, 2.5 wt.% MgO, and 30 wt.% Al<sub>2</sub>O<sub>3</sub>. Fig. 3.45 illustrates the SEM micrographs of porous structured ceramics sintered at the three distinct temperatures: 1400°C, 1500°C, or 1600°C. The SEM micrographs illustrate a comparison of the pore sizes that developed on the ceramic surface during sintering at various temperatures. Compared to the microstructures that sintered at 1400°C or 1500°C, porous ceramics that sintered at 1600°C have larger pores and a more uniform pore morphology. When the samples sintered at 1600 °C, the pores in the fabricated porous ceramics exceeded 100 µm in size, while the pores that were created in the samples that sintered at a temperature of 1400°C or 1500°C were smaller than 100 µm in diameter. In general, the increase in porosity in the porous structure as a result of lower sintering temperature 1400°C or 1500°C, can reduce the pore size and pore shape regularity. The increase of pore size with higher sintering temperatures may also be attributed to many interconnected phenomena during ceramic sintering, including surface shrinkage, pore coarsening (Ostwald ripening) [164], pore coalescence, and grain growth. The surface shrinkage that occurs during sintering may actually enlarge the surface pores of a porous ceramic. Sintering causes the ceramic to shrink as the grains enclose one another, and the overall volume of the voids reduces.

Smaller voids or neck areas between grains on the surface exhibit more curvature, hence elevating their local surface energy.

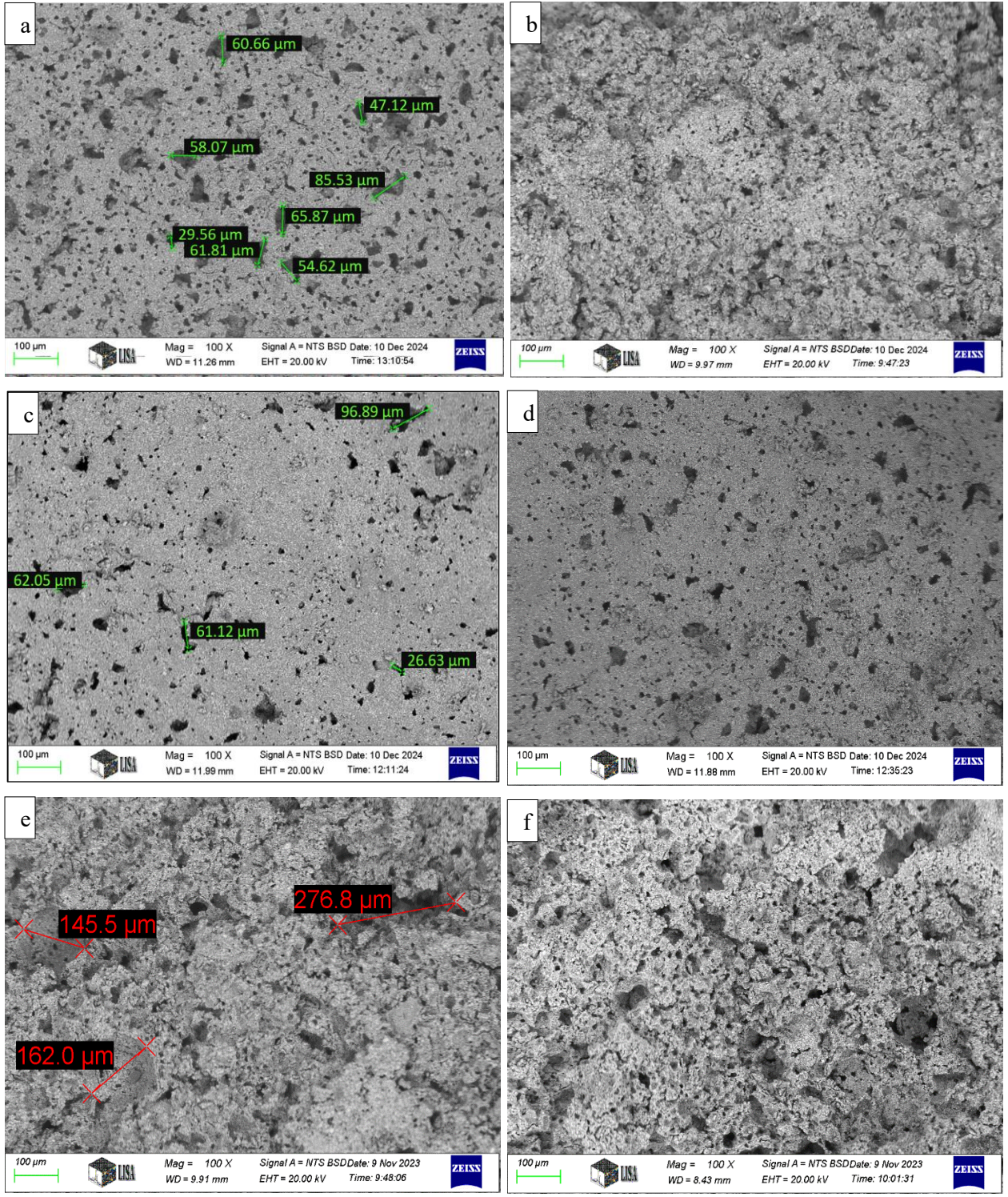


Fig. 3.45 SEM micrographs for porous ceramics sintered at:1400°C (a, b), 1500°C (c, d), and 1600°C (e, f).

To minimize free energy, the system is driven to minimize the surface tension of the ceramic. Surface tension at the ceramic interface compels the system to reduce free energy. This may lead to the merging of tiny surface voids into bigger ones. Ostwald ripening in porous ceramics entails a transfer of material from smaller grains to larger ones, motivated by disparities in surface energy. It happens spontaneously during high-temperature sintering. Pores may enlarge when smaller grains that surround them disintegrate and relocate to larger grains. This may lead to diminished porosity (if pores occlude because of densification) and increased pore size (if smaller pores amalgamate into bigger ones). At higher sintering temperatures, pore coalescence can occur. When the temperature rises, smaller voids in the vicinity are more likely to combine into larger pores. The improved material dispersion and pore mobility are responsible for this. Merging the tiny voids causes a little reduction in total void volume but an increase in pore size. The results of the SEM investigation indicated that there was a distinct difference between brighter and darker areas, which corresponded to the ZrO<sub>2</sub> and Al<sub>2</sub>O<sub>3</sub> phases, respectively. To verify more thoroughly the phase distribution, energy dispersive x-ray spectroscopy (EDS) was performed at two distinct sites on the samples as shown in Figs. 3.46 and 3.47.

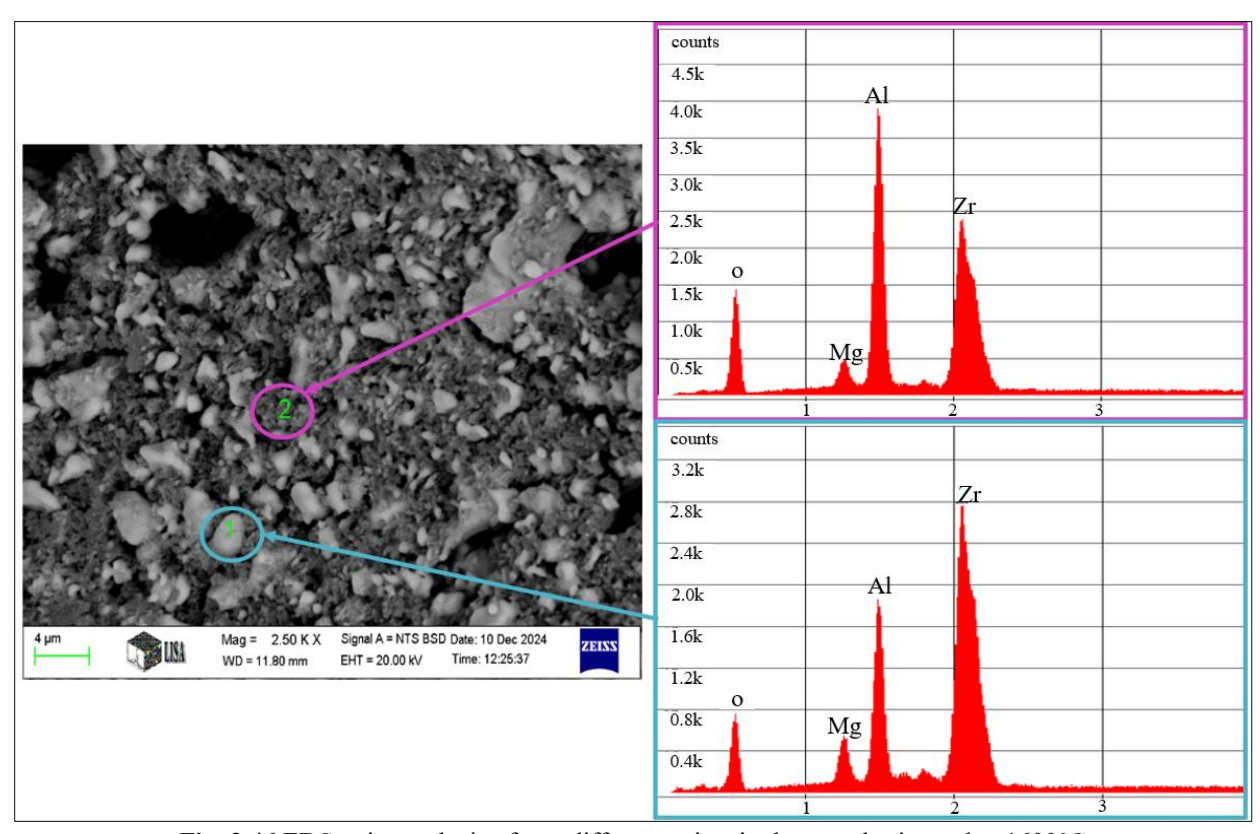


Fig. 3.46 EDS point analysis of two different points in the sample sintered at 1600°C

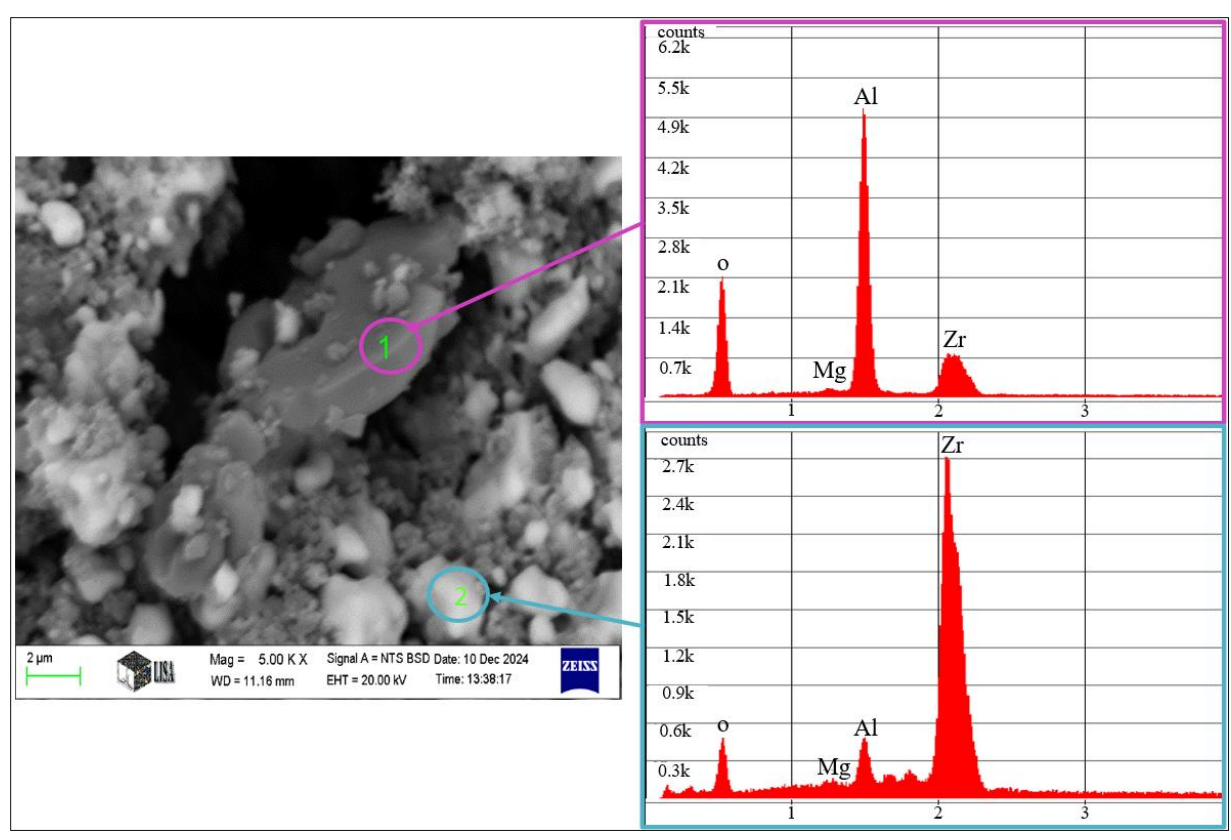


Fig. 3.47 EDS point analysis of two different points in the sample sintered at 1400°C

The samples shown in Figs. 3.46 and 3.47 consisted of 67.5 wt.% m-ZrO<sub>2</sub>, 2.5 wt.% MgO, and 30 wt.% Al<sub>2</sub>O<sub>3</sub>. The sample in Fig. 3.46 underwent sintering at 1600°C, while the sample in Fig. 3.47 was sintered at 1400°C. The EDS spectrum obtained from point 1 (Fig. 3.46) reveals that zirconium (Zr) is the predominant element, which corresponds to the m-ZrO<sub>2</sub> phase. Additionally, there are measurable quantities of aluminium (Al) derived from Al<sub>2</sub>O<sub>3</sub>, and magnesium (Mg) derived from MgO. On the other hand, the EDS spectrum obtained from point 2 (Fig. 3.46) has a larger Al peak intensity, which indicates that Al<sub>2</sub>O<sub>3</sub> is more concentrated in this region, despite the fact that Zr and Mg are still present. The findings in Figs. 3.46 and 3.47 validated the existence of Zr, Al, and Mg at both analysed locations, however local discrepancies in peak intensity were noted owing to phase variations in every location. These variations are anticipated in multi-phase porous ceramics and correspond with the inherent microstructural variability that occurs during sintering. Fig. 3.48 illustrates the SEM micrographs with higher magnification for porous structured ceramics sintered at three distinct temperatures: 1400°C, 1500°C, and 1600°C. The samples shown in Fig. 3.48 consisted of 67.5 wt.% m-ZrO<sub>2</sub>, 2.5 wt.% MgO, and 30 wt.% Al<sub>2</sub>O<sub>3</sub>.

The results illustrate the features of micro-void morphology that developed between ceramic grains and the connectivity of grains in sintered ceramics.

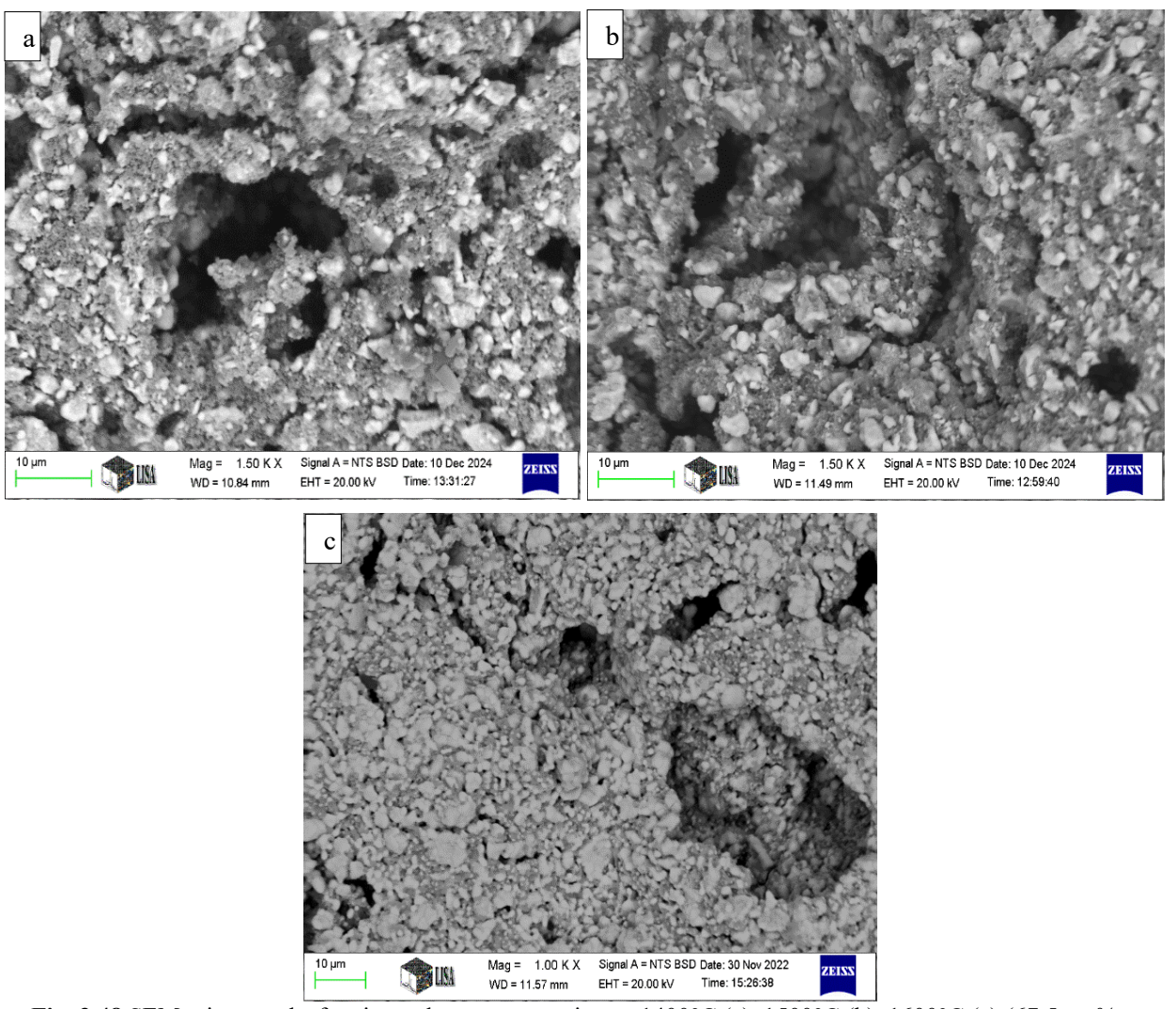
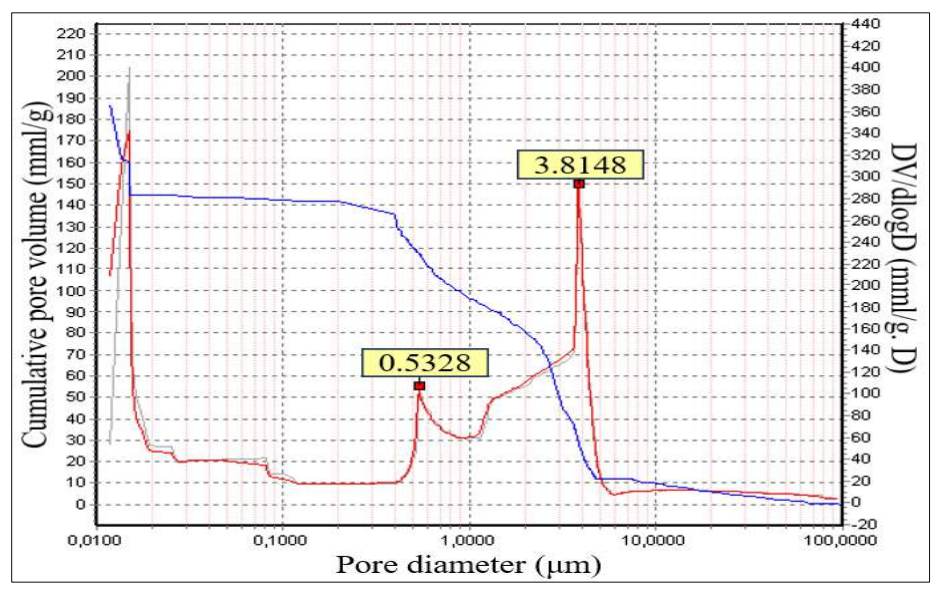


Fig. 3.48 SEM micrographs for sintered porous ceramics at:  $1400^{\circ}$ C (a),  $1500^{\circ}$ C (b),  $1600^{\circ}$ C (c) (67.5 wt.% m-ZrO<sub>2</sub>, 2.5 wt.% MgO, and 30 wt.% Al<sub>2</sub>O<sub>3</sub>)

The findings indicated that when the sintering temperature increased from 1400°C to 1600°C, the ceramic grains connectivity increased, and the micro-voids between the grains were decreased. The strong network formed by the connectivity of grains enabled the sintered ceramics to achieve high mechanical strength. Grain boundary migration or viscous movement of the material may happen at high sintering temperatures, further lowering porosity when smaller voids collapse or shrink. Reduced overall porosity may be attributed, in part, to grain growth, which often occurs during high-temperature sintering, which can push or absorb tiny voids that are locked at grain borders. At 1400°C, sintering is less advanced, leaving smaller grains and a network of interconnected pores. These interconnected pores contribute to high apparent porosity but may not

always be visible or prominent on the surface of the sample. At 1600°C, densification and grain growth during sintering likely reduce the connectivity of internal pores, creating more dense structure while potentially enlarging or exposing pores on the surface. This can lead to lower apparent porosity (less inter-connected pores in the bulk) and higher surface porosity (visible pores appear larger or more prominent in SEM). Figs. 3.49, 3.50, and 3.51 show the cumulative pore volume as a function of pore diameter resulted from the MIP investigation.



**Fig. 3.49** Pore size distribution of porous structured sample sintered at 1400°C (67.5 wt.% m-ZrO<sub>2</sub>, 2.5 wt.% MgO, and 30 wt.% Al<sub>2</sub>O<sub>3</sub>)

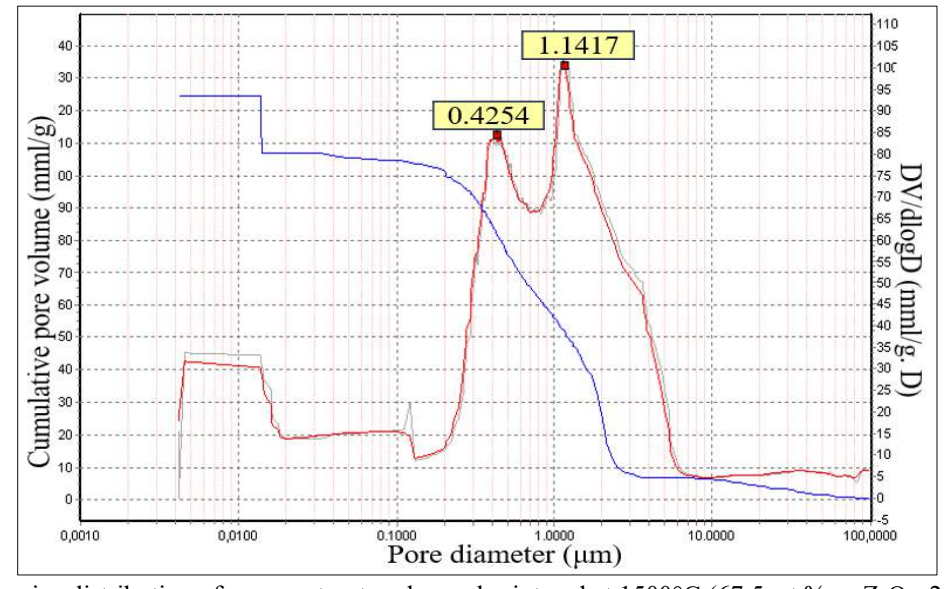


Fig. 3.50 Pore size distribution of porous structured sample sintered at  $1500^{\circ}$ C (67.5 wt.% m-ZrO<sub>2</sub>, 2.5 wt.% MgO, and 30 wt.% Al<sub>2</sub>O<sub>3</sub>)

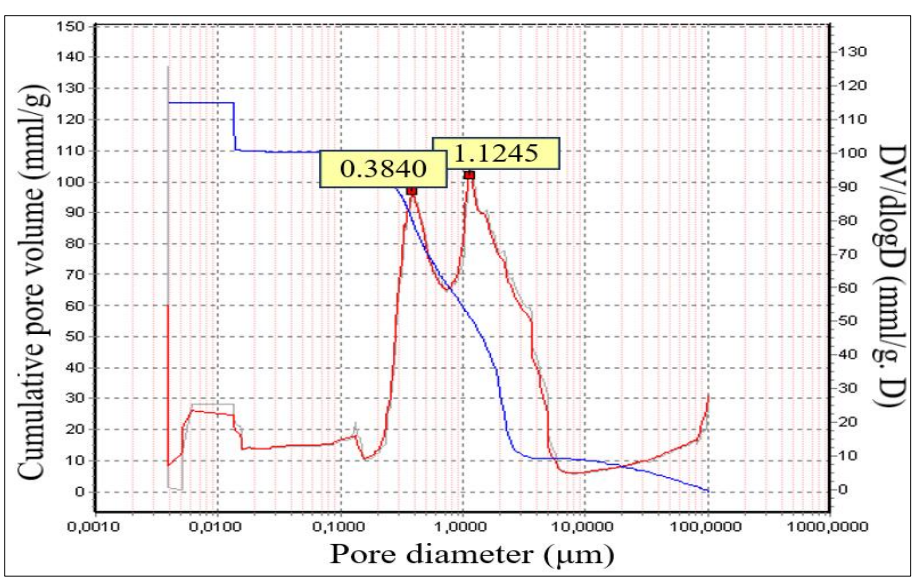


Fig. 3.51 Pore size distribution of porous structured sample sintered at 1600°C (67.5 wt.% m-ZrO<sub>2</sub>, 2.5 wt.% MgO, and 30 wt.% Al<sub>2</sub>O<sub>3</sub>)

The findings quantify the extent to which mercury penetrates the porous material under rising pressure, enabling accurate characterization of channel opening diameters. All the samples that were used in this test consist of 76.5 wt.% ZrO<sub>2</sub>, 2.5 wt.% MgO, and 30 wt.% Al<sub>2</sub>O<sub>3</sub>. As can be observed from the pore size distribution Figs., the cumulative pore-volume curves (blue curves) of all the samples sintered at various temperatures show similar tendencies. All have an S-shape, flattened at both ends and steep in the central region, signifying that substantial quantities of mercury permeate the mesopores and tiny pores in the centre area. Furthermore, mesopores and tiny pore channels, with a diameter range of 0.1-10 µm, constitute a significant fraction of the total pore volume in the samples. At increased pore opening sizes (reduced pressures), a plateau in the curves indicates a restricted occurrence of macropore openings or larger pore openings inside the ceramic matrix. Steep changes in the cumulative pore volume curve indicate prevailing pore size ranges. This signifies that most pores are concentrated within certain size ranges, illustrating the pore size distribution of the material. At reduced pore sizes (elevated pressures), a plateau in the curves indicates that all available pores were filled with mercury. Differential pore volume (dV/dlogD) denotes the incremental pore volume corresponding to each pore size range. It indicates the proportion of the total pore volume attributed to pores of a certain size, often expressed in mL/g or cm<sup>3</sup>/g. Each peak represents a predominant pore size inside the material. Sharp peaks indicate distinct pore sizes, but broader slopes signify a more extensive variation of pore diameters. The occurrence of several peaks indicates bimodal or multimodal porosity,

indicating that the material has pore openings of various different sizes. The height of the peak indicates the volume of pores at that particular size. A higher peak indicates an increased volume of pores within that diameter range. The existence of two peaks in the Figs. Indicates that the samples exhibit a bimodal pore size distribution, signifying the presence of two discrete groups of pore sizes. The first peak in Fig. 3.49 signifies a predominant pore size of around 0.53 µm, whilst a subsequent peak denotes a predominant pore size of roughly 3.81 µm. In Fig. 3.50, the first peak indicates a significant pore size of around 0.42 µm, whereas the next peak represents a prominent pore size of about 1.14 µm. The first peak in Fig. 3.51 shows a significant pore size of around 0.38 μm, whereas the subsequent peak signifies a noticeable pore size of approximately 1.12 μm. The volume ratio of the pores that have a specific size of 3.81, 1.14, and 1.12 is larger than that of the other pores. The findings of the MIP tests show that when the sintering temperature increases, the size of the pore openings (the pore throat) decrease. The densification tendency is the reason for this; as the sintering temperature rises, the particles connect more tightly to one another, resulting in less spaces between them. The increase in pore openings size at lower sintering temperature (1400°C) results in the largest apparent porosity of the samples, as seen in Fig. 3.39. The assessment of apparent porosity relies on measuring the amount of water that infiltrates the open pores and openings on the surface; as the dimensions of these pores and openings enlarge, the apparent porosity of the sample increases. Table 3.11 presents the most significant findings from the MIP testing.

Table 3.11 MIP results

Sintering temperature (°C)	Total intruded volume (mm³/g)	Total pore surface area (m²/g)	Median pore size (μm)
1400	187.08	13.297	1.122
1500	124.64	5.942	0.795
1600	125.52	5.486	0.778

In order to measure the degree of correlation between the experimental data, the Pearson correlation coefficient values were computed. Table 3.12 displays the experimental results after sintering at various temperatures together with the Pearson correlation matrix. The findings show that the apparent density and volume shrinkage values drop as the Al<sub>2</sub>O<sub>3</sub> content increases, suggesting a weak negative correlation between the two variables. Furthermore, the findings demonstrate a positive correlation between the apparent porosity and the Al<sub>2</sub>O<sub>3</sub> wt.%. Despite the fact that there is a very weak positive correlation between Al<sub>2</sub>O<sub>3</sub> and compression strength. The findings indicate a strong positive correlation between the temperature and the apparent density,

volume shrinkage, and the compressive strength. In addition, there is a strong negative correlation between the temperature and the apparent porosity. The compressive strength of the produced porous structured ceramics was enhanced when the Al<sub>2</sub>O<sub>3</sub> content, sintering temperature, and apparent porosity, were raised. However, when apparent density and volume shrinkage increases, it decreases.

**Table 3.12** The Pearson correlation matrix of the experimental data.

	Al <sub>2</sub> O <sub>3</sub> (wt.%)	Temp. (°C)	AD	AP	VS	σ
Al <sub>2</sub> O <sub>3</sub> (wt.%)	1					
Temp. (°C)	0	1				
AD	-0.3542	0.9036	1			
AP	0.6051	-0.7551	-0.8621	1		
VS	-0.4098	0.8547	0.9372	-0.9012	1	
σ	0.2472	0.9511	-0.7719	0.5644	-0.6823	1

Figs. 3.52 (after sintering at 1400°C or 1500°C) and 3.53 (after sintering at 1600°C) illustrate a pair plot of four research parameters: apparent density, apparent porosity, volume shrinkage, and compressive strength. The diagonal subplot illustrates the distribution of an individual variable, while the off-diagonal plots provide scatter plots that demonstrate the interactions between pairs of variables. It can be concluded from the results that the apparent density, volume shrinkage, and compressive strength increase, while apparent porosity decreases with rising sintering temperature. Table 3.13 summarize the type of correlation between the variables in Figs. 3.52 and 3.53.

Table 3.13 Correlation relationships between the variables after sintering at different temperature

Variables	AD	AP	VS	σ
AD	_	Negative	Positive	Negative
AP	Negative	_	Negative	Positive
VS	Positive	Negative	-	Negative
σ	Negative	Positive	Negative	_

Apparent density has a negative correlation with apparent porosity and compressive strength, while demonstrating a positive correlation with volume shrinkage. At high temperatures, the accelerated diffusion promotes pore coarsening and pore migration towards grain boundaries, resulting in the disappearance of numerous small pores while the remaining pores enlarge and occasionally merge into fewer, larger pores. This phenomenon can enhance the apparent density (due to the closure of small, numerous pores) while concurrently generating larger pores that diminish compressive strength, leading to a reduction in strength despite an increase in density.

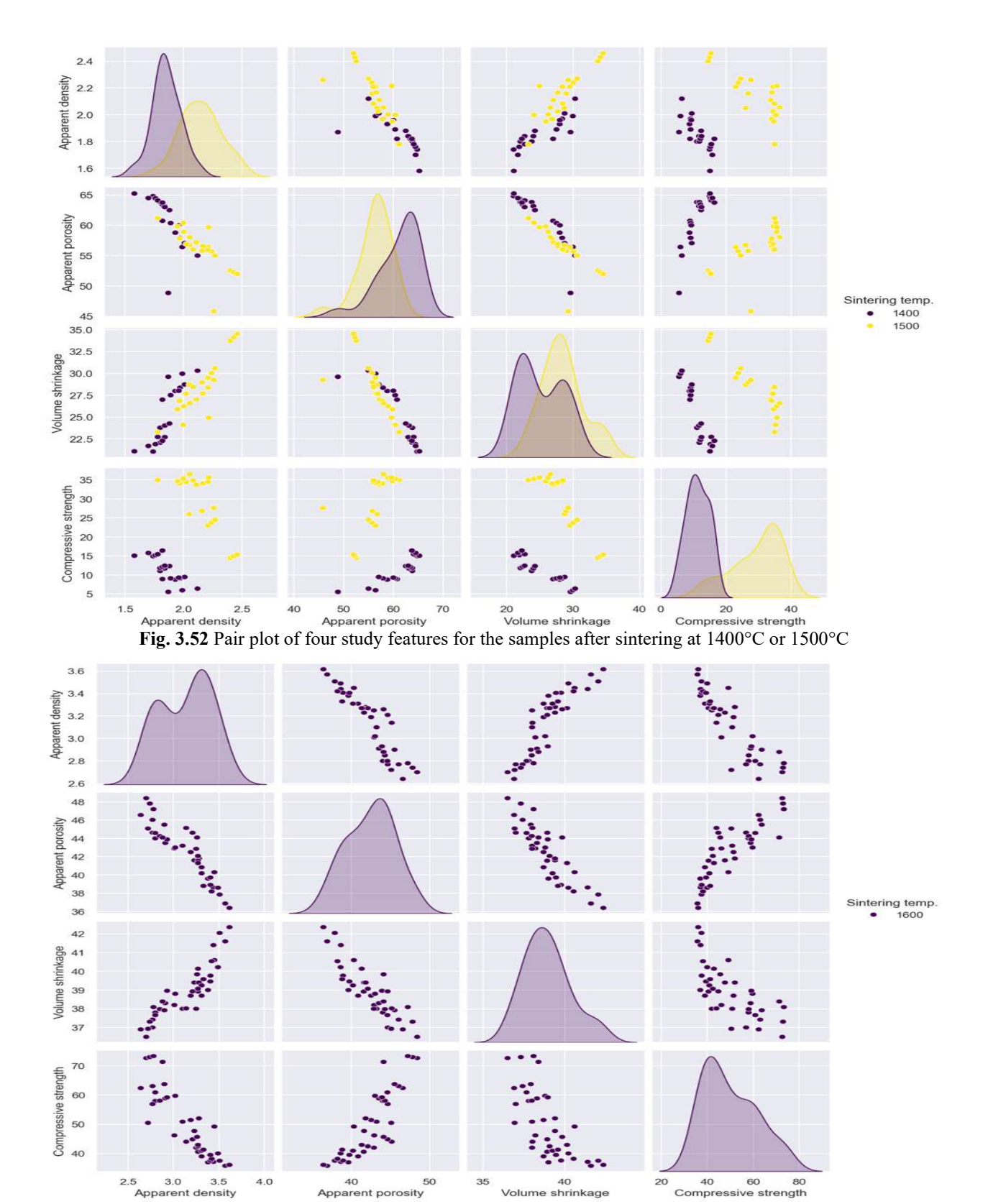


Fig. 3.53 Pair plot of four study features for the samples after sintering at 1600°C

The apparent porosity diminishes as volume shrinkage increases, as shrinking leads to the closure of small pores (channels between the large pores) and the densification of the structure. With increasing volume shrinkage of ceramics, the pore openings size (the size of channels between the pores) reduced, leading to a reduction in apparent porosity (depending on the open surface pores). The results also indicate that the apparent porosity correlates more positively with compressive strength when the sintering temperature increases from 1400°C to 1600°C.

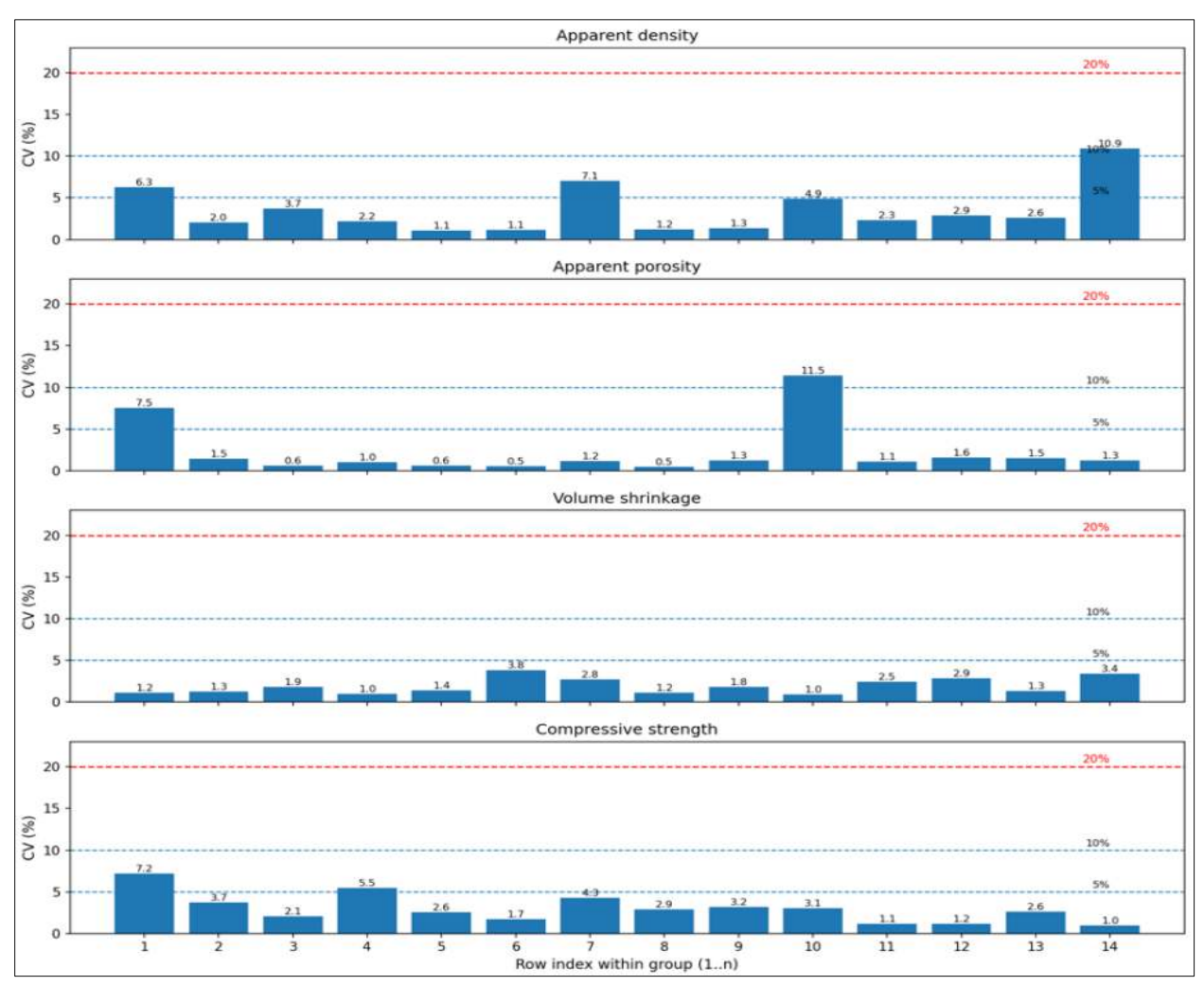


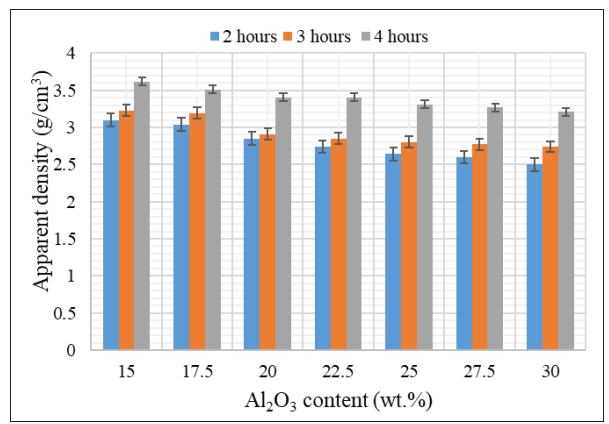
Fig. 3.54 Bar plot of the coefficient of variation (CV%)

In Figs. 3.52 and 3.53, the correlation between the variables in the pair plot exhibits a very distinct pattern compared to the previous pair plots in the Figs. 3.17, 3.18, 3.19, and 3.34. Figs. 3.52 and 3.53 illustrate the correlations among the variables as the sintering temperature rises, indicating that the sintering conditions influence the structure of the created ceramics, subsequently affecting their properties and the interrelations among those properties. As a brief explanation of the changes that occur as the sintering temperature rises: as the sintering

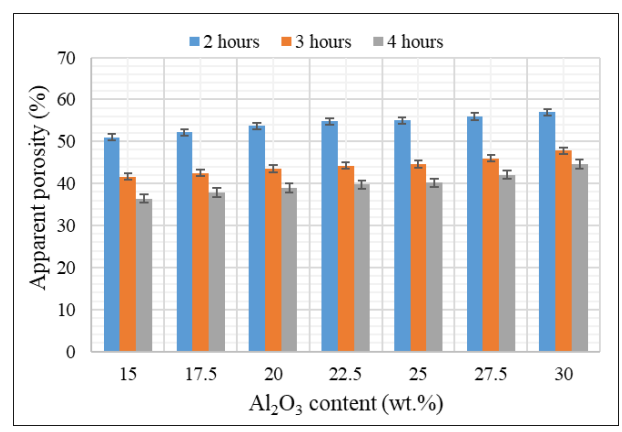
temperature rises, the apparent density increases, resulting in decreased interarticular spacing, which subsequently causes increased volume shrinkage. As apparent density and volume shrinkage increases, the size of the pore openings (channels between the pores) diminishes (as previously shown using MIP analysis), resulting in a decrease in apparent porosity while simultaneously increasing the surface pore size. The decrease in pore opening size resulted in decreased compressive strength. Fig. 3.54 illustrates four bar charts, each indicating the coefficient of variation (CV%) for a particular feature measured over 14 group (each group is the average of 3 samples). The plots indicate that the majority of samples display CV (%) values under 10%, implying strong measurement consistency and minimal data dispersion. The findings indicate that the experimental measures are mostly reliable, with the majority of data sets remaining within acceptable variability thresholds (under 20%). From the previous results of this study, it can be concluded that the porous-structured ceramics sintered at 1600°C are appropriate for use in porous bone replacement applications due to their higher porosity (51 - 57%), pore size (more than 100 μm) and better mechanical compressive strength (43 - 49MPa).

#### 3.2.4 Test results of studying the effect of using different sintering holding time

Sintering holding time is crucial in determining the final characteristics of a porous ceramic structure. The holding time must be optimized to preserve the appropriate density and porosity without compromising mechanical integrity. Fig. 3.55 shows the effect of using different sintering holding times on the apparent density of the prepared samples.



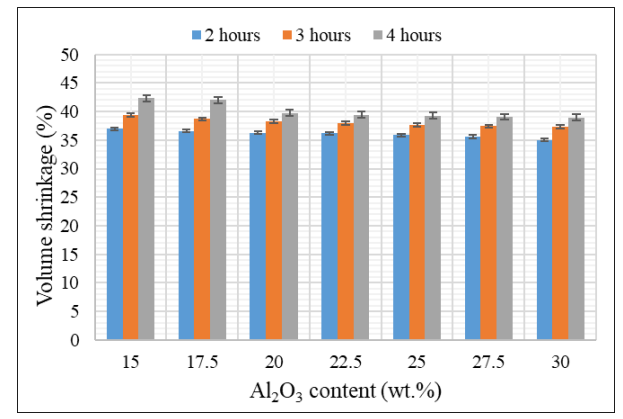
**Fig. 3.55** Apparent density at different sintering holding time



**Fig. 3.56** Apparent porosity at different sintering holding time

The present investigation used a sintering temperature of 1600°C, based on the results of the third study. The findings indicate that extending the sintering holding time from 2 to 4 hours consistently improves the apparent density of the samples, irrespective of Al<sub>2</sub>O<sub>3</sub> contents. This

enhancement is ascribed to more comprehensive densification after extended heat exposure, facilitating augmented particle bonding and a decrease in open porosity. Despite prolonged sintering holding time, densification is less effective in materials with higher Al<sub>2</sub>O<sub>3</sub> content. At lower Al<sub>2</sub>O<sub>3</sub> contents, the apparent density is highest, reaching 3.6 g/cm<sup>3</sup> after 4 hours sintering holding time. Fig. 3.56 illustrates the effect of sintering holding time on the apparent porosity of the prepared samples. The findings demonstrate that increasing the holding time from 2 to 4 hours resulted in a significant decrease in porosity, attributable to improved diffusion and grain boundary migration that facilitate pore reduction and densification. Even at the maximum holding time of 4 hours, the porosity of samples with increased Al<sub>2</sub>O<sub>3</sub> content remained higher, reached about 45%. Fig. 3.57 shows the effect of sintering holding time on the volume shrinkage of the prepared samples.



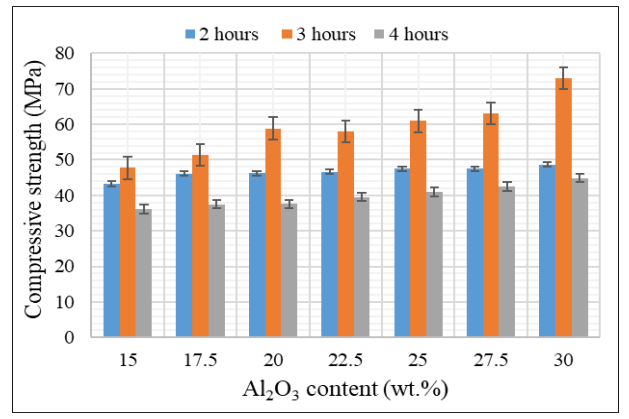


**Fig. 3.57** Volume shrinkage at different sintering holding time

**Fig. 3.58** Compressive strength at different sintering holding time

At each Al<sub>2</sub>O<sub>3</sub> content, shrinkage is minimal at 2 hours, increases at 3 hours, and reaches its highest values at 4 hours sintering time. Moreover, for a certain holding time, volume shrinkage is often reduced as the Al<sub>2</sub>O<sub>3</sub> content increases from 15 wt.% to 30 wt.%. Fig. 3.58 illustrates the compressive strength of the porous ceramics subsequent to sintering at 1600°C for 2 hours, 3 hours, or 4 hours holding time. Compressive strength generally rises with more Al<sub>2</sub>O<sub>3</sub> content throughout all sintering holding times, suggesting that Al<sub>2</sub>O<sub>3</sub> enhances the mechanical integrity of the porous structure. Among the three holding durations, samples sintered for 3 hours consistently demonstrated the highest compressive strength across all Al<sub>2</sub>O<sub>3</sub> contents, indicating that this duration facilitates appropriate densification without excessive grain growth or pore coarsening. Notably, prolonging the sintering holding time to 4 hours resulted in reduced compressive strength relative to 3 hours, due to the initiation of microstructural deterioration. SEM micrograph, as

shown in Fig. 3.59, demonstrates that the sample exhibits surface cracks after 4 hours sintering holding time. The formation of cracks is imperceptible during sintering for a holding time of 2 or 3 hours.

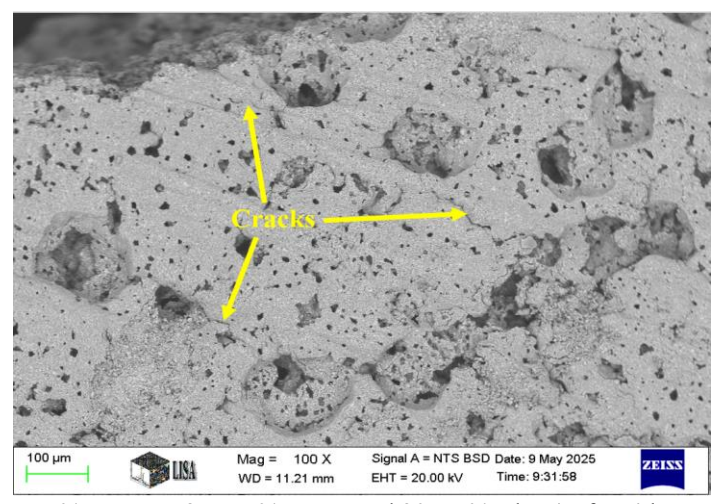
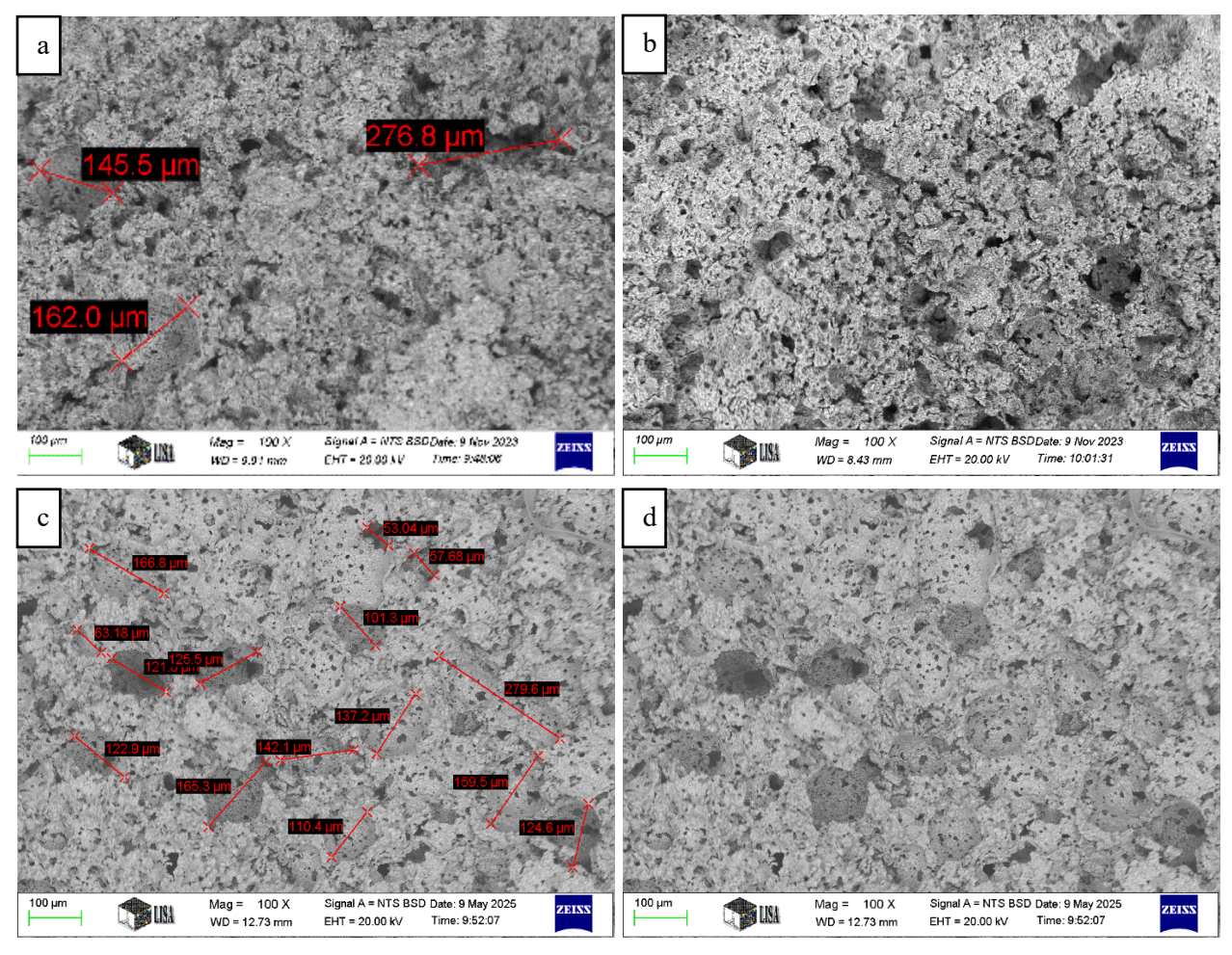
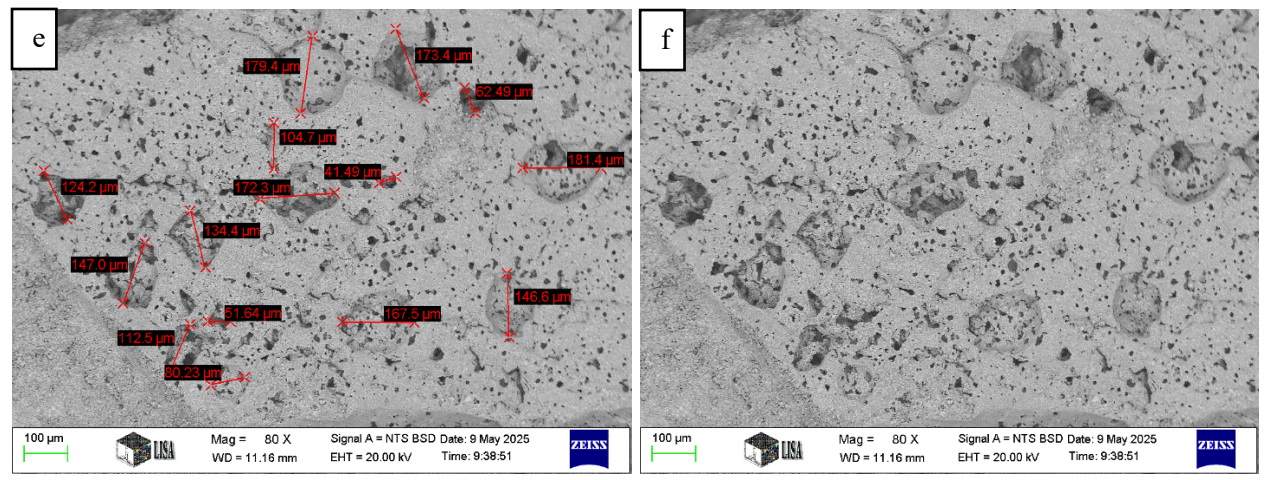


Fig. 3.59 Sample (67.5 wt.% m-ZrO<sub>2</sub>, 2.5 wt.% MgO, and 30 wt.% Al<sub>2</sub>O<sub>3</sub>) after 4 hours sintering holding time





**Fig. 3.60** SEM micrographs for porous ceramics (67.5 wt.% m-ZrO<sub>2</sub>, 2.5 wt.% MgO, and 30 wt.% Al<sub>2</sub>O<sub>3</sub>) sintered at 1600°C for: 2 hours (a, b), 3 hours (c, d), and 4 hours (e, f)

Fig. 3.60 presents a comparison of the SEM micrographs of the produced porous ceramics sintered at 1600°C for 2 hours, 3 hours, or 4 hours holding time. All the samples that were used in the SEM test consist of 76.5 wt.% ZrO<sub>2</sub>, 2.5 wt.% MgO, and 30 wt.% Al<sub>2</sub>O<sub>3</sub>. Sintering porous ceramics for varying holding time could generally exhibit distinct and progressive changes in surface morphology. Shorter sintering times (2 hours) result in minimal grain densification. Pores tend to have increased irregularity, and interconnectedness. The structure appears to have increased openness and porosity. Prolonged sintering time (3 hours) enhances the activity of sintering processes resulting in partial pore closure. More rounded pores and a decrease in porosity are seen compared to the samples sintered for 2 hours. Following an extended sintering holding time of 4 hours, the microstructure exhibits a considerable increase in density. After 4 hours of sintering time, total porosity is much less and the structure is more condensed. With an increase in sintering holding time, pore morphology often transitions from irregular to more rounded configurations, reflecting the natural tendency of the system to reduce surface energy. The irregular pores with sharper edges possess higher surface energy. During sintering, atomic diffusion promotes the redistribution of material to diminish this energy. This results in the reduction of sharp characteristics and the development of more equiaxed, rounder pores. The transition to rounded pores is influenced by thermodynamic and kinetic processes that aim to reduce the free energy of the system over time. As shown in Fig. 3.60, after 2 hours of sintering, the surfaces of the samples exhibit a rough texture and a loosely packed structure, characterized by conspicuous pore networks. As the sintering time increases from 2 to 4 hours, the surfaces of the samples tend to be smoother and denser. Fig. 3.61 shows the XRD pattern of the sample

composed of 67.5 m-ZrO<sub>2</sub>, 2.5 wt.% MgO, and 30 wt.% Al<sub>2</sub>O<sub>3</sub>, after sintering at 1600°C for 3 hours.

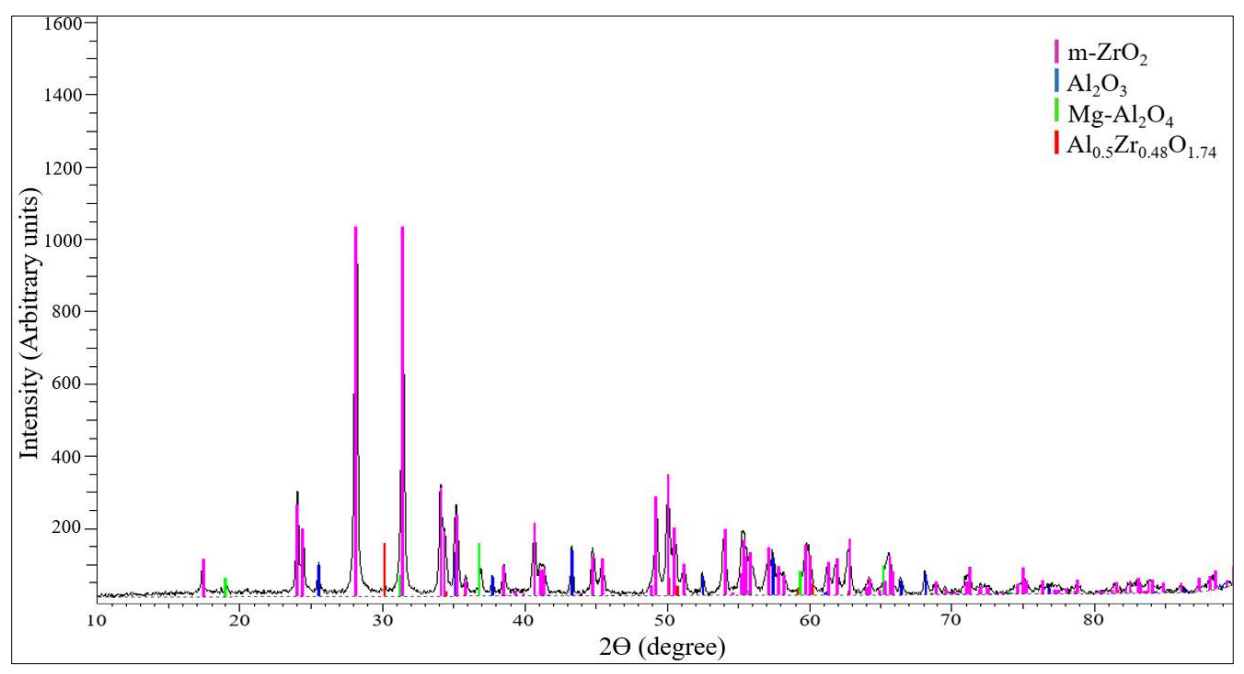


**Fig. 3.61** XRD pattern for sintered porous ceramic (67.5 wt.% m-ZrO<sub>2</sub>, 2.5 wt.% MgO, and 30 wt.% Al<sub>2</sub>O<sub>3</sub>) at 1600°C for 3 hours

In contrast to the samples sintered at 1600°C for 2 hours (Fig. 3.29), the XRD pattern of the sample sintered at 1600°C for 3 hours (Fig. 3.61) shows the formation of more crystalline phases. The principal diffraction peaks (in Fig. 3.29 and 3.61) belong to m-ZrO<sub>2</sub>, as seen by the pronounced and distinct reflections. The peaks are significant within the  $2\theta$  range of  $27^{\circ}$  to  $35^{\circ}$ , affirming the stability and persistence of the m-ZrO<sub>2</sub> at elevated temperatures, potentially attributable to inadequate stabilisation or insufficient MgO content to achieve complete conversion to the tetragonal phase. Additional peaks corresponding to corundum (α-Al<sub>2</sub>O<sub>3</sub>) can be observed particularly in the mid-20 region, indicating that the Al<sub>2</sub>O<sub>3</sub> retained its crystalline structure and thermal stability after sintering. The formation of MgAl<sub>2</sub>O<sub>4</sub> spinel is seen after 3 hours of sintering, as shown in Fig. 3.61, with typical peaks at about  $2\theta = 36^{\circ}$  and  $45^{\circ}$ , signifying an interaction between MgO and Al<sub>2</sub>O<sub>3</sub> that results in partial spinel production. Nonetheless, the MgAl<sub>2</sub>O<sub>4</sub> phase exhibits lower intensity relative to the predominant Al<sub>2</sub>O<sub>3</sub> and m-ZrO<sub>2</sub> peaks, indicating its status as a secondary phase. Fig. 3.61 also reveals peaks related to aluminium zirconium oxide (Al<sub>0.5</sub>Zr<sub>0.48</sub>O<sub>1.74</sub>), suggesting possible interdiffusion or solid-state reactions involving Al<sub>2</sub>O<sub>3</sub> and ZrO<sub>2</sub> at 1600 °C after 3 hours sintering time. In comparison to Fig. 3.29, the pronounced sharpness and intensity of the peaks in Fig. 3.61 indicate that the sample is highly crystalline; nonetheless,

the presence of various phases implies inadequate solid-state reaction or phase segregation during sintering. The production of the MgAl<sub>2</sub>O<sub>4</sub> phase inside the ZrO<sub>2</sub>-Al<sub>2</sub>O<sub>3</sub>-MgO system happens only under certain temperature and sintering holding time conditions: at 1400°C or 1500°C for 2 hours (Fig. 3.43), and at 1600°C only after an extended holding time of 3 hours (Fig. 3.61). This behaviour illustrates the kinetics of solid-state reactions and the diffusion-controlled mechanisms necessary for MgAl<sub>2</sub>O<sub>4</sub> production. The synthesis of spinel between MgO and Al<sub>2</sub>O<sub>3</sub> is a diffusionlimited process, necessitating the migration of Mg<sup>2+</sup> ions into the Al<sub>2</sub>O<sub>3</sub> lattice [165]. At reduced temperatures, the reaction may occur owing to advantageous thermodynamics; nevertheless, it is significantly influenced by diffusion distances and particle contact, which are comparatively limited during the first stages of sintering. At 1600°C, despite enough thermal energy, the kinetics of MgAl<sub>2</sub>O<sub>4</sub> production may be initially impeded by increased grain growth or the development of dense MgO and Al<sub>2</sub>O<sub>3</sub> areas that diminish interfacial contact between the reactants. Consequently, MgAl<sub>2</sub>O<sub>4</sub> does not easily develop during brief sintering holding time at this temperature. Only with an extension of the holding duration to 4 hours does enough diffusion and atomic mobility transpire, enabling the interaction of Mg<sup>2+</sup> and Al<sup>3+</sup> ions to yield the thermodynamically stable MgAl<sub>2</sub>O<sub>4</sub> spinel phase. The measurements of pore size distribution, shown in Figs. 3.62 and 3.63, were conducted on three distinct samples.

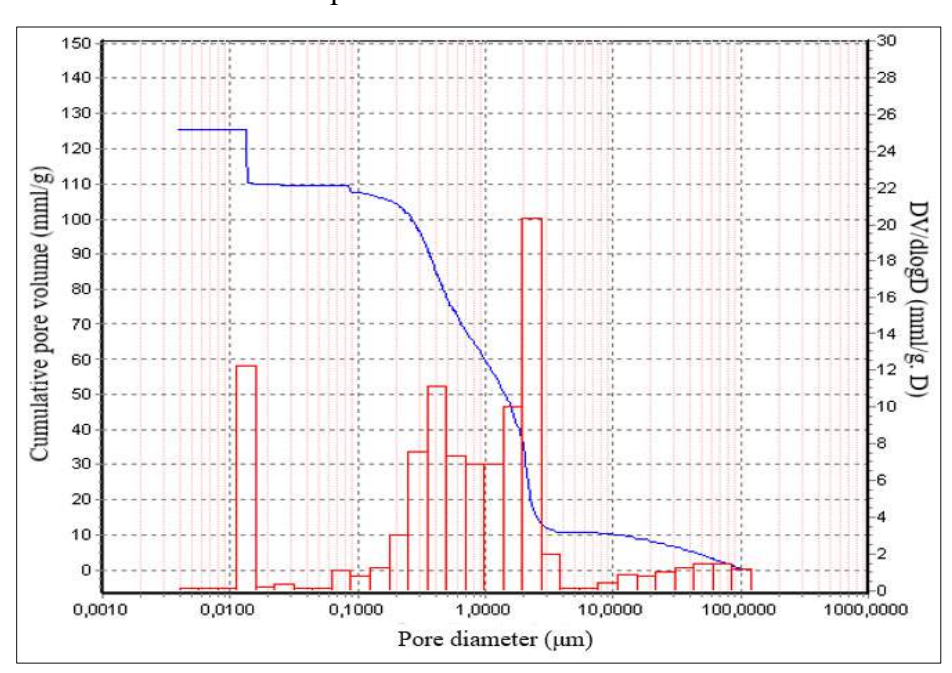
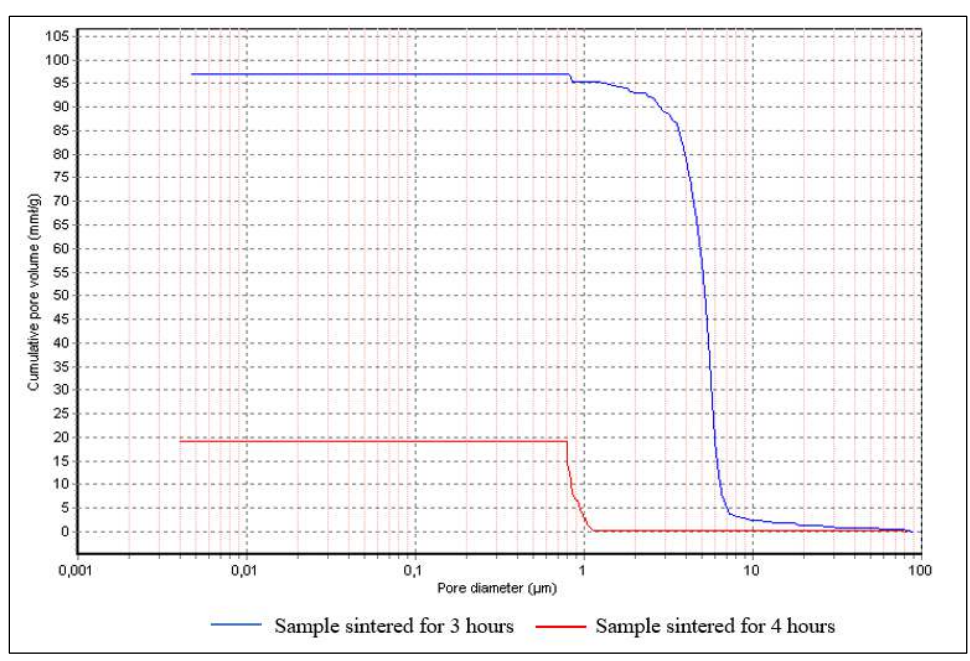


Fig. 3.62 The pore size distribution of the sample (67.5 wt.% m-ZrO<sub>2</sub>, 2.5 wt.% MgO, and 30 wt.% Al<sub>2</sub>O<sub>3</sub>) sintered at 1600°C for 2 hours



**Fig. 3.63** The pore size distribution of the sample (67.5 wt.% m-ZrO<sub>2</sub>, 2.5 wt.% MgO, and 30 wt.% Al<sub>2</sub>O<sub>3</sub>) sintered at 1600°C for 3 or 4 hours

The sample in Fig. 3.62 was sintered at  $1600^{\circ}$ C for 2 hours, while the two samples in Fig. 3.63 include one sintered at  $1600^{\circ}$ C for 3 hours and another sintered at  $1600^{\circ}$ C for 4 hours. The three samples that were used in this test consist of 76.5 wt.%  $ZrO_2$ , 2.5 wt.% MgO, and 30 wt.%  $Al_2O_3$ . The cumulative pore volume curves of the three samples exhibit comparable trends. All exhibit an S-shape, with flattened ends and a steep core section, suggesting that large amounts of mercury are absorbed by the mesopores and small pores in the middle region. Additionally, a considerable portion of the total pore volume in the samples of mesopores and small pore channels have a diameter ranging from 0.1 to 3  $\mu$ m for the sample sintered for 2 hours, ranging from 1 to 7  $\mu$ m for the sample sintered for 3 hours, and ranging from 0.8 to 1.2  $\mu$ m for the sample sintered for 4 hours. The findings reveal that the three samples exhibit distinct total pore volumes, as seen by the divergence of the curves towards varying cumulative pore volumes in the Figs. The findings unequivocally demonstrate that cumulative pore volumes decrease as sintering holding time increases from 2 to 4 hours. Table 3.14 presents the most significant findings from the MIP testing.

Table 3.14 MIP results of the samples (67.5 wt.% m-ZrO<sub>2</sub>, 2.5 wt.% MgO, and 30 wt.% Al<sub>2</sub>O<sub>3</sub>)

Sintering time (hours)	Total intruded volume (mm³/g)	Total pore surface area (m²/g)	Median pore size (μm)
2	125.52	5.486	0.8778
3	96.89	0.088	5.2339
4	19.27	0.088	0.8449

Table 3.15 shows the Pearson correlation matrix of the experimental data. The experimental data are denoted by ST (hours) for sintering time in hours. The different measured experimental data entered into separate columns to create the correlation matrix which contain the Pearson correlation coefficient values. The results indicate that there is a very strong negative correlation between the sintering time and the apparent porosity, which means that with increasing sintering time, the apparent porosity decreases. The results also show that there is a strong positive correlation between the sintering time and the apparent density and volume shrinkage.

**Tables 3.15** The Pearson correlation matrix of the experimental data.

		1				
	Al <sub>2</sub> O <sub>3</sub> (wt.%)	ST (hours)	AD	AP	VS	σ
Al <sub>2</sub> O <sub>3</sub> (wt.%)	1					
ST (hours)	0	1				
AD	-0.5374	0.7887	1			
AP	0.3301	-0.9177	-0.8477	1		
VS	-0.4343	0.8688	0.9122	-0.9411	1	
σ	0.4141	-0.2947	-0.6424	0.2429	-0.4221	1

Figs. 3.64 (for sintered samples after 2 hours sintering holding time) and 3.65 (for sintered samples after 3 hours or 4 hours sintering holding time) illustrate a pair plot of four research parameters: apparent density, apparent porosity, volume shrinkage, and compressive strength. It can be concluded from the Figs. That the apparent density and volume shrinkage increase, while the apparent porosity decreases with rising sintering holding time. The compressive strength of the samples increased first when the sintering holding time increased from 2 to 3 hours, then reduced to the lowest values when the sintering holding time increased to 4 hours. The reduction in compressive strength after 4 hours of sintering holding time is attributable to the formation of surface cracks. Table 3.16 summarize the type of correlation between the variables in Figs. 3.64 and 3.65.

Table 3.16 Correlation relationships between the variables after sintering for different holding time

Variables	AD	AP	VS	σ
AD	_	Negative	Positive	Negative
AP	Negative	_	Negative	Positive
VS	Positive	Negative	-	Negative
σ	Negative	Positive	Negative	_

The findings demonstrate that the correlation between the variables becomes very strong (either positively or negatively) when the sintering holding time extends from 2 hours to 4 hours.

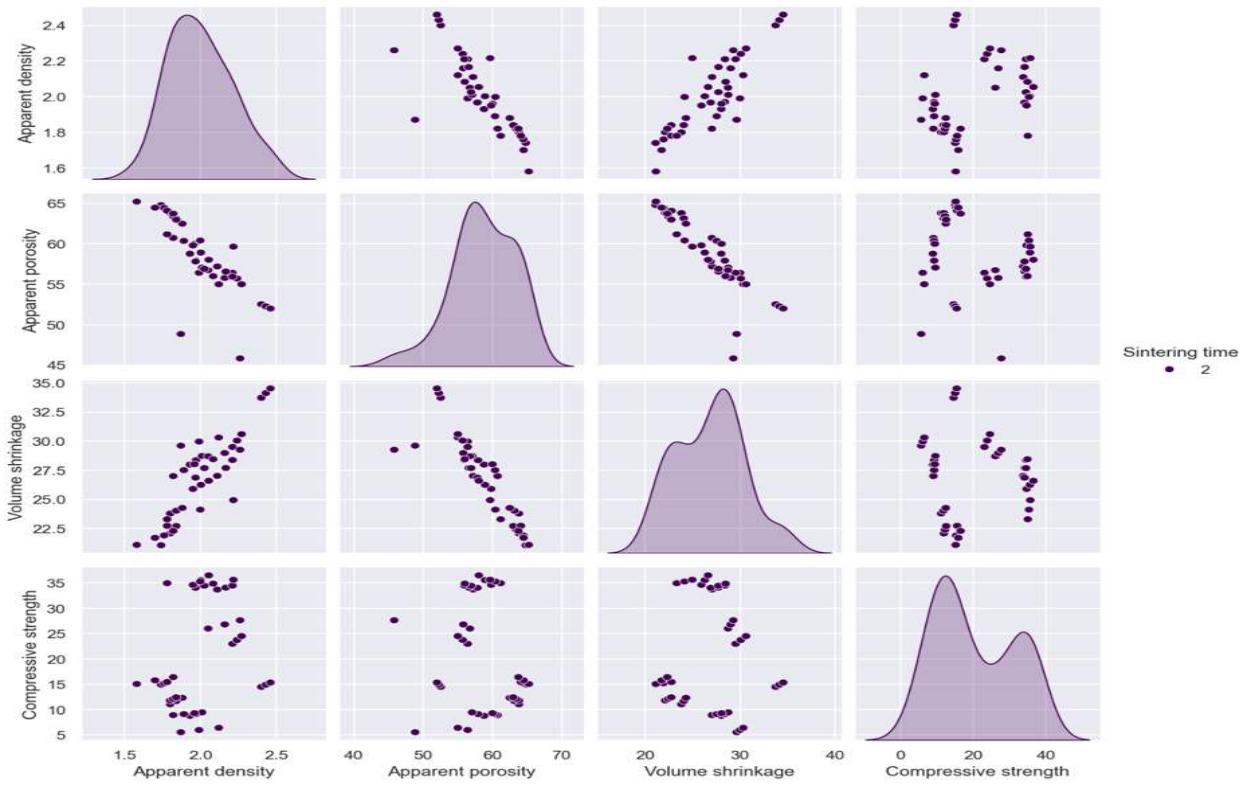


Fig. 3.64 Pair plot of four study features for the samples after 2 hours sintering holding time

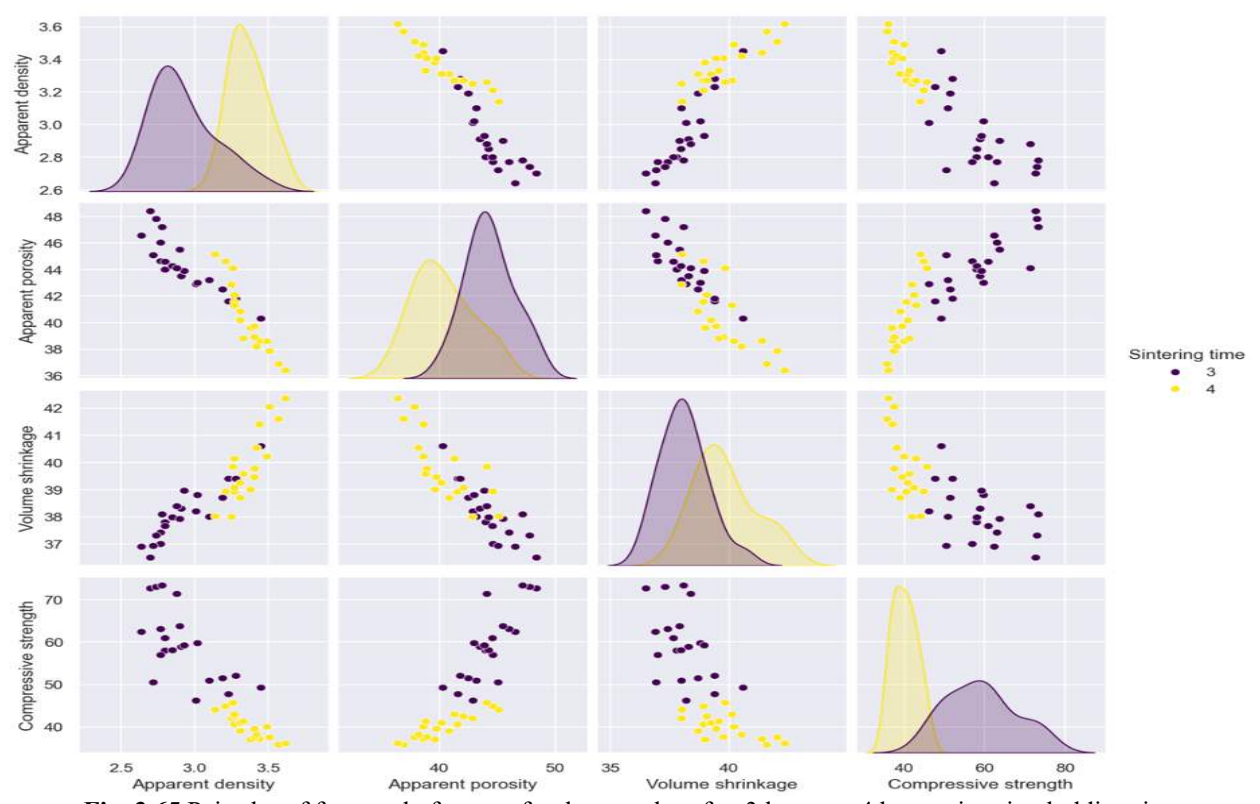


Fig. 3.65 Pair plot of four study features for the samples after 3 hours or 4 hours sintering holding time

Figs. 3.64 and 3.65 illustrate the correlations among the variables as the sintering holding time rises, indicating that the sintering conditions influence the structure of the prepared ceramics, subsequently affecting their properties and the interrelations among those properties. As a brief explanation of the changes that occur as the sintering holding time rises: as the sintering holding time rises, the apparent density increases and the surface becomes smoother and denser (as previously shown using SEM), resulting in decreased interarticular spacing, which subsequently causes increased volume shrinkage. With the longer sintering holding time, the pore shape transforms to a more rounded pore shape (as previously shown using SEM) to reduce the surface free energy, leading to an increase in apparent porosity. The existence of these less stressconcentrated, rounded-shape pores, along with the enhanced smoothness and densification of the surface, can improve the compressive strength of the prepared porous ceramics. Prolonged sintering holding times (4 hours) can result in surface cracking of the samples, thereby diminishing compressive strength. Fig. 3.66 illustrates four bar charts, each indicating the coefficient of variation (CV%) for a particular feature measured over 14 group (each group is the average of 3 samples). In the measurement of apparent density, the majority of coefficient of variance values are around 5%, with the exception of samples in group one, which attain about 6 - 7%. This indicates that the apparent density measurements are very precise. All coefficients of variation values for apparent porosity, volume shrinkage, and compressive strength measurements are below 5%, indicating stability and consistency of the measurements across all samples. The findings indicate that the experimental measures are mostly reliable, with the majority of data sets remaining within acceptable variability thresholds (under 20%). In conclusion to this study, the porous-structured ceramics sintered at 1600°C for 3 hours are more suitable for porous bone replacement applications, owing to their higher porosity (51% - 57%), large pore size (exceeding 100  $\mu$ m), larger pore openings (median pore size  $\sim 5.2 \mu$ m), and enhanced mechanical compressive strength (47.7 - 73 MPa).

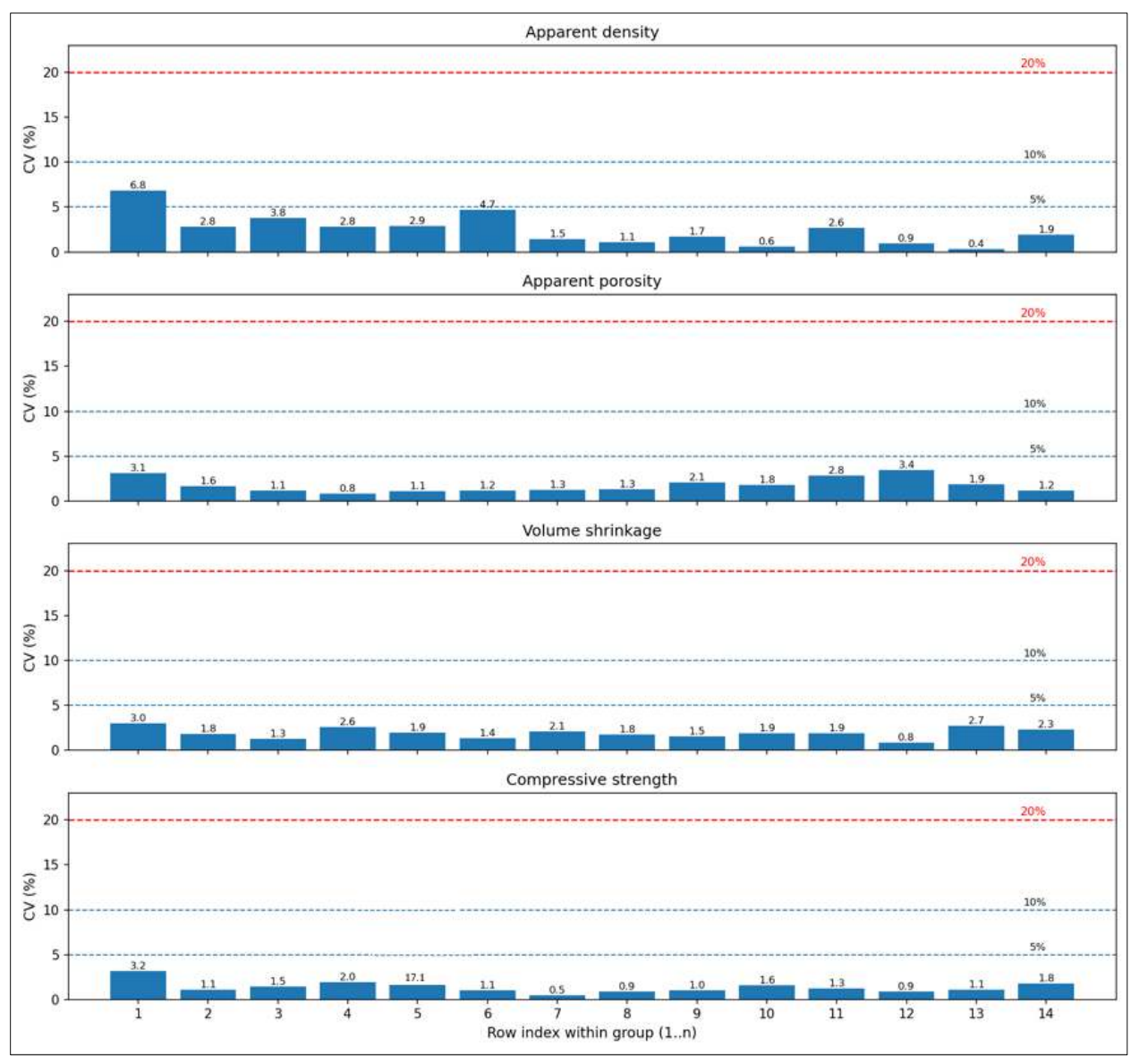


Fig. 3.66 Bar plot of the coefficient of variation (CV%)

#### 4. Chapter Four - Conclusions

## 4.1 Conclusion of studying the effect of different content and type of starches with different distilled water content

This study used different types (potato and tapioca) and contents (10, 20, and 30 wt.%) of starches with diverse suspension concentrations (60, 65, 68, and 70 wt.% based on the solid) to produce the ceramic porous structure. After drying, the samples were progressively sintered at 1600°C for a holding time of 2 hours. Based on the experimental test results and Pearson correlation matrix of the experimental data, it can be concluded that:

- The apparent densities of the samples decrease with increasing quantities of starches.
- The concentration of the suspension has no consistent effect on the apparent densities.
- The samples that prepared with using potato starch have apparent densities less than the samples prepared with tapioca starch due to the swelling factor and particle size of potato starch is larger than tapioca starch.
- The apparent porosity of the samples increases with the increasing of starch content.
- The increasing of the suspension concentration resulted in a reduction in apparent porosity.
- The apparent porosity is higher for the samples that prepared using potato starch due to the swelling factor and particle size of potato starch is higher than that of tapioca starch.
- The volume shrinkage is increased by an increase in the amount of starch.
- As the proportion of ceramic powder in the suspension increases and the water content decreases, the volume shrinkage reduces.
- From the SEM results, it is possible to conclude that the pore size decreased, and the shape irregularity increased with increasing of the starch content.
- SEM analysis indicated that the ceramic shells are discernible inside the pores, forming due to the interaction between ceramic powder particles and starch.
- The compressive strength decreased with an increase in starch content.
- The compressive strength increased with an increase in suspension concentration.
- The compressive strength of the samples that produced with tapioca starch higher than that
   of potato starch duo to the reduced apparent porosity and higher apparent density.
- Compressive strength testing shows that the produced samples have values between 2.7 and 15.87 MPa, which is comparable to trabecular bone (0.1 30 MPa).

Upon concluding the first study of the thesis, it was determined that using a 20 wt.% starch content combined with a 60 wt.% suspension concentration yields favourable porosity, density, and mechanical properties that are appropriate for bone replacement applications.

### 4.2 Conclusion of studying the effect of different content of Al<sub>2</sub>O<sub>3</sub> with different types of starches

This study included the manufacture of porous ceramics using varying Al<sub>2</sub>O<sub>3</sub> contents combined with various starch types (potato, tapioca, or a 50:50 combination of potato and tapioca). The samples were progressively pre-sintered and then sintered at 1600°C for 2 hours. From the experimental test results and the Pearson correlation matrix of the data, it can be identified that:

- As the Al<sub>2</sub>O<sub>3</sub> content in the pre-sintered and sintered samples increases, the apparent densities and volume shrinkage decrease while the apparent porosity increases.
- The maximum apparent density was determined for a sample made with tapioca starch,
   while the highest apparent porosity and volume shrinkage were observed in samples created using potato starch.
- Compared to microstructures produced using tapioca starch, porous ceramics
   manufactured with potato starch have larger pores and a longitudinal pore morphology.
- The microstructures produced using 50:50 wt.% potato and tapioca starches have varying pore shape and diameters. The interaction between these two forms of starch leads to the formation of extremely large pores.
- The largest pore has a significant size of more than 200 μm, which results from the interaction between the two distinct types of starch granules.
- Mixing between the two types of starch produces pores that do not have regularity because
  it depends on the surface contact that occurs between the starch granules.
- During the sintering process, the ceramic particles at the surface of the pores undergo volume shrinkage, resulting in a decrease in pore size.
- In general, the pore morphology of the produced porous structure depends on the type and amount of pore-forming agent and on the sintering conditions.
- The XRD results clearly show that the highest two peaks, which are (111) and (-111), are
   both for monoclinic crystal structure (baddeleyite).

- Sintering improves the crystallinity of materials by facilitating the reorganization and bonding of atoms inside the crystal lattice.
- The XRD findings show a reduction in the peak intensity of the ZrO<sub>2</sub> phase as the Al<sub>2</sub>O<sub>3</sub> content increases from 15 wt.% to 30 wt.%. As the content of Al<sub>2</sub>O<sub>3</sub> rises, the fraction of ZrO<sub>2</sub> in the composite drops.
- From the MIP results, it can be concluded that the prepared porous-structured ceramics have a multi-modal pore structure.
- The predominant portion of the overall pore volume in all samples exists in pores with a diameter exceeding 1 μm.
- The median pore channel sizes for samples without starch, tapioca starch, potato starch, and (50:50) P+T were found to be 1.19, 3.29, 5.32, and 24.08 μm, respectively.
- The pore size distribution curve clearly demonstrates a change towards smaller pore openings sizes when no starch is used, suggesting a denser microstructure of the samples.
- The sample that is prepared without starch exhibits around 42% of the pore-opening volume within a  $1 2 \mu m$  range. About 39% of the pore opening volume in the sample with tapioca starch is between the  $3 7 \mu m$  range and about 10% less than 0.01 μm. On the other hand, the potato starch sample has a larger opening, which makes up around 45% of the volume of the pores in the  $6 9 \mu m$  range and about 12% less than 0.01 μm.
- In the sample produced with a (50:50) mixture of potato and tapioca starches, almost 17% of the volume of pore openings had a diameter less than 0.01  $\mu$ m, 4% had a diameter between 0.03 and 0.05  $\mu$ m, 6% had a diameter between 2 and 6  $\mu$ m, and approximately 17% had larger openings with diameters ranging from 10 to 100  $\mu$ m.
- There is a positive correlation between the compressive strength of the produced porousstructured ceramics and the amount of Al<sub>2</sub>O<sub>3</sub> present.
- The highest calculated compressive strength was 76.89 MPa for a sample with a porous structure, which was manufactured using 20 wt.% tapioca starch and 30 wt.% Al<sub>2</sub>O<sub>3</sub> content. While the lowest calculated compressive strength was 25.82 MPa for a sample that prepared using 20 wt.% potato starch and 17.5 wt.% Al<sub>2</sub>O<sub>3</sub> content.
- The main advantage of Al<sub>2</sub>O<sub>3</sub> is its ability to improve compressive strength serving as a barrier against fracture development.

- MIP and SEM analysis reveals that the ceramic grain matrix has two distinct varieties of pores: the larger, that were produced by starch granules, and the smaller void-like channels that are interspersed among the ceramic particles after sintering.
- Upon completing the second study of the thesis, it was concluded that a 50:50 wt.% combination of tapioca and potato starches results in a larger pore size (larger than 100 μm) with desirable pore openings (median pore openings size about 25 μm), apparent porosity (51 57%), apparent density (2.5 3.1 g/cm³), and compressive strength (~43 48 MPa) suitable for bone replacement applications. The progressive pre-sintering and sintering process may diminish the occurrence of cracks on the sample surfaces.

## 4.3 Conclusion of studying the effect of progressive pre-sintering and sintering at different temperatures

The study included the production of porous ceramics using different Al<sub>2</sub>O<sub>3</sub> content with a starch blend of 50:50 wt.% tapioca and potato starch. The samples underwent a gradual presintering process followed by sintering at 1400°C, 1500°C, and 1600°C for a holding time of 2 hours. The experimental test findings and the Pearson correlation matrix indicate that:

- SEM analysis indicates that progressive pre-sintering and sintering effectively decreases the occurrence of cracks in the surfaces of ceramic matrices.
- The pre-sintering decreases the rate of shrinkage during the final sintering process and mitigates thermal stresses.
- The compressive strength is significantly higher in the progressively pre-sintered and sintered samples.
- With a rise in Al<sub>2</sub>O<sub>3</sub> content, apparent density and volume shrinkage decrease, while apparent porosity and compressive strength increase.
- With a rise in sintering temperature, apparent porosity decreases, but apparent density,
   volume shrinkage, and compressive strength increase.
- The dilatometric analysis test result illustrates that the sample (with composition of 67.5 wt.% ZrO<sub>2</sub>, 30 wt.% Al<sub>2</sub>O<sub>3</sub>, and 2.5 wt.% MgO) experience a maximum shrinkage of 25% of their original length after sintering to 1500°C.
- The XRD pattern reveals that the predominant phase produced after sintering is m-ZrO<sub>2</sub>.
- A significant decrease in XRD peak intensity can be observed when comparing the sample sintered at 1600°C to that sintered at 1400°C.

- The spinel (Mg-Al<sub>2</sub>O<sub>4</sub>) phase is formed when the Al<sub>2</sub>O<sub>3</sub> and MgO react after progressive sintering at 1400°C or 1500°C, however this reaction does not occur while sintering at 1600°C.
- In comparison to the microstructures sintered at 1400°C or 1500°C, the porous ceramics sintered at 1600°C exhibit larger pores and a more homogeneous pore morphology.
- When the temperature of the sintering process increased from 1400°C to 1600°C, the
   ceramic grains connectivity increased, and the micro-voids between the grains decreased.
- EDS and SEM analysis of the microstructure illustrates that in all the pre-sintered and sintered samples, large areas with a uniform distribution of Al<sub>2</sub>O<sub>3</sub> and ZrO<sub>2</sub> grains were present. It confirms the effectiveness of the mixing procedure that was followed to produce a good dispersion of Al<sub>2</sub>O<sub>3</sub> particles in the ZrO<sub>2</sub> matrix.
- The findings of the MIP tests show that when the sintering temperature increases, the size
  of the pore openings (the pore throat) decreases.
- To summarize, porous-structured ceramics sintered at 1600°C are appropriate for use in porous bone replacement applications due to their high porosity (51 57%), pore size (more than 100 μm) and better compressive strength (43 49 MPa).

#### 4.4 Conclusion of studying the effect of different sintering holding time

The study involved the production of porous ceramics using varying Al<sub>2</sub>O<sub>3</sub> content combined with a starch mixture of 50:50 wt.% tapioca and potato starch. The samples had a progressive presintering procedure, followed by sintering at 1600°C for periods of 2, 3, and 4 hours. The results of the experimental tests and the Pearson correlation matrix demonstrate that:

- Extended the sintering holding time consistently enhances the apparent density of the samples, attributed to increased densification during prolonged heat exposure, which promotes enhanced particle bonding and a reduction in open porosity.
- Increasing the holding time resulted in a significant decrease in porosity, attributable to improved diffusion and grain boundary migration that facilitate pore reduction and densification.
- Volume shrinkage increases with the increasing of sintering holding time.
- The samples sintered for 3 hours consistently demonstrated the highest compressive strength across all Al<sub>2</sub>O<sub>3</sub> contents, indicating that this duration facilitates appropriate densification without excessive grain growth or pore coarsening.

- Prolonging the sintering holding time to 4 hours resulted in reduced compressive strength relative to 3 hours, due to the initiation of microstructural deterioration.
- Shorter sintering times (2 hours) result in minimal densification. Pores tend to have increased size, irregularity, and interconnectedness. The structure appears to have increased openness and porosity.
- Prolonged sintering time (3 hours) enhances the activity of sintering processes resulting in partial pore closure. Smaller, more rounded pores and a decrease in porosity are seen compared to the samples sintered for 2 hours.
- After 4 hours of sintering time, total porosity is much less, and the structure is more condensed.
- With an increase in sintering holding time, pore morphology often transitions from irregular to more rounded configurations, reflecting the natural tendency of the system to reduce surface energy.
- As the sintering time increases from 2 to 4 hours, the surfaces of the samples tend to be smoother and denser.
- The XRD pattern of the sample sintered at 1600°C for 3 hours shows the formation of several crystalline phases (m-ZrO<sub>2</sub> as a main phase, α-Al<sub>2</sub>O<sub>3</sub>, MgAl<sub>2</sub>O<sub>4</sub>, and Al<sub>0.5</sub>Zr<sub>0.4</sub>8O<sub>1.74</sub>).
- The pronounced sharpness and intensity of the peaks in the XRD pattern indicate that the sample is highly crystalline.
- The cumulative pore volumes and the median pore size decrease as sintering time increases.

In conclusion to all of the PhD research studies, the produced porous ceramic composites (comprising 20 wt.% of a 50:50 mixture of potato and tapioca starches, with a 60 wt.% suspension concentration, progressively pre-sintered at 1100°C and subsequently sintered at 1600°C for 2 or 3 hours) exhibit significant potential as load-bearing, osteoconductive scaffolds for cancellous bone defects and as substitutes for dental/maxillofacial bone grafts (including sinus lift and ridge augmentation). It can also function as a coating on metallic load-bearing implants (hip, knee, and dental implants) to promote osseointegration.

#### 5. Chapter Five - Claims/New scientific results

From the comprehensive experimental investigation of bone replacement porous m-ZrO<sub>2</sub>-Al<sub>2</sub>O<sub>3</sub>-MgO ceramic composites fabricated by an economical starch consolidation casting method, the following new scientific findings were obtained:

### Claim 1: Preparation of innovative bone replacement porous ceramic composites using costeffective starch consolidation casting.

I have experimentally proved that innovative bone replacement porous ceramic composites can be synthesized exhibiting an apparent density (2.5 - 3.2 g/cm³), apparent porosity (~42 - 57%), pore size (~50 - 300 μm), and mechanical compressive strength (~44 - 73 MPa), utilizing zirconium dioxide (monoclinic phase, m-ZrO<sub>2</sub>) (67.5 - 82.5 wt.%) combined with aluminium oxide (corundum phase, α-Al<sub>2</sub>O<sub>3</sub>) (15 - 30 wt.%) and magnesium oxide (periclase phase, c-MgO) (2.5 wt.%). ZrO<sub>2</sub>-based porous ceramic composites were fabricated using starch consolidation casting method, employing a mixture (50:50 wt.%) of potato with tapioca starches (the swelling factor for potato starch was 41, whereas for tapioca starch it was 32) as pore and body forming agents. The ceramic slurries were produced with 20 wt.% (based on solid ceramics) of starches mixture and 60 wt.% (based on solid materials) of suspension concentration according to the conditions shown in Table C1.

**Table C1.** The mixed compositions with the preparation conditions

m-ZrO <sub>2</sub> (wt.%)	α-Al <sub>2</sub> O <sub>3</sub> (wt.%)	c-MgO (wt.%)	50:50 P+T (wt.%)	Sus. Conc. (wt.%)	Heating conditions	Pre-sintering conditions	Sintering conditions
82.5 80.0 77.5 75.0 72.5 70.0 67.5	15 17.5 20 22.5 25 27.5 30	2.5 2.5 2.5 2.5 2.5 2.5 2.5 2.5	20 20 20 20 20 20 20 20	60 60 60 60 60 60	80 °C for 2 hours	500 °C (1 hour), then 1100 °C (2 hours) with 2 °C/min heating rate	300°C (1 hour), then 500°C (1 hour), then 1600°C (2 - 3 hours) with 2 °C/min heating rate

Where 50:50 P+T wt.% denoted to a mixture (50:50 wt.%) of potato with tapioca starches, whereas Sus. Conc. (wt.%) refers to the suspension concentration.

<u>Related publication:</u> **Rusul Ahmed Shakir**, Róbert Géber, Marwan T. Mezher, Tomasz Trzepieciński. (2025). Exploring influence of sintering temperature on the structure and technical characteristics of ATZ ceramic composites. Results in Engineering. Volume 28, 107139. https://doi.org/10.1016/j.rineng.2025.107139 (Q1)

# Claim 2: The impact of incorporating various amounts and types of starches with various amounts of distilled water on the technical properties of the produced porous ceramics.

A. I have statistically determined the Pearson correlation matrix (Tables C2.1 and C2.2) of the experimental data to analyse the correlation between the amounts and types of starches, the amounts of distilled water, and the properties of the produced bone replacement porous m-ZrO<sub>2</sub>-Al<sub>2</sub>O<sub>3</sub>-MgO ceramics. Pearson correlation matrix demonstrated that starch content (10 wt.%, 20 wt.%, and 30 wt.%) correlates with essential material (bone replacement porous m-ZrO<sub>2</sub>-Al<sub>2</sub>O<sub>3</sub>-MgO ceramics) properties, exhibiting a negative correlation with apparent density (strong correlation with using potato starch, r = -0.738, and very strong correlation with using tapioca starch, r = -0.873). Additionally, there is a strong negative correlation with compressive strength. The Pearson matrix showed that the starch content has a positive correlation with apparent porosity (very strong correlation with using potato starch, r = 0.819, and strong correlation with using tapioca starch, r = 0.726). The results also demonstrated a negative correlation between suspension concentration and volume shrinkage (strong correlation with using potato starch and very strong correlation with using tapioca starch, indicating that reduced water content reduces shrinkage.

**Table C2.1** The correlation matrix with using potato starch

		01				
	Starch (wt.%)	Sus. (wt.%)	AD	AP	VS	σ
Starch (wt.%)	1					
Sus. (wt.%)	0	1				
AD	-0.738	-0.268	1			
AP	0.819	-0.499	-0.549	1		
VS	0.545	-0.737	-0.031	0.769	1	
σ	-0.761	0.517	0.292	-0.848	-0.842	1

**Table C2.2** The correlation matrix with using tapioca starch

	Starch (wt.%)	Sus. (wt.%)	AD	AP	VS	σ
Starch (wt.%)	1					
Sus. (wt.%)	0	1				
AD	-0.873	-0.095	1			
AP	0.726	-0.472	-0.774	1		
VS	0.187	-0.909	-0.084	0.574	1	
σ	-0.798	0.516	0.639	-0.265	-0.371	1

Where AD: apparent density, AP: apparent porosity, VS: volume shrinkage, σ: compressive strength, Sus.: suspension concentration.

#### Related publications:

- 1. **Rusul Ahmed Shakir**, Róbert Géber. (2023). Structure and properties of ZrO<sub>2</sub>-Al<sub>2</sub>O<sub>3</sub>-MgO porous ceramic for biomedical applications. Results in Engineering. 18, 101104. https://doi.org/10.1016/j.rineng.2023.101104 (Q1)
- 2. Rusul Ahmed Shakir, Róbert Géber. (2024). POROSITY AND PORE MORPHOLOGY CHARACTERISTICS OF ZIRCONIA-ALUMINA BIOCERAMICS. POLLACK PERIODICA, An International Journal for Engineering and Information Sciences. 19, 3, 107 114. DOI:10.1556/606.2024.01099 (Q3)

**B.** To comprehensively visualise the interactions between the variables, pair plots (Fig. C2.1 for the samples with 0, 10, 20, and 30 wt.% potato starch; Fig. C2.2 for the samples with 0, 10, 20, and 30 wt.% tapioca starch; and Fig. C2.3 for the samples with 60, 65, 68, and 70 wt.% suspension concentration) of four research parameters (apparent density, apparent porosity, volume shrinkage, and compressive strength) were employed using the Seaborn library in Python. Table C2.3 and C2.4 summarize the type of correlation between the variables.

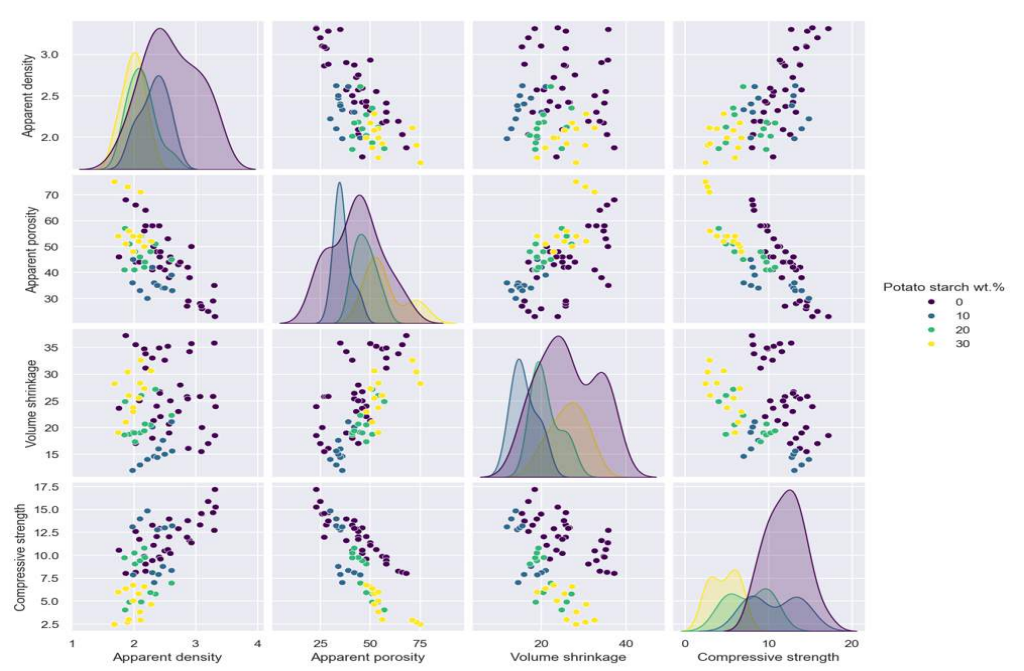


Fig. C2.1 Pair plot of four study features of samples prepared with different potato starch wt.%

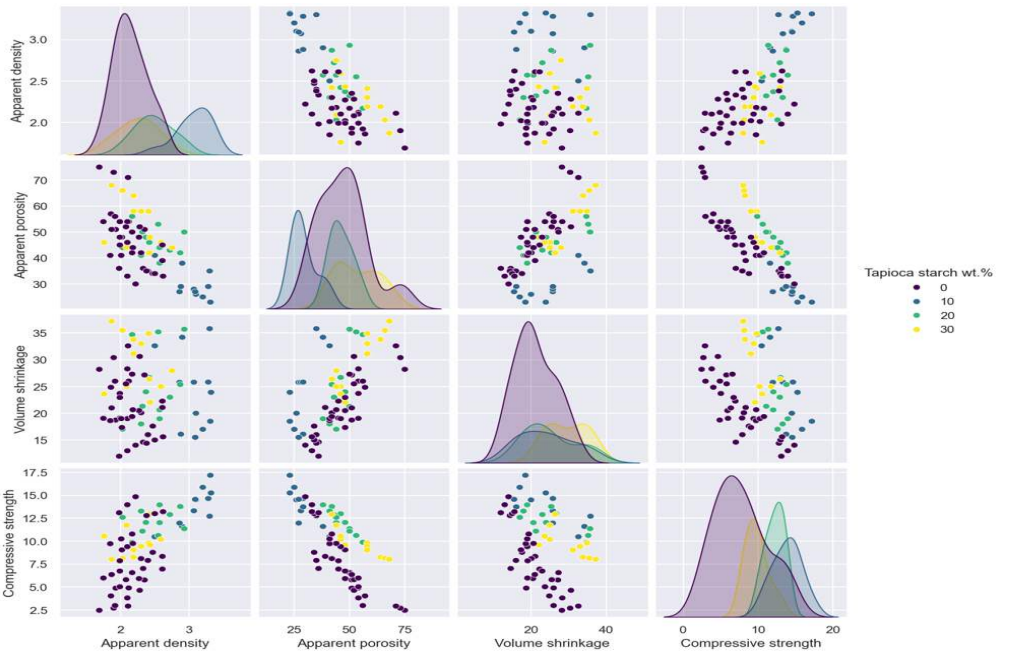


Fig. C2.2 Pair plot of four study features of samples prepared with different tapioca starch wt.%

**Table C2.3** Correlation relationships between the variables for samples prepared with potato and tapioca starches

Variables	AD	AP	VS	σ
AD	_	Negative	Weak	Positive
AP	Negative	_	Positive	Negative
VS	Weak	Positive	_	Negative
σ	Positive	Negative	Negative	_

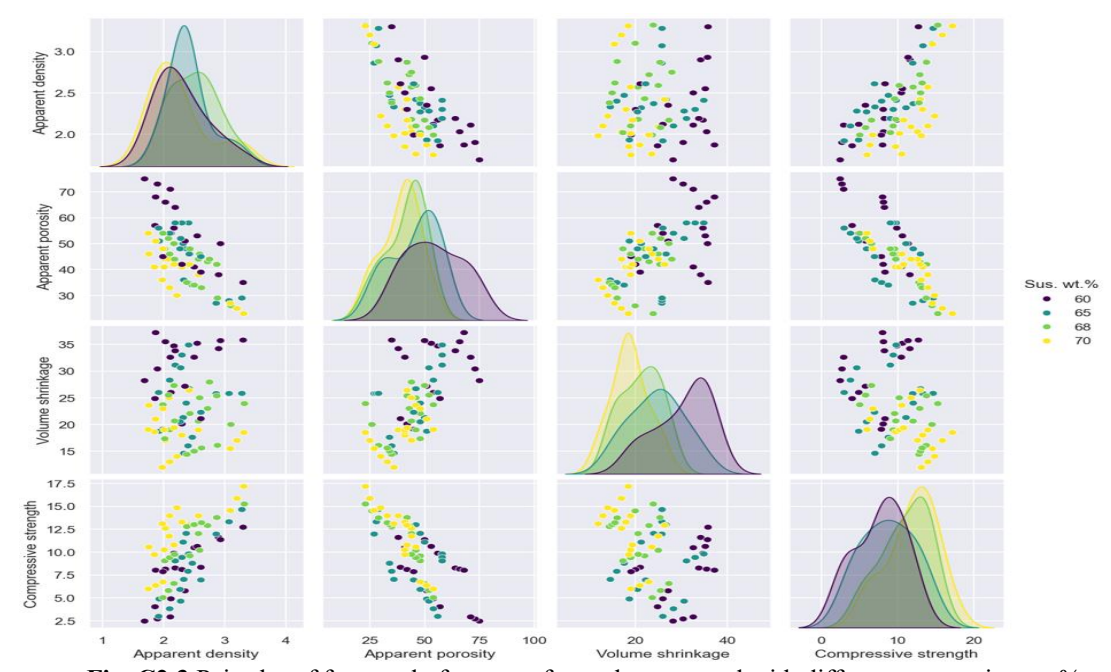


Fig. C2.3 Pair plot of four study features of samples prepared with different suspension wt.%

**Table C2.4** Correlation relationships between the variables for samples prepared with different suspension wt.%

Variables	AD	AP	VS	σ
AD	_	Negative	Weak	Positive
AP	Negative	_	Positive	Negative
VS	Weak	Positive	_	Negative
σ	Positive	Negative	Negative	_

# Claim 3: The influence of Al<sub>2</sub>O<sub>3</sub> content in determining the essential correlations between microstructural characteristics and mechanical properties.

**A.** I have statistically determined the Pearson correlation matrix of the experimental data to analyse the correlation between the  $Al_2O_3$  content (15, 17.5, 20, 22.5, 25, 27.5, and 30 wt.%), and the properties of the produced bone replacement porous m-ZrO<sub>2</sub>-Al<sub>2</sub>O<sub>3</sub>-MgO ceramics. The Pearson correlation matrix (Tables C3.1 - C3.3) established that  $Al_2O_3$  content has a very strong negative correlation (r = -0.80 to -1.00) with apparent density and volume shrinkage, while concurrently exhibiting a very strong positive correlation (r = 0.80 to 1.00) with apparent porosity and compressive strength.

Table C3.1 Pearson correlation matrix for the experimental data using tapioca starch

	Al <sub>2</sub> O <sub>3</sub> (wt.%)	AD	AP	VS	σ
Al <sub>2</sub> O <sub>3</sub> (wt.%)	1				
AD	-0.9664	1			
AP	0.9871	-0.9691	1		
VS	-0.9886	0.1482	-0.1582	1	
σ	0.8794	0.7101	-0.8979	-0.3591	1

**Table C3.2** Pearson correlation matrix for the experimental data using potato starch

	Al <sub>2</sub> O <sub>3</sub> wt.%	AD	AP	VS	σ
Al <sub>2</sub> O <sub>3</sub> (wt.%)	1				
AD	-0.9728	1			
AP	0.9905	-0.9493	1		
VS	-0.9368	0.1439	-0.1509	1	
σ	0.8579	0.7661	-0.8253	-0.3905	1

**Table C3.3** Pearson correlation matrix for the experimental data using potato + tapioca starch

	Al <sub>2</sub> O <sub>3</sub> (wt.%)	AD	AP	VS	σ
Al <sub>2</sub> O <sub>3</sub> (wt.%)	1				
AD	-0.9858	1		_	
AP	0.9863	-0.9891	1		
VS	-0.9828	0.1546	-0.1679	1	
σ	0.9208	0.7071	-0.9346	-0.3266	1

<u>Related publication:</u> Rusul Ahmed Shakir, Róbert Géber, Marwan T. Mezher, Tomasz Trzepiecinski, Ferenc Móricz. (2024). Effect of Alumina Proportion on the Microstructure and Technical and Mechanical Characteristics of Zirconia-Based Porous Ceramics. Journal of Composites Science. 517. https://doi.org/10.3390/jcs8120517 (Q1)

**B.** To comprehensively visualize the variables interactions, pair plots (for the samples with varying Al<sub>2</sub>O<sub>3</sub> content of 15, 17.5, 20, 22.5, 25, 27.5, and 30 wt.%) of four research parameters (apparent density, apparent porosity, volume shrinkage, and compressive strength) were employed using Seaborn library in Python (Fig. C3.1). Table C3.4 summarizes the type of correlation between the variables.

Table C3.4 Correlation relationships between the variables for the samples with different Al<sub>2</sub>O<sub>3</sub> wt.%

Variables	AD	AP	VS	σ
AD	_	Negative	Weak	Positive
AP	Negative	_	Weak	Negative
VS	Weak	Weak	_	Negative
σ	Positive	Negative	Negative	_

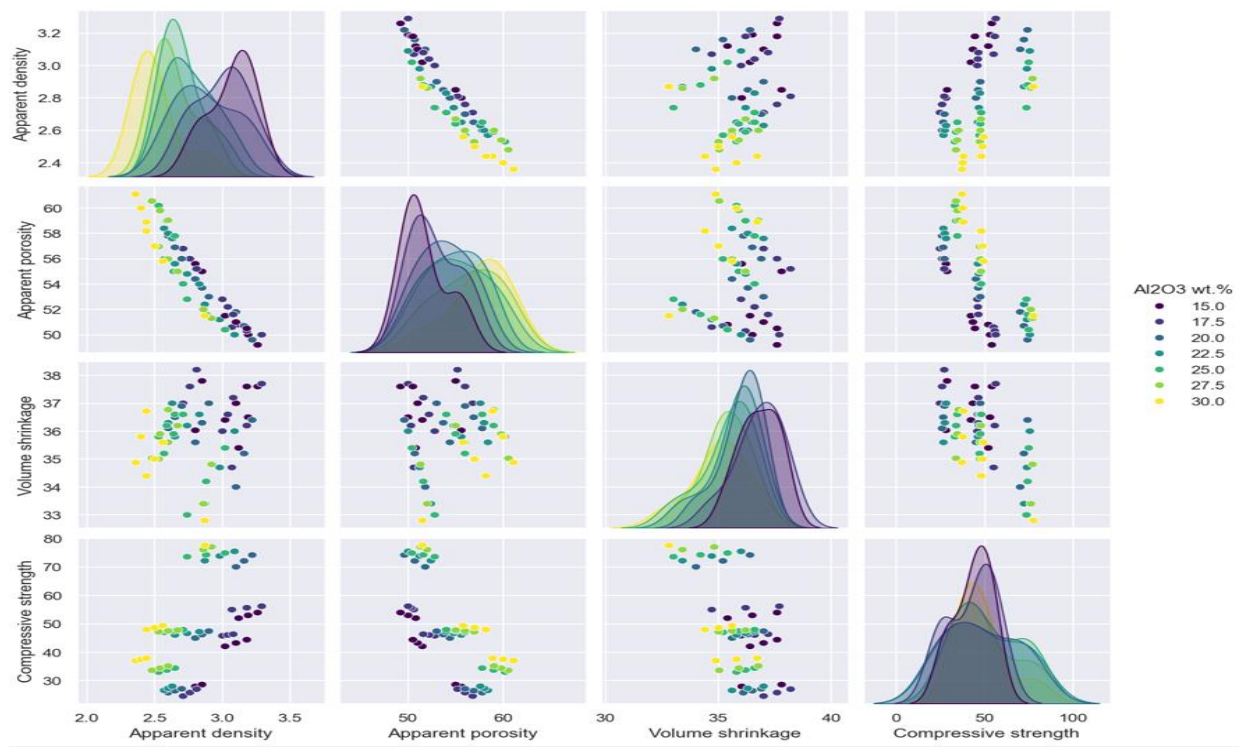


Fig. C3.1 Pair plot of four study features of samples prepared with different Al<sub>2</sub>O<sub>3</sub> wt.%

# Claim 4: Improvement of the pore size by utilizing 50:50 wt.% potato and tapioca starches together

I experimentally proved by using scanning electron microscopy (Fig. C4.1) and mercury intrusion porosimetry (Fig. C4.2) methods that using a combined starch composition (50:50 wt.% potato with tapioca starches together), as a body and pore forming agent, produces larger pore diameters (exceeding 200 μm) with larger pore openings in the produced bone replacement porous m-ZrO<sub>2</sub>-Al<sub>2</sub>O<sub>3</sub>-MgO ceramics compared to those made with individual starch types. The enlarged pores result from the interaction of the two starches, facilitating the development of larger and more interconnected pores.

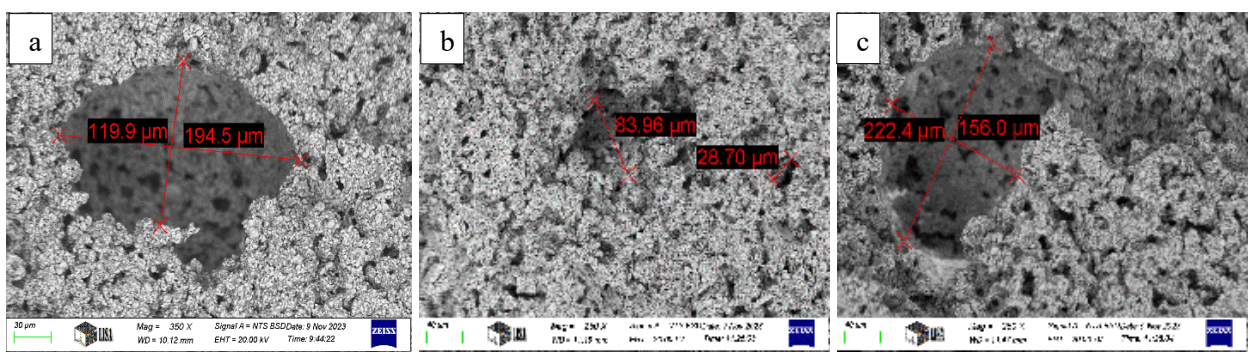


Fig. C4.1 SEM micrographs of porous ceramics (67.5 wt.% ZrO<sub>2</sub>, 2.5 wt.% MgO, and 30 wt.% Al<sub>2</sub>O<sub>3</sub>) after sintering, (a) using potato starch, (b) using tapioca starch, and (c) using 50:50 wt.% tapioca + potato

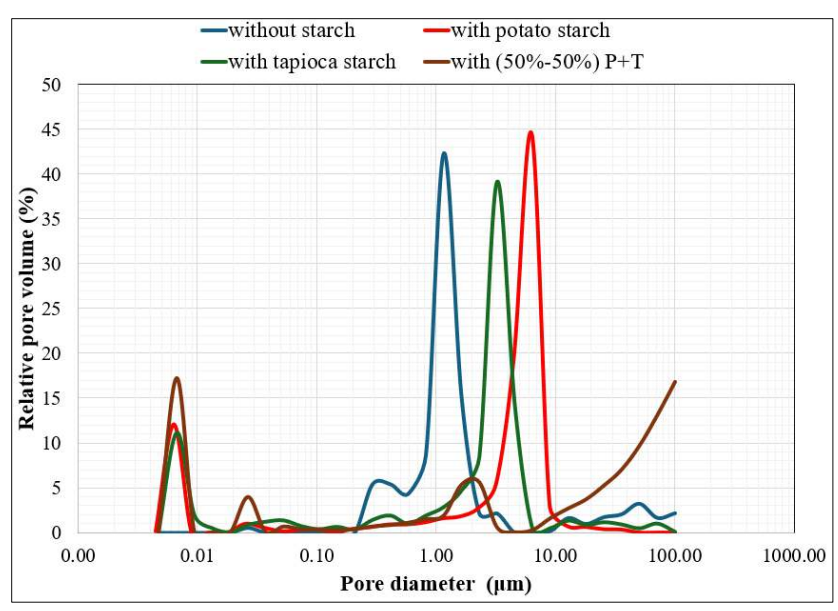
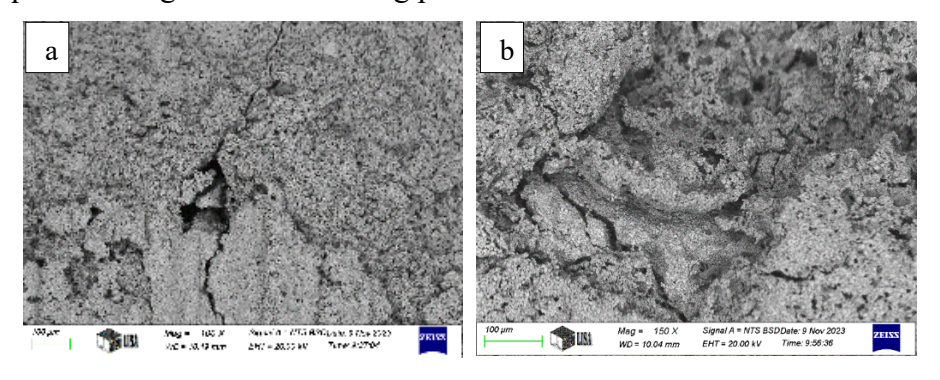


Fig. C4.2 The pore size distribution via relative pore volume

<u>Related publication:</u> **Rusul Ahmed Shakir**, Róbert Géber, Marwan T. Mezher, Tomasz Trzepiecinski, Ferenc Móricz. (2024). Effect of Alumina Proportion on the Microstructure and Technical and Mechanical Characteristics of Zirconia-Based Porous Ceramics. Journal of Composites Science. 517. https://doi.org/10.3390/jcs8120517 **(Q1)** 

# Claim 5: Progressive pre-sintering reduces the rate of shrinkage and mitigate thermal stresses.

**A.** I established by using scanning electron microscopy (Fig. C5.1) that the pre-sintering process (at 500°C for 1 hour and then at 1100°C for 2 hours with a heating rate of 2 °C/min) of the prepared bone replacement porous (m-ZrO<sub>2</sub>-Al<sub>2</sub>O<sub>3</sub>-MgO) ceramic composites decreases the rate of shrinkage during the final sintering process and mitigates the thermal stresses that cause the surface cracking. The reduction occurred by allowing a fraction of densification and particle rearrangement to take place during the pre-sintering stage, which minimises the additional shrinkage required during the final sintering process.



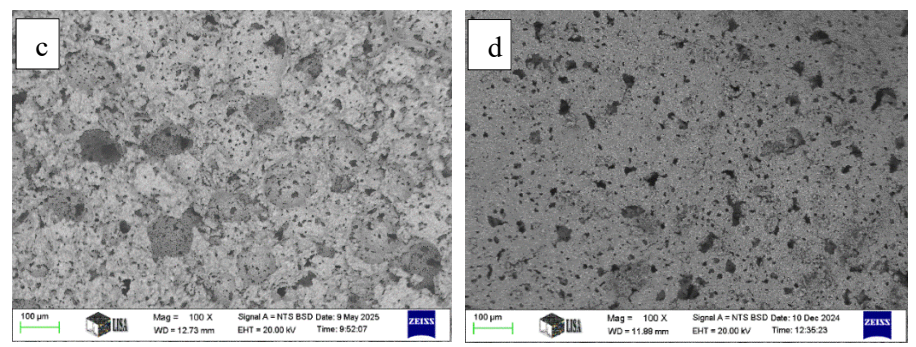


**Fig. C5.1** SEM micrographs of sintered porous ceramics (67.5 wt.% m-ZrO<sub>2</sub>, 2.5 wt.% MgO, and 30 wt.% Al<sub>2</sub>O<sub>3</sub>): (a) and (b) without pre-sintering, (c) and (d) with pre-sintering

<u>Related publication:</u> **Rusul Ahmed Shakir**, Róbert Géber, Marwan T. Mezher, Tomasz Trzepiecinski, Ferenc Móricz. (2024). Effect of Alumina Proportion on the Microstructure and Technical and Mechanical Characteristics of Zirconia-Based Porous Ceramics. Journal of Composites Science. 517. https://doi.org/10.3390/jcs8120517 (Q1)

**B.** I established that the changes in the sintering parameters resulted in an increase of the compressive strength of the prepared bone replacement ceramic composites. The samples (77.5 wt.% m-ZrO<sub>2</sub> - 20 wt.% Al<sub>2</sub>O<sub>3</sub> - 2.5 wt.% MgO) that pre-sintered (at 500°C for 1 hour and then at 1100°C for 2 hours with a heating rate of 2 °C/min) and then sintered (at 300°C and 500°C for 1 hour and then at 1600°C for 2 hours with a heating rate of 2 °C/min) have higher compressive strength (72.12 MPa with using 20 wt.% tapioca starch and 26.48 MPa with using 20 wt.% potato starch) as compared with the samples (with the same composition) that sintered without presintering process (10.62 MPa with using 20 wt.% tapioca starch and 4.9 MPa with using 20 wt.% potato starch as shown in Fig. C5.2).

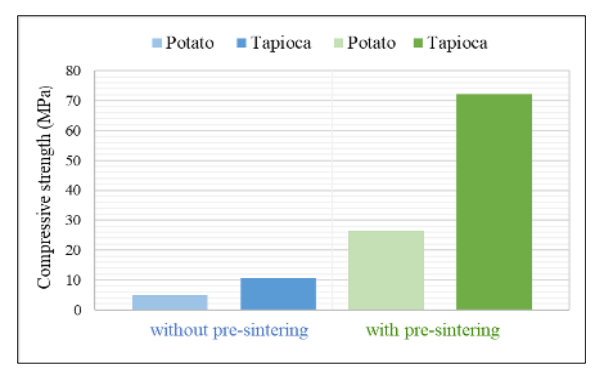


Fig. C5.2 Compressive strength of the samples

#### Related publications:

- 1. Rusul Ahmed Shakir, Róbert Géber, Marwan T. Mezher, Tomasz Trzepiecinski, Ferenc Móricz. (2024). Effect of Alumina Proportion on the Microstructure and Technical and Mechanical Characteristics of Zirconia-Based Porous Ceramics. Journal of Composites Science. 517. https://doi.org/10.3390/jcs8120517 (Q1)
- 2. Rusul Ahmed Shakir, Róbert Géber. (2023). Structure and properties of ZrO<sub>2</sub>-Al<sub>2</sub>O<sub>3</sub>-MgO porous ceramic for biomedical applications. Results in Engineering. 18, 101104. https://doi.org/10.1016/j.rineng.2023.101104 (Q1)

# Claim 6: Impact of sintering temperature on the pore morphology and the properties of the produced porous ceramics.

**A.** I have experimentally proved that the prepared bone replacement porous m-ZrO<sub>2</sub>-Al<sub>2</sub>O<sub>3</sub>-MgO ceramics that pre-sintered (at 500°C for 1 hour and then at 1100°C for 2 hours with a heating rate of 2 °C/min) and then sintered (at 300°C and 500°C for 1 hour and then at 1600°C for 2 hours with a heating rate of 2 °C/min) exhibit larger pores and a more uniform pore morphology as compared with the samples that progressively pre-sintered (at 500°C for 1 hour and then at 1100°C for 2 hours with a heating rate of 2 °C/min) and then sintered (at 300°C and 500°C for 1 hour and then at 1400°C or 1500°C for 2 hours with a heating rate of 2 °C/min) (Fig. C6.1).

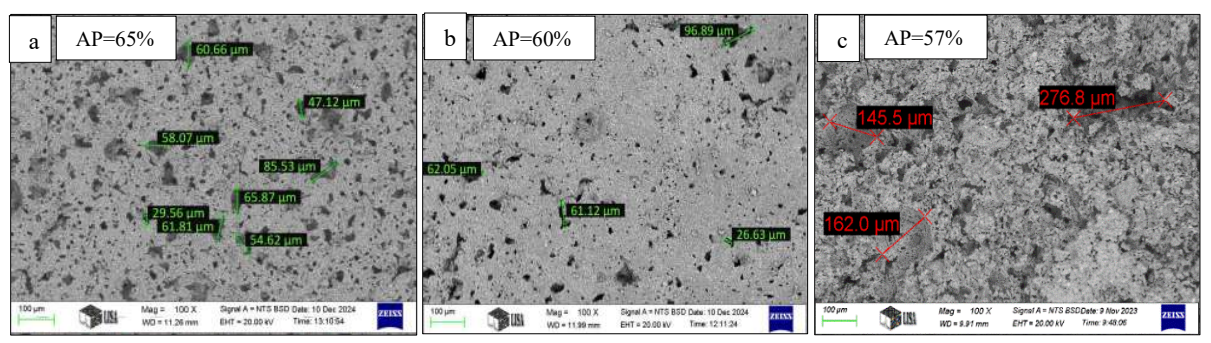
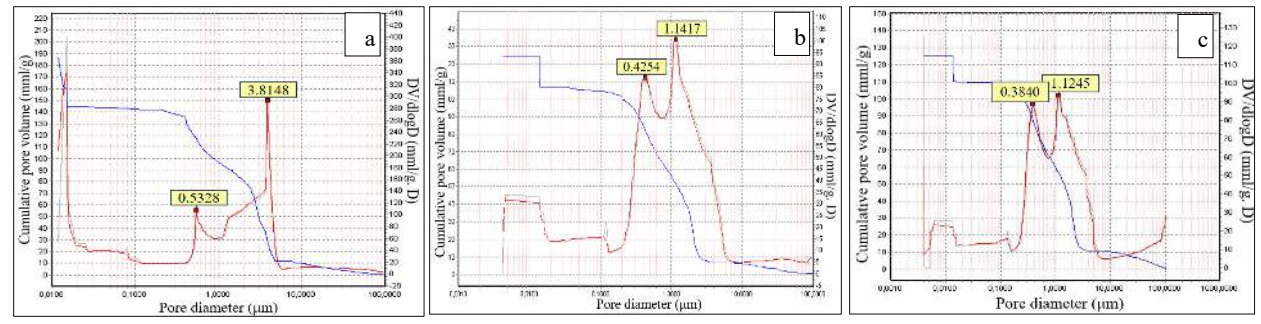


Fig. C6.1 SEM micrographs for porous ceramics (67.5 wt.% m-ZrO<sub>2</sub>, 2.5 wt.% MgO, and 30 wt.% Al<sub>2</sub>O<sub>3</sub>) sintered at: 1400°C (a), 1500°C (b), and 1600°C (c), where AP: apparent porosity

<u>Related publication:</u> **Rusul Ahmed Shakir**, Róbert Géber, Marwan T. Mezher, Tomasz Trzepieciński. (2025). Exploring influence of sintering temperature on the structure and technical characteristics of ATZ ceramic composites. Results in Engineering. Volume 28, 107139. https://doi.org/10.1016/j.rineng.2025.107139 (Q1)

**B.** Using mercury intrusion porosimetry, I have experimentally demonstrated that when the sintering temperature rises (from 1400 to 1600°C), the size of the pore openings (the pore throat) of bone replacement porous ceramic composite (67.5 wt.% m-ZrO<sub>2</sub>, 2.5 wt.% MgO, and 30 wt.% Al<sub>2</sub>O<sub>3</sub>) diminishes (median pore openings size ~1.12 μm after sintering at 1400°C for 2 hours and ~0.77 μm after sintering at 1600°C for 2 hours) (Fig. C6.2).



**Fig. C6.2** Pore size distribution of porous ceramics (67.5 wt.% m-ZrO<sub>2</sub>, 2.5 wt.% MgO, and 30 wt.% Al<sub>2</sub>O<sub>3</sub>) sintered at: 1400°C (a), 1500°C (b), and 1600°C (c)

<u>Related publication:</u> **Rusul Ahmed Shakir**, Róbert Géber, Marwan T. Mezher, Tomasz Trzepieciński. (2025). Exploring influence of sintering temperature on the structure and technical characteristics of ATZ ceramic composites. Results in Engineering. Volume 28, 107139. https://doi.org/10.1016/j.rineng.2025.107139 (Q1)

C. I have statistically determined the Pearson correlation matrix (Table C6.1) of the experimental data to analyse the correlation between the sintering temperatures and the properties of the prepared bone replacement porous m-ZrO<sub>2</sub>-Al<sub>2</sub>O<sub>3</sub>-MgO ceramic. To comprehensively visualize the variables interactions, pair plots (Figs. C6.3, for the samples after sintering at 1400°C or 1500°C, and C6.4, for the samples after sintering at 1600°C) (Table C6.2) of four research parameters (apparent density, apparent porosity, volume shrinkage, and compressive strength) were employed using Seaborn library in Python.

**Table C6.1** The Pearson correlation matrix of the experimental data.

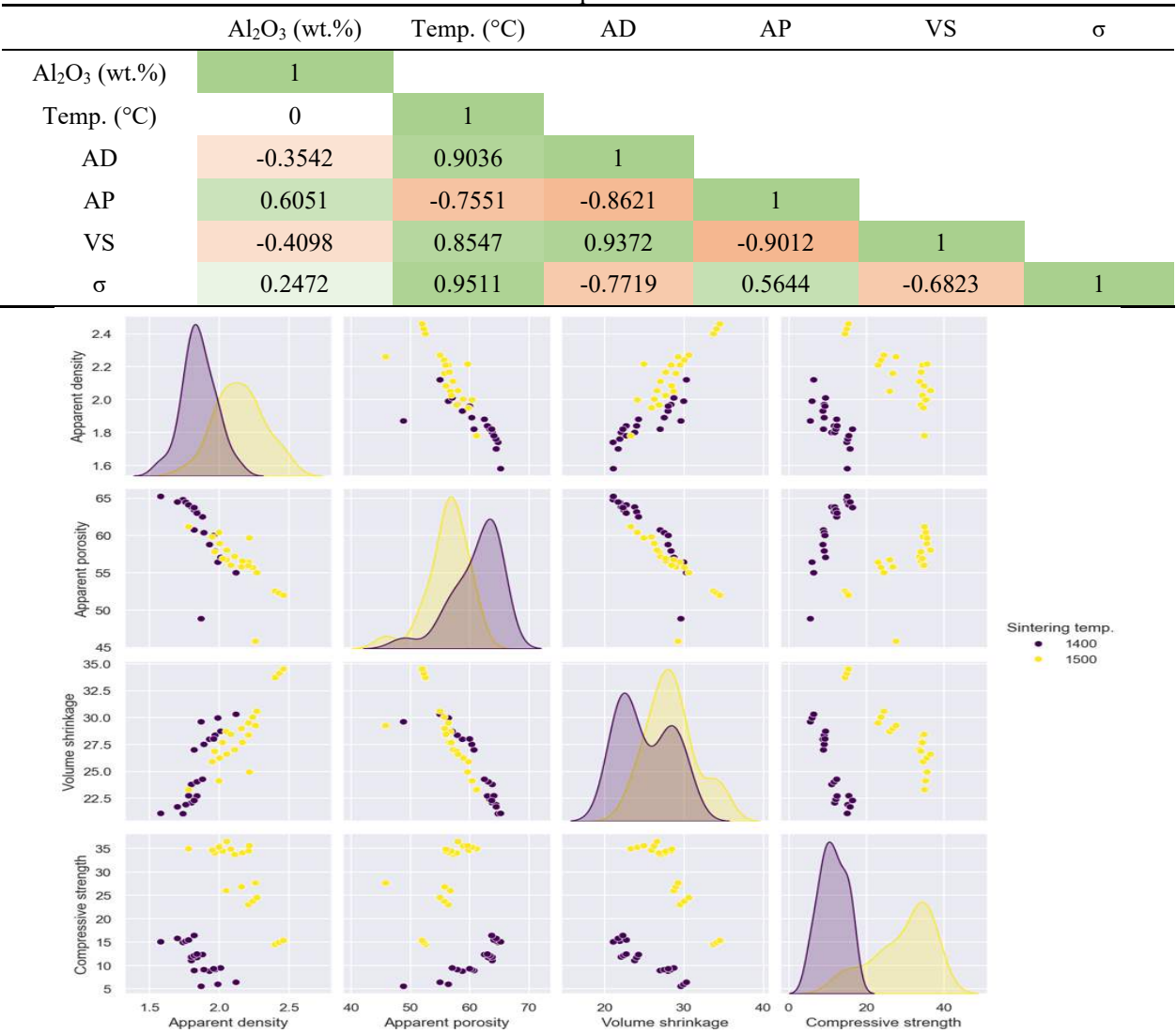


Fig. C6.3 Pair plot of four study features for the samples after sintering at 1400°C or 1500°C

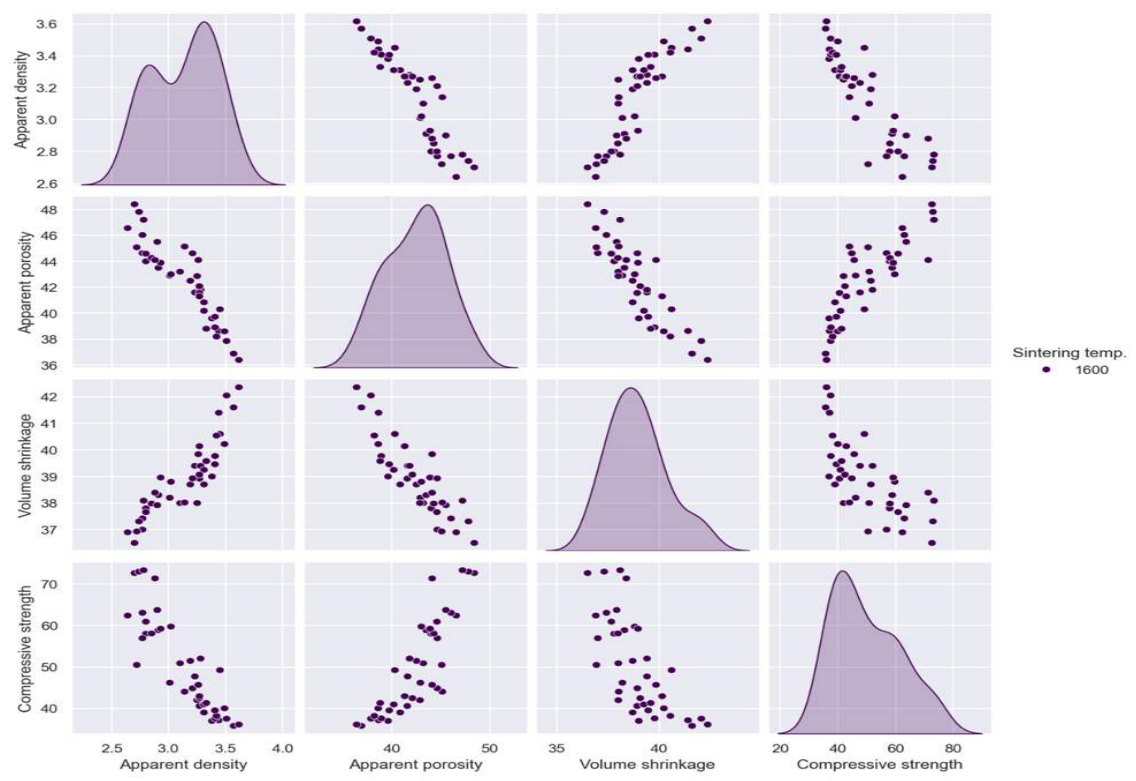


Fig. C6.4 Pair plot of four study features for the samples after sintering at 1600°C

**Table C6.2** Correlation relationships between the variables after sintering at different temperature

Variables	AD	AP	VS	σ
AD	_	Negative	Positive	Negative
AP	Negative	_	Negative	Positive
VS	Positive	Negative	_	Negative
σ	Negative	Positive	Negative	_

## Claim 7: Establishment of MgAl<sub>2</sub>O<sub>4</sub> spinel structure under specific sintering conditions

I have experimentally proved by using X-ray diffraction method that the production of the MgAl<sub>2</sub>O<sub>4</sub> phase inside the developed bone replacement porous structured ZrO<sub>2</sub>-Al<sub>2</sub>O<sub>3</sub>-MgO ceramic system (67.5 wt.% m-ZrO<sub>2</sub>, 2.5 wt.% MgO, and 30 wt.% Al<sub>2</sub>O<sub>3</sub>) occurred only under the following sintering conditions: after 1400°C or 1500°C sintering temperature for 2 hours sintering time with 2 °C/min heating rate (Fig. C7.1), and after 1600°C sintering temperature only after an extended sintering time of 3 hours with 2 °C/min heating rate (Fig. C7.2).

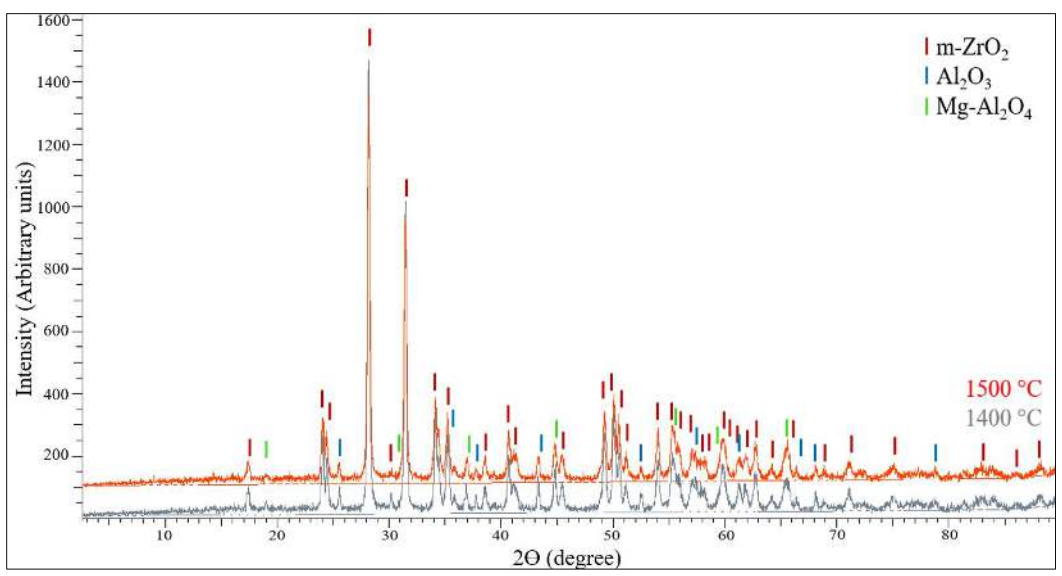


Fig. C7.1 XRD pattern after sintering at 1400°C or 1500°C for 2 hours (67.5 wt.% m-ZrO<sub>2</sub>, 2.5 wt.% MgO, and 30 wt.% Al<sub>2</sub>O<sub>3</sub>)

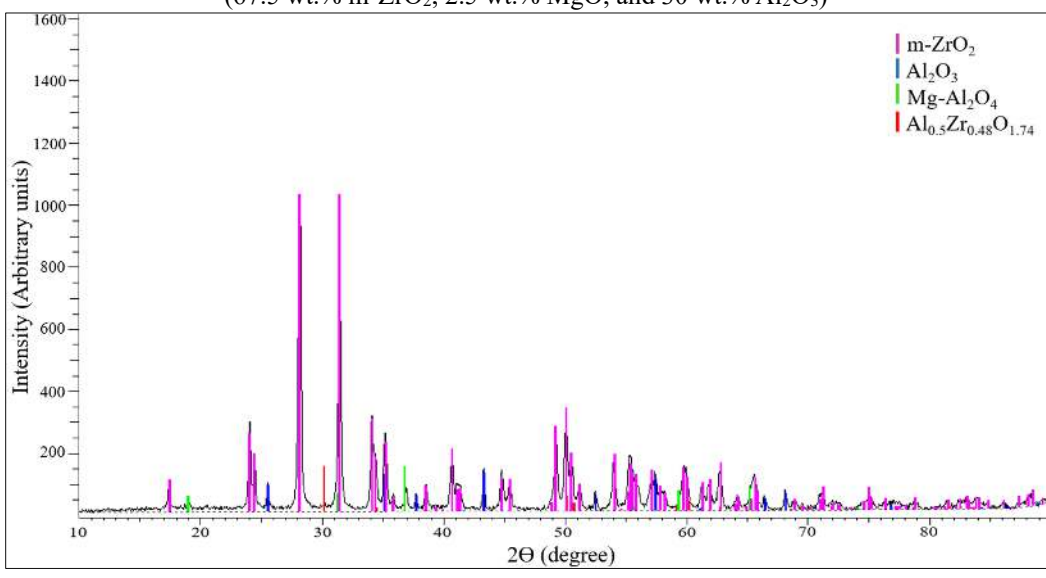


Fig. C7.2 XRD pattern after sintering at 1600°C for 3 hours (67.5 wt.% m-ZrO<sub>2</sub>, 2.5 wt.% MgO, and 30 wt.% Al<sub>2</sub>O<sub>3</sub>)

<u>Related publication:</u> **Rusul Ahmed Shakir**, Róbert Géber, Marwan T. Mezher, Tomasz Trzepieciński. (2025). Exploring influence of sintering temperature on the structure and technical characteristics of ATZ ceramic composites. Results in Engineering. Volume 28, 107139. https://doi.org/10.1016/j.rineng.2025.107139 (Q1)

# Claim 8: Impact of sintering holding time on the microstructural characteristics of the produced porous ceramics.

**A.** I established that increasing sintering holding time (from 2 to 3 or 4 hours) affects the properties of the bone replacement porous structured ZrO<sub>2</sub>-Al<sub>2</sub>O<sub>3</sub>-MgO ceramics. Shorter sintering holding time (2 hours) results in lower apparent density (2.5 - 3.1 g/cm<sup>3</sup>), higher apparent porosity

(51-57 %), whereas extended sintering holding time (3 or 4 hours) results in higher apparent density (2.7 - 3.2 g/cm<sup>3</sup> after 3 hours and 3.2 - 3.6 g/cm<sup>3</sup> after 4 hours), lower apparent porosity (42 - 49 % after 3 hours and 36 - 45 % after 4 hours) (Fig. C8. 1).

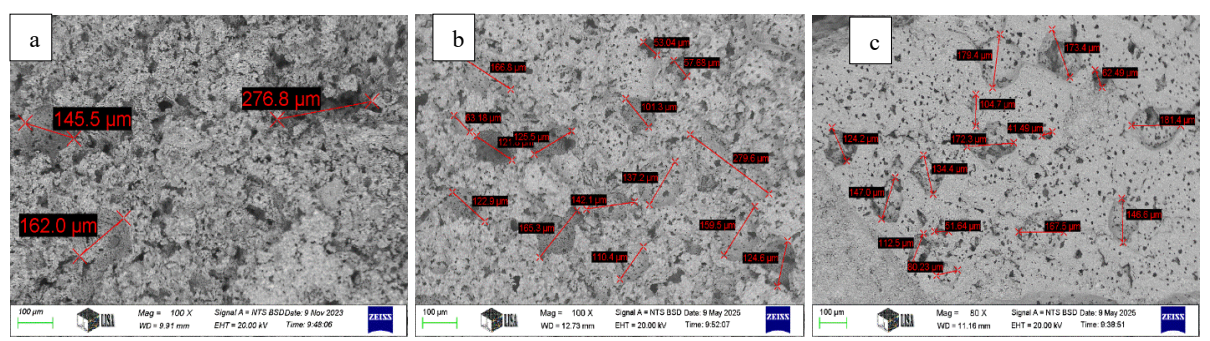


**Fig. C8. 1** SEM micrographs for porous ceramics (67.5 wt.% m-ZrO<sub>2</sub>, 2.5 wt.% MgO, and 30 wt.% Al<sub>2</sub>O<sub>3</sub>) sintered at 1600°C for: 2 hours (a), 3 hours (b), and 4 hours (c)

**B.** I established that among the three-sintering holding time (2, 3 or 4 hours), the porous ceramics (Table C8.1) sintered at 1600°C for 3 hours demonstrated the highest compressive strength (48 - 73 MPa), indicating that this holding time (3 hours) facilitates densification without excessive grain growth or pore coarsening. As a comparison with 3 hours sintering time, the shorter sintering holding time (2 hours) results in reduced apparent density (2.5 - 3.1 g/cm³) and higher apparent porosity (51 -57 %), tend to be reduced compressive strength (43 - 49 MPa). Whereas extended sintering holding time to 4 hours resulted in reduced compressive strength (36 - 45 MPa) relative to 2 or 3 hours, due to the initiation of microstructural deterioration (Fig. C8.2).

**Table C8.1** Mix compositions (in wt.%)

m-ZrO <sub>2</sub>	MgO	Al <sub>2</sub> O <sub>3</sub>	Dolapix CE 64	50:50 P+T	Suspension Conc.
82.5	2.5	15	1.5	20	60
80	2.5	17.5	1.5	20	60
77.5	2.5	20	1.5	20	60
75	2.5	22.5	1.5	20	60
72.5	2.5	25	1.5	20	60
70	2.5	27.5	1.5	20	60
67.5	2.5	30	1.5	20	60

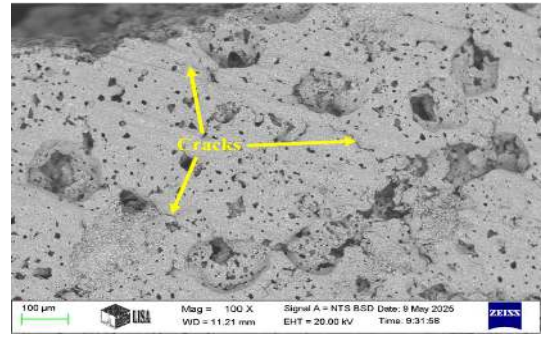


Fig. C8.2 Sample (67.5 wt.% m-ZrO<sub>2</sub>, 2.5 wt.% MgO, and 30 wt.% Al<sub>2</sub>O<sub>3</sub>) after 4 hours sintering time

C. I have statistically determined the Pearson correlation matrix (Table C8.2) of the experimental data to determine the correlation between the sintering holding times and the properties of the prepared bone replacement (ZrO<sub>2</sub>-Al<sub>2</sub>O<sub>3</sub>-MgO) porous ceramics. To comprehensively visualize the variables interactions, pair plots (Figs. C8.3, for sintered samples after 2 hours sintering holding time) and C8.4 (for sintered samples after 3 hours or 4 hours sintering holding time) (Table C8.3) of four research parameters (apparent density, apparent porosity, volume shrinkage, and compressive strength) were used employing Seaborn library in Python.

**Tables C8.2** The Pearson correlation matrix of the experimental data.

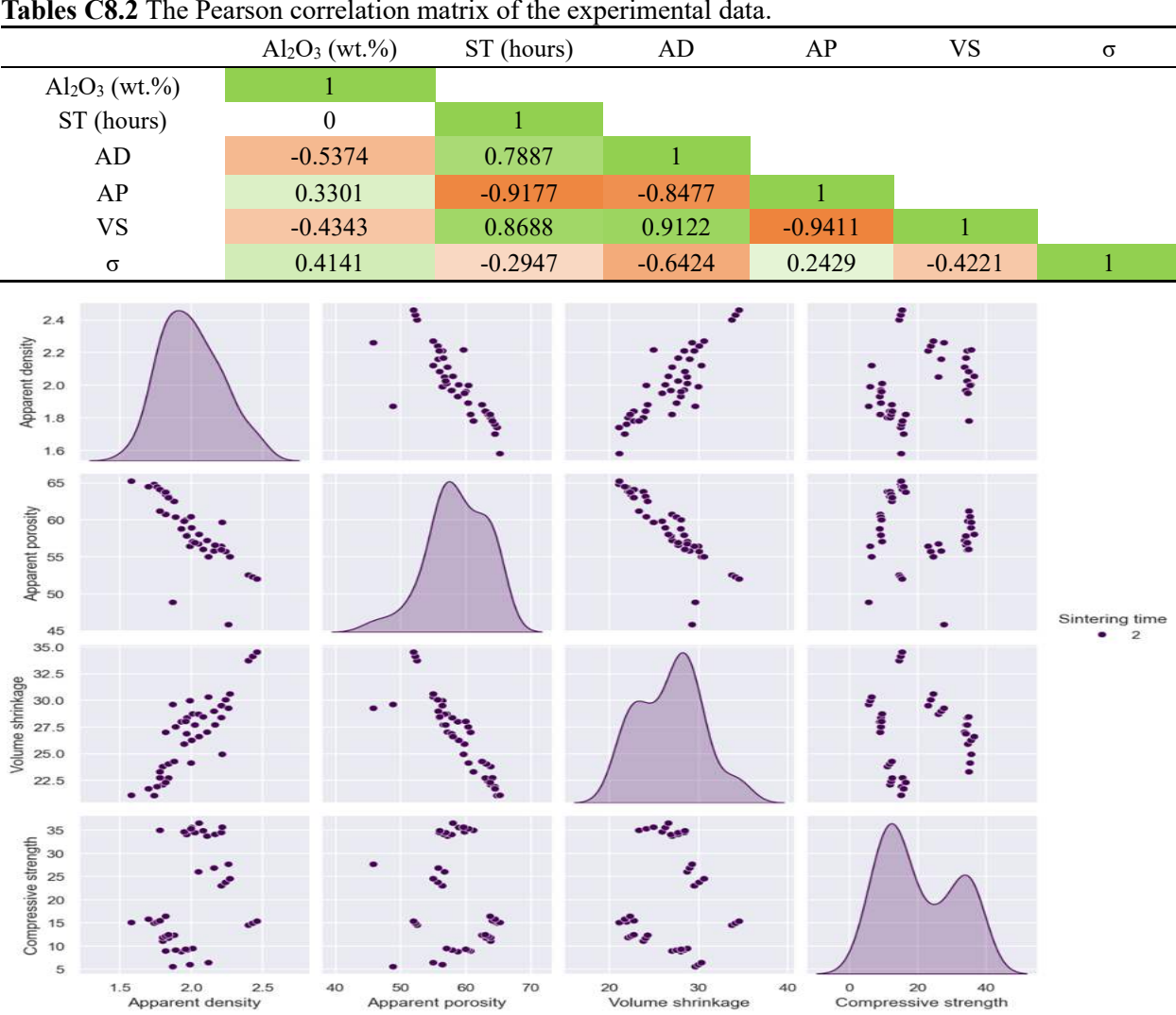


Fig. C8.3 Pair plot of four study features for the samples after 2 hours sintering holding time

Table C8.3 Correlation relationships between the variables after sintering for different holding time

Variables	AD	AP	VS	σ
AD	_	Negative	Positive	Negative
AP	Negative	_	Negative	Positive
VS	Positive	Negative	_	Negative
σ	Negative	Positive	Negative	ı

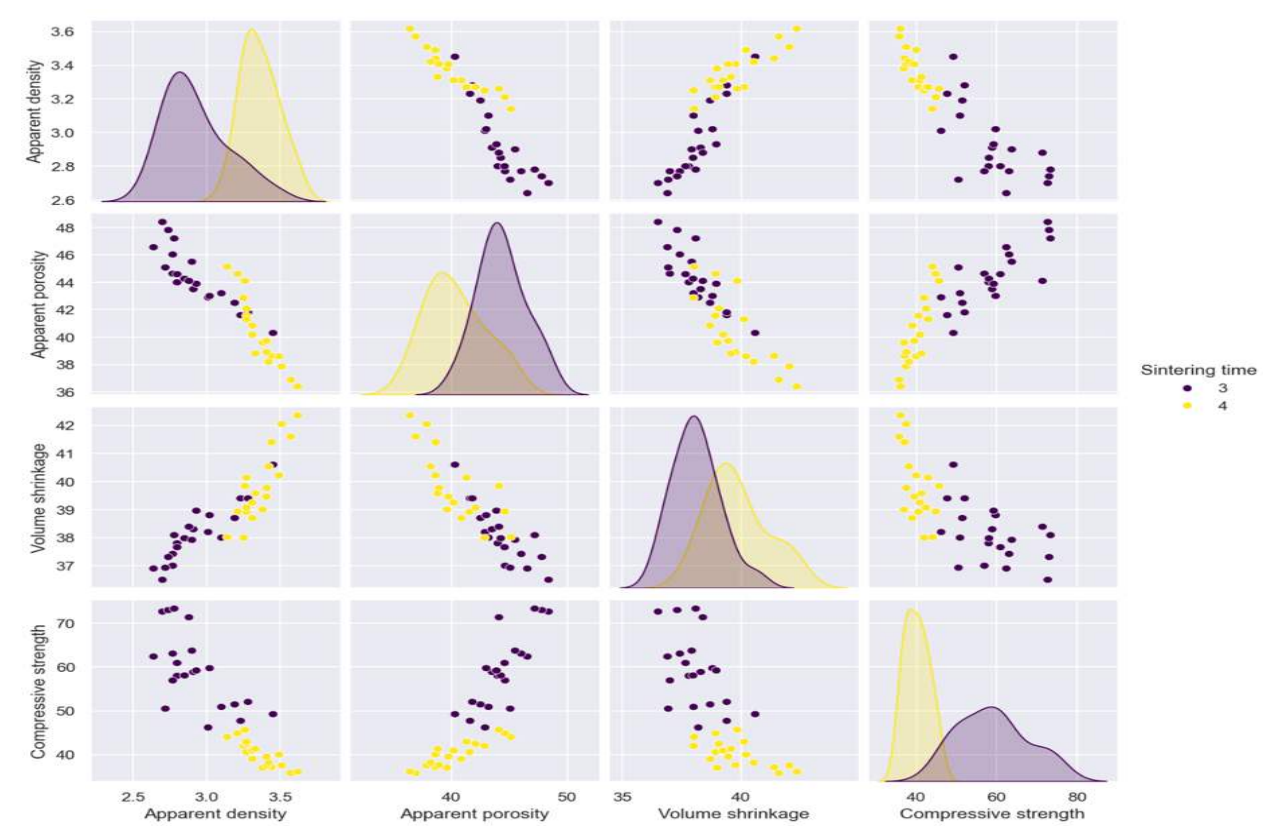


Fig. C8.4 Pair plot of four study features for the samples after 3 hours or 4 hours sintering holding time

# Claim 9: Impact of sintering holding time on the interaction between zirconia and alumina phases.

I have experimentally proved by using X-ray diffraction method that the increasing of sintering holding time (from 2 hours to 3 hours) influences the phase evolution in the 67.5 wt.% m-ZrO<sub>2</sub>, 2.5 wt.% MgO, and 30 wt.% Al<sub>2</sub>O<sub>3</sub> system. The prolonged sintering holding time (3 hours) promotes diffusion-driven solid-state reactions that result in the formation of MgAl<sub>2</sub>O<sub>4</sub> spinel and Al<sub>0.5</sub>Zr<sub>0.48</sub>O<sub>1.74</sub> phases (Fig. C9).

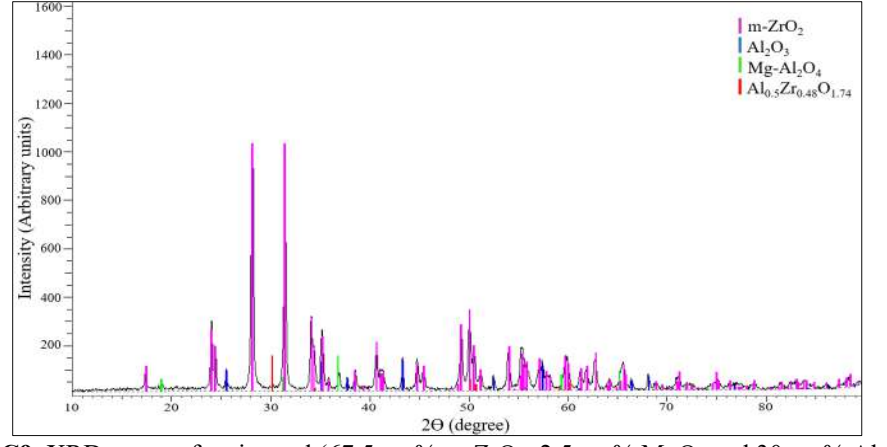


Fig. C9. XRD pattern for sintered (67.5 wt.% m-ZrO<sub>2</sub>, 2.5 wt.% MgO, and 30 wt.% Al<sub>2</sub>O<sub>3</sub>)

#### Claim 10: Impact of sintering holding time on the pore openings size distribution.

I have experimentally proved by using mercury intrusion porosimetry test that the cumulative pore volumes (Fig. C10) of the bone replacement porous ceramics (67.5 wt.% m-ZrO<sub>2</sub>, 2.5 wt.% MgO, and 30 wt.% Al<sub>2</sub>O<sub>3</sub>, sintered at 1600°C for various sintering holding time) decrease as sintering holding time increases (from 2 to 4 hours).

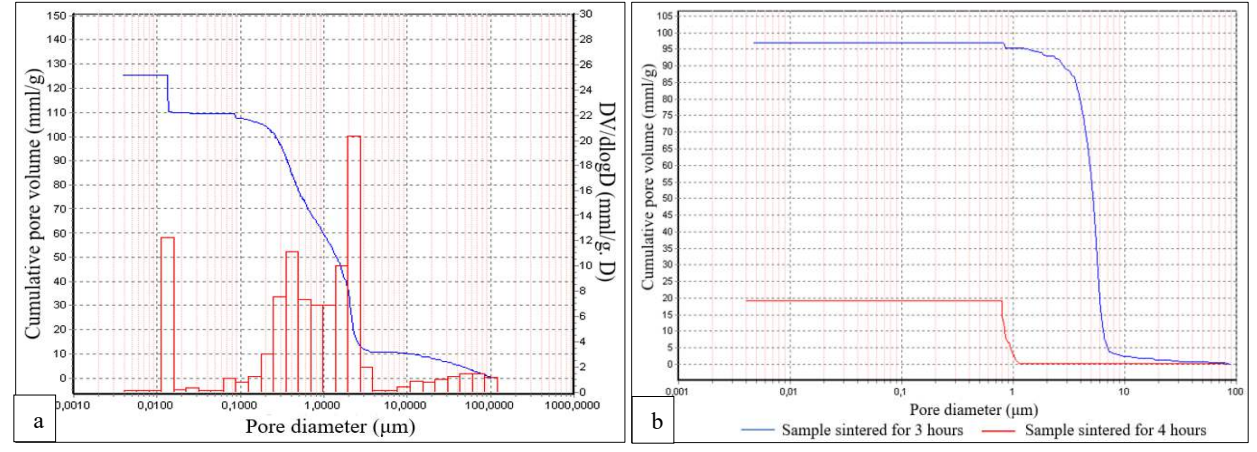


Fig. C10. The cumulative pore size distribution of sample: (a) sintered for 2 hours, (b) sintered for 3 or 4 hours

#### **List of Publications**

#### **International Journal articles**

- Rusul Ahmed Shakir, Róbert Géber, Marwan T. Mezher, Tomasz Trzepieciński. (2025).
   Exploring influence of sintering temperature on the structure and technical characteristics of ATZ ceramic composites. Results in Engineering. Volume 28, 107139.

   <a href="https://doi.org/10.1016/j.rineng.2025.107139">https://doi.org/10.1016/j.rineng.2025.107139</a> (Q1)
- Rusul Ahmed Shakir, Róbert Géber, Marwan T. Mezher, Tomasz Trzepiecinski, Ferenc Móricz. (2024). Effect of Alumina Proportion on the Microstructure and Technical and Mechanical Characteristics of Zirconia-Based Porous Ceramics. Journal of Composites Science. 517. <a href="https://doi.org/10.3390/jcs8120517">https://doi.org/10.3390/jcs8120517</a> (Q1)
- 3. **Rusul Ahmed Shakir**, Róbert Géber. (2023). Structure and properties of ZrO<sub>2</sub>-Al<sub>2</sub>O<sub>3</sub>-MgO porous ceramic for biomedical applications. Results in Engineering. 18, 101104. <a href="https://doi.org/10.1016/j.rineng.2023.101104">https://doi.org/10.1016/j.rineng.2023.101104</a> (Q1)
- 4. **Rusul Ahmed Shakir**, Róbert Géber. (2025). ZIRCONIA-ALUMINA CERAMICS: A STUDY OF THEIR PROPERTIES. POLLACK PERIODICA, An International Journal for Engineering and Information Sciences. DOI: 10.1556/606.2025.01253 (Q3)

5. **Rusul Ahmed Shakir**, Róbert Géber. (2024). POROSITY AND PORE MORPHOLOGY CHARACTERISTICS OF ZIRCONIA-ALUMINA BIOCERAMICS. POLLACK PERIODICA, An International Journal for Engineering and Information Sciences. 19, 3, 107 - 114. DOI:10.1556/606.2024.01099 (Q3)

# Paper published in conference proceeding:

Rusul Ahmed Shakir, Róbert Géber. (2022). STARCH CONSOLIDATION CASTING METHOD FOR PREPARATION OF ZrO<sub>2</sub>-Al<sub>2</sub>O<sub>3</sub>-MgO POROUS STRUCTURE.
 Multidiszciplináris tudományok. 12. kötet. (2022) 4 sz. pp. 232-241. https://doi.org/10.35925/j.multi.2022.4.25

#### Papers published in Almanach:

- 1. **Rusul Ahmed Shakir.** (2024). Exploring the behaviour of starch swelling in starch consolidation casting method for the production of porous structured ceramics. Almanach 2024-1.kötet/1.volume. 125. ISSN 2939-7294
- 2. **Rusul Ahmed Shakir.** (2023). Preparation of ZrO<sub>2</sub> based porous composite using potato starch as a pore- and body-forming agents. Almanach. 2023-1.kötet/1.volume. 8. ISSN 2939-7294.
- 3. **Rusul Ahmed Shakir**. (2022). Preparation of ZrO<sub>2</sub>-Based Porous Structure via the Utilization of Starch as a Pore-Forming Agent. Almanach. 2022-1.kötet/1.volume. 51. ISSN 2939-7294.

#### **Conference presentations**

- Rusul Ahmed Shakir. (2024) Structure and Characteristics of Porous Ceramic Composites
  Based on ZrO<sub>2</sub>. Oral presentation. MAGYAR TUDOMÁNY ÜNNEPE, "KERÁMIA- ÉS
  SZILIKÁTIPARI KUTATÁSOK A MISKOLCI EGYETEMEN". Hungary, 2024
  November 5<sup>th</sup>.
- 2. **Rusul Ahmed Shakir.** (2023) Structure and Properties of ZrO<sub>2</sub>-Al<sub>2</sub>O<sub>3</sub>-MgO Porous Ceramics for Biomedical Applications. Oral presentation. A MAGYAR TUDOMÁNYOS AKADÉMIA, MAGYAR TUDOMÁNY ÜNNEPE, "KERÁMIA- ÉS SZILIKÁTIPARI KUTATÁSOK A MISKOLCI EGYETEMEN". Hungary, 2023 November 8<sup>th</sup>.

### Other publications

1. M.T. Mezher, A. Pereira, **Rusul Ahmed Shakir**, T. Trzepieciński. (2024). Application of machine learning and neural network models based on experimental evaluation of

dissimilar resistance spot-welded joints between grade 2 titanium alloy and AISI 304 stainless steel. Heliyon, 10(24), e40898.

doi: https://doi.org/10.1016/j.heliyon.2024.e40898 (Q1)

- 2. M.T. Mezher & **Rusul Ahmed Shakir**. (2023). Modelling and evaluation of the post-hardness and forming limit diagram in the single point incremental hole flanging (SPIHF) process using ANN, FEM and experimental. Results in Engineering, 20, 101613. doi: <a href="https://doi.org/10.1016/j.rineng.2023.101613">https://doi.org/10.1016/j.rineng.2023.101613</a> (Q1)
- 3. O.S. Barrak, O.F. Taresh, M.M. Hamzah, & **Rusul Ahmed Shakir**. (2023). An investigation of joining polyamide (PA) to stainless steel AISI 316L by hot press process. Journal of Techniques, 5(1), 114–121. doi: https://doi.org/10.51173/jt.v5i1.1280
- 4. **Rusul Ahmed Shakir**, M.T. Mezher, & R. Geber. (2022). Synthesis and characterization of erbium doped lead zirconate titanate thin films. Revue Des Composites Et Des Matériaux Avancés, 32(3), 111–116. doi: <a href="https://doi.org/10.18280/rcma.320301">https://doi.org/10.18280/rcma.320301</a> (Q3)
- M.T. Mezher, S.M. Khazaal, Rusul Ahmed Shakir, N.S.M. Namer. (2021). A comparative analysis study of hole flanging by incremental sheet forming process of AA1060 and DC01 sheet metals. Journal of Engineering Science and Technology, 16(6), pp. 4383–4403. (Q2).

#### References

[1] P. F. Manicone, P. Rossi Iommetti, and L. Raffaelli, "An overview of zirconia ceramics: Basic properties and clinical applications" *Journal of Dentistry*, vol. 35, no. 11, pp. 819–826, Nov. 2007. https://doi.org/10.1016/j.jdent.2007.07.008

[2] Y Y.-W. Chen, J. Moussi, J. L. Drury, and J. C. Wataha, "Zirconia in biomedical applications" *Expert Review of Medical Devices*, vol. 13, no. 10, pp. 945–963, Sep. 2016.

https://doi.org/10.1080/17434440.2016.1230017

- [3] J. Kelly and I. Denry, "Stabilized zirconia as a structural ceramic: An overview" *Dental Materials*, vol. 24, no. 3, pp. 289–298, Mar. 2008. https://doi.org/10.1016/j.dental.2007.05.005
- [4] L. Keerthana, C. Sakthivel, and I. Prabha, "MgO-ZrO<sub>2</sub> mixed nanocomposites: fabrication methods and applications" *Materials Today Sustainability*, vol. 3–4, p. 100007, Mar. 2019.

#### https://doi.org/10.1016/j.mtsust.2019.100007

[5] A. Alagarsamy, S. Chandrasekaran, and A. Manikandan, "Green synthesis and characterization studies of biogenic zirconium oxide (ZrO<sub>2</sub>) nanoparticles for adsorptive removal of methylene blue dye" *Journal of Molecular Structure*, vol. 1247, p. 131275, Jan. 2022. <a href="https://doi.org/10.1016/j.molstruc.2021.131275">https://doi.org/10.1016/j.molstruc.2021.131275</a>

[6] P. Duran and C. Moure, "Sintering at near theoretical density and properties of PZT ceramics chemically prepared" *Journal of Materials Science*, vol. 20, no. 3, pp. 827–833, Mar. 1985.

### https://doi.org/10.1007/bf00585722

- [7] J. Chevalier and L. Gremillard, "Zirconia as a Biomaterial" Comprehensive Biomaterials II, pp. 122–144, 2017. https://doi.org/10.1016/b978-0-12-803581-8.10245-0
- [8] B. Nait-Ali, K. Haberko, H. Vesteghem, J. Absi, and D. S. Smith, "Thermal conductivity of highly porous zirconia" *Journal of the European Ceramic Society*, vol. 26, no. 16, pp. 3567–3574, Jan. 2006. https://doi.org/10.1016/j.jeurceramsoc.2005.11.011
- [9] M. P. Rigney, E. F. Funkenbusch, and P. W. Carr, "Physical and chemical characterization of microporous zirconia" *Journal of Chromatography A*, vol. 499, pp. 291–304, Jan. 1990. https://doi.org/10.1016/s0021-9673(00)96980-2
- [10] R. van Brakel, M. S. Cune, A. J. van Winkelhoff, C. de Putter, J. W. Verhoeven, and W. van der Reijden, "Early bacterial colonization and soft tissue health around zirconia and titanium abutments: an in vivo study in man" *Clinical Oral Implants Research*, vol. 22, no. 6, pp. 571–577, Nov. 2010.

#### https://doi.org/10.1111/j.1600-0501.2010.02005.x

- [11] E. Lucchini and S. Maschio, "Alumina Zirconia Ceramics: Preparation and Properties" Zirconia'88, pp. 161–170, 1989. https://doi.org/10.1007/978-94-009-1139-0\_15
- [12] J. Chevalier, L. Gremillard, and S. Deville, "Low-Temperature Degradation of Zirconia and Implications for Biomedical Implants" *Annual Review of Materials Research*, vol. 37, no. 1, pp. 1–32, Aug. 2007. <a href="https://doi.org/10.1146/annurev.matsci.37.052506.084250">https://doi.org/10.1146/annurev.matsci.37.052506.084250</a>
- [13] M. Inokoshi et al., "Influence of sintering conditions on low-temperature degradation of dental zirconia" *Dental Materials*, vol. 30, no. 6, pp. 669–678, Jun. 2014.

# https://doi.org/10.1016/j.dental.2014.03.005

[14] F. Mussano, T. Genova, L. Munaron, M. G. Faga, and S. Carossa, "Ceramic biomaterials for dental implants: current use and future perspectives" *Dental Implantology and Biomaterial*, Aug. 2016.

#### https://doi.org/10.5772/62701

- [15] E. de S. Lima, C. C. Gall, M. F. R. P. Alves, J. B. de Campos, T. M. B. Campos, and C. dos Santos, "Development and characterization of alumina-toughened zirconia (ATZ) ceramic composites doped with a beneficiated rare-earth oxide extracted from natural ore" *Journal of Materials Research and Technology*, vol. 16, pp. 451–460, Jan. 2022. https://doi.org/10.1016/j.jmrt.2021.11.141
- [16] A. Maji and G. Choubey, "Microstructure and Mechanical Properties of Alumina Toughened Zirconia (ATZ)" *Materials Today: Proceedings*, vol. 5, no. 2, pp. 7457–7465, 2018.

https://doi.org/10.1016/j.matpr.2017.11.417

- [17] C. Goswami, I. K. Bhat, S. Bathula, T. Singh, and A. Patnaik, "Physico-mechanical and surface wear assessment of magnesium oxide filled ceramic composites for hip implant application" *Silicon*, vol. 11, no. 1, pp. 39–49, May 2018. https://doi.org/10.1007/s12633-018-9880-6
- [18] A. Arab, Z. Sktani, Q. Zhou, Z. Ahmad, and P. Chen, "Effect of MgO addition on the mechanical and dynamic properties of zirconia toughened alumina (ZTA) ceramics" *Materials*, vol. 12, no. 15, p. 2440, Jul. 2019.

#### https://doi.org/10.3390/ma12152440

[19] C. W. Park and D. Y. Yoon, "Effects of SiO<sub>2</sub>, CaO<sub>2</sub>, and MgO Additions on the Grain Growth of Alumina" *Journal of the American Ceramic Society*, vol. 83, no. 10, pp. 2605–2609, Oct. 2000.

#### https://doi.org/10.1111/j.1151-2916.2000.tb01596.x

- [20] R. B. Tokas, S. Jena, and S. Thakur, "Indentation modulus and microstructural properties of Zirconia Alumina Magnesia composite thin films deposited by electron beam evaporation under varying oxygen pressure" *Thin Solid Films*, vol. 712, p. 138310, Oct. 2020. https://doi.org/10.1016/j.tsf.2020.138310
- [21] R. K, Y. S V, M. B S, Dr. S. V, and M. K, "Evaluation of thermo mechanical properties of zircon-alumina-magnesia composite in the field of refractory application" *International Journal of Scientific Research in Engineering and Management*, vol. 08, no. 12, pp. 1–9, Dec. 2024.

#### https://doi.org/10.55041/ijsrem40393

- [22] S. Kultayeva, Y.-W. Kim, and I.-H. Song, "Effects of dopants on electrical, thermal, and mechanical properties of porous SiC ceramics" *Journal of the European Ceramic Society*, vol. 41, no. 7, pp. 4006–4015, Jul. 2021. https://doi.org/10.1016/j.jeurceramsoc.2021.01.049
- [23] A. Chen, L. Li, C. Wang, and Q. Wang, "Novel porous ceramic with high strength and thermal performance using MA hollow spheres" *Progress in Natural Science: Materials International*, vol. 32, no. 6, pp. 732–738, Dec. 2022. https://doi.org/10.1016/j.pnsc.2022.09.015
- [24] J. Lou, C. He, A. Shui, and H. Yu, "Enhanced sound absorption performance of porous ceramics with closed-pore structure" *Ceramics International*, vol. 49, no. 23, pp. 38103–38114, Dec. 2023.

#### https://doi.org/10.1016/j.ceramint.2023.09.140

[25] Y. Zhang et al., "High-strength thermal insulating mullite nanofibrous porous ceramics" *Journal of the European Ceramic Society*, vol. 40, no. 5, pp. 2090–2096, May 2020.

#### https://doi.org/10.1016/j.jeurceramsoc.2020.01.011

- [26] M. W. Qin, C. Peng, M. Lv, and J. Wu, "Preparation and properties of high-purity porous alumina support at low sintering temperature" *Ceramics International*, vol. 40, no. 8, pp. 13741–13746, Sep. 2014. https://doi.org/10.1016/j.ceramint.2014.05.044
- [27] A. Uthaman, H. M. Lal, and S. Thomas, "Porous Ceramic Properties and Its Different Fabrication Process" *Advanced Functional Porous Materials*, pp. 475–497, Nov. 2021.

#### https://doi.org/10.1007/978-3-030-85397-6 16

[28] X. Xu, X. Liu, J. Wu, C. Zhang, S. Zhou, and C. Wu, "Fabrication and characterization of porous mullite ceramics with ultra-low shrinkage and high porosity via sol-gel and solid state reaction methods" *Ceramics International*, vol. 47, no. 14, pp. 20141–20150, Jul. 2021.

#### https://doi.org/10.1016/j.ceramint.2021.04.020

[29] T. Dele-Afolabi, M. Azmah Hanim, D. Jung, R. Ilyas, R. Calin, and A. Nurul Izzah, "Rice Husk as a Pore-Forming Agent: Impact of Particle Size on the Porosity and Diametral Tensile Strength of Porous Alumina Ceramics" *Coatings*, vol. 12, no. 9, p. 1259, Aug. 2022. <a href="https://doi.org/10.3390/coatings12091259">https://doi.org/10.3390/coatings12091259</a> [30] M M. Kütemeyer, L. Schomer, T. Helmreich, S. Rosiwal, and D. Koch, "Fabrication of ultra high temperature ceramic matrix composites using a reactive melt infiltration process" *Journal of the European Ceramic Society*, vol. 36, no. 15, pp. 3647–3655, Nov. 2016.

#### https://doi.org/10.1016/j.jeurceramsoc.2016.04.039

[31] T. Ohji and M. Fukushima, "Macro-porous ceramics: processing and properties" *International Materials Reviews*, vol. 57, no. 2, pp. 115–131, Mar. 2012.

#### https://doi.org/10.1179/1743280411y.0000000006

[32] X. Zhu, D. Jiang, and S. Tan, "Preparation of silicon carbide reticulated porous ceramics" *Materials Science and Engineering: A*, vol. 323, no. 1–2, pp. 232–238, Jan. 2002.

### https://doi.org/10.1016/s0921-5093(01)01352-1

- [33] Y. Chen, X. Tian, K. Su, Y. Wang, X. Liu, and F. Zhao, "Preparation and properties of porous mullite-based ceramics fabricated by solid state reaction" *Ceramics International*, vol. 49, no. 19, pp. 31846–31854, Oct. 2023. https://doi.org/10.1016/j.ceramint.2023.07.144
- [34] E. Fiume, J. Massera, D. D'Ambrosio, E. Verné, and F. Baino, "Robocasting of multicomponent solgel—derived silicate bioactive glass scaffolds for bone tissue engineering" *Ceramics International*, vol. 48, no. 23, pp. 35209–35216, Dec. 2022. https://doi.org/10.1016/j.ceramint.2022.08.121
- [35] R. Yeetsorn, S. Tungkamani, and Y. Maiket, "Fabrication of a Ceramic Foam Catalyst Using Polymer Foam Scrap via the Replica Technique for Dry Reforming" *ACS Omega*, vol. 7, no. 5, pp. 4202–4213, Jan. 2022. <a href="https://doi.org/10.1021/acsomega.1c05841">https://doi.org/10.1021/acsomega.1c05841</a>
- [36] L. Lin et al., "Low sintering shrinkage porous mullite ceramics with high strength and low thermal conductivity via foam-gel casting" *Journal of the American Ceramic Society*, vol. 106, no. 6, pp. 3800–3811, Feb. 2023. https://doi.org/10.1111/jace.19035
- [37] S. Deville, "Freeze-Casting of Porous Biomaterials: Structure, Properties and Opportunities" *Materials*, vol. 3, no. 3, pp. 1913–1927, Mar. 2010. https://doi.org/10.3390/ma3031913
- [38] S. Roy, "Properties and advanced applications of porous ceramic composites" *Open Ceramics*, vol. 21, p. 100714, Mar. 2025. <a href="https://doi.org/10.1016/j.oceram.2024.100714">https://doi.org/10.1016/j.oceram.2024.100714</a>

- [39] R. Saidi, M. Fathi, H. Salimijazi, and M. Mohammadrezaie, "Fabrication and characterization nanostructured forsterite foams with high compressive strength, desired porosity and suitable bioactivity for biomedical applications" *Journal of Sol-Gel Science and Technology*, vol. 81, no. 3, pp. 734–740, Nov. 2016. https://doi.org/10.1007/s10971-016-4240-8
- [40] W. Zhou et al., "Fabrication of mullite-corundum foamed ceramics for thermal insulation and effect of micro-pore-foaming agent on their properties" *Journal of Alloys and Compounds*, vol. 785, pp. 1030–1037, May 2019. https://doi.org/10.1016/j.jallcom.2019.01.212
- [41] M. Zhou, X. Ge, H. Wang, L. Chen, and X. Chen, "Effect of the CaO content and decomposition of calcium-containing minerals on properties and microstructure of ceramic foams from fly ash" *Ceramics International*, vol. 43, no. 12, pp. 9451–9457, Aug. 2017. <a href="https://doi.org/10.1016/j.ceramint.2017.04.122">https://doi.org/10.1016/j.ceramint.2017.04.122</a>
- [42] T. Liu, Y. Tang, Z. Li, T. Wu, and A. Lu, "Red mud and fly ash incorporation for lightweight foamed ceramics using lead-zinc mine tailings as foaming agent" *Materials Letters*, vol. 183, pp. 362–364, Nov. 2016. https://doi.org/10.1016/j.matlet.2016.07.041
- [43] Z. Li, H. Mao, P. A. Korzhavyi, and M. Selleby, "Thermodynamic re-assessment of the Co–Cr system supported by first-principles calculations" *Calphad*, vol. 52, pp. 1–7, Mar. 2016.

https://doi.org/10.1016/j.calphad.2015.10.013

- [44] J.-H. Eom, Y.-W. Kim, and S. Raju, "Processing and properties of macroporous silicon carbide ceramics: A review" *Journal of Asian Ceramic Societies*, vol. 1, no. 3, pp. 220–242, Sep. 2013. https://doi.org/10.1016/j.jascer.2013.07.003
- [45] R. M. Khattab, M. M. S. Wahsh, and N. M. Khalil, "Preparation and characterization of porous alumina ceramics through starch consolidation casting technique" *Ceramics International*, vol. 38, no. 6, pp. 4723–4728, Aug. 2012. https://doi.org/10.1016/j.ceramint.2012.02.057
- [46] R. He, Z. Qu, and X. Cheng, "Effects of starch addition amount on microstructure, mechanical properties and room temperature thermal conductivity of porous Y<sub>2</sub>SiO<sub>5</sub> ceramics" *Ceramics International*, vol. 42, no. 2, pp. 2257–2262, Feb. 2016. <a href="https://doi.org/10.1016/j.ceramint.2015.10.019">https://doi.org/10.1016/j.ceramint.2015.10.019</a>
- [47] R. M. Khattab, A. M. EL-Rafei, and M. F. Zawrah, "Fabrication of Porous TiO<sub>2</sub> Ceramics Using Corn Starch and Graphite as Pore Forming Agents" *Interceram International Ceramic Review*, vol. 67, no. 4, pp. 30–35, Jul. 2018. <a href="https://doi.org/10.1007/s42411-018-0024-1">https://doi.org/10.1007/s42411-018-0024-1</a>
- [48] K. Ishii, M. Shimizu, H. Sameshima, S. Samitsu, T. Ishigaki, and T. Uchikoshi, "Fabrication of porous (Ba,Sr)(Co,Fe)O<sub>3-δ</sub> (BSCF) ceramics using gelatinization and retrogradation phenomena of starch as poreforming agent" *Ceramics International*, vol. 46, no. 9, pp. 13047–13053, Jun. 2020.

https://doi.org/10.1016/j.ceramint.2020.02.075

- [49] L. Fang, C. Chen, and Y. Wang, "Carbon Fibers and Graphite as Pore-Forming Agents for the Obtention of Porous Alumina: Correlating Physical and Fractal Characteristics" *Fractal and Fractional*, vol. 6, no. 9, p. 501, Sep. 2022. <a href="https://doi.org/10.3390/fractalfract6090501">https://doi.org/10.3390/fractalfract6090501</a>
- [50] Z. Živcová, E. Gregorová, and W. Pabst, "Porous alumina ceramics produced with lycopodium spores as pore-forming agents" *Journal of Materials Science*, vol. 42, no. 20, pp. 8760–8764, Jul. 2007. https://doi.org/10.1007/s10853-007-1852-y
- [51] S. Abhinay, P. Dixit, and R. Mazumder, "Effect of pore former sucrose on microstructure and electrical properties of porous BZT-0.5BCT ceramics" *Ferroelectrics*, vol. 557, no. 1, pp. 18–27, Mar. 2020. https://doi.org/10.1080/00150193.2020.1713359
- [52] H. Yang et al., "Preparation and properties of porous silicon nitride ceramics with polymethyl methacrylate as pore-forming agent" *Ceramics International*, vol. 46, no. 10, pp. 17122–17129, Jul. 2020. <a href="https://doi.org/10.1016/j.ceramint.2020.03.204">https://doi.org/10.1016/j.ceramint.2020.03.204</a>
- [53] G. Pia, L. Casnedi, and U. Sanna, "Porous ceramic materials by pore-forming agent method: An intermingled fractal units analysis and procedure to predict thermal conductivity" *Ceramics International*, vol. 41, no. 5, pp. 6350–6357, Jun. 2015. <a href="https://doi.org/10.1016/j.ceramint.2015.01.069">https://doi.org/10.1016/j.ceramint.2015.01.069</a>
- [54] A. Çelik, G. Çağlar, and Y. Çelik, "Fabrication of porous Al<sub>2</sub>O<sub>3</sub> ceramics using carbon black as a pore forming agent by spark plasma sintering" *Ceramics International*, vol. 48, no. 19, pp. 28181–28190, Oct. 2022. <a href="https://doi.org/10.1016/j.ceramint.2022.06.121">https://doi.org/10.1016/j.ceramint.2022.06.121</a>
- [55] C. Wu, Z. Li, Y. Li, J. Wu, Y. Zhao, and Y. Liao, "Effect of starch on pore structure and thermal conductivity of diatomite-based porous ceramics" *Ceramics International*, vol. 49, no. 1, pp. 383–391, Jan. 2023. https://doi.org/10.1016/j.ceramint.2022.08.352
- [56] L. Hu, R. Benitez, S. Basu, I. Karaman, and M. Radovic, "Processing and characterization of porous Ti<sub>2</sub>AlC with controlled porosity and pore size" *Acta Materialia*, vol. 60, no. 18, pp. 6266–6277, Oct. 2012. https://doi.org/10.1016/j.actamat.2012.07.052
- [57] K. Huang et al., "Mechanism of porous ceramic fabrication using Second Aluminum Dross assisted by corn stalk as pore-forming agent" *Environmental Technology & Innovation*, vol. 31, p. 103195, May 2023. https://doi.org/10.1016/j.eti.2023.103195
- [58] N. Nikolopoulos, L. A. Parker, A. Wickramasinghe, O. van Veenhuizen, G. Whiting, and B. M. Weckhuysen, "Addition of Pore-Forming Agents and Their Effect on the Pore Architecture and Catalytic Behavior of Shaped Zeolite-Based Catalyst Bodies" *Chemical & Chemical & Chemical Maging*, vol. 1, no. 1, pp. 40–48, Mar. 2023. https://doi.org/10.1021/cbmi.2c00009
- [59] Y. Wu, F. Chen, W. Han, and T. Zhao, "Synthesis and pyrolysis of non-oxide precursors for ZrC/SiC and HfC/SiC composite ceramics" *Ceramics International*, vol. 46, no. 14, pp. 22102–22107, Oct. 2020. https://doi.org/10.1016/j.ceramint.2020.05.260

- [60] Y. Chen, N. Wang, O. Ola, Y. Xia, and Y. Zhu, "Porous ceramics: Light in weight but heavy in energy and environment technologies" *Materials Science and Engineering: R: Reports*, vol. 143, p. 100589, Jan. 2021. https://doi.org/10.1016/j.mser.2020.100589
- [61] J. Gu et al., "Sintering highly dense ultra-high temperature ceramics with suppressed grain growth" *Journal of the European Ceramic Society*, vol. 40, no. 4, pp. 1086–1092, Nov. 2019.

#### https://doi.org/10.1016/j.jeurceramsoc.2019.11.056

- [62] R. Gan et al., "Pore structure regulation of three-dimensional ordered Si<sub>3</sub>N<sub>4</sub> porous ceramics templated from Pickering emulsion" *Journal of the European Ceramic Society*, vol. 45, no. 12, p. 117417, Sep. 2025. https://doi.org/10.1016/j.jeurceramsoc.2025.117417
- [63] B. Liu, J. Fan, H. Nian, Y. Li, H. Xiang, and Y. Zhou, "Sintering-resistant porous BaZrO<sub>3</sub> ceramics using a particle-stabilized foam method for thermal insulation applications" *Journal of the American Ceramic Society*, vol. 108, no. 5, Dec. 2024. <a href="https://doi.org/10.1111/jace.20345">https://doi.org/10.1111/jace.20345</a>
- [64] H. Lin, H. Guo, and H. Tang, "Tailoring zirconia ceramic lattice structures with controlled porosity via nanoparticle jetting" *Journal of the Japan Society of Powder and Powder Metallurgy*, vol. 72, no. Supplement, pp. S1495–S1498, Mar. 2025. https://doi.org/10.2497/jjspm.16p-t10-02
- [65] X. Li, Z. Ye, H. Jiao, K. Zhao, and Z. Yan, "Al<sub>2</sub>O<sub>3</sub> porous ceramics with high strength by protein foaming method" *Scientific Reports*, vol. 15, no. 1, Feb. 2025.

#### https://doi.org/10.1038/s41598-025-90007-1

- [66] L. Gui et al., "Fracture behavior of MgO-Al<sub>2</sub>O<sub>3</sub>-CaO-based porous ceramics prepared with carbon black as pore-forming agent" *Construction and Building Materials*, vol. 473, p. 141059, Apr. 2025. https://doi.org/10.1016/j.conbuildmat.2025.141059
- [67] C. Liu et al., "Synthesis of alumina porous ceramics to enhance heat transfer and control Supercooling in sugar alcohol phase change materials for thermal energy storage" *Journal of Energy Storage*, vol. 113, p. 115627, Mar. 2025. https://doi.org/10.1016/j.est.2025.115627
- [68] A. S. Buyakov, "Structure kinetics of porous zirconia ceramics during solid-state sintering" *Russian Physics Journal*, vol. 66, no. 1, pp. 58–65, May 2023. https://doi.org/10.1007/s11182-023-02905-4
- [69] X. He, Z. Zhang, S. Wang, and F. Su, "Microstructure and properties of hierarchical porous ZrO<sub>2</sub>/Al<sub>2</sub>O<sub>3</sub> ceramics prepared by gel-foaming method" *Journal of the Australian Ceramic Society*, vol. 59, no. 4, pp. 905–914, Apr. 2023. https://doi.org/10.1007/s41779-023-00883-x
- [70] R. Vemoori, S. Bejugama, and A. K. Khanra, "Fabrication and characterization of alumina and zirconia-toughened alumina porous structures" *Ceramics International*, vol. 49, no. 13, pp. 21708–21715, Jul. 2023. https://doi.org/10.1016/j.ceramint.2023.03.310

[71] Q. Leng, D. Yao, Y. Xia, H. Liang, and Y.-P. Zeng, "Microstructure and permeability of porous zirconia ceramic foams prepared via direct foaming with mixed surfactants" Journal of the European Ceramic Society, vol. 42, no. 16, pp. 7528–7537, Dec. 2022.

https://doi.org/10.1016/j.jeurceramsoc.2022.08.060

- [72] N. Zhang et al., "Facile processing of oriented macro-porous ceramics with high strength and low thermal conductivity" Journal of the European Ceramic Society, vol. 42, no. 15, pp. 7196–7202, Dec. 2022. https://doi.org/10.1016/j.jeurceramsoc.2022.07.044
- [73] D. Liu, B. Shi, Y. Wang, and B. Xu, "Fiber reinforced porous (La<sub>1/5</sub>Nd<sub>1/5</sub>Sm<sub>1/5</sub>Gd<sub>1/5</sub>Yb<sub>1/5</sub>)<sub>2</sub>Zr<sub>2</sub>O<sub>7</sub> ceramics with enhanced compressive strength" *Journal of the American Ceramic Society*, vol. 105, no. 11, pp. 6816–6825, Jun. 2022. https://doi.org/10.1111/jace.18612
- [74] P. Ji et al., "Fabrication and characterisation of ZrO<sub>2</sub>-reinforced porous mullite ceramics" *Advances in Applied Ceramics*, vol. 121, no. 5–8, pp. 185–192, Nov. 2022.

https://doi.org/10.1080/17436753.2022.2155369

[75] W. Liu et al., "Waste recycling of coal fly ash: A novel approach to prepare hierarchically porous coal fly ash/Al<sub>2</sub>O<sub>3</sub> ceramic composite with high porosity and high strength templated by emulsion-assisted self-assembly" *Ceramics International*, vol. 48, no. 13, pp. 18588–18595, Jul. 2022.

https://doi.org/10.1016/j.ceramint.2022.03.130

- [76] C. Zhao, C. Huang, M. Zhuo, J. Yin, and C. Shen, "Effects of CaCO<sub>3</sub> and ZrO<sub>2</sub> on microstructure and properties of silicon-bonded SiC porous ceramics" *Materials Chemistry and Physics*, vol. 290, p. 126605, Oct. 2022. https://doi.org/10.1016/j.matchemphys.2022.126605
- [77] J. Zhao et al., "Fabrication of porous Al<sub>2</sub>TiO<sub>5</sub>-Al<sub>2</sub>O<sub>3</sub> ceramics using Al<sub>2</sub>O<sub>3</sub> hollow spheres coated with TiO<sub>2</sub> sol" *Ceramics International*, vol. 48, no. 19, pp. 27349–27359, Oct. 2022.

https://doi.org/10.1016/j.ceramint.2022.05.155

- [78] C.-Y. Lee, S. Lee, J.-H. Ha, J. Lee, I.-H. Song, and K.-S. Moon, "The effects of a zirconia addition on the compressive strength of reticulated porous zirconia-toughened alumina" *Applied Sciences*, vol. 11, no. 19, p. 9326, Oct. 2021. https://doi.org/10.3390/app11199326
- [79] M. Mohammadi et al., "Robocasting of single and multi-functional calcium phosphate scaffolds and its hybridization with conventional techniques: design, fabrication and characterization" *Applied Sciences*, vol. 10, no. 23, p. 8677, Dec. 2020. <a href="https://doi.org/10.3390/app10238677">https://doi.org/10.3390/app10238677</a>
- [80] K. S. Kamyshnaya and T. A. Khabas, "Fabrication of Al<sub>2</sub>O<sub>3</sub>–ZrO<sub>2</sub> ceramics with high porosity and strength" *Ceramics International*, vol. 47, no. 2, pp. 1666–1671, Jan. 2021.

https://doi.org/10.1016/j.ceramint.2020.08.283

- [81] X. Li et al., "Microstructure and permeability of porous YSZ ceramics fabricated by freeze casting of oil-in-water suspension" *Journal of the European Ceramic Society*, vol. 40, no. 15, pp. 5845–5851, Dec. 2020. https://doi.org/10.1016/j.jeurceramsoc.2020.05.067
- [82] S. Rezaee, K. Ranjbar, and A. R. Kiasat, "Characterization and strengthening of porous alumina-20 wt% zirconia ceramic composites" *Ceramics International*, vol. 46, no. 1, pp. 893–902, Jan. 2020. https://doi.org/10.1016/j.ceramint.2019.09.047
- [83] T. Yu. Sablina, I. N. Sevostyanova, V. V. Gorbatenko, L. N. Ryzhova, and S. N. Kulkov, "Investigation of the strain inhomogeneity in ZrO<sub>2</sub>-(Y<sub>2</sub>O<sub>3</sub>) porous ceramics under 'Brazilian' test" Proceedings of The International Conference on Physical Mesomechanics. Materials with Multilevel Hierarchical Structure and Intelligent Manufacturing Technology, vol. 2310, p. 020285, 2020.

#### https://doi.org/10.1063/5.0034673

- [84] W. Huo, X. Zhang, Y. Chen, Z. Hu, D. Wang, and J. Yang, "Ultralight and high-strength bulk alumina/zirconia composite ceramic foams through direct foaming method" *Ceramics International*, vol. 45, no. 1, pp. 1464–1467, Jan. 2019. https://doi.org/10.1016/j.ceramint.2018.09.095
- [85] Y. Li, X. Yang, D. Liu, J. Chen, D. Zhang, and Z. Wu, "Permeability of the porous Al<sub>2</sub>O<sub>3</sub> ceramic with bimodal pore size distribution" *Ceramics International*, vol. 45, no. 5, pp. 5952–5957, Apr. 2019. https://doi.org/10.1016/j.ceramint.2018.12.064
- [86] L. Yuan et al., "Fibrous ZrO<sub>2</sub>-mullite porous ceramics fabricated by a hydratable alumina based aqueous gel-casting process" *Ceramics International*, vol. 45, no. 7, pp. 8824–8831, May 2019. https://doi.org/10.1016/j.ceramint.2019.01.209
- [87] R. Zhang, C. Ye, and B. Wang, "Novel Al<sub>2</sub>O<sub>3</sub>–SiO<sub>2</sub> aerogel/porous zirconia composite with ultra-low thermal conductivity" *Journal of Porous Materials*, vol. 25, no. 1, pp. 171–178, May 2017. https://doi.org/10.1007/s10934-017-0430-1
- [88] Yu. I. Golovin, V. V. Korenkov, S. S. Razlivalova, and V. V. Rodaev, "Physicomechanical Properties of Porous Zirconia Ceramics" *Russian Metallurgy (Metally)*, vol. 2018, no. 10, pp. 961–967, Oct. 2018. https://doi.org/10.1134/s0036029518100063
- [89] R. Zhang, X. Hou, C. Ye, and B. Wang, "Enhanced mechanical and thermal properties of anisotropic fibrous porous mullite–zirconia composites produced using sol-gel impregnation" *Journal of Alloys and Compounds*, vol. 699, pp. 511–516, Jan. 2017. https://doi.org/10.1016/j.jallcom.2017.01.007
- [90] S. V. Uvarov, M. M. Davydova, and V. V. Chudinov, "Energy absorption and strength of ceramics with different porosity under dynamic loading" *AIP Conference Proceedings*, vol. 1785, p. 030033, 2016. https://doi.org/10.1063/1.4967054
- [91] W. Huo et al., "Highly Porous Zirconia Ceramic Foams with Low Thermal Conductivity from Particle-Stabilized Foams" *Journal of the American Ceramic Society*, vol. 99, no. 11, pp. 3512–3515, Oct. 2016.

#### https://doi.org/10.1111/jace.14555

- [92] Z. Živcová, E. Gregorová, and W. Pabst, "Low- and High-temperature Processes and Mechanisms in the Preparation of Porous Ceramics via Starch Consolidation Casting" *Starch Stärke*, vol. 62, no. 1, pp. 3–10, Jan. 2010. <a href="https://doi.org/10.1002/star.200900139">https://doi.org/10.1002/star.200900139</a>
- [93] O. Lyckfeldt and J. M. F. Ferreira, "Processing of porous ceramics by 'starch consolidation" *Journal of the European Ceramic Society*, vol. 18, no. 2, pp. 131–140, Jan. 1998.

#### https://doi.org/10.1016/s0955-2219(97)00101-5

- [94] J. E. Dominguez-Ayala, A. Soler, G. Mendez-Montealvo, and G. Velazquez, "Supramolecular structure and techno functional properties of starch modified by high hydrostatic pressure (HHP): A review" *Carbohydrate Polymers*, vol. 291, p. 119609, Sep. 2022. <a href="https://doi.org/10.1016/j.carbpol.2022.119609">https://doi.org/10.1016/j.carbpol.2022.119609</a>
- [95] C. Cui et al., "Recent advances in the preparation, characterization, and food application of starch-based hydrogels" *Carbohydrate Polymers*, vol. 291, p. 119624, Sep. 2022.

#### https://doi.org/10.1016/j.carbpol.2022.119624

[96] I. Chakraborty, P. N, S. S. Mal, U. C. Paul, Md. H. Rahman, and N. Mazumder, "An Insight into the Gelatinization Properties Influencing the Modified Starches Used in Food Industry: A review" *Food and Bioprocess Technology*, vol. 15, no. 6, pp. 1195–1223, Feb. 2022.

#### https://doi.org/10.1007/s11947-022-02761-z

[97] R. Jia et al., "A review of starch swelling behavior: Its mechanism, determination methods, influencing factors, and influence on food quality" *Carbohydrate Polymers*, vol. 321, p. 121260, Dec. 2023.

#### https://doi.org/10.1016/j.carbpol.2023.121260

- [98] J. Alzukaimi and R. Jabrah, "Porous alumina-based ceramics with very low thermal conductivity prepared by the starch consolidation route" *International Journal of Ceramic Engineering & Science*, vol. 6, no. 4, Jun. 2024. https://doi.org/10.1002/ces2.10226
- [99] E. Gregorová, P. Šimonová, W. Pabst, T. Uhlířová, and V. Nečina, "Temperature dependence of Young's modulus and the occurrence of an elastic anomaly in porous alumina-mullite composites prepared by starch consolidation casting" *Ceramics International*, vol. 50, no. 4, pp. 6309–6323, Feb. 2024.

#### https://doi.org/10.1016/j.ceramint.2023.11.359

- [100] L. Meira, I. Celestina, C. Ojaimi, K. Ramos, A. Chinelatto, and A. Chinelatto, "Starch consolidation casting of porous alumina and functional gradient porosity development" *Processing and Application of Ceramics*, vol. 18, no. 1, pp. 87–97, 2024. https://doi.org/10.2298/pac2401087m
- [101] Y. Zhang, H. Gu, L. Fu, A. Huang, and M. Zhang, "Fabrication and properties of lightweight zirconia with fine closed porosity" *Journal of Iron and Steel Research International*, vol. 31, no. 6, pp. 1449–1458, Sep. 2023. https://doi.org/10.1007/s42243-023-01086-1

[102] C. Alvarado, H. Alvarado-Quintana, and R. Siche, "Ceramic thermal insulator based on diatomite obtained by starch consolidation casting" *Materials*, vol. 16, no. 11, p. 4028, May 2023.

#### https://doi.org/10.3390/ma16114028

- [103] N. F. A. Rahman, H. A. Rahman, W. M. S. W. Azhan, and N. H. Yatim, "Linear shrinkage, strength and porosity of alumina-based ceramic foam with corn starch as pore former" *Solid State Phenomena*, vol. 317, pp. 75–80, May 2021. https://doi.org/10.4028/www.scientific.net/ssp.317.75
- [104] Z. Chen, G. Xu, H. Cui, X. Zhang, and X. Zhan, "Preparation of porous Al<sub>2</sub>O<sub>3</sub> ceramics by starch consolidation casting method" *International Journal of Applied Ceramic Technology*, vol. 15, no. 6, pp. 1550–1558, Jun. 2018. https://doi.org/10.1111/jjac.13043
- [105] M. L. Sandoval, M. H. Talou, A. G. Tomba Martinez, M. A. Camerucci, E. Gregorová, and W. Pabst, "Porous cordierite-based ceramics processed by starch consolidation casting Microstructure and high-temperature mechanical behavior" *Ceramics International*, vol. 44, no. 4, pp. 3893–3903, Mar. 2018. https://doi.org/10.1016/j.ceramint.2017.11.180
- [106] G. Xu, Z. Chen, X. Zhang, H. Cui, Z. Zhang, and X. Zhan, "Preparation of porous Al<sub>2</sub>TiO<sub>5</sub>-Mullite ceramic by starch consolidation casting and its corrosion resistance characterization" *Ceramics International*, vol. 42, no. 12, pp. 14107–14112, Sep. 2016. <a href="https://doi.org/10.1016/j.ceramint.2016.06.024">https://doi.org/10.1016/j.ceramint.2016.06.024</a> [107] H. E. H. Sadek, R. M. Khattab, and M. F. Zawrah, "Preparation of porous forsterite ceramic using waste silica fumes by the starch consolidation method," *Interceram International Ceramic Review*, vol. 65, no. 4–5, pp. 174–178, Aug. 2016. <a href="https://doi.org/10.1007/bf03401166">https://doi.org/10.1007/bf03401166</a>
- [108] Z. Nie, and Y. Lin, "Fabrication of porous alumina ceramics with corn starch in an easy and low-cost way" *Ceramics Silikaty*, vol. 59, no. 4, pp. 348–352, Dec. 2015.
- [109] M. H. Talou and M. A. Camerucci, "Processing of porous mullite ceramics using novel routes by starch consolidation casting" *Journal of the European Ceramic Society*, vol. 35, no. 3, pp. 1021–1030, Mar. 2015. <a href="https://doi.org/10.1016/j.jeurceramsoc.2014.10.011">https://doi.org/10.1016/j.jeurceramsoc.2014.10.011</a>
- [110] C.B. Emrullahoğlu, and T. Yanar, "Porous alumina-zirconia composites prepared with starch as a pore forming agent" *Machines, Technologies, Materials*, 2013.
- [111] Z. Živcová-Vlčková, J. Locs, M. Keuper, I. Sedlářová, and M. Chmelíčková, "Microstructural comparison of porous oxide ceramics from the system Al<sub>2</sub>O<sub>3</sub>–ZrO<sub>2</sub> prepared with starch as a pore-forming agent" *Journal of the European Ceramic Society*, vol. 32, no. 10, pp. 2163–2172, Aug. 2012.

#### https://doi.org/10.1016/j.jeurceramsoc.2012.02.005

[112] W. Pabst, E. Gregorová, I. Sedlářová, and M. Černý, "Preparation and characterization of porous alumina–zirconia composite ceramics" *Journal of the European Ceramic Society*, vol. 31, no. 14, pp. 2721–2731, Nov. 2011. <a href="https://doi.org/10.1016/j.jeurceramsoc.2011.01.011">https://doi.org/10.1016/j.jeurceramsoc.2011.01.011</a>

- [113] L. B. Garrido, M. P. Albano, L. A. Genova, and K. P. Plucknett, "Influence of starch type on characteristics of porous 3Y-ZrO<sub>2</sub> prepared from a direct consolidation casting method" *Materials Research*, vol. 14, no. 1, pp. 39–45, Apr. 2011. https://doi.org/10.1590/s1516-14392011005000016
- [114] E. Gregorova, Z. Živcova, W. Pabst, M. Černý, and P. Kolomazník, "Porous alumina-zirconia composite ceramics prepared by starch consolidation casting" *11th International Conference and Exhibition of the European Ceramic Society*, pp. 564–568, 2009.
- [115] R. C. Garvie, R. H. Hannink, and R. T. Pascoe, "Ceramic steel?" *Nature*, vol. 258, no. 5537, pp. 703–704, Dec. 1975. <a href="https://doi.org/10.1038/258703a0">https://doi.org/10.1038/258703a0</a>
- [116] C. Hadjicharalambous, O. Prymak, K. Loza, A. Buyakov, S. Kulkov, and M. Chatzinikolaidou, "Effect of porosity of alumina and zirconia ceramics toward pre-osteoblast response" *Frontiers in Bioengineering and Biotechnology*, vol. 3, Oct. 2015. https://doi.org/10.3389/fbioe.2015.00175
- [117] B. Altmann et al., "Assessment of novel long-lasting ceria-stabilized zirconia-based ceramics with different surface topographies as implant materials" *Advanced Functional Materials*, vol. 27, no. 40, Aug. 2017. https://doi.org/10.1002/adfm.201702512
- [118] D. Chopra, A. Jayasree, T. Guo, K. Gulati, and S. Ivanovski, "Advancing dental implants: Bioactive and therapeutic modifications of zirconia" *Bioactive Materials*, vol. 13, pp. 161–178, Jul. 2022. https://doi.org/10.1016/j.bioactmat.2021.10.010
- [119] X. Yang, J. Guo, Y. Li, and X. Yang, "Compressive fracture behavior of zirconia/resin composites prepared by fused deposition modeling combined with vacuum infiltration" *Materials*, vol. 17, no. 9, p. 1989, Apr. 2024. https://doi.org/10.3390/ma17091989
- [120] A. Afzal, "Implantable zirconia bio ceramics for bone repair and replacement: A chronological review" *Materials Express*, vol. 4, no. 1, pp. 1–12, Feb. 2014. https://doi.org/10.1166/mex.2014.1148
- [121] V. Thakare, "Progress in synthesis and applications of Zirconia" *International Journal of Engineering Research and Development*, vol. 5, no. 1, Nov. 2012, pp. 25-28, e-ISSN: 2278-067X, p-ISSN: 2278-800X.
- [122] P. Christel et al., "Biomechanical Compatibility and Design of Ceramic Implants for Orthopedic Surgery" *Annals of the New York Academy of Sciences*, vol. 523, no. 1, pp. 234–256, Jun. 1988.

https://doi.org/10.1111/j.1749-6632.1988.tb38516.x

[123] X. Cui et al., "Mechanical properties of polymer-infiltrated ZrO<sub>2</sub> ceramic network improved by incorporation of SiO<sub>2</sub> component" *Materials & Design*, vol. 252, p. 113739, Apr. 2025.

https://doi.org/10.1016/j.matdes.2025.113739

[124] M. Khakzad, Z. Sepasi, M. Mosadegh, Z. Alsup, and M. Minary-Jolandan, "Porous ceramics via vat photopolymerization: Influence of particles relative roundness on porosity in fully sintered ceramics" *Ceramics International*, vol. 51, no. 14, pp. 19355–19365, Jun. 2025.

https://doi.org/10.1016/j.ceramint.2025.02.112

- [125] F. Wang et al., "Additive manufacturing of interconnected hierarchically porous zirconia: Utilizing both microspherical and filamentary pore-forming agents via direct ink printing" *Ceramics International*, vol. 50, no. 9, pp. 15740–15749, May 2024. https://doi.org/10.1016/j.ceramint.2024.02.054
- [126] G. Herranz et al., "Design and manufacturing by fused filament technique of novel YSZ porous grafts infiltrated with PCL/PVA/AgNPS for large bone defects repairing" *Journal of Materials Research and Technology*, vol. 29, pp. 3393–3408, Mar. 2024. https://doi.org/10.2139/ssrn.4650264
- [127] E. Kocyło, G. Franchin, P. Colombo, A. Chmielarz, and M. Potoczek, "Hydroxyapatite-coated ZrO<sub>2</sub> scaffolds with a fluorapatite intermediate layer produced by direct ink writing" *Journal of the European Ceramic Society*, vol. 41, no. 1, pp. 920–928, Jan. 2021.

https://doi.org/10.1016/j.jeurceramsoc.2020.08.021

- [128] K. Sakthiabirami et al., "Hybrid porous zirconia scaffolds fabricated using additive manufacturing for bone tissue engineering applications" *Materials Science and Engineering: C*, vol. 123, p. 111950, Apr. 2021. https://doi.org/10.1016/j.msec.2021.111950
- [129] Y. Cao et al., "Fabrication and properties of zirconia/hydroxyapatite composite scaffold based on digital light processing" *Ceramics International*, vol. 46, no. 2, pp. 2300–2308, Feb. 2020. https://doi.org/10.1016/j.ceramint.2019.09.219
- [130] Q. Wang, Z. Ma, Y. Wang, L. Zhong, and W. Xie, "Fabrication and characterization of 3D printed biocomposite scaffolds based on PCL and zirconia nanoparticles" *Bio-Design and Manufacturing*, vol. 4, no. 1, pp. 60–71, Aug. 2020. <a href="https://doi.org/10.1007/s42242-020-00095-3">https://doi.org/10.1007/s42242-020-00095-3</a>
- [131] J. Zhang et al., "Zirconia toughened hydroxyapatite biocomposite formed by a DLP 3D printing process for potential bone tissue engineering" *Materials Science and Engineering: C*, vol. 105, p. 110054, Dec. 2019. https://doi.org/10.1016/j.msec.2019.110054
- [132] S.-Y. Fu, B. Yu, H.-F. Ding, G.-D. Shi, and Y.-F. Zhu, "Zirconia Incorporation in 3D Printed β-Ca<sub>2</sub>SiO<sub>4</sub> Scaffolds on Their Physicochemical and Biological Property" *Journal of Inorganic Materials*, vol. 34, no. 4, p. 444, 2019. https://doi.org/10.15541/jim20180466
- [133] Daniela Brazete, Ana S. Neto, José M. F. Ferreira, "OPTIMIZATION OF ZIRCONIA INKS TO FABRICATE 3D POROUS SCAFFOLDS BY ROBOCASTING" *Lekar a technika Clinician and Technology*, vol. 49(1), pp. 5-10, 2019, ISSN 0301-5491 (Print), ISSN 2336-5552 (Online).
- [134] A. D. R. Silva et al., "Surface modification using the biomimetic method in alumina-zirconia porous ceramics obtained by the replica method" *Journal of Biomedical Materials Research Part B: Applied Biomaterials*, vol. 106, no. 7, pp. 2615–2624, Jan. 2018. https://doi.org/10.1002/jbm.b.34078
- [135] A.-M. Stanciuc et al., "Robocast zirconia-toughened alumina scaffolds: Processing, structural characterisation and interaction with human primary osteoblasts" *Journal of the European Ceramic Society*, vol. 38, no. 3, pp. 845–853, Mar. 2018. <a href="https://doi.org/10.1016/j.jeurceramsoc.2017.08.031">https://doi.org/10.1016/j.jeurceramsoc.2017.08.031</a>

- [136] M. Sa, B. B. Nguyen, R. A. Moriarty, T. Kamalitdinov, J. P. Fisher, and J. Y. Kim, "Fabrication and evaluation of 3D printed BCP scaffolds reinforced with ZrO<sub>2</sub> for bone tissue applications" *Biotechnology and Bioengineering*, vol. 115, no. 4, pp. 989–999, Jan. 2018. https://doi.org/10.1002/bit.26514
- [137] V. G. Thakare, P. A. Joshi, R. R. Godse, V. B. Bhatkar, P. A. Wadegaokar, and S. K. Omanwar, "Fabrication of polycaprolactone/zirconia nanofiber scaffolds using electrospinning technique" *Journal of Polymer Research*, vol. 24, no. 12, Nov. 2017. https://doi.org/10.1007/s10965-017-1388-z
- [138] P. S. Sapkal, A. M. Kuthe, S. Mathankar, and A. A. Deshmukh, "3D Bio-Plotted Tricalcium Phosphate/Zirconia Composite Scaffolds to Heal Large Size Bone Defects" *Molecular & Cellular Biomechanics*, vol. 14, no. 2, pp. 125–136, 2017. https://doi.org/10.3970/mcb.2017.014.123
- [139] P. S. Sapkal, A. M. Kuthe, R. S. Kashyap, A. R. Nayak, S. A. Kuthe, and A. P. Kawle, "Indirect casting of patient-specific tricalcium phosphate zirconia scaffolds for bone tissue regeneration using rapid prototyping methodology" *Journal of Porous Materials*, vol. 24, no. 4, pp. 1013–1023, Dec. 2016.

#### https://doi.org/10.1007/s10934-016-0341-6

- [140] G. Cadafalch Gazquez et al., "Flexible Yttrium-Stabilized Zirconia Nanofibers Offer Bioactive Cues for Osteogenic Differentiation of Human Mesenchymal Stromal Cells" *ACS Nano*, vol. 10, no. 6, pp. 5789–5799, Jun. 2016. https://doi.org/10.1021/acsnano.5b08005.s001
- [141] S. U. Kadam, B. K. Tiwari, and C. P. O'Donnell, "Improved thermal processing for food texture modification" *Modifying Food Texture*, pp. 115–131, 2015.

## https://doi.org/10.1016/b978-1-78242-333-1.00006-1

- [142] C. Qian et al., "The effect of particle size distribution on the microstructure and properties of Al<sub>2</sub>O<sub>3</sub> ceramics formed by stereolithography" *Ceramics International*, vol. 48, no. 15, pp. 21600–21609, Aug. 2022. https://doi.org/10.1016/j.ceramint.2022.04.133
- [143] K. Miyake, Y. Hirata, T. Shimonosono, and S. Sameshima, "The Effect of particle shape on sintering behavior and compressive strength of porous alumina" *Materials*, vol. 11, no. 7, p. 1137, Jul. 2018.

#### https://doi.org/10.3390/ma11071137

- [144] Zhao Ting, Qin Yi, Wu Tong, Wang Bo, Yang Jianfeng, "Effect of Particle Size on the Sintering Behavior, Microstructure and Flexural Strength of Lithium Disilicate Glass-Ceramics," *Rare Metal Materials and Engineering*, 43(S1): 024-028, 2014.
- [145] J. S. Reed, A review of: "INTRODUCTION TO THE PRINCIPLES OF CERAMIC PROCESSING, John Wiley & Sons, New York, NY 485 pages, hardcover, 1988.

#### https://doi.org/10.1080/10426919008953237

[146] M. W. Barsoum, Fundamentals of Ceramics. CRC Press, 2019.

https://doi.org/10.1201/9781498708166

- [147] F. J. O'Brien, "Biomaterials & scaffolds for tissue engineering" *Materials Today*, vol. 14, no. 3, pp. 88–95, Mar. 2011. https://doi.org/10.1016/s1369-7021(11)70058-x
- [148] V. Karageorgiou and D. Kaplan, "Porosity of 3D biomaterial scaffolds and osteogenesis" *Biomaterials*, vol. 26, no. 27, pp. 5474–5491, Sep. 2005.

#### https://doi.org/10.1016/j.biomaterials.2005.02.002

- [149] S. J. Hollister, "Porous scaffold design for tissue engineering" *Nature Materials*, vol. 4, no. 7, pp. 518–524, Jul. 2005. https://doi.org/10.1038/nmat1421
- [150] J. L. Xu et al., "Effect of pore sizes on the microstructure and properties of the biomedical porous NiTi alloys prepared by microwave sintering" *Journal of Alloys and Compounds*, vol. 645, pp. 137–142, Oct. 2015. https://doi.org/10.1016/j.jallcom.2015.05.006
- [151] C.-L. Lin, J.-H. Lin, J.-J. Lin, and Y.-H. Chang, "Properties of high-swelling native starch treated by heat—moisture treatment with different holding times and iterations" *Molecules*, vol. 25, no. 23, p. 5528, Nov. 2020. https://doi.org/10.3390/molecules25235528
- [152] L. Liao, H. Liu, Z. Gan, and W. Wu, "Structural properties of sweet potato starch and its vermicelli quality as affected by heat-moisture treatment" *International Journal of Food Properties*, vol. 22, no. 1, pp. 1122–1133, Jan. 2019. https://doi.org/10.1080/10942912.2019.1626418
- [153] L. B. Garrido, M. P. Albano, L. A. Genova, and K. P. Plucknett, "Influence of starch type on characteristics of porous 3Y-ZrO<sub>2</sub> prepared from a direct consolidation casting method" *Materials Research*, vol. 14, no. 1, pp. 39–45, Apr. 2011. <a href="https://doi.org/10.1590/s1516-14392011005000016">https://doi.org/10.1590/s1516-14392011005000016</a>
- [154] Gregorová E., Živcová Z., Pabst W., "Porous ceramics made using potato starch as a pore-forming agent," *Fruit, Vegetable and Cereal Science and Biotechnology*, 3, 115- 127, 2009.
- [155] Gregorová E., Živcová Z., Pabst W., Kunertová A., "Starch-processed ceramics with porosity and pore size gradients," *Proceedings of the 10<sup>th</sup> ECerS Conference*, pp 439-446, 17–21 June, 2007.
- [156] J. F. Shackelford and W. Alexander, Eds., Materials Science and Engineering Handbook. CRC Press, 2000. https://doi.org/10.1201/9781420038408
- [157] E. F. Morgan, G. U. Unnikrisnan, and A. I. Hussein, "Bone Mechanical Properties in Healthy and Diseased States" *Annual Review of Biomedical Engineering*, vol. 20, no. 1, pp. 119–143, Jun. 2018. https://doi.org/10.1146/annurev-bioeng-062117-121139
- [158] R. J. O'Toole et al., "Particle atomic layer deposition of alumina for sintering yttria-stabilized cubic zirconia" *Journal of the American Ceramic Society*, vol. 102, no. 5, pp. 2283–2293, Oct. 2018. https://doi.org/10.1111/jace.16091
- [159] F. Rubino, G. Rotella, M. Perrella, P. Carlone, and T. S. Sudarshan, "Microstructural and mechanical properties of Al<sub>2</sub>O<sub>3</sub> and Al<sub>2</sub>O<sub>3</sub>/TiB<sub>2</sub> ceramics consolidated by plasma pressure compaction" *Journal of Materials Engineering and Performance*, vol. 32, no. 10, pp. 4391–4403, Sep. 2022.

#### https://doi.org/10.1007/s11665-022-07403-1

[160] C. G. Sammis and M. F. Ashby, "The failure of brittle porous solids under compressive stress states" *Acta Metallurgica*, vol. 34, no. 3, pp. 511–526, Mar. 1986. <a href="https://doi.org/10.1016/0001-6160(86)90087-8">https://doi.org/10.1016/0001-6160(86)90087-8</a> [161] S. Meille, M. Lombardi, J. Chevalier, and L. Montanaro, "Mechanical properties of porous ceramics in compression: On the transition between elastic, brittle, and cellular behavior" *Journal of the European Ceramic Society*, vol. 32, no. 15, pp. 3959–3967, Nov. 2012.

#### https://doi.org/10.1016/j.jeurceramsoc.2012.05.006

- [162] M. F. Ashby and C. G. Sammis, "The damage mechanics of brittle solids in compression" *pure and applied geophysics*, vol. 133, no. 3, pp. 489–521, May 1990. https://doi.org/10.21236/ada201653
- [163] E. B. Watson and J. D. Price, "Kinetics of the reaction MgO +  $Al_2O_3 \rightarrow MgAl_2O_4$  and Al-Mg interdiffusion in spinel at 1200 to 2000°C and 1.0 to 4.0 GPa" *Geochimica et Cosmochimica Acta*, vol. 66, no. 12, pp. 2123–2138, Jun. 2002. https://doi.org/10.1016/s0016-7037(02)00827-x
- [164] M. A. Sainz, A. D. Mazzoni, E. F. Aglietti, and A. Caballero, "Thermochemical stability of spinel (MgO·Al<sub>2</sub>O<sub>3</sub>) under strong reducing conditions" *Materials Chemistry and Physics*, vol. 86, no. 2–3, pp. 399–408, Aug. 2004. https://doi.org/10.1016/j.matchemphys.2004.04.007
- [165] J. Schmelzer, J. Möller, and V. V. slezov, "Ostwald ripening in porous materials: The case of arbitrary pore size distributions" *Journal of Physics and Chemistry of Solids*, vol. 56, no. 8, pp. 1013–1022, Aug. 1995. <a href="https://doi.org/10.1016/0022-3697(95)00021-6">https://doi.org/10.1016/0022-3697(95)00021-6</a>

#### Appendix A.

**Table** Various outcomes of using distinct manufacturing processes in the fabrication of ceramic porous structures

Fabrication technique	Ceramic material	Sintering conditions	Pore size	Porosity	Other properties	Application	Ref.
Ice templating	8 mol.% YSZ	1390°C, 6 h	2.5 - 38.1 μm	54 - 75%	CO <sub>2</sub> permeance = $1.5 \times 10^{-7}$ mol Pa <sup>-1</sup> ·s <sup>-1</sup> ·m <sup>-2</sup>	Membrane support	[62] 2025
Particle- stabilized foam	BaZrO <sub>3</sub>	1300°C - 1600°C, 6 h	-	92.9 - 94.6%	k = 0.088 - 0.193 $W/(m \cdot K),$ $\sigma = 0.30 - 1.31$ MPa	Thermal insulation	[63] 2025
3D printing	3 mol% YSZ	1450°C, 180 min	-	60, 70, and 80%	σ = 109 - 1029 MPa	-	[64] 2025
Protein foaming	Al <sub>2</sub> O <sub>3</sub>	1500°C, 1 h	150 - 240 μm	11.2 - 38.8%	$\sigma = 84 - 140 \text{ MPa}$	Thermal insulation	[65] 2025
Use of pore formers	MgO- Al <sub>2</sub> O <sub>3</sub> - CaO	1225°C, 3 h	-	62.7%	UTS = 14.76 MPa	Thermal insulation	[66] 2025
Freeze- casting	Al <sub>2</sub> O <sub>3</sub>	1400°C, 90 min	-	62 - 83	k = 4.82 W/(m·K)	Thermal energy storage	[67] 2025

Solid-state sintering	MgO- TZP	1500°C, 2 h	1.9 - 42.5μm	48 - 69%	VS = 64 - 70 %, $\sigma = 30 - 80 \text{ MPa}$	-	[68] 2023
Gel-forming	ZrO <sub>2</sub> / Al <sub>2</sub> O <sub>3</sub>	1350°C, 1450°C, and 1550°C, 1 h	450 - 640 μm	34 – 74 %	$\sigma = 5.8 - 129 \text{ MPa}$	-	[69] 2023
Use of pore formers	Al <sub>2</sub> O <sub>3</sub> - ZrO <sub>2</sub>	1650°C	10 - 40 μm	21.9 - 69%	$\sigma = 4.5 - 658 \text{ MPa}$	Insulation	[70] 2023
Direct foaming	8 mol. % YSZ	1500°C, 2 h	-	45 - 84%	$\sigma = 1.5 - 267 \text{ MPa}$	Insulation	[71] 2022
Mixing and accumulative rolling	3 mol. % YSZ - graphite flakes	1550°C, 2 h	0.43 - 1.05 μm	15 - 44 vol%	$\sigma = \\ 150 \text{ MPa} - 1.5 \\ \text{GPa}, \\ k = 0.92 - 1.85 \\ \text{Wm}^{-1} \text{K}^{-1}$	Thermal insulation	[72] 2022
Foam-gel- casting with freeze-drying	$\begin{array}{c} (La_{1/5}Nd_1\\ _{/5}Sm_{1/}\\ _{5}Gd_{1/5}Yb\\ _{1/5})_2Zr_2O_7 \end{array}$	1000°C - 1500°C, 2h	0.5 - 110 μm,	92.4 - 94.8%	$\sigma = 0.8 - 4.15 \text{ MPa}$	Thermal insulation	[73] 2022
Foam-gel- casting	Mullite/ ZrO <sub>2</sub>	1600°C	47 - 261 μm	66.9 - 77.4%	$\sigma = 14 - 34 \text{ MPa},$ $\sigma_f = 2 - 11 \text{ MPa}$	Thermal insulation	[74] 2022
Particle stabilized foam	Coal fly ash/ Al <sub>2</sub> O <sub>3</sub>	1300°C, 2 h	1 - 15 μm	49.3 - 68.1%	$\sigma = 81.7 - 159.33$ MPa	-	[75] 2022
Partial sintering	SiC/ZrO <sub>2</sub> -CaCO <sub>3</sub>	1450°C, 2 h	2 - 15 μm	38.86%	$\sigma_f$ up to 68.7 MPa	Filtration	[76] 2022
Co- precipitation and sintering	Al <sub>2</sub> TiO <sub>5</sub> / Al <sub>2</sub> O <sub>3</sub>	1450°C, 1500°C, and 1550°C, 2h	-	30.4 - 46.8%	$\sigma = 33.5 - 53.1$ MPa	-	[77] 2022
Replica technique	Al <sub>2</sub> O <sub>3</sub> / ZrO <sub>2</sub>	1600°C, 3 h	45 PPI	-	σ up to 4.17 MPa	Diesel particulate filters and radar- absorbing materials	[78] 2021
Partial sintering	Al <sub>2</sub> O <sub>3</sub> / Fap/TiO <sub>2</sub>	1500°C, 1 - 5 h	43 - 280 μm	21 - 49 %	$\sigma = 17 - 30 \text{ MPa}$	Bone scaffold	[79] 2021
Freeze- casting	Al <sub>2</sub> O <sub>3</sub> / ZrO <sub>2</sub>	1580°C, 2 h	-	59.6%	$\sigma$ = 92.3 MPa	Filtration	[80] 2021
Freeze casting	ZrO <sub>2</sub> - Y <sub>2</sub> O <sub>3</sub>	1250°C - 1550°C, 2 h	0.2 - 10.7 μm	56.1 - 81.8%	$\sigma = 2.2 - 31.7 \text{ MPa}$	Filters and membrane support	[81] 2020
Use of pore formers	Al <sub>2</sub> O <sub>3</sub> - ZrO <sub>2</sub>	1600°C, 3 h	0.9 - 15.3 μm	10 - 57	$\sigma = 60 - 260 \text{ MPa},$ $K = 1.63 - 5.48$ $MPa\sqrt{m},$ $HV = 89 - 1050$ $HV$	-	[82] 2020
Compressing	ZrO <sub>2</sub> – 5.5 wt% Y <sub>2</sub> O <sub>3</sub>	1600°C, 1 h	-	27 - 42%	UTS = 0 - 35 MPa	-	[83] 2020
Direct foaming	Al <sub>2</sub> O <sub>3</sub> - ZrO <sub>2</sub>	1500°C, 2 h	-	95.82 - 96.7%	σ = 0.62 - 1.52 MPa	Insulation	[84] 2019
Die pressing	Al <sub>2</sub> O <sub>3</sub>	1350°C, 2 h	0 - 2μm	34.9 - 54.9%	-	Filtration	[85] 2019

Aqueous gel- casting	ZrO <sub>2</sub> / mullite	1600°C, 4 h	5 μm	55.6%	$\sigma = 18.8 \text{ MPa}$	-	[86] 2019
Vacuum squeeze moulding with impregnation	Al <sub>2</sub> O <sub>3</sub> – SiO <sub>2</sub> aerogel/ porous ZrO <sub>2</sub>	1400°C, 1 h	-	91 - 92.8 %.	$\sigma = 0.22 - 0.91$ MPa, $k = 0.06 - 0.076$ W/(m/K)	Thermal insulation	[87] 2018
Specification	CaO stabilized ZrO <sub>2</sub>	1000°C, 1100°C, 1200°C, 1300°C, 4 h	353 - 410 nm	1 – 38%	H = 0.17 - 17.8 GPa, E = 2.5 - 274 $GPa$	1	[88] 2018
Vacuum squeeze moulding with sol-gel impregnation	Al <sub>2</sub> O <sub>3</sub> - SiO <sub>2</sub> aerogel/ porous mullite -ZrO <sub>2</sub>	1400°C, 1 h	-	78.1%	$\sigma = 1.36 \text{ MPa}$	Thermal insulation	[89] 2017
Compressing	ZrO <sub>2</sub> (8.6 mol.% MgO)	1550°C, 1 h	-	10 - 60 %	EA = 0.8 - 3  J/g	Energy absorption	[90] 2016
Pickering foam templating	ZrO <sub>2</sub>	1350°C - 1500°C, 2 h	-	96 - 98 %	$k = 0.02$ $W \cdot (m \cdot K)^{-1}$ , $\sigma = 0.26$ MPa	Thermal insulation	[91] 2016

Table Some results from using various pore-forming agents in the fabrication of ceramic porous structures.

Ceramic Materials	PFA	PFA content	Sintering conditions	Pore size	Porosity	Other properties	Ref.
Al <sub>2</sub> O <sub>3</sub> - TiO <sub>2</sub>	Corn starch	2.5, 5, 7.5, and 10 wt.%	1400°C, 2 h	9-232 μm	54-76 vol%	$k = 0.06 \text{-} 0.1 \text{ W/m.K}, \\ \rho = 3.6 \text{-} 600 \text{ G}\Omega \cdot \text{m}, \\ \sigma \text{ up to } 2.8 \text{ MPa}$	[98] 2024
Al <sub>2</sub> O <sub>3</sub> - mullite	Corn starch	20, 40 vol%	1570°C	1	43-57%	LS = 1.5-12, E = 19.7-69.2 GPa	[99] 2024
$Al_2O_3$	Potato starch	5-15 %	1500°C, 2 h	18-55 μm	8-56%	$\sigma = 60 \text{ MPa, linear}$ LS = 14.4-17.4 %	[100] 2024
m-ZrO <sub>2</sub>	Corn starch	5 wt.%	1750°C, 3 h	4.4-10.7 μm	5.1-16.5 %	$k = 1.37 \text{ W m}^{-1} \text{ K}^{-1}$ .	[101] 2024
Diatomite	Corn starch	0-40%	1000°C, 1 h	-	46.54- 59.28%	$k = 0.0984 \text{ W/m} \cdot \text{K},$ WA = 58.45%, $\sigma = 3.45 \text{ MPa}$	[102] 2023
$Al_2O_3$	Corn starch	4-10 wt.%	1250°C, 2 h	-	54.05- 70.70%.	LS = 1.07-3.39 %, $\sigma_f = 0.5-1.9 \text{ MPa}$	[103] 2021
Al <sub>2</sub> O <sub>3</sub> - SiO <sub>2</sub> - MgO	Corn starch	0, 5, 10, 15, 20, and 25	1100°C, 1200°C, 1300°C, 1400°C, 1450°C, and 1500°C, 2 h	1-4 μm	47.67%	$\sigma_f = 44.31 \text{ MPa}$	[104] 2018
Kaolin- talc- Al <sub>2</sub> O <sub>3</sub>	Potato starch, corn starch	15 vol.%	1275°C, 1300°C and 1330°C, 4 h	11-19 µm with potato starch, and 7-8 µm with corn starch	42-49 with corn starch 49-56 with potato starch	$\sigma_f = 5.3-9 \text{ MPa}$	[105] 2018

Al <sub>2</sub> TiO <sub>5</sub> (AT)- mullite	Corn starch	10 wt.%	1400°C, 1450°C, and 1500°C, 2 h	1-15 μm	54.7%	$\sigma_f = 11.5 \text{ MPa}$	[106] 2016
Forsterite	Corn starch	2.8, 7.3, 11.3%	1400°C, 1450°C and 1500°C, 2 h	16-14 μm	45.5 -80.5%	$\sigma = 38.1-20.2 \text{ MPa}$	[107] 2016
Al <sub>2</sub> O <sub>3</sub>	Corn starch	0-50 vol. %	1500°C, 3 h	-	14.8-55.3	$\sigma = 5-24 \text{ MPa}$	[108] 2015
Mullite	Corn, potato and cassava starches	9-10 vol.%	1400°C, 1500°C and 1650°C, 2 h	-	39-64%	VS = 6.6-42.8 %	[109] 2015
α-Al <sub>2</sub> O <sub>3</sub> - m-ZrO <sub>2</sub> - MgO	Corn starch	10, 20 and 30 wt.%	1300°C, 1400°C, 1460°C and 1550°C, 2 h	-	43-60%	WA = 16-34 %, $\sigma_f = 0$ -17 MPa	[110] 2013
Al <sub>2</sub> O <sub>3</sub> – ZrO <sub>2</sub>	Rice and corn starches	10, 20, 25, 30, and 50 vol.%	1530°C, 2 h	-	50%.	LS = 10-40%	[111] 2012
Al <sub>2</sub> O <sub>3</sub> - ZrO <sub>2</sub>	Corn starch	10-50. vol.%	1100°C - 1530°C, 2 h	0.1-17 μm	50-71%	E = 331-383  GPa	[112] 2011
3Y-ZrO <sub>2</sub>	Corn and potato starches	0.45-0.71 vol.%	1300°C, 1400°C or 1500°C, 2 h	7-10 µm with corn starch, 50 µm with potato starch.	38-52 vol.% with corn starch, 50 - 54 vol.% with potato starch.	LS = 30-50 %	[113] 2011
Al <sub>2</sub> O <sub>3</sub> -3Y- ZrO <sub>2</sub>	Corn starch	10 - 50 vol.%	1530°C, 2 h	-	26 - 51%	LS = 16 - 22 %	[114] 2009

**Table** Some results of the use of ZrO<sub>2</sub>-based ceramics in biomedical applications

Materials	Fabrication techniques	Sintering temperature	Pore size (µm)	Porosity (%)	Other properties	Application	Ref.
ZrO <sub>2</sub> /SiO <sub>2</sub> / PICN	Extrusion Moulding and pressure less sintering	750, 1000°C, 2h	-	44-50	$\sigma_f = 249 \text{ MPa},$ $E = 23 \text{ GPa},$ $H = 2 \text{ GPa},$ $K = 2$ $MPa.m^{1/2}$	Inlays and anterior crowns in dental	[123] 2025
8YSZ	DLP 3D printing	1450°C, 3 h	-	20-41	$\sigma_f = 25-71$ MPa	Biomedical implants	[124] 2025
3YSZ	Direct ink printing	1325°C, 1350°C, and 1375°C, 1 h, 1.5 h, and 2 h	0.1-400	80	$\sigma = 24 \text{ MPa}$	Osteogenic differentiation and bone regeneration	[125] 2024
3YSZ	Fused filament fabrication	1100°C - 1500°C, 1 h	1	-	UTS = 90-105 $MPa$	Large bone segmental	[126] 2024
YSZ	Direct ink writing	1450°C, 2 h	-	61.1-75.3	$\sigma = 20.8-62.9$ MPa	Scaffolds for bone tissue	[127] 2021
YSZ	FDM and freeze drying	1450°C, 2 h	300-450	40	$\sigma = 68.2-89.8$ MPa, E = 1.7-2.6 GPa	Scaffolds for bone tissue	[128] 2021

YSZ /HA	DLP	1400°C, 1.5 h	-	54.6	$\sigma = 52.25 \text{ MPa}$	Scaffolds for bone tissue	[129] 2020
ZrO <sub>2</sub> –PCL	FDM	Room temperature	459.2- 462.7	46.2-47	σ = 5.5-7.9 MPa, E = 43-67 MPa	Scaffolds for bone tissue	[130] 2020
ZrO <sub>2</sub> -HA	DLP	1100°C, 1200°C, and 1250°C, 2 h	-	-	$\sigma_t = 29.4 \%,$ $\sigma_f = 23.9 \%$	Bone tissue engineering	[131] 2019
ZrO <sub>2</sub> - β-Ca <sub>2</sub> SiO <sub>4</sub>	3D Bio plotter	1000°C, 1100°C, 1200°C, 3 h	-	67-73	$\sigma = 3.9-6.1$ MPa	Scaffolds for bone tissue	[132] 2019
YSZ	Robocasting	1350°C, 1 h	200-500	-	-	Scaffolds for bone tissue	[133] 2019
Al <sub>2</sub> O <sub>3</sub> /ZrO <sub>2</sub>	Replica method	1500°C, 1 h	5-2560	78.8	$\sigma = 6.5 \text{ MPa}$	Replacement or bone filling	[134] 2018
YSZ-Al <sub>2</sub> O <sub>3</sub>	Robocasting	1350°C, 2 h	245	50	-	Substrate for bone cells ingrowth	[135] 2018
ZrO <sub>2</sub> -BCP	FDM	1100°C, 2 h	350	-	$\sigma = 0.5 \text{ MPa}$	Scaffolds for bone tissue	[136] 2018
PCL/ZrO <sub>2</sub>	Electrospinning	Room temperature, 2 h	1	-	Excellent fibroblast cell attachment and proliferation	Bone regeneration	[137] 2017
ZrO <sub>2</sub> - β-TCP	3D Bio plotter	1500°C, 5 h	160-226	60-76	$\sigma = 7-12 \text{ MPa}$	Bone regeneration	[138] 2017
ZrO <sub>2</sub> - β-TCP	3D Rapid Prototype / impregnation	1500°C, 5 h	3-705	68-82	σ = 3-15 MPa; E= 184-396 MPa	Bone tissue regeneration	[139] 2017
YSZ-PVP	Electrospinning	850°°°, 2 h	-	-	E = 1.11 MPa	Bone regeneration	[140] 2016

# Appendix B.

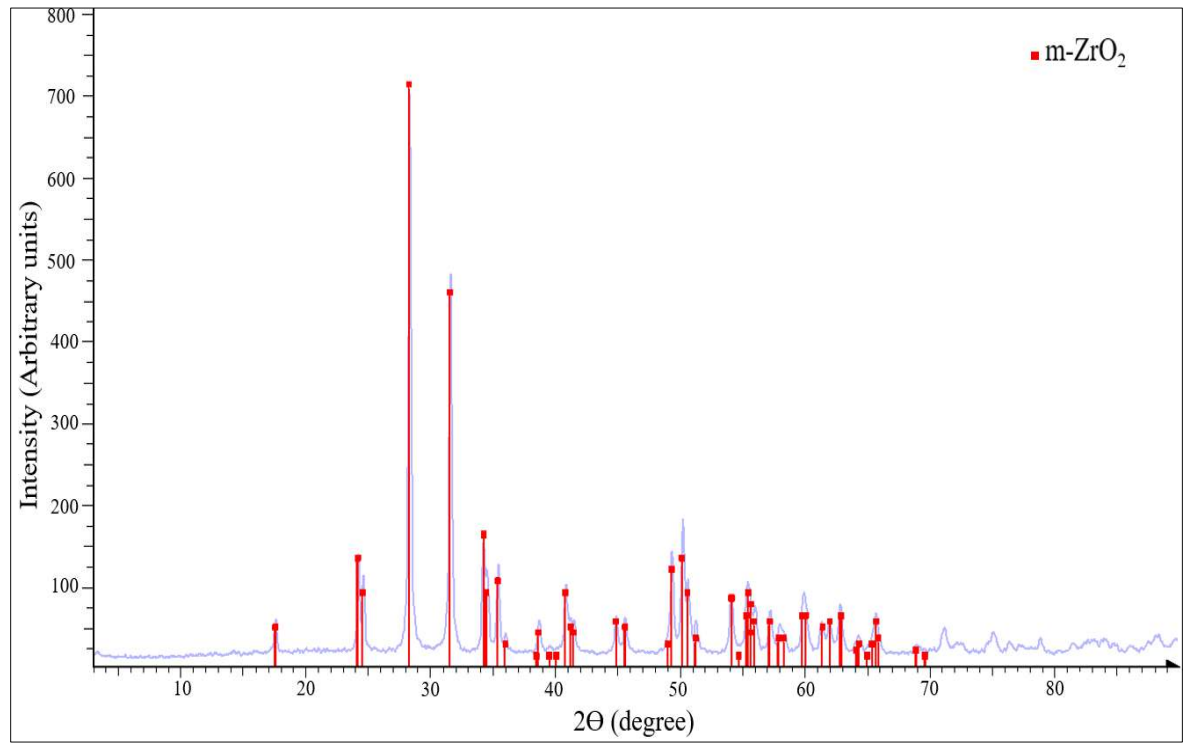


Fig. XRD pattern for m-ZrO<sub>2</sub> powder

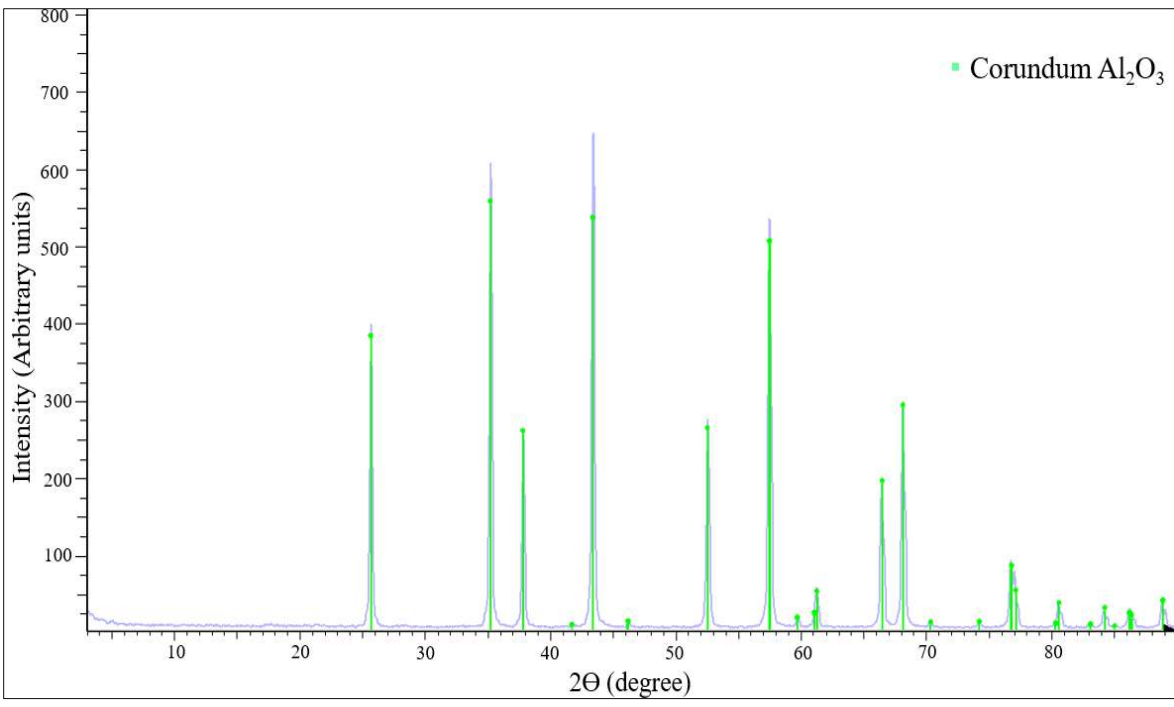


Fig. XRD pattern for Al<sub>2</sub>O<sub>3</sub> powder

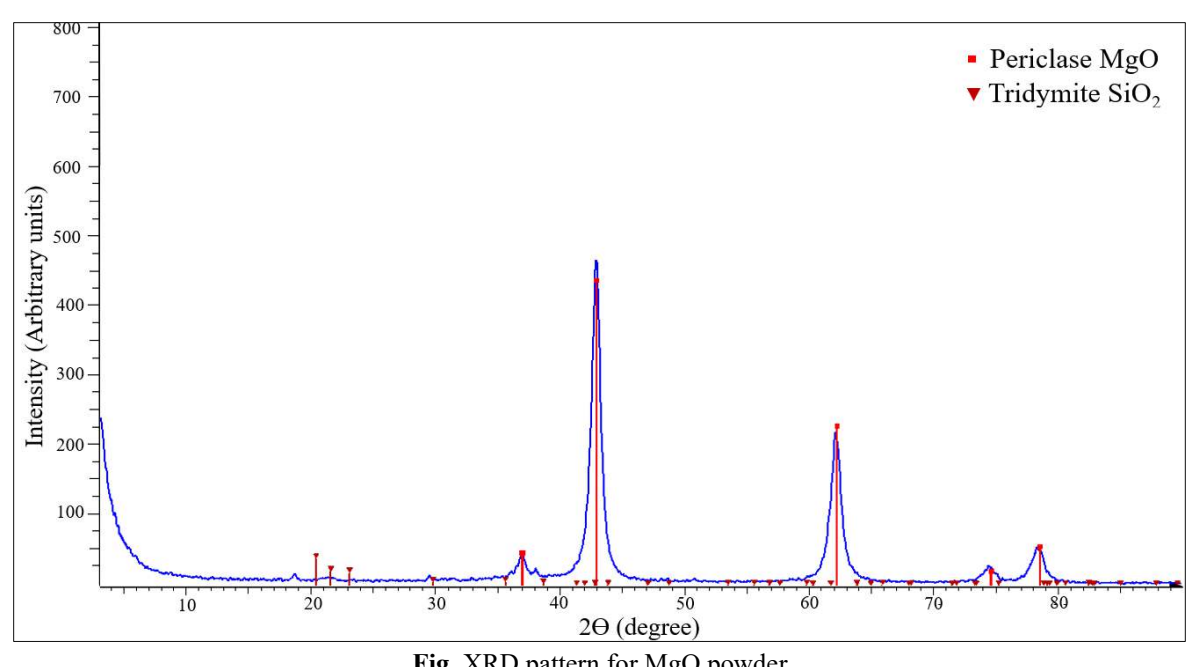


Fig. XRD pattern for MgO powder